



**HAL**  
open science

# Expansion and stresses induced by crystallization in cement-based materials in presence of sulfates

Nam Nghia Bui

► **To cite this version:**

Nam Nghia Bui. Expansion and stresses induced by crystallization in cement-based materials in presence of sulfates. Materials. Université Paris-Est, 2016. English. NNT: 2016PESC1096 . tel-01459137

**HAL Id: tel-01459137**

**<https://pastel.hal.science/tel-01459137>**

Submitted on 7 Feb 2017

**HAL** is a multi-disciplinary open access archive for the deposit and dissemination of scientific research documents, whether they are published or not. The documents may come from teaching and research institutions in France or abroad, or from public or private research centers.

L'archive ouverte pluridisciplinaire **HAL**, est destinée au dépôt et à la diffusion de documents scientifiques de niveau recherche, publiés ou non, émanant des établissements d'enseignement et de recherche français ou étrangers, des laboratoires publics ou privés.



UNIVERSITÉ PARIS-EST  
ÉCOLE DOCTORALE SCIENCE INGÉNIERIE ET ENVIRONNEMENT

THÈSE

présentée pour l'obtention du diplôme de

**DOCTEUR**

**DE**

**L'UNIVERSITÉ PARIS-EST**

Spécialité: *Science des Matériaux*

par

Nam Nghia BUI

Sujet de la thèse :

Expansion and stresses induced by  
crystallization in cement-based materials in  
presence of sulfates

Thèse soutenue le 28 Janvier 2016 devant le jury composé de :

<i>Rapporteurs :</i>	<b>Prof. Robert FLATT</b>	ETH Zürich
	<b>Prof. George SCHERER</b>	Princeton University
<i>Examineurs :</i>	<b>Dr. Rémi BARBARULO</b>	LafargeHolcim Centre de Recherche
	<b>Prof. Denis DAMIDOT</b>	Ecole Nationale Supérieure des Mines de Douai
	<b>Dr. Matthieu VANDAMME</b>	Ecole des Ponts ParisTech
<i>Directeur de thèse :</i>	<b>Dr. Jean-Michel PEREIRA</b>	Ecole des Ponts ParisTech



*A tribute to Dr. Gilles Chanvillard...*  
*To my loving family...*

*If you cannot explain it simply, you do not understand it well enough*  
Albert Einstein



# Remerciements

Ces trois années ont été riches en rencontres et en expériences qui ont participé, de près ou de loin, à l'avancée de ces travaux.

Je tiens avant tout à remercier sincèrement mon équipe d'encadrant pour leur direction scientifique et la confiance qu'ils m'ont accordée. Un grand merci au Dr. Jean-Michel Pereira qui, en plus d'être un très bon directeur de thèse, m'a permis de profiter de son expertise en physique et mécanique des sols. Merci particulièrement au Dr. Matthieu Vandamme, dont les connaissances et la curiosité scientifique m'étonneront toujours, pour avoir épaulé mon travail pendant ces trois années. Je tiens à remercier sincèrement Dr. Rémi Barbarulo pour ses conseils précieux et sa gentillesse, ainsi que pour m'avoir permis de profiter de sa forte expertise sur les matériaux cimentaires. Leurs connaissances, leurs performances scientifiques, leur rigueur et leur efficacité m'ont beaucoup impressionné et m'ont permis d'évoluer progressivement dans un environnement très motivant.

J'aimerais également remercier l'ensemble des membres du jury pour l'intérêt qu'ils ont manifesté pour ces travaux et leurs questions et remarques constructives. J'exprime mes plus sincères remerciements aux Professeurs George Scherer (Princeton University) et Robert Flatt (ETH Zürich) pour le temps qu'ils ont consacré au rapport sur mon manuscrit. Je remercie également Prof. Denis Damidot (École nationale supérieure des mines de Douai) pour m'avoir fait l'honneur de présider ce jury. Leurs présenter mes travaux, qui était un grand rêve en début de thèse, est un grand honneur pour un jeune travaillant sur le sujet de la 'cristallisation dans les milieux poreux'.

J'aimerais dédier les résultats obtenus dans ce travail au Dr. Gilles Chanvillard avec toute ma reconnaissance. Un grand merci au Dr. Gilles Chanvillard que je considère comme 'le père du projet', pour ses conseils scientifiques, sa gentillesse et son excellent soutien au cours du projet.

Je tiens à remercier Emmanuel De Laure, Baptiste Chabot, Marine Lemaire, Hocine Delmi et Xavier Boulay pour leur aide très professionnelle et efficace

pendant ce travail. J'espère qu'ils m'excuseront de toutes mes incursions intempestives dans leur bureau, lorsque j'arrivais en disant « Désolé, le capteur est cassé » ou « Merci beaucoup, ça marche très bien » ! J'en profite pour remercier Mohamed Saad qui m'a initié à la subtilité des méthodes d'analyse chimique. Un grand merci à Vinh Phuc Tran pour nos discussions très profitables sur les méthodes et outils numériques qui m'ont permis d'analyser mes données expérimentales volumineuses plus efficacement.

La plus grande partie des caractérisations microstructurales et minéralogiques a été réalisée au LafargeHolcim Centre de Recherche. Je tiens à remercier Sylvette, Sébastien, Samuel, Frédérique, Fabienne, Didier, Anthony, Sandrine, Quoc-Huy, Hoang-Chien, car en plus de leur gentillesse et de leur travail de qualité, ils m'ont beaucoup aidé à mener à bien les analyses expérimentales. Merci vivement aux Dr. Bruno Huet, Dr. Pipat Termkhajornkit et Dr. Ellis Gartner (actuellement à Imperial College, London) pour nos discussions qui m'ont permis de profiter au mieux de leur grande expertise sur les matériaux cimentaires.

J'en profite pour remercier les Dr. Grégory Tricot (Université de Lille) et Dr. Jørgen Skibsted (Aarhus University) pour leurs résultats de grande valeur en Résonance Magnétique Nucléaire ( $^{27}\text{Al-NMR}$ ), qui ont contribué considérablement à mes études.

Ces travaux n'auraient bien sûr pas vu le jour sans le soutien financier et technique du laboratoire Navier, de l'École Nationale des Ponts ParisTech et de LafargeHolcim Centre de Recherche. Mes remerciements au Prof. Karam Sab, directeur laboratoire et au Dr. Michel Bornert, chef de l'équipe Multi-Echelle, pour m'avoir accueilli au laboratoire Navier.

Un grand merci à Cécile Blanchemanche, Rachida Atmani, Brigitte Vigo et Marie-Françoise Kaspi, qui, en plus de m'avoir apporté un support administratif très professionnel, m'ont permis de travailler dans un environnement très sympathique et agréable.

Merci particulièrement à mes amis, Ababacar, Abdessamad, Abudushalamu, Benoit, Dong, Géraldine, Hafsa, Jamie, Laurent, Nathan, Nicolas, Vinh-Du et Van-Tri pour leur amitié et leur bonne humeur qui m'ont permis d'évoluer dans un environnement plaisant et convivial.

Pour finir, je remercie chaleureusement mes parents et mes beaux-parents Thi Kim Thanh Nguyen, Vinh Long Bui, Thi Chi Vu et Tuan Hiep Hoang pour leur soutien infailible : ils sont indispensables à mon équilibre. Ces trois années en France m'ont permis de rencontrer celle qui partage aujourd'hui ma vie, Thao Nguyen Hoang. Merci à ma compagne pour son soutien sans faille pendant toutes ces années. Et bienvenue à Louise Bui, qui a déjà changé nos jours et nos nuits!



# Abstract

In-pore crystallization of salt can lead to a macroscopic deformation and eventually to a damage of the porous materials in which crystallization occurs. The damage of these materials (e.g., stones, bricks, or cement-based materials) translates into a decrease of the lifespan of the structures or of the structural elements (e.g., building foundations, bridge pillars) made with these materials. This phenomenon is also widely recognized as a significant threat to the long-term survival of ancient buildings, to civil-engineering structures with marine exposures, or to the long-term reliability of nuclear waste storage. A better understanding of how crystallization induces deformation of porous materials is a prerequisite to designing efficient ways of mitigating the detrimental effects of salt crystallization.

In this thesis, we aim at understanding how crystallization leads to expansion, for cement-based materials in the specific case of the presence of sulfate ions, which is a case representative of sulfate attacks. With respect to other porous materials, a specificity of cement-based materials is that they are complex porous multiscale materials in which the matrix can react chemically with foreign chemical products: e.g., sulfates from the pore solution can react with monosulfoaluminates and calcium phases to produce ettringite or gypsum.

The main originality of the study was to perform experiments with granular materials compacted into oedometric or isochoric cells. The tested samples were manufactured by grinding  $C_3S$  pastes, regular Portland cement pastes, or mixtures of phases of which those pastes are made (e.g., monosulfoaluminate AFm or portlandite CH), and then compacting them within the cell into 2-cm-high cylindrical specimens. In the cells, the highly permeable compacted samples could be flushed with sodium sulfate solutions in less than 1 hour. In an oedometric cell, the sample is prevented from expanding radially, but is allowed to expand axially: we measured how injections of solutions induced an axial expansion. In an isochoric cell, the sample is prevented from expanding both radially and axially: we measured how in-

jections of solutions induced the development of axial and radial stresses. Thanks to the original protocol we developed, expansion or development of stresses started immediately after the injection of solution, stabilized after a few days to a few dozen days, and crystallization occurred homogeneously throughout the height of the sample.

With the developed protocol, with the oedometric cells, we investigated the role of various parameters on crystallization-induced expansions/stresses, e.g., role of mineralogy, or importance of relative localization of monosulfoaluminate or ettringite w.r.t. C-S-H. To address those questions, before and after testing, mineralogical and microstructural characterizations of the samples were performed by using a variety of techniques, including: X-ray fluorescence (XRF), thermogravimetric analysis (TGA), X-ray diffraction (XRD), aluminum nuclear magnetic resonance ( $^{27}\text{Al}$ -NMR) and scanning electron microscopy with X-ray analysis (SEM-EDS). One interesting conclusion is that, even when ettringite crystallizes in macropores, i.e., outside of the C-S-H gel porosity, ettringite can lead to an expansion. Also, we showed that gypsum crystallization contributes to expansion.

In the isochoric cell, we performed experiments in which various sodium sulfate solutions were injected, whose concentration in sulfates ranged from 3 to 1190 mmol/L. A salient feature of the isochoric cells we developed is that all solution flushed throughout the sample could be recovered: thus, from the measurements of concentrations and volumes of input and output solutions, the amount of sulfate remaining in the sample over the experiments could be determined. The evolutions of the output concentrations and of the mineralogy over the injection process could be well predicted with the geochemical modeling software CHESS and the thermodynamic database Cemdata14. Experimental results of the campaign, in conjunction with results from mineralogical and microstructural characterizations, made it possible to reveal what the main parameters are that govern expansion. Among others, we show that both crystallization of ettringite and of gypsum can induce stresses, and that the magnitude of those stresses is linearly related to the volume of those crystals formed.

The conclusions drawn from this experimental study make it possible

to better understand the physical processes through which crystallization induces expansion or stresses in porous solids, and thus to orient the modeling of sulfate attacks in cement-based materials.

*Keywords:* Cementitious materials, sulfate attacks, expansion, crystallization, crystallization pressure, crystal growth, ettringite, gypsum, thermodynamic modeling, SEM-EDS,  $^{27}\text{Al}$ -NMR.



# Résumé

La cristallisation du sel dans les pores peut conduire à une déformation macroscopique et par la suite à un endommagement des matériaux poreux, dans lequel la cristallisation se produit. Les dégâts de ces matériaux (par exemple, des pierres, des briques, ou des matériaux à base de ciment) se traduit par une diminution de la durée de vie des structures ou des éléments de structure (par exemple, les fondations du bâtiment, piliers de pont) fabriqués avec ces matériaux. Ce phénomène est aussi largement reconnu comme une menace importante pour la survie à long terme des anciens bâtiments, à des structures de génie civil avec des expositions marines, ou à la fiabilité à long terme de stockage de déchets nucléaires. Une meilleure compréhension de la façon dont la cristallisation induit la déformation des matériaux poreux est une condition préalable à la conception de moyens efficaces d'atténuer les effets néfastes de la cristallisation du sel.

Dans cette thèse, nous cherchons à comprendre comment la cristallisation conduit à l'expansion, pour les matériaux à base de ciment dans le cas spécifique de la présence d'ions sulfate, qui est un cas représentatif d'attaques sulfatiques. En ce qui concerne d'autres matériaux poreux, une spécificité de matériaux à base de ciment est qu'ils sont des matières poreuses complexes multi-échelles dans lesquelles la matrice peut réagir chimiquement avec des produits étrangers: par exemple, les sulfates de la solution interstitielle peuvent réagir avec les monosulfoaluminates et les phases de calcium afin pour produire de l'ettringite ou du gypse.

La principale originalité de l'étude était de réaliser des expériences avec des matériaux granulaires compactés dans des cellules ou œdométriques isochores. Les échantillons testés ont été fabriqués par broyage  $C_3S$  pâtes, des pâtes de ciment Portland ordinaire, ou des mélanges de phases dont les pâtes sont faites (par exemple, monosulfoaluminate AFm ou portlandite CH), puis de les compacter dans des éprouvettes cylindriques sur une hauteur de 2 cm. Dans les cellules, les échantillons compactés sont très perméables et peuvent être saturés avec des solutions de sulfate de sodium en moins de 1 heure.

Dans une cellule œdométrique, l'échantillon est empêché de se dilater radialement, mais est autorisé à s'étendre axialement: nous avons mesuré comment des injections de solutions induisent une expansion axiale. Dans une cellule isochore, l'échantillon est empêché de se dilater à la fois radialement et axialement: nous avons mesuré comment des injections de solutions provoquent le développement de contraintes axiales et radiales. Grâce à ce protocole original que nous avons développé, l'expansion ou le développement de contrainte a commencé immédiatement après l'injection de la solution, s'est stabilisé au bout de quelques jours à quelques dizaine de jours, et la cristallisation a eu lieu de façon homogène sur toute la hauteur de l'échantillon.

Avec le protocole mis au point, avec les cellules œdométriques, nous avons étudié le rôle des différents paramètres sur des expansions/ contraintes d'expansion induits par cristallisation, par exemple, le rôle de la minéralogie, ou l'importance de la localisation relative de monosulfoaluminate ou ettringite par rapport aux C-S-H. Pour répondre à ces questions, avant et après le test, les caractérisations minéralogiques et microstructurales des échantillons ont été effectuées en utilisant une variété de techniques, y compris: la fluorescence X (FX), analyse thermogravimétrique (ATG), diffraction des rayons X (DX), résonance magnétique nucléaire d'aluminium ( $^{27}\text{Al-NMR}$ ) et la microscopie électronique à balayage avec analyse aux rayons X (MEB-EDX). Une conclusion intéressante est que, même lorsque l'ettringite cristallise dans les macropores, à savoir, en dehors de la porosité de gel C-S-H, l'ettringite peut conduire à une expansion. En outre, nous avons montré que la cristallisation du gypse contribue à l'expansion.

Dans la cellule isochore, nous avons réalisé des expériences dans lesquelles diverses solutions de sulfate de sodium ont été injectés, dont la concentration en sulfates variait de 3 à 1190 mmol/L. Un point notable des cellules isochores que nous avons développé est que toute solution s'évacue le long de l'échantillon et peut être récupérée: ainsi, à partir des mesures des concentrations et des volumes de solutions d'entrée et de sortie, la quantité de sulfate restant dans l'échantillon au cours des expériences pourrait être déterminée. Les évolutions des concentrations de sortie et de la minéralogie sur le processus d'injection pourraient être bien prédits avec le logiciel CHESS de

modélisation géochimique et de la base de données thermodynamiques Cemdata14. Les résultats expérimentaux de la campagne, en conjonction avec les résultats des caractérisations minéralogiques et microstructurales, ont permis de révéler quels sont les principaux paramètres qui régissent l'expansion. Entre autres, nous montrons que les deux cristallisation d'ettringite et de gypse peuvent induire des contraintes, et que l'amplitude de ces contraintes est en relation linéaire avec le volume de ces cristaux formés.

Les conclusions tirées de cette étude expérimentale permettent de mieux comprendre les processus physiques à travers lesquels la cristallisation entraîne l'expansion ou les contraintes dans des solides poreux, et permettent d'orienter la modélisation des attaques sulfate dans les matériaux à base de ciment.

*Mots clés* : Matériaux cimentaires, attaques sulfatiques, expansion, cristallisation, pression de cristallisation, croissance de cristal, ettringite, gypse, modélisation thermodynamique, MEB-EDS, RMN-<sup>27</sup>Al



# Contents

<b>Contents</b>	<b>17</b>
<b>List of Figures</b>	<b>23</b>
<b>List of Tables</b>	<b>33</b>
<b>1 Introduction</b>	<b>37</b>
1.1 Sulfate attacks of cement-based structures . . . . .	39
1.2 Synthesis of laboratory studies of sulfate-induced expansions in cement-based materials . . . . .	42
1.2.1 Typical experiments . . . . .	42
1.2.2 Respective role of ettringite and gypsum in expansion of cementitious materials subjected to sulfate attacks . . . . .	44
1.2.3 Role of sulfate concentration . . . . .	49
1.2.4 Role of mechanical load or restraint . . . . .	50
1.2.5 Conclusions . . . . .	51
1.3 Other cases of crystallization-induced expansion . . . . .	52
1.3.1 Other cases of crystallization-induced expansion in cement- based materials . . . . .	52
1.3.2 Cases of crystallization-induced expansion in other ma- terials . . . . .	54
1.4 Applications subjected to crystallization-induced expansion . . . . .	55
1.4.1 Underground storage of nuclear waste . . . . .	55
1.4.2 Historic monuments conservation . . . . .	57
1.4.3 Durability of civil engineering structures . . . . .	58

## CONTENTS

---

1.5	Mechanisms through which crystallization induces an expansion	59
1.5.1	Crystallization pressure: historical overview, Correns's law and its extensions	60
1.5.2	Highlights in crystallization pressure theory	63
1.5.3	Alternative proposed mechanisms	66
1.6	Motivations and objectives	67
1.7	General strategy and thesis outline	68
<b>2</b>	<b>Materials and methods</b>	<b>71</b>
2.1	Materials	73
2.1.1	Ingredients	73
2.1.2	Grinding and mixing of ingredients	76
2.1.3	Materials preparation	76
2.2	Compaction and testing	79
2.2.1	Compaction and testing in oedometric cell	80
2.2.2	Compaction and testing in isochoric cell	84
2.2.3	Rationale for grinding and compaction protocol	87
2.2.4	Measurement of sulfate concentrations	90
2.3	Methods for characterization of phase assemblage and microstructure	92
2.3.1	Characterization of aluminates phases by $^{27}\text{Al}$ -NMR	93
2.3.2	Other analytical methods: XRF, XRD, TGA, SEM	95
2.3.3	New method of characterization of phase assemblage based on a combination of results from XRF, XRD, TGA and $^{27}\text{Al}$ -NMR	96
2.4	Thermodynamic modeling	97
2.4.1	Thermodynamic calculations of phase assemblage	98
2.4.2	Thermodynamic modeling of evolution of phase assemblage	99
2.5	Comparison between methods for characterizing phase assemblage	103
2.5.1	Method 'Combi': justification and validation	103

2.5.2	Characterization of initial phase assemblage of samples CH-AFm4, C3S-AFm4-a, and C3S-AFm8-a . . . . .	109
2.5.3	Characterization of initial phase assemblage of samples C3S-AFm4-b and C3S-AFm8-b . . . . .	112
2.5.4	Characterization of initial phase assemblage of samples OPC . . . . .	112
2.5.5	Characterization of phase assemblage of samples after exposure to sulfates . . . . .	117
2.5.6	Conclusion on the comparison between various meth- ods for characterization of phase assemblage . . . . .	123
2.6	Experimental program . . . . .	125
2.6.1	List of materials . . . . .	125
2.6.2	List of experiments . . . . .	125
2.7	Summary . . . . .	126
<b>3</b>	<b>Oedometric study of kinetics and role of mineralogy and mi- crostructure</b>	<b>131</b>
3.1	Introduction . . . . .	134
3.2	Materials and methods . . . . .	135
3.3	Results and discussion . . . . .	137
3.3.1	Qualitative description of test on sample OPC . . . . .	139
3.3.2	On the necessity of the presence of C-S-H to observe an expansion . . . . .	141
3.3.3	Correlation between expansion and various composi- tional factors . . . . .	143
3.3.4	Location of AFt leading to expansion . . . . .	146
3.4	Conclusions . . . . .	148
<b>4</b>	<b>Oedometric study of the role of gypsum crystallization in expansion</b>	<b>153</b>
4.1	Introduction . . . . .	155
4.2	Materials and methods . . . . .	156
4.3	Results . . . . .	158

## CONTENTS

---

4.3.1	Qualitative description of evolution of strains . . . . .	158
4.3.2	Predictions of evolution of mineralogy with thermodynamic modeling . . . . .	162
4.3.3	Observation of initial and final mineralogy and microstructure . . . . .	167
4.4	Discussion . . . . .	174
4.4.1	Comparison between experiments C3S-AFm4-a-66 and C3S-AFm4-a-66-1190 . . . . .	175
4.4.2	Respective roles of ettringite and gypsum on expansion	178
4.4.3	Combined roles of ettringite and gypsum in expansion	181
4.5	Results on OPC samples . . . . .	185
4.6	Conclusions . . . . .	191
<b>5</b>	<b>Isochoric study of factors governing expansion stress</b>	<b>195</b>
5.1	Introduction . . . . .	198
5.2	Materials and methods . . . . .	199
5.3	Results and discussion . . . . .	206
5.3.1	Qualitative description of evolution of expansion stress	206
5.3.2	Evolution of anisotropy of stresses . . . . .	212
5.3.3	Qualitative description of evolution of output concentration . . . . .	217
5.3.4	Role of amount of sulfate in sample . . . . .	219
5.3.5	Evolution of phase assemblage and relationship with output sulfate concentration . . . . .	224
5.3.6	Evolution of phase assemblage: the specific case of OPC-3 . . . . .	230
5.3.7	Role of formed solid phases . . . . .	234
5.4	Conclusions . . . . .	243
<b>6</b>	<b>Conclusions and perspectives</b>	<b>245</b>
6.1	Conclusions . . . . .	246
6.1.1	Conclusions on methodology and protocol . . . . .	247

6.1.2	Conclusions on mechanisms of expansion of cement-based materials in presence of sodium sulfates . . . . .	248
6.2	Perspectives . . . . .	249
<b>A</b>	<b>Materials and Methods</b>	<b>251</b>
A.1	Behavior of the compacted powder materials . . . . .	251
A.2	Characterization of aluminate phases by <sup>27</sup> Al NMR . . . . .	251
A.3	Phase Assemblage . . . . .	251
<b>B</b>	<b>Oedometric study of kinetics and role of mineralogy and microstructure</b>	<b>257</b>
B.1	Deformation evolution of referent samples: OPC-Ref(O), C3S-AFm4-a-Ref and C3S-AFm4-b-Ref . . . . .	257
B.2	SEM-EDS analysis on various samples . . . . .	257
<b>C</b>	<b>Oedometric study of the role of gypsum crystallization in expansion</b>	<b>263</b>
C.1	Oedometric study of material OPC . . . . .	263
C.2	Loading effect on expansion . . . . .	265
<b>D</b>	<b>Isochoric study of factors governing expansion stress</b>	<b>269</b>
D.1	Thermodynamic modelling in relation with amount of sulfate remaining in sample . . . . .	269
D.2	Delay of axial stress . . . . .	274
D.3	Evolution of permeability . . . . .	274
D.4	Loading effect on expansion stress? . . . . .	276
	<b>Bibliography</b>	<b>279</b>

## CONTENTS

---

# List of Figures

1.1	California residential house foundation attacked by sulfate-containing ground waters . . . . .	39
1.2	Schematic of formation of zones in OPC exposed to $\text{Na}_2\text{SO}_4$ at $20^\circ\text{C}$ . . . . .	43
1.3	Ettringite needles observed within a tested sample (C3S-AFm4-a) after expansion testing in the present works . . . . .	46
1.4	a. Schematic of stress cell consisting of thin-walled hollow mortar cylinders and central tension bar, b. Spring and tension bared with various diameter and a complete stress cell with mortar cylinder . . . . .	51
1.5	A standard concrete container of the Long-lived and High-level waste (waste B) . . . . .	56
1.6	Disposal cell of Long-lived and High-level waste (waste B). The cell is closed by a bentonite plug and a concrete plug . . .	56
1.7	An example of salt-induced damage which has been recognized in the statue of a soldier in La Rochelle, France . . . . .	58
1.8	Illustration of the crystallization experiments performed by <a href="#">Taber (1916)</a> . . . . .	61
1.9	Crystals in cylindrical pore (left) and in spherical pore (right) with small pore entrances ( <a href="#">Steiger, 2005b</a> ) . . . . .	64
2.1	Schematics of the experimental process. . . . .	73
2.2	Ball mill used for the present work, consisting in a motor, a ceramic container, and ceramic balls. . . . .	76

## LIST OF FIGURES

---

2.3	Grain size distribution of ground $C_3S$ paste and ground OPC paste. . . . .	77
2.4	Schematics of mixing and machine used for mixing. . . . .	79
2.5	Schematics of an oedometer cell and pictures of the oedometer setup. . . . .	81
2.6	Powder materials placed into the oedometer cell. The powder was compacted manually before being compacted mechanically with the loading frame. . . . .	82
2.7	Load profile and resulting strain evolution of sample OPC during compaction into an oedometer cell. . . . .	83
2.8	Compression curve (i.e., mechanical response during compaction into an oedometer cell) of the compacted powder material OPC. . . . .	83
2.9	Pore size distribution of various powder materials compacted into the oedometer cell, as obtained by mercury intrusion porosimetry. . . . .	84
2.10	Schematic of an isochoric cell and photograph of the isochoric setting. . . . .	85
2.11	Stresses during compaction of powder material OPC into an isochoric cell. . . . .	87
2.12	Permeability of material OPC versus the stress of compaction. . . . .	89
2.13	Sulfate concentrations measured by photometry . . . . .	91
2.14	Thermodynamic modeling of the evolution of the phase assemblage of material OPC upon exposure to a solution of sodium sulfate with a concentration equal to 66 mM. . . . .	101
2.15	Phase assemblage of material OPC after exposure to a solution of sodium sulfate with a concentration equal to 66 mM, as predicted with thermodynamic modeling and measured with the method ‘Combi’. . . . .	102
2.16	Chemical composition of material OPC after exposure to a solution of sodium sulfate with a concentration equal to 66 mM, as predicted with thermodynamic modeling and measured with the method XRF. . . . .	102

2.17	Elemental composition of sample OPC obtained with XRF, with the method ‘Combi’ (which includes a correction for carbonation), and with a method ‘Combi’ in which no correction for carbonation would be used. . . . .	105
2.18	Chemical compositions calculated from the phase assemblage obtained with the method ‘Combi’ and measured with XRF: samples (a) CH-AFm4, (b) C3S-AFm4-a and (c) C3S-AFm8-a. . . . .	111
2.19	Chemical compositions calculated from the phase assemblage obtained with the method ‘Combi’ and measured with XRF: samples (a) C3-AFm4-b and (b) C3S-AFm8-b. . . . .	114
2.20	Chemical compositions of 3 OPC samples, measured with XRF. . . . .	115
2.21	SEM-EDS measurement of the Ca/Si and Al/Si ratio of the C-(A)-S-H in material OPC flushed with water only. . . . .	117
2.22	Chemical compositions calculated from the phase assemblage obtained with the method ‘Combi’ and measured with XRF: samples (a) OPC(1), (b) OPC(2), and (c) OPC(3). . . . .	118
2.23	SEM-EDS measurements performed on the C-(A)-S-H gel of sample C3S-AFm8-a after exposure to a sodium sulfate solution with a concentration equal to 66 mM . . . . .	121
2.24	Chemical compositions obtained from phase assemblage determined with the method ‘Combi’, with XRD, and with XRF, for samples (a) C3S-AFm8-a, (b) C3S-AFm8-b and (c) OPC. . . . .	122
3.1	Evolution of deformation induced by injections of water or sodium sulfate solution into samples: (a) OPC, (b) CH-AFm4, (c) C3S-AFm4-a, (d) C3S-AFm8-a, (e) C3S-AFm4-b, and (f) C3S-AFm8-b . . . . .	138
3.2	Phase composition of sample OPC throughout the height of the sample. Surface fractions were determined by SEM-EDS. . . . .	141
3.3	Axial strain versus the normalized amount of sulfate injected . . . . .	142
3.4	Final axial strain of the various tested samples . . . . .	145
3.5	SEM-EDS results on sample OPC . . . . .	147
3.6	SEM-EDS results on sample C3S-AFm4-a . . . . .	149

LIST OF FIGURES

---

4.1	Evolution of axial strain over experiment (a) C3S-sand, (b) C3S-AFm8-a, (c) C3S-AFm4-a-66, and (d) C3S-AFm4-a-66-1190. . . . .	160
4.2	Phase assembly evolution and profile of solution injection of various samples predicted by thermodynamic: (a) C3S-AFm4-a-66 and (b) C3S-AFm4-a-66-1190. . . . .	163
4.3	Phase assembly evolution and profile of solution injection of various samples predicted by thermodynamic: (a) C3S-AFm8-a and (b) C3S-sand. . . . .	164
4.4	Phase assemblage of various samples given by thermodynamic modeling in compared with method Combi . . . . .	165
4.5	Chemical composition given by modeling in compared with XRF	166
4.6	A typical microstructure of sample C3S-AFm4-a before testing	167
4.7	Pockets of ettringite observed by SEM in various samples . . .	168
4.8	Formation of gypsum observed by SEM in various samples . .	169
4.9	SEM-EDS measurements on the sample C3S-sand . . . . .	170
4.10	Chemical composition obtained from phase assembly of various samples before testing . . . . .	171
4.11	Chemical composition obtained from phase assembly of various samples after testing . . . . .	172
4.12	SEM-EDS measurements on the C-S-H gel of sample C3S-AFm8-a after testing . . . . .	173
4.13	Deformation evolution in related with normalized mass of injected sulfate $m_{\text{SO}_4^-}^{\text{in}}/m^0$ . . . . .	175
4.14	Evolution of axial strain over experiment OPC-66-water. . . .	176
4.15	Phase assembly evolution together with the strain evolution of various samples: (a) C3S-AFm4-a-66 and (b) C3S-AFm4-a-66-1190. . . . .	179
4.16	Phase assembly evolution together with the strain evolution of various samples: (a) C3S-AFm8-a and (b) C3S-sand. . . .	180
4.17	Strain resulted by the formation of: a. Ettringite, b. Gypsum.	182
4.18	Strain in function of the volume of the ettringite and gypsum formations. . . . .	183

---

4.19	Schematic of crystallization in pore . . . . .	184
4.20	Strain evolution in various samples: (a) OPC-66(O), (b) OPC-140(O), (c) OPC-315(O), (d) OPC-540(O), and (e) OPC-1190(O). . . . .	187
4.21	Evolution of phase assemblage and expansion for experiments (a) OPC-66(O) ( $\alpha=0.8$ ) and (b) OPC-140(O) ( $\alpha=1.0$ ). . . . .	188
4.21	Strain evolution resulted by volume of the formation of ettringite and gypsum within the sample OPC-66(O) . . . . .	190
4.22	Strain evolution resulted by volume of the formation of ettringite and gypsum within various samples: a. OPC-66(O), b. OPC-140(O), c. OPC-315(O), d. OPC-540(O) and e. OPC-1190(O). . . . .	190
5.1	Chemical composition before testing, back-calculated from the phase assemblage given in Tab. 5.2, and determined by XRF . . . . .	204
5.2	Chemical composition after testing, back-calculated from the phase assemblage given in Tab. 5.2, and determined by XRF . . . . .	205
5.3	Evolution of stresses induced by injection of sodium sulfate solution for experiments (a) OPC-3 and (b) OPC-3-66. . . . .	207
5.4	Evolution of stresses induced by injection of sodium sulfate solution for experiments (a) OPC-66 and (b) OPC-1190. . . . .	208
5.5	Evolution of mean stress induced by injection of sodium sulfate solution for experiments (a) OPC-3 and (b) OPC-3-66. . . . .	209
5.6	Evolution of mean stress induced by injection of sodium sulfate solution for experiments (a) OPC-66 and (b) OPC-1190. . . . .	210
5.7	Variation of mean stress and aqueous fraction of the output solution versus the normalized amount of sulfate injected for experiments (a) OPC-3 and (b) OPC-3-66. . . . .	213
5.8	Variation of mean stress and aqueous fraction of the output solution versus the normalized amount of sulfate injected for experiments (a) OPC-66 and (b) OPC-1190. . . . .	214
5.9	Variations of axial and radial stress versus the normalized amount of injected sulfate for experiments (a) OPC-3 and (b) OPC-3-66. . . . .	215

## LIST OF FIGURES

---

5.10	Variations of axial and radial stresses versus the normalized amount of injected sulfate for experiments (a) OPC-66 and (b) OPC-1190. . . . .	216
5.11	Variation of mean stress versus the normalized amount of sulfate remaining in the sample for experiments (a) OPC-3 and (b) OPC-3-66. . . . .	220
5.12	Variation of mean stress versus the normalized amount of sulfate remaining in the sample for experiments (a) OPC-66 and (b) OPC-1190. . . . .	221
5.13	Variation of mean stress versus the normalized amount of sulfate remaining in the sample for experiments OPC-3, OPC-66, OPC-3-66, and OPC-1190. . . . .	223
5.14	Evolution of phase assemblages and aqueous fractions of output solution for experiments (a) OPC-3 when assuming $\alpha = 1$ (where $\alpha$ is defined in Eq. (5.1) and (5.2)), (b) OPC-3-66, and (c) OPC-3 when assuming $\alpha = 0.4$ . . . . .	225
5.15	Evolution of phase assemblages and aqueous fractions of output solution for experiments (a) OPC-66 and (b) OPC-1190. . . . .	226
5.16	Chemical composition after testing, obtained with thermodynamic modeling and XRF for samples (a) OPC-3, (b) OPC-66, (c) OPC-3-66, (d) OPC-1190, and (e) OPC-3 when assuming $\alpha = 0.4$ (where $\alpha$ is defined in Eq. (5.1) and (5.2)). . . . .	229
5.17	Evolution of aqueous fractions of output solution for experiment OPC-66 predicted by thermodynamic modeling with solid phases submitted to atmospheric pressure, 1.5 MPa and 2.7 MPa. The aqueous phases are at atmospheric pressure in those calculations. The evolution phase assemblage here displayed is the one predicted with calculations at atmospheric pressure. . . . .	231
5.18	SEM-EDS analysis of sample OPC-3: (a) Ratio Al/Ca against to S/Ca and (b) Ratio Si/Ca against Al/Ca. . . . .	232

5.19	Evolution of phase assemblages and variation of mean stress for experiments (a) OPC-3 (when assuming $\alpha=0.4$ ) and (b) OPC-3-66. . . . .	235
5.20	Evolution of phase assemblages and variation of mean stress for experiments (a) OPC-66 and (b) OPC-1190. . . . .	236
5.21	Variation of mean stress versus the normalized variation of solid volume, during experiments OPC-3, OPC-66, OPC-3-66, and OPC-1190. . . . .	237
5.22	Variation of mean stress versus the normalized volume of (a) formed ettringite, (b) formed gypsum, and (c) formed ettringite and gypsum. On all figures, the slope of the dashed lines is 3.42 MPa. . . . .	239
5.23	SEM-EDS analysis of material OPC before testing (i.e., before injection of solution). An intimate mixture of AFm with the C-S-H gel is observed in this material. . . . .	240
5.24	SEM picture of sample OPC-66 after testing (i.e., after injection of solution). Pockets of ettringite are observed. . . . .	240
5.25	SEM-EDS analysis of samples (a) OPC-3-66 and (b) OPC-66, after testing. An intimate mixture of AFt with the C-S-H gel is observed in these samples. . . . .	241
5.26	Variation of mean stress versus the normalized volume of formed ettringite and gypsum, where the evolutions of phase assemblage were calculated based on the measured amounts of sulfates remained in the sample. On all figures, the slope of the dashed lines is 3.42 MPa. . . . .	242
A.1	Behavior of various material: (a) CH-AFm4, (b) C3S, (c) C3S-sand, (d) C3S-AFm4-a, (e) C3S-AFm4-b, (f) C3S-AFm8-a, (g) C3S-AFm8-b and (h) OPC. . . . .	252
A.2	Chemical compositions obtained in various materials based on various $^{27}\text{Al}$ -NMR measurements . . . . .	255
B.1	Evolution of deformation of referent tests induced by injections of water . . . . .	258

LIST OF FIGURES

---

B.2	SEM-EDS results on the sample ‘C3S-AFm4-a-Ref’ . . . . .	259
B.3	SEM-EDS results on the sample ‘OPC-Ref(O)’ . . . . .	260
B.4	SEM-EDS results on the sample ‘OPC-66(O)’ flushed by a solution at 66 mM . . . . .	261
B.5	SEM-EDS results on the sample ‘C3S-AFm8-b’ flushed by a solution at 66 mM . . . . .	262
C.1	Phase assemblage evolution in function of normalized amount of injected sulfate in various samples: (a) OPC-315(O), (b) OPC-540(O) and (c) OPC-1190(O). . . . .	264
C.2	The phase assembly predicted by thermodynamic modeling in various samples: (a) OPC-66(O), (b) OPC-140(O), (c) OPC- 315(O), (d) OPC-540(O) and (e) OPC-1190(O). . . . .	266
C.3	The final chemical composition predicted by thermodynamic modeling in various samples: (a) OPC-66(O), (b) OPC-140(O), (c) OPC-315(O), (d) OPC-540(O) and (e) OPC-1190(O). . . . .	267
C.4	In case of OPC-66(O): Pore structures of material before and after testing obtained by MIP. . . . .	268
C.5	Expansion evolution in various samples: OPC(0.52), OPC(0.52), OPC(0.88) and OPC(1.44). . . . .	268
D.1	Phases evolution with amount of sulfate remaining in sample: (a) OPC-3, (b) OPC-66, (c) OPC-3-66 and (d) OPC-1190. . . . .	270
D.2	Thermodynamic prediction based on amount of injected sul- fate: chemical composition in compared with XRF on various samples after experiments: (a) OPC-3, (b) OPC-66, (c) OPC- 3-66 and (d) OPC-1190. . . . .	271
D.3	Thermodynamic prediction based on amount of remaining sul- fate: phases composition compared with experimental charac- terizations on various samples after experiments: (a) OPC-3, (b). OPC-66, (c). OPC-3-66 and (d). OPC-1190. . . . .	272
D.4	Volume change of solid phases of various samples such as OPC-3, OPC-66, OPC-3-66 and OPC-1190, which is based on amount of sulfate remaining in sample. . . . .	272

D.5 a. Expansion stress in function of normalized amount of: (a) Ettringite; (b) Gypsum and (c) Ettringite and gypsum. On all figures, the slope of the dashed lines is 3.42 MPa. . . . . 273

D.6 Axial stress in function of volume of Ettringite and Gypsum formed which is normalized with initial volume of pores. The slope of the red dashed line is 2.7 MPa. . . . . 274

D.7 Evolution of permeability in function of amount of injected sulfate . . . . . 275

D.8 Variation of means stress in function of amount of sulfate remaining in samples . . . . . 276

D.9 Mineralogy distribution over the height of sample OPC-I(O.52).277

## LIST OF FIGURES

---

# List of Tables

2.1	Chemical composition of the Ordinary Portland cement clinker used, in mass percent. XRF and XRD stand for X-ray fluorescence and X-ray diffraction, respectively. . . . .	74
2.2	Mineralogical composition of C <sub>3</sub> S clinker and C <sub>3</sub> A clinker used, estimated by qualitative XRD. ‘SP’ stands for ‘strong probability’, ‘PP’ stands for ‘possible phases or suggested phases’, and ‘-’ stands for ‘not detected’. . . . .	75
2.3	Phase assemblage of the various materials prepared, as obtained by X-ray diffraction, in mass percentage. . . . .	78
2.4	Solid phase density of the prepared powders, as measured by helium pycnometry. . . . .	80
2.5	Properties of the tested samples. The porosity $\phi$ is the porosity of the sample after compaction, but before injection. . . . .	89
2.6	Sources of uncertainties in the measurement of the concentrations in sulfates. . . . .	90
2.7	Distribution of Al <sub>2</sub> O <sub>3</sub> in various materials before injection of sulfates, characterized by <sup>27</sup> Al-NMR. . . . .	94
2.8	Phase assemblage of material OPC, after grinding, and after flushing with water. . . . .	104
2.9	Ratios CaO/SiO <sub>2</sub> , Al <sub>2</sub> O <sub>3</sub> /SiO <sub>2</sub> , H <sub>2</sub> O/SiO <sub>2</sub> and density $\rho_{C(A)SH}$ of the C-(A)-S-H gel for all materials before exposure to sulfates. . . . .	107

LIST OF TABLES

---

2.10	Ratios $\text{CaO}/\text{SiO}_2$ , $\text{Al}_2\text{O}_3/\text{SiO}_2$ , $\text{H}_2\text{O}/\text{SiO}_2$ considered for the C-(A)-S-H gel for the chemical composition calculated from the phase assemblages measured with the method ‘Combi’ to be close to the one measured with XRF, for samples after exposure to sulfates . . . . .	108
2.11	Initial phase assemblage of samples CH-AFm4, C3S-AFm4-a, and C3S-AFm8-a, obtained with various methods. . . . .	110
2.12	Initial phase assemblage of samples C3S-AFm4-b and C3S-AFm8-b, obtained with various methods. . . . .	113
2.13	Initial phase assemblage of 3 OPC samples, obtained by various methods of characterization. Notation: Fe–Mc stands for Fe-monocarboaluminate. . . . .	116
2.14	Distribution of aluminate phases in samples after exposure to a sodium sulfate solution with a concentration equal to 66 mM, characterized with $^{27}\text{Al}$ -NMR. . . . .	119
2.15	Phase assemblage of samples C3S-AFm8-a, C3S-AFm8-b, and OPC, after exposure to a sodium sulfate solution with a concentration equal to 66 mM, obtained with various methods of characterization. . . . .	120
2.16	Phase assemblage of all materials manufactured in this thesis, as obtained with the method ‘Combi’, in mass percentage . . .	125
2.17	First part of list of experiments carried-out in this thesis . . .	127
2.18	Second part of list of experiments carried-out in this thesis . .	128
3.1	Phase composition of the various samples before and after the experiments, obtained by X-ray diffraction, in mass percentage, with an accuracy of measurement of $\pm 2\%$ . . . . .	136
3.2	Properties of the tested samples. The porosity $\phi$ is the porosity of the sample after compaction, but before injection. . . . .	136
4.1	Mass percentage of the various phases in the various samples, before and after the experiment . . . . .	157

---

4.2	Properties of the tested samples. The porosity $\phi$ is the porosity of the sample after compaction, but before injection of sodium sulfate solution. . . . .	158
4.3	Qualitative mineralogical and microstructural analysis of the various samples. . . . .	162
4.4	Aluminate phases in sample C3S-AFm8-a, provided by $^{27}\text{Al}$ -NMR and by XRD . . . . .	174
4.5	Comparison between two samples C3S-AFm4-a-66 and C3S-AFm4-a-66-1190 . . . . .	177
5.1	Properties of the tested samples. The porosity $\phi$ and the permeability of the samples were obtained after compaction, but before injection of water. The bulk modulus is measured at 880 kPa . . . . .	200
5.2	Phase assemblage of samples OPC-3, OPC-3-66, OPC-66, and OPC-1190, before and after testing. . . . .	201
5.3	Distribution of aluminate phases $\text{Al}_2\text{O}_3$ characterized by $^{27}\text{Al}$ -NMR, before and after testing, for samples OPC-3, OPC-3-66, OPC-66, and OPC-1190. . . . .	203
5.4	Density $\rho_{\text{C(A)SH}}$ ( $\text{g}/\text{cm}^3$ ) of C-(A)-S-H that needs to be chosen to retrieve the density of the solid phase measured by helium pycnometry. . . . .	203
5.5	Mass fraction of aluminate and sulfate phases, as predicted by thermodynamic modeling (label ‘Model’) and as characterized with the method ‘Combi’. . . . .	228
A.1	Phases distribution in $\text{Al}_2\text{O}_3$ characterized by $^{27}\text{Al}$ -NMR of various materials. These results are given from Laboratory ‘Laboratoire de Spectrochimie Infrarouge et Raman (LASIR)’, Lille University of Science and Technology, France, by Grégory Tricot. . . . .	253

## LIST OF TABLES

---

A.2	Phases distribution in $\text{Al}_2\text{O}_3$ characterized by $^{27}\text{Al}$ -NMR of various materials. These results are given by $^{27}\text{Al}$ -NMR characterizations, performed at Department of Chemistry, Aarhus University, Denmark. . . . .	254
A.3	Ratios $\text{CaO}/\text{SiO}_2$ , $\text{Al}_2\text{O}_3/\text{SiO}_2$ , $\text{H}_2\text{O}/\text{SiO}_2$ and density $\rho_{\text{C(A)SH}}$ of the C-(A)-S-H gel for various samples based on various $^{27}\text{Al}$ -NMR measurements . . . . .	254
A.4	Phase assemblage of other tested samples in this thesis, as obtained with the method ‘Combi’, in mass percentage. . . . .	256
A.5	Ratios $\text{CaO}/\text{SiO}_2$ , $\text{Al}_2\text{O}_3/\text{SiO}_2$ of various material before testing were obtained by methods SEM-EDS and $^{27}\text{Al}$ -NMR. The density of C-(A)-S-H $\rho_{\text{C(A)SH}}$ was estimated based on phase assembly displayed in Tab. 2.16 to retrieve the density of the solid phase displayed in Tab. 2.4. . . . .	256

# Chapter 1

## Introduction

---

**T**HIS CHAPTER presents an overview of the phenomenon of expansion and/or damage of porous solids induced by salt crystallization, and of the applications for which studying this phenomenon is of interest. We first introduce the topic of sulfate attacks in cement-based materials, which can significantly limit the lifespan of concrete constructions. An adequate bibliographic study allows us to better identify the actual key challenges posed, before formulating the main questions to be answered in this thesis. We also review other cases of damages caused by salt in cementitious materials (*i.e.*, delayed ettringite formation (noted DEF), and freeze-thaw cycles) and in other porous solids (*e.g.*, stone, soils). We highlight applications for which crystallization-induced deformations play a role, namely: nuclear waste storage, conservation of historical monuments, or durability of civil engineering infrastructures. Various hypotheses that can be found in the literature to explain why in-pore crystallization can induce expansion and/or damage (*e.g.*, crystallization pressure, hydration force, increase of solid volume) are reviewed; the limits of those approaches are underlined, in particular with respect to the specific case of cement-based materials subjected to sulfate attacks. From the actual state of art, we infer the main scientific questions of this thesis and propose a strategy to answer them, from which the thesis outline follows.

---

**C**E CHAPITRE présente une vision globale du phénomène d'expansion et/ou d'endommagement de solides poreux induits par une cristallisation de sel, et des applications pour lesquelles étudier ce phénomène est d'intérêt. Nous introduisons tout d'abord le sujet des attaques sulfatiques dans les matériaux à base cimentaire, qui peuvent limiter significativement la durée de vie des constructions en béton. Une étude bibliographique adéquate sur ce sujet nous permet de mieux identifier les principaux défis existants, avant de formuler les principales questions à résoudre dans cette thèse. Nous examinons également d'autres cas d'endommagement induit par le sel dans les matériaux cimentaires (par exemple, formation différée d'ettringite, gel-dégel) ainsi que dans d'autres matériaux poreux (par exemple, la pierre, les sols). Nous soulignons les applications pour lesquelles les déformations induites par la cristallisation jouent un rôle, telles que : le stockage des déchets nucléaires, la conservation des monuments historiques, ou la durabilité des infrastructures du génie civil. Diverses hypothèses qui peuvent être trouvées dans la littérature pour expliquer pourquoi la cristallisation dans les pores peut induire une expansion ou un endommagement (par exemple, la pression de cristallisation, les forces d'hydratation, ou l'augmentation du volume solide) sont passées en revue ; les limites de ces approches sont soulignées, en particulier vis-à-vis du cas particulier des matériaux cimentaires soumis à des attaques sulfatiques. Partant de l'état de l'art, nous établissons les questions scientifiques principales de cette thèse et proposons une stratégie pour y répondre. De ce cheminement découle le plan de thèse.

---

## 1.1 Sulfate attacks of cement-based structures

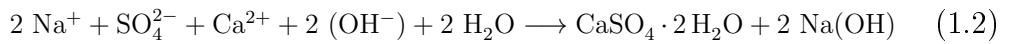
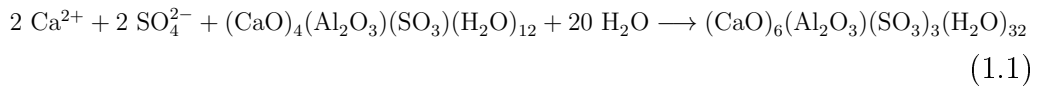
Sulfate attacks have been widely recognized as a serious threat towards the long-term durability of cement-based material since [Le Chatelier \(1887\)](#), [Candlot \(1898\)](#), and [Lafuma \(1929\)](#). Such attacks are typically observed in concrete foundations exposed to groundwater ([Tulliani et al., 2002](#); [Marchand et al., 2002a](#)) or seawater ([Mather, 1964](#)). Damage is observed after months or even years ([Schmidt et al., 2009](#); [Chabrelie, 2010](#); [Yu et al., 2013](#)) and manifests itself through the apparition of cracks and spalling ([Reading, 1982](#); [Chabrelie, 2010](#); [Gollop and Taylor, 1996](#); [Yu et al., 2013](#)). [Photo 1.1](#) shows the typical damage of a foundation of a residential house in Southern California, which has been exposed to ground water containing high levels of sulfates: the attack induced a volumetric expansion, spalling, and efflorescence ([Rzonca et al., 1990](#); [Novak and Colville, 1989](#); [Haynes, 2002](#); [Marchand et al., 2002a](#)). Nowadays, this issue still poses significant challenges for civil engineers in terms of the long-term behavior of cementitious structures (e.g., for bridge foundations or nuclear waste storage) in their environment ([Le Bescop and Solet, 2006](#); [Escadeillas and Hornain, 2008](#); [ANDRA, 2005b](#)).



Figure 1.1: Foundation of residential house in California, attacked by sulfate-rich ground waters. The attack caused volumetric expansion, spalling, and efflorescence. Pictures credit: J. Skalny.

Cement-based materials are complex multi-scale porous solids (Ulm et al., 2004) whose solid matrix can react chemically with solutions containing sulfates (Chanvillard and Barbarulo, 2011; Lothenbach et al., 2010). The sulfates may originate from various sources such as: regulators of cement setting added directly to the mix (i.e., gypsum), polluted aggregates, groundwater, rainwater, seawater, and so on (Taylor, 1996; Meijer and Van Rosmalen, 1984; Kreijger, 1983; Le Bescop and Solet, 2006; Meybeck, 2003). Depending on where sulfates originate from, the sulfate attacks are referred to as either external or internal (Ouyang et al., 1988; Taylor, 1998).

During external sulfate attacks, upon the diffusive ingress of sulfate ions through the porosity of the material, chemical reactions occur, which lead to the crystallization of gypsum and ettringite according to the following reactions (Taylor, 1998; Escadeillas and Hornain, 2008; Gollop and Taylor, 1992):



where  $\text{CaSO}_4 \cdot 2\text{H}_2\text{O}$  is gypsum (noted C\$H<sub>2</sub> in cement chemistry notation),  $(\text{CaO})_4(\text{Al}_2\text{O}_3)(\text{SO}_3)(\text{H}_2\text{O})_{12}$  is monosulfoaluminate (noted AFm in cement chemistry notation), and  $(\text{CaO})_6(\text{Al}_2\text{O}_3)(\text{SO}_3)_3(\text{H}_2\text{O})_{32}$  is ettringite (noted AFt in cement chemistry notation). External attacks can lead to various consequences such as leaching, decalcification of calcium silicate hydrates (noted C-S-H) which manifests itself from a decrease of their ratio  $\text{CaO}/\text{SiO}_2$ , volumetric expansion, damage (e.g., occurrence of cracking or spalling) (Taylor, 1998; Escadeillas and Hornain, 2008). In case of mutual occurrence of sulfate attack and carbonation, thaumasite  $(\text{CaO})_3(\text{SiO}_2)(\text{SO}_3)(\text{CO}_2)(\text{H}_2\text{O})_{15}$   $3 \text{CaOSiO}_2\text{SO}_3\text{CO}_2 \cdot 15 \text{H}_2\text{O}$  can form if certain conditions are met, which are: temperature of 5-10°C, adequate supplies of  $\text{SO}_4^{2-}$  and  $\text{CO}_3^{2-}$  ions, and pres-

## 1.1. SULFATE ATTACKS OF CEMENT-BASED STRUCTURES

---

ence of reactive aluminates  $\text{Al}_2\text{O}_3$  (Cramond, 1985; Schmidt, 2007; Schmidt et al., 2008). Such formation can cause damage but was identified as a main cause of deterioration in very few cases (Taylor, 1998). With sodium sulfate  $\text{Na}_2\text{SO}_4$ , the chemical reactions only involve  $\text{SO}_4^{2-}$  ions but not the  $\text{Na}^+$  ions, while, with magnesium sulfate  $\text{MgSO}_4$ , the  $\text{Mg}^{2+}$  ions also participate to the chemical reactions, leading to the formation of brucite  $\text{Mg}(\text{OH})_2$  and poorly crystalline serpentine  $3\text{MgO} \cdot \text{SiO}_2 \cdot 2\text{H}_2\text{O}$ . Many studies reported that a solution of  $\text{MgSO}_4$  was more aggressive than a solution of  $\text{Na}_2\text{SO}_4$  (Bonen and Cohen, 1992b,a; Gollop and Taylor, 1992; Rasheeduzzafar and Abduljauwad, 1994; Gollop and Taylor, 1996).

Polluted aggregates, notably in the Maurienne region in France, contain gypsum which can cause internal sulfate attacks (Colas, 2013), in the sense that the sulfates are directly present in the initial mix. Gypsum also releases  $\text{Ca}^{2+}$  and  $\text{SO}_4^{2-}$  ions, which react with monosulfoaluminate to form an expansion-inducing ettringite, with little or no dissolution of portlandite (noted CH in cement chemistry notation) and no decalcification of C-S-H (Cramond, 1984; Chengsheng Ouyang and Wen F. Chang, 1987).

In practice, one can provide recommendations of both physical and chemical types to limit damage resulting from external sulfate attacks in cementitious structures. The first recommended measure is to reduce the ability of sulfate ions to penetrate into the cementitious materials (Taylor, 1998; Escadeillas and Hornain, 2008). A good compaction, a decrease of the water-to-binder ratio ( $w/c$ ), an addition of fines and ultrafines are efficient solutions to limit the accessibility of aggressive agents from the surrounding environment (Goto and Roy, 1981; Hjorth, 1983). Another measure is to decrease the amount of tricalcium aluminate  $3\text{CaOAl}_2\text{O}_3$  (noted  $\text{C}_3\text{A}$  in cement chemistry notation) in the material, as it was shown to be correlated with the magnitude of the expansion (Ouyang et al., 1988). In addition, mineral additions such as slag or fly ash to ordinary Portland cements (noted OPC) can improve efficiently their resistance to an ingress of sodium sulfate  $\text{Na}_2\text{SO}_4$  (Cramond, 1985; Gollop and Taylor, 1995; Plowman and Cabrera, 1996; Ping and Beaudoin, 1992b; Scrivener and Campas, 2003).

## 1.2 Synthesis of laboratory studies of sulfate-induced expansions in cement-based materials

### 1.2.1 Typical experiments

Often, laboratory studies of sulfate-induced expansion of cementitious materials are designed to characterize the potential expansion significantly faster than would occur in the real structure. According to the literature (Gollop and Taylor, 1992; Schmidt et al., 2009; Rozière et al., 2009; Chabrelie, 2010; Yu et al., 2013), the usual protocol for expansion testing includes the following:

- The samples usually are rectangular prisms of mortar prepared in standard conditions (i.e., curing for 90 days in saturated limewater at 20°C).
- The samples are immersed into a solution containing sulfate ions (often, sodium sulfate). The volume of solution is much larger than that of the sample.
- No mechanical stress is applied to the sample.
- Expansion (i.e., free expansion) is measured regularly (e.g., weekly), and the solution is regularly renewed.
- Microstructural and mineralogical characterizations on tested samples are performed after a certain testing duration (e.g., after 120 and 300 days in Chabrelie (2010)).

Following such protocol, sulfate attacks are found to lead to a penetration of reaction fronts from the exposed surface toward the inside of the material (Gollop and Taylor, 1992). Such movement is illustrated in Fig. 1.2, which shows the formation of zones of various compositions (which induce a heterogeneity in the material) in an OPC paste exposed to  $\text{Na}_2\text{SO}_4$  at 20°C. The formation of such zones was observed in a variety of experimental studies

## 1.2. SYNTHESIS OF LABORATORY STUDIES OF SULFATE-INDUCED EXPANSIONS IN CEMENT-BASED MATERIALS

(Irassar et al., 2003; Maltais et al., 2004; Le Bescop and Solet, 2006; Escadeillas and Hornain, 2008) and is a direct consequence of the ingress of sulfate transport from the surface (in contact with the solution) toward the interior of the sample. The ingress of sulfate ions is very slow, so that a significant expansion can usually be observed after only several months and, even after several years, the expansion has not reached any asymptotic value (Chabrelie, 2010; Yu et al., 2013). The formation of the various zones is not correlated with the expansion and damage of the sample (Scrivener, 2012).

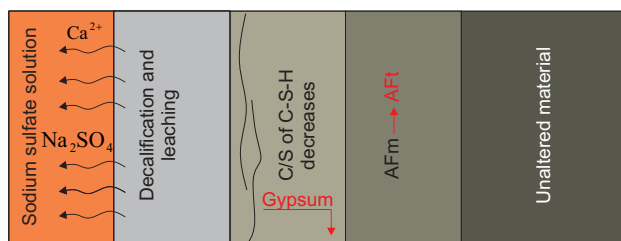


Figure 1.2: Schematics of the formation of zones of various compositions in an OPC sample exposed to a solution of  $\text{Na}_2\text{SO}_4$  at  $20^\circ\text{C}$  (Gollop and Taylor, 1992).

Gollop and Taylor (1992) proposed that the reactions occurring first corresponding to the zones at the greatest distance from the surface: the deeper zone is where monosulfoaluminate is transformed into ettringite; closer to the surface CH is consumed, the average ratio  $\text{CaO}/\text{SiO}_2$  of C-S-H decreases and a formation of gypsum  $\text{C}\$\text{H}_2$  within the C-S-H gel or in cracks parallel to the surface is observed; in the layer nearest to the surface of the tested sample, further leaching and decalcification of C-S-H occur.

During such an experiment, once the deformation of the sample has overcome the typical elastic limit of cementitious materials (which is around 0.1 %), the sample is damaged. In such case, the mechanical and physical properties of the tested material can vary tremendously over time and hence differ significantly from the ones measured before the experiment. The expansion measured with the protocol here presented is therefore a direct consequence of a complex process in which we must take into account, on top of the crystallization process itself, other phenomena such as leaching, de-

calcification, the kinetics of diffusion, damage-induced softening of material, and so on. This complexity makes it very difficult to correlate the measured expansions to evolutions of the mineralogy and of the microstructure.

To accelerate expansion tests, a variety of tricks was proposed: using high sulfate concentrations, storing the samples at high temperature (i.e., greater than 25°C) before exposure, reducing the size of the samples, and so on (Chabreli e, 2010). Let us note that Yu et al. (2013) showed that expansion is observed much earlier with a sample of smaller size than with a sample of greater size.

In summary, with the usual protocol of testing consisting in immersing a macroscopic sample into a sodium sulfate solution, three complexities are encountered mostly: 1) the experiments are very long, which is inconvenient, and 2) the sample responds in a heterogeneous manner since the ingress of sulfates leads to the formation of zones with different mineralogies, and 3) the damage of material over the experiment leads to a significant variation of the physical and mechanical features of the sample, which makes it difficult to understand the origin of the measured expansion. In the present work, we will aim at alleviating those complexities.

### **1.2.2 Respective role of ettringite and gypsum in expansion of cementitious materials subjected to sulfate attacks**

According to Eqs. (1.1) and (1.2), sulfate attacks lead to crystallization of ettringite (AFt) and gypsum (C\$H<sub>2</sub>) in the sample, as confirmed by many (Gollop and Taylor, 1992; Irassar and Di Maio, 1996; Schmidt et al., 2009) also in numerical modelling (Lothenbach et al., 2010; Kunther, 2012; Bary et al., 2014). Here, we focus on what is known of the contribution of each of those two crystals to the observed expansion.

## 1.2. SYNTHESIS OF LABORATORY STUDIES OF SULFATE-INDUCED EXPANSIONS IN CEMENT-BASED MATERIALS

---

### Role of ettringite

AFt phases form hexagonal prismatic or acicular crystals (Moore and Taylor, 1970). Figure 1.3, which was obtained by scanning electron microscopy (SEM), shows ettringite needles formed in one of the samples we tested, after exposure to sulfates (see more details in Chap. 3). Lafuma (1929) suggested that damage could be caused by a directional crystal growth of ettringite. Mehta (1983) proposed that ettringite crystals of colloidal dimensions, when in presence of lime, absorb water, which makes them swell, hence producing a pressure that causes the expansion of the material. In contrast, Gollop and Taylor (1992) suggested that the expansion can be an indirect consequence of the formation of the ettringite. Schmidt et al. (2009), Yu et al. (2013), Müllauer et al. (2013), Yu et al. (2015), and Feng et al. (2015) proposed that expansion is mostly attributed to the formation of ettringite crystals in a confined environment, i.e., in the C-S-H gel or in pores of nanometric dimensions. This hypothesis is in good agreement with the crystallization pressure theory which was discussed in depth in Scherer (1999) and Flatt (2002b). However, Bizzozero et al. (2014) and Bizzozero (2014) found that an expansion can be observed in calcium aluminate cement pastes intermixed with various mass fractions of gypsum, which do not contain C-S-H. They also found that a theory based on elasticity and the crystallization of ettringite in coarse pores connected through pore entries of nanometric dimensions could not capture accurately how the magnitude of expansion evolved with the ettringite saturation index. According to modeling results obtained by Bary (2008) and Bary et al. (2014), damage of cementitious materials is at least partially induced by the crystallization of ettringite, but the magnitude of the crystallization pressures it creates (e.g., in the C-S-H gel) is not sufficient to explain the magnitude of the macroscopic expansions observed experimentally (Basista, 2008; Bary et al., 2014). We note also that ettringite formed during the early hydration of most Portland cements does not contribute to the expansion (Escadeillas and Hornain, 2008).

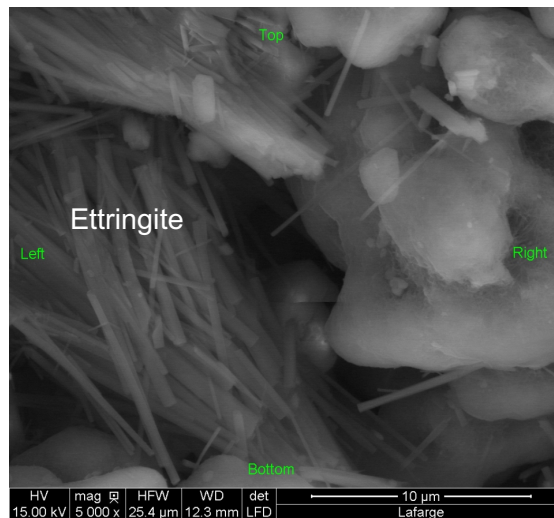


Figure 1.3: SEM observation of needles of ettringite in one of the samples we tested (i.e., sample C3S-AFm4-a, see Chap. 3), after exposure to sulfates.

### Gypsum as a crystal not contributing to expansion

Gollop and Taylor (1992) investigated the microstructural and microanalytical changes of Portland cement pastes stored for 6 months in solutions of sodium sulfate or magnesium sulfate. They proposed that the expansion may be an indirect consequence of the formation of ettringite. They proposed also that, in most samples, the gypsum veins appear to be formed by recrystallizations that could not contribute to expansion. However, they also suggested that the expansion of a material already very weak may be attributed to the formation of gypsum.

Mather (1996) rejected the fact that gypsum is an expansive product. He proposed that gypsum forms from the supersaturated solution by evaporation. He used the following analogy to support his argument: “You cannot break a bottle full of saturated solution by removing the cork and letting the water evaporate.”

According to Scrivener (2012) and Yu et al. (2013), gypsum appears to be formed after cracking and expansion is expected to be caused by the formation of ettringite crystals that precipitated in a confined environment (e.g., in the C-S-H gel). They proposed that the sulfate ions penetrate freely

## 1.2. SYNTHESIS OF LABORATORY STUDIES OF SULFATE-INDUCED EXPANSIONS IN CEMENT-BASED MATERIALS

into micro-cracks generated by the expansion and then react with CH to form gypsum within the cracks. The formation of gypsum was not believed to be a significant factor governing the expansion. However, from their study, how the magnitude of expansion was correlated with the amounts of ettringite and gypsum formed remained unclear, as discussed in Sec. 1.2.1.

### Gypsum as a crystal contributing to expansion

Thorvaldson (1954) found that  $C_3S$  pastes are very slowly attacked by 0.15 molar  $Na_2SO_4$ , over several years, and that  $\beta-C_2S$  pastes can be also attacked by a solution of sodium sulfate at a greater concentration. He attributed the expansion observed during these attacks to formation of gypsum.

Mehta et al. (1979) observed no significant expansion of  $C_3S$  mortars subjected to 10% sulfate solution (5%  $Na_2SO_4$  and 5%  $MgSO_4$ ), but observed some loss of adhesion and strength in the long term. However, Mehta (1992) reported that the formation of gypsum caused the expansion and spalling of alite pastes subjected to sulfate attacks.

Bonen and Sarkar (1993) reported the deposition of gypsum with a thickness up to 50  $\mu m$  in the interfacial zone (i.e., in the zone between aggregates and bulk paste), which precipitated according to a through-solution mechanism. They concluded that the crystallization pressure due to the formation of gypsum may overcome the tensile strength of the material and cause its disruptive expansion.

The role of the interfacial zone during the attack process was investigated by Yang et al. (1996). Their hypothesis is that sulfate reacts with CH and AFm in the interfacial zone, leading to expansion and cracking. The disintegration of the cement mortar results from the propagation of these cracks from the interfacial zone toward the bulk paste.

Based on his experimental data on Portland cement pastes exposed to a solution of sodium sulfate, Wang (1994) suggested that a greater amount of gypsum formed leads to more significant damage.

The mechanism of sulfate attacks in low-C3A Portland cement in which

the  $C_3S$  content varied from 40 to 74% was investigated by [Gonzalez and Irassar \(1997\)](#). They concluded that a greater expansion occurs in the cement of higher  $C_3S$  content, which was attributed to the precipitation of gypsum in a localized manner at interfaces between aggregates and paste.

[Tian and Cohen \(2000\)](#) observed that  $C_3S$  pastes (in absence of  $C_3A$ ) that have been exposed to solutions of  $Na_2SO_4$  and  $(NH_4)_2SO_4$  exhibit a significant expansion and a formation of gypsum. However, they provided very few data of quantitative mineralogical analysis to support their conclusions. It is interesting to note that these results suggested also that C-S-H could react with the sulfate solution.

[Müllauer et al. \(2013\)](#) proposed that the free expansion mechanism of Portland cement mortar consists of three stages. In the first stage, in which is observed a slight expansion and no damage, the sulfates having diffused react with AFm to form ettringite AFt and this reaction leads to a build up of crystallization pressure on the walls of small pores (with a diameter on the order of 10-50 nm). The second stage corresponds to a stage of significant expansion, during which the crystallization pressure of ettringite exceeds the tensile strength of the material. The expansion reaches maximal values in a third stage in which almost all monosulfoaluminate has been consumed. The authors proposed also that the formation of gypsum in the second stage contributes to the expansion of the unrestrained samples and promotes their damage.

In summary, in spite of the number of research works dedicated to the topic, the role of crystallization of gypsum is still poorly understood and widely discussed. In contrast, there seems to be a consensus on the fact that crystals of ettringite can contribute to the expansion when they precipitate in a confined environment (e.g., in the C-S-H gel or in pores with a size smaller than about 100 nm). One of the main difficulties to draw conclusions on the topic is the lack of data making it possible to scrutinize any potential correlation between expansion and the amount of ettringite or gypsum formed ([Gollop and Taylor, 1992](#); [Taylor, 1998](#)). Providing such data will be one of the goals of this thesis.

## 1.2. SYNTHESIS OF LABORATORY STUDIES OF SULFATE-INDUCED EXPANSIONS IN CEMENT-BASED MATERIALS

### 1.2.3 Role of sulfate concentration

Generally, most investigators found that a higher sulfate concentration accelerates the chemical reactions, the expansion, and the damages. Also, a higher sulfate concentration leads to the precipitation of a greater amount of gypsum, and at moderate or lower sulfate concentrations, only little gypsum (if any) can be observed (Irassar et al., 2003; Bellmann et al., 2006; Müllauer et al., 2013).

Damidot and Glasser (1993) and Damidot et al. (2011) determined phase diagrams in function of the sulfate concentration  $[\text{SO}_4^{2-}]$ , calcium concentration  $[\text{Ca}^{2+}]$  and aluminate concentration  $[\text{Al}^{3+}]$ . Therefore, the sulfate concentration is as an important variable indicating which phase is most stable thermodynamically in given conditions. According to Damidot and Glasser (1993), for the system of  $\text{CaO-Al}_2\text{O}_3\text{-CaSO}_4\text{-H}_2\text{O}$  at  $25^\circ\text{C}$ , gypsum appears at concentrations  $[\text{SO}_4^{2-}]$  higher than 11.4 mM, while ettringite appears at concentrations  $[\text{SO}_4^{2-}]$  higher than 0.015 mM.

Barbarulo (2002) investigated the adsorption of sulfate on synthetic C-S-H at  $20^\circ\text{C}$  as a function of the sulfate concentration. He found that gypsum appears beyond a certain value of sulfate concentration.

Following the theory of crystallization pressure (see Sec. 1.5.1 for more details), Ping and Beaudoin (1992a), Ping and Beaudoin (1992b), Flatt and Scherer (2008), and Yu et al. (2013) proposed that the maximal pressure exerted on pore walls and resulting from crystallization of ettringite and gypsum (which is called crystallization pressure) depends on the sulfate concentration  $[\text{SO}_4^{2-}]$ .

Schmidt (2007) and Schmidt et al. (2009) found more physical damage and greater expansion in samples exposed to a higher sulfate concentration, in which they also observed a greater amount of gypsum. They suggested that the greater expansion may be a direct consequence of this greater amount of gypsum formed.

Yu et al. (2013) reported the influence of sulfate concentration on the expansion of mortar exposed to sodium sulfate solutions. After 120 days of exposure, a greater sulfate concentration led to a greater expansion. They

also proposed an estimation of the maximal pressure exerted on the pore walls from the confined ettringite crystals in the C-S-H gel, which is directly related to the sulfate concentration. The maximal pressure was estimated to approximately 21.45 MPa.

According to the actual literature, the sulfate concentration seems to be a significant factor governing the expansion of cementitious materials. In the present study, we will aim at determining its role in more details.

### 1.2.4 Role of mechanical load or restraint

As mentioned in Sec. 1.2.1, almost all experimental studies were performed with cementitious samples on which no mechanical stress was applied during testing. These tests are referred to as ‘free’ expansion tests. To the best of our knowledge, the work of Müllauer et al. (2013) is the unique one in which is investigated the effect of mechanical restraint on the expansion of cementitious materials subjected to sulfate attacks. Müllauer et al. (2013) studied the expansion of mortar cylinders with a specially constructed stress cell displayed in Fig. 1.4. In their device, both sides of a mortar cylinder are restrained by two stainless steel disks linked by a stainless steel rod. During the expansion process, the axial stress that is applied on the sample can be determined through the elongation of the tension rod and its stiffness. The samples were immersed in solutions of sodium sulfate with concentrations of 1.5 or 30 g/L. Various degrees of axial restraint were applied by varying the diameter of the tension rod and hence its stiffness, as displayed in Fig. 1.4 (b). They found that the expansion was smaller for the sample to which was applied a greater restraint (i.e., with a greater diameter of the tension rod). Unfortunately, the authors did not clearly identify how the sulfate ions migrated into the sample or the resulting mineralogical distribution. Therefore, according to us, the expansion mechanism that they proposed is not very convincing.

For what concerns the influence of stresses *per se*, based on thermodynamic principles, Lecampion (2010) showed that, theoretically, crystallization-induced swelling should be favored in the direction of the greatest applied

## 1.2. SYNTHESIS OF LABORATORY STUDIES OF SULFATE-INDUCED EXPANSIONS IN CEMENT-BASED MATERIALS

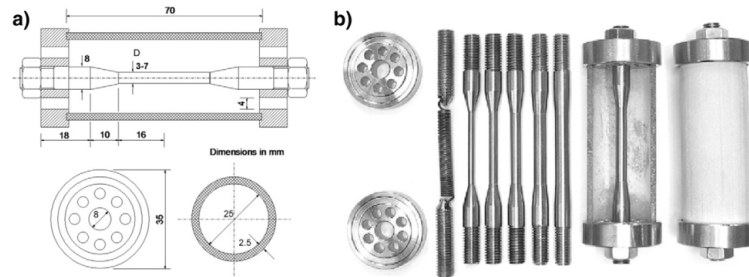


Figure 1.4: a) Schematic of a stress cell consisting in thin-walled hollow mortar cylinders and a central tension bar, b) Spring and tension bars with various diameters and a complete stress cell with a mortar cylinder. Picture credit: [Müllauer et al. \(2013\)](#).

stress.

### 1.2.5 Conclusions

In spite of numerous works dedicated to the study of the expansion of cementitious materials subjected to sulfate attacks, a variety of questions remain, typically:

- While there is an agreement on the fact that ettringite can induce an expansion if it precipitates in a confined environment, what about pockets of ettringite (i.e., crystals of ettringite precipitating in pores larger than 100 nm)?
- Is C-S-H necessary to observe an expansion?
- Does gypsum contribute to the expansion?
- How does the sulfate concentration influence expansion?
- How does a mechanical stress or restraint influence expansion?
- What are the main factors governing expansion?

The difficulty in answering such questions stems from the complexity of the experimental study of sulfate attacks in cement-based materials. This

complexity is due to a variety of reasons, typically: the expansion usually progresses over months or even years; the damage induces a significant variation of the physical and mechanical features of the sample over the experiment; the material is composed of a variety of phases, which leads to complex thermo-chemical equilibria; the process usually leads to a heterogeneous sample, which makes it difficult to correlate the expansion to mineralogical or microstructural changes. Because of this complexity, predicting the outcome of sulfate attacks in cementitious materials is a challenge, which presents a high scientific interest. Moreover, predicting this outcome is of high societal interest as well.

### **1.3 Other cases of crystallization-induced expansion**

#### **1.3.1 Other cases of crystallization-induced expansion in cement-based materials**

Crystallization-induced damage in cement-based materials is not limited to sulfate attacks. For instance, it may also originate from delayed ettringite formation (DEF) (Taylor et al., 2001; Barbarulo, 2002) or from freeze-thaw cycles (Taylor, 1998; LCPC, 2003).

Delayed ettringite formation occurs in concrete, mortar and cementitious paste that have been subjected to a temperature above 65°C and then exposed either intermittently or continuously to a saturated water vapor atmosphere (Lawrence, 1995; Taylor et al., 2001; Barbarulo, 2002). DEF leads to material's expansion and damage. Its effects can be observed typically in railway sleepers or precast concrete structural elements. The temperature rise which causes DEF may be due to the exothermic hydration reaction, or to any external source, either during heat curing (case of precast concrete elements, for instance) or during service. Taylor et al. (2001) explained that heating induces a recrystallization of ettringite and calcium hydroxide within cracks, cement-aggregate interfaces and C-S-H gel. Among those precipita-

### 1.3. OTHER CASES OF CRYSTALLIZATION-INDUCED EXPANSION

---

tions, they suggested that the main contribution to expansion is the ettringite recrystallization within the C-S-H gel. Bouzabata et al. (2012) studied the effect of mechanical restraint on DEF-induced expansion by using an original device in which the samples are restrained by two stainless steel plates connected by four threaded stainless steel rods. Two experiments have been performed at distinct restraint levels by varying the rods diameter (i.e., 2 and 5 mm diameter). They show that DEF-induced expansion is isotropic in stress-free conditions while it is anisotropic under restrained conditions. They have also highlighted that a greater restraint level leads to a smaller DEF expansion in the restrained direction.

Damage of concrete and cement paste induced by freeze-thaw cycles manifests itself typically through the appearance of flakes on the surface and gradual progression inward through deep cracks. Early theories suggested that this damage was directly associated with volumetric expansion of water occurring upon freezing. This expansion can lead to damage if the freezing water is sufficiently confined. Powers (1945) suggested that the expansion of water freezing in pores near the material surface forces the remaining liquid water to flow toward small pores. Therefore, the pressure in small pores increases sufficiently to overcome the material strength, thus inducing damage. Scherer (1993, 1999) have proposed that the growth of ice crystals, which is driven by undercooling, could generate a pressure on the pores wall (so-called crystallization pressure, see Sec. 1.5.1 for more details). This pressure would be higher in small pores, and could damage concrete if the crystals grow enough to pass through pores as small as the breakthrough radius, giving them access to the percolating network controlling water transport (Scherer, 1999). Coussy and Monteiro (2007, 2008) and Zeng et al. (2011) have developed theoretical models able to capture the behavior (e.g., freezing strain) of cementitious materials subjected to freezing. They have also highlighted two competing processes governing the freezing-induced expansion: (i) the excess of liquid expelled from freezing sites leads to a pressure build-up in unfrozen sites and to an overall expansion of the material; (ii) when cooling continues, liquid water flows from remaining unfrozen sites toward the already crystallized sites. This process is called cryosuction and leads to an

overall reduction of freezing-induced expansion. [Coussy and Monteiro \(2007, 2008\)](#); [Zeng et al. \(2011\)](#) have also emphasized the efficiency of entrained air-voids on the frost resistance of cement. Those large pores are expected to act as both expansion reservoirs and efficient cryo-pumps.

### 1.3.2 Cases of crystallization-induced expansion in other materials

Salts have been well known as an important factor of damage of various building materials since ancient times. For instance, Herodotus<sup>1</sup> wrote in 440 B.C.E.: ‘I observed [...] that salt exuded from the soil to such an extent as even to injure the pyramid’. Salt crystallization-induced expansion and/or damage not only concerns cementitious materials but also other porous materials such as stone, brick, soils, etc. ([Zeza and Mad, 1995](#); [Goudie and Viles, 1997](#); [Rodriguez-Navarro, 1999](#); [Rodriguez-Navarro et al., 2000](#); [Scherer, 2004](#); [Espinosa-Marzal et al., 2008](#); [Chwast et al., 2014](#)). Damage of building materials due to salt precipitation is usually associated with various macroscopic observations such as swelling (expansion), spalling, cracking, efflorescence, etc. ([Rijniers, 2004](#); [Saidov, 2012](#); [Gupta, 2013](#)). Salts attacking building materials may have various origins: sea water, ground water containing high level of dissolved salts, air pollution, etc. Numerous research works have investigated salt damage mechanisms during the last decade ([Doehne and Clifford, 2010](#)). One of the most celebrated outcomes of this research is the crystallization pressure theory. It has been first proposed by [Correns and Steinborn \(1939\)](#); [Correns \(1949\)](#) (see Sec. 1.5.1 for more details) and then further advanced by [Scherer \(1999\)](#); [Flatt \(2002b\)](#); [Steiger \(2005a\)](#); [Coussy \(2006\)](#). This theory is based on the fact that the driving force of crystallization pressure originates from supersaturation (here defined as the difference of chemical potential between the solution and the crystal ([Coussy, 2011](#))) and from the energy mismatch between the crystal and the pore wall, which may be due to electrostatic and van der Waals forces ([Scherer, 1999](#)). By accounting for the crystallization pressure hy-

---

<sup>1</sup><http://classics.mit.edu/Herodotus/history.2.ii.html>

pothesis, [Espinosa-Marzal et al. \(2008\)](#); [Espinosa-Marzal and Scherer \(2008\)](#); [Espinosa-Marzal et al. \(2011\)](#) have proposed a simple idea to explain salt damage phenomenon: the growth of damaging salt crystals in a supersaturated solution can generate a stress on pores wall able to cause swelling and/or damage of the material. [Coussy \(2006\)](#); [Flatt et al. \(2014\)](#) have successfully proposed theoretical models able to predict when damage occurs in porous materials subjected to salt precipitation.

## 1.4 Applications subjected to crystallization-induced expansion

### 1.4.1 Underground storage of nuclear waste

Nuclear energy is the main source of electric power in France. In 2011, nuclear power plants produced about 78 % of the total electricity supply ([OECD, 2006](#); [ANDRA, 2012](#)). Storage of nuclear waste is considered as an element of the national waste management strategy to protect people and the environment.

Certain wastes present a significant radioactivity over a very long period of time, up to several centuries ([ANDRA, 2005b](#)). To ensure the safety and security of radioactive materials over such a time scale and to isolate them from human environment, a deep underground disposal facility called CIGÉO is being developed by ANDRA with a concept of multi-barriers. The projected barriers consist in the waste packages and the geological barrier [ANDRA \(2005a\)](#). The Long-lived and High-level wastes (wastes B) can be protected by the container made of reinforced high performance concrete, as described in [Fig. 1.5](#). These packages are then placed in the underground disposal cells which are closed by a bentonite plug and a concrete plug as described in [Fig. 1.6](#). The disposal cell is expected to be located in a cavity excavated in an argillite host rock (geological barrier).

During service, the ground water in equilibrium with the argillite rock may contain sulfate ions with sulfate concentrations which vary from 0.03

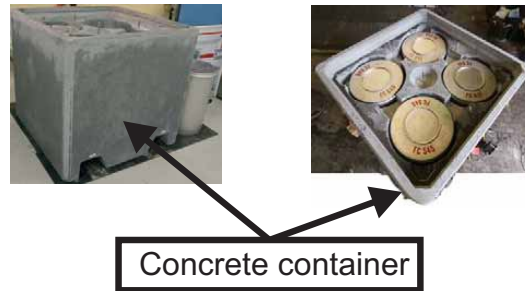


Figure 1.5: A standard concrete container of the Long-lived and High-level waste (waste B). Photo credit: [ANDRA \(2005b\)](#).

to 76 mM ([Michaux, 1994](#); [Roy and Fouillac, 2004](#); [Wakim, 2006](#)). Therefore, the concrete barriers can be subjected to sulfate attacks that may cause serious damage and their disruption (see Sec. 1.2.2). Such damage would accelerate the migration of radionuclides toward the surrounding environment.

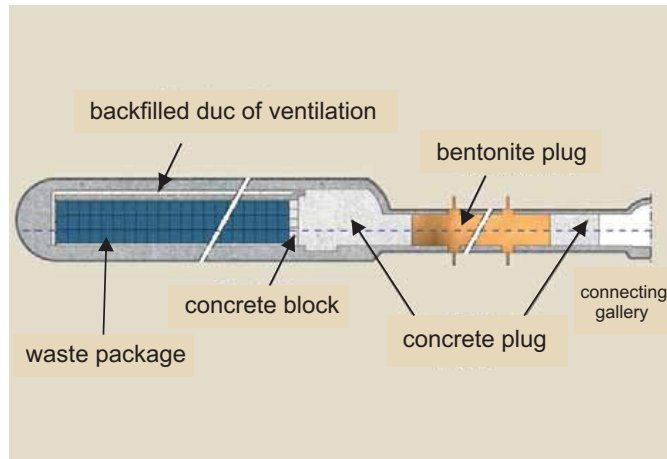


Figure 1.6: Disposal cell of Long-lived and High-level waste (waste B). The cell is closed by a bentonite plug and a concrete plug. Picture credit: [ANDRA \(2005b\)](#).

Therefore, the characterization of the long-term behavior of cementitious materials under various environmental factors including sulfate attacks is necessary. A better understanding of sulfate attacks in cementitious materials may contribute not only to a better assessment of the storage integrity, but also to propose efficient concepts for concrete barriers protection, thus

## 1.4. APPLICATIONS SUBJECTED TO CRYSTALLIZATION-INDUCED EXPANSION

---

maximizing the safety and security of nuclear waste storage over sufficiently long periods of time.

### 1.4.2 Historic monuments conservation

Nowadays, cultural heritage plays also an important role in local economies with a remarkable contribution in terms of job creations and associated multiple sources of income (Convention France-UNESCO, 2006; The Getty Conservation Institute, 2000; Bowitz and Ibenholt, 2009). However, a considerable number of cultural heritage monuments are endangered by a combination of socio-economic pressures and environmental threats such as climate change (EU, 2009).

Numerous historic monuments have been affected by salt weathering, especially in coastal zones (EC, 1996; EU, 2009) e.g., brickworks in Venice-Italy or Netherlands; hard stone statues (like the one in La Rochelle-France, displayed in Fig. 1.7 (Cardell et al., 2003; Germinario et al., 2014)). Salt has also been widely recognized as a main cause of deterioration of historical architecture, archaeological structures and objects over the world such as Angkor Watt, historical education buildings in Western Anatolia (Turkey), Great Sphinx of Giza (Doehne, 2002; Bo, 2007; Siedel and Leisen, 2008; Reed, 2002).

Historical monuments can be subjected to salt attacks in many ways, such as: air pollution, which is well known as a source of nitrates and sulfates; invasive salts by rising damp; salt carried by the wind from the sea (Zezza and Mad, 1995; EU, 2009). Environmental factors (e.g., temperatures cooling below freezing point, evaporation, chemical reactions, etc. (Scherer, 1999)) are considered as primary cause of initiation and increase of salt crystallization in porous materials. Salt damage does not occur only in outdoor environments. Indeed, severe damage to stonework held in uncontrolled museum environments has been observed (Rodriguez-Navarro and Doehne, 1998).

Therefore, salt weathering has been widely recognized as a serious issue for historical monuments (Doehne and Clifford, 2010). A better understanding of the mechanisms of salt-induced damage of porous materials is necessary



Figure 1.7: An example of salt-induced damage which has been recognized in the statue of a soldier in La Rochelle, France. Photo credit: Rob van Hees.

to propose efficient prevention solutions and to protect historical monuments on the long-term (EU, 2009).

### 1.4.3 Durability of civil engineering structures

Cement is an essential material in manufacturing concrete, which is considered as the most widely used construction material in the world with a total annual production of more than 2 billion metric tons (Gt) (CEMBUREAU, 2014). Nowadays, the cement industry has to reduce its impact on the environment (e.g., reduction of CO<sub>2</sub> emission) as part of a sustainable development (Añ, 2000).

In case of important concrete structures in which construction's lifespan must be superior to 100 years e.g., Vasco de Gama Bridge in Lisbon-Portugal, Viaduc de Millau in France, the durability of concrete works over time is one of the most important requirements to not only ensure the safety during service, but also to reduce the financial investment (Kretz et al., 2011; Association française de Normalisation, 2004). Damage to concrete structures can lead to a significant loss of money and requires time to repair or reconstruct partially or totally (Padgett et al., 2008). Indeed, one third to one half of annual investments in construction is devoted to maintenance or rehabilitation activities (Parnell and Oldfield, 2014). Sometimes damage can

## 1.5. MECHANISMS THROUGH WHICH CRYSTALLIZATION INDUCES AN EXPANSION

---

lead to judiciary conflicts with multi-million dollars settlements or judgments (Haynes, 2002). Concrete durability has thus been widely recognized as a key problematic for cement industry.

Among various issues related to concrete durability, sulfate attacks (e.g., sodium sulfate, magnesium sulfate, calcium sulfate, etc.) have been widely recognized as a damage source that can significantly reduce the lifespan of constructions (Escadeillas and Hornain, 2008; Taylor, 1998). Typical structures such as dams, building foundations or bridges are concerned by sulfate attacks (see in Fig. 1.1) (Auger, 2009; Marchand et al., 2002b). Such phenomena are more likely to concern concrete works built in aggressive environments (e.g., rivers, sea coast, sulfate-rich soils, etc.) (Marchand et al., 2002b; Mather, 1964; Meijer and Van Rosmalen, 1984) which may be an abundant source of sulfate salts (Meybeck, 2003; Salome and Sigurdsson, 2014; Texas Department of Transportation, 2005).

In road construction industry, it has been reported that salt crystallization (e.g., crystallization of ettringite or gypsum) may also cause significant swelling of soils under bridge foundations or roadways (Ramon and Alonso, 2012; Ouhadi and Yong, 2008). Such a swelling can generate heterogeneous deformation at the structure scale (e.g., differential displacement between bridge pillars) that can damage the structure.

In summary, crystallization-induced expansion or damage of building materials is a serious issue for durability of civil constructions. It reduces significantly the lifespan of constructions. For civil engineers, a good knowledge of this topic allows to propose adequate protection solutions improving the service life of concrete structures.

## 1.5 Mechanisms through which crystallization induces an expansion

Salt crystallization can be considered as a case of phase transition. The driving force of salt crystallization is supersaturation which can be produced by evaporation, undercooling and chemical reactions (Scherer, 1999, 2004;

Coussy, 2011).

How crystallization can induce expansion (i.e., why crystals would ‘push’ on the pores wall) is usually explained through Correns’ law [Correns \(1949\)](#), according to which the pressure exerted by the crystal on the solid skeleton is a consequence of the supersaturation in the solution. For a thorough description of Correns’ law, readers should refer to [Flatt et al. \(2006\)](#). However, alternative explanations have been proposed based, in particular, on the existence of hydration forces (see [Mortensen \(1933\)](#); [Parsegian \(2011\)](#)), increase of solid volume ([Polivka, 1973](#)), etc.

### 1.5.1 Crystallization pressure: historical overview, Correns’s law and its extensions

The first scientific statement about salt crystallization pressure was made by [Lavalle \(1853\)](#). According to his experiments, he concluded that salt would be able to push away a certain weight. [Becker and Day \(1916\)](#) performed an experiment with crystals of 1 cm diameter: the crystal could be able to lift 1 kg. [Taber \(1916, 1917\)](#) showed that a crystal in a supersaturated solution is not always able to lift a weight through two experiments displayed in [Fig. 1.8](#): in both experiments, crystals are immersed in a supersaturated solution created by evaporation. In the upper experiment, only one loaded crystal is immersed and it grows in the supersaturated solution; in the lower experiment, an unloaded crystal is also immersed in the solution. This latter grows and consumes the supersaturation while the loaded crystal does not grow. [Taber \(1916\)](#) stated that if there is no evaporation of the solution, the loaded crystal will dissolve to create a supersaturated solution with respect to the unloaded crystal that leads to the growth of the unloaded crystal.

In contrast to the previous observations, experiments performed by [Kopp \(1855\)](#) and by [Bruhms and Meckelenburg \(1913\)](#) did not show that the salt could lift a weight.

[Correns and Steinborn \(1939\)](#); [Correns \(1949\)](#) first derived an expression for the crystallization pressure as a function of supersaturation. Considering

## 1.5. MECHANISMS THROUGH WHICH CRYSTALLIZATION INDUCES AN EXPANSION

---

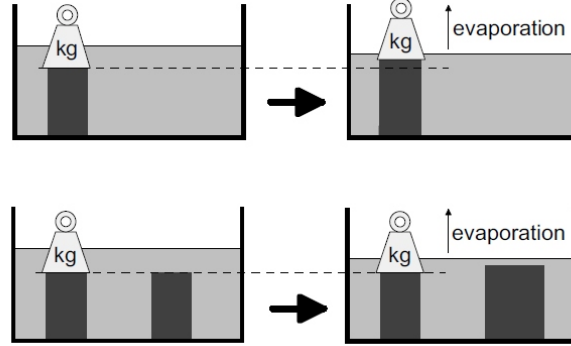


Figure 1.8: Illustration of the crystallization experiments performed by [Taber \(1916\)](#). In both studied cases (upper and lower experiment), the supersaturated solution has been created by evaporation. In the upper experiment, the crystal can grow under stress. In the lower experiment the crystal under stress did not grow while the growth of the crystal without stress has been observed. Photo credit: [\(Rijniers, 2004\)](#).

thermodynamic equilibrium, [Correns \(1949\)](#) proposed the following formula:

$$p_C - p_L = \frac{RT}{V_C} \ln\left(\frac{C}{C_0}\right) \quad (1.3)$$

where  $p_C - p_L$  stands for crystallization pressure (pressure in excess to reference state in equilibrium with saturated solution);  $R$  stands for perfect gas constant;  $T$  stands for temperature (K);  $V_C$  stands for molar volume of crystal;  $C$  and  $C_0$  stand for concentration of supersaturated and saturated solution respectively (M);  $\frac{C}{C_0}$  is defined as supersaturation degree. This equation is uniquely applicable to an ideal solution and molecular crystals, but is not applicable to monovalent electrolytes such as NaCl, for instance. [Correns \(1949\)](#) presented an experimental demonstration of the existence of crystallization pressure and their experimental results showed very good agreement with calculated crystallization pressure by using Eq. (1.3). However, until now, no one could reproduce these experiments due to the lack of various experimental informations e.g., how did they sustain and measure the supersaturation? what is the size of crystal? etc. ([Désarnaud, 2009](#); [Caruso and](#)

Flatt, 2014b,a).

(Flatt, 2002b) have proposed an equation of crystallization pressure for multivalent hydrous/anhydrous crystal in the case of an ideal solution:

$$p_C - p_L = \frac{RT}{V_C} \left[ n_{ions} \ln \left( \frac{x}{x_0} \right) + n_{water} \ln \left( \frac{1 - n_{ions}x}{1 - n_{ions}x_0} \right) \right] \quad (1.4)$$

where  $x$  and  $x_0$  stand for molar fraction of supersaturated and saturated solution respectively;  $n_{ions}$  and  $n_{water}$  stand for number of ions of crystal and number of water molecules respectively. By taking into account the non ideality of the solution, Steiger proposed the following equation:

$$p_C - p_L = \nu \frac{RT}{V_C} \left[ \ln \left( \frac{m}{m_0} \right) + \ln \left( \frac{\gamma_{\pm}}{\gamma_{\pm,0}} \right) + \frac{\nu_0}{\nu} \ln \left( \frac{a_w}{a_{w,0}} \right) \right] \quad (1.5)$$

where  $m$  and  $m_0$  stand for molality of supersaturated and saturated solution respectively;  $\gamma_{\pm}$  and  $\gamma_{\pm,0}$  stand for mean activity coefficient of supersaturated and saturated solution respectively;  $\nu$  and  $\nu_0$  stand for total number of ions and number of water molecules released upon complete dissociation of crystal, respectively.

Generally, the crystallization pressure obtained by Eq. (1.3) is lower than those given by Eq. (1.4) and (1.5). In practice, the crystallization pressure can be determined as follow:

$$p_C - p_L = \frac{RT}{V_C} \ln \left( \frac{IAP}{K_p} \right) \quad (1.6)$$

where  $IAP$  and  $K_p$  stand for ion activity product and equilibrium constant respectively. In case of sulfate attacks in cementitious materials, the maximal crystallization pressure of ettringite is expected to be around 50 MPa (Kunther et al., 2013) which is significantly greater than the tensile strength of cement paste and concrete.

According to Ping and Beaudoin (1992a,b); Scherer (1999); Flatt (2002b), the crystallization of gypsum can contribute also to the expansion of cement-based materials if the growth of gypsum crystals occurs within confined pores (i.e., small pores) with a highly supersaturated solution with respect to gyp-

## 1.5. MECHANISMS THROUGH WHICH CRYSTALLIZATION INDUCES AN EXPANSION

---

sum. A supersaturation ratio equal to 2 can result in a crystallization pressure of gypsum of 28 MPa that is also much greater than the tensile strength of cementitious materials (Escadeillas and Hornain, 2008).

### 1.5.2 Highlights in crystallization pressure theory

Scherer (1999); Flatt (2002b); Scherer (2004); Steiger (2005a,b); Flatt et al. (2006); Coussy (2006) have recently advanced the theoretical framework for understanding the degradation of porous materials induced by salt crystallization. These theoretical models are based on the concept of ‘crystallization pressure’ proposed by Correns and Steinborn (1939); Correns (1949) as well as the effect of surface energy Wellman and Wilson (1965, 1968): the origin of crystallization pressure lies not only in the supersaturation but also in the mismatch between the pore wall and the crystal which may be due to electrostatic and van der Waals forces. Therefore, a solution layer of a few nanometers exists between the crystal and the pore wall. This solution film permits the transport of ions for the crystal growth. There is also a ‘disjoining pressure’ in this layer of solution to satisfy the mechanical equilibrium. This model suggested also that the crystallization pressure would be greater in a smaller pore. Rijniers et al. (2005) found that the maximum salt crystallization pressure can lead to the damage of porous materials if salt crystallization occurs within pores in the size about 30 nm.

However, such model was not able to explain the salt-induced damage of certain building materials such as brick and mortar which does not present much of nanometric pores. Scherer (2004) proposed another theoretical model for salt crystallization without equilibrium. Due to certain conditions (e.g., rapid evaporation), the solution film in contact with large crystals can be discontinuous and supersaturated due to the fact that there is no exchange between the bulk solution and this solution film. Steiger (2005b) has proposed a theoretical model for salt growth within large pores connected through small entry pores of nanometric size to explain the occurrence of significant crystallization pressures within large pores. Fig. 1.9 displays the crystal in cylindrical (left) and spherical (right) pores with small pore en-

trances. The maximal crystallization pressure exerting on large pores walls can be determined as follows (Steiger, 2005b):

$$\Delta p = \gamma_{cl} \left( \frac{2}{r_e} - \frac{1}{r_p} \right) \quad (1.7)$$

$$\Delta p = \gamma_{cl} \left( \frac{2}{r_e} - \frac{2}{r_p} \right) \quad (1.8)$$

where  $\gamma_{cl}$ ,  $r_e$  and  $r_p$  stand for surface free energy of the crystal/liquid interface, radii of pore entrance and crystal size respectively. It is noted that Eq. (1.7) and (1.8) are applicable for cylindrical and spherical pores respectively. These models allowed to explain the deterioration of porous materials with few nanometric pores.

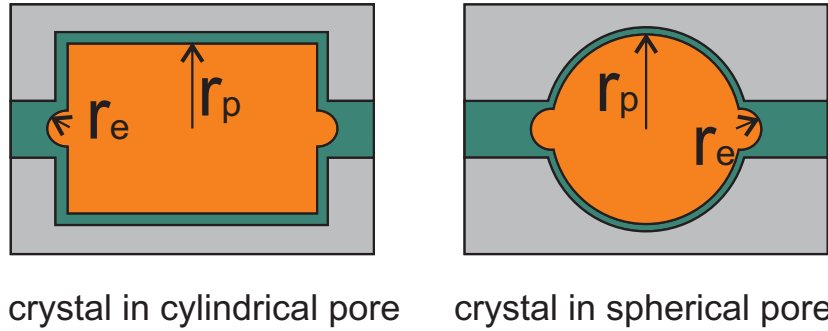


Figure 1.9: Crystals in cylindrical pore (left) and in spherical pore (right) with small pore entrances (Steiger, 2005b).

Steiger (2005a,b) suggested also that the evolution crystallization pressure in porous material seems to be a dynamic process, without being at equilibrium. Such a process would be governed by kinetic properties such as evaporation, temperature cooling, etc. Saidov et al. (2015) has investigated experimentally the crystallization of sodium sulfate in various porous materials such as fired-clay brick, Cordova Cream limestone, and Indiana limestone by using NMR and optical measurements. He found that the crystallization pressure obtained by a thermodynamic approach is equal to the one obtained by the poroelastic approach in equilibrium conditions, where

## 1.5. MECHANISMS THROUGH WHICH CRYSTALLIZATION INDUCES AN EXPANSION

---

the concentration is constant.

A theoretical investigation of the crystallization-induced deformation and fracture of porous materials has been performed by [Coussy \(2006\)](#) by using a thermodynamic framework and brittle poroelasticity. He has emphasized the influence of pore size distribution and the role of the amount of crystals formed on the ultimate resistance of a stone subjected to salt weathering. By using a poromechanics approach, [Flatt et al. \(2014\)](#) have also suggested that the strain energy failure criterion is able to predict when the crystallization-induced damage occurs. [Rijniers et al. \(2004, 2005\)](#) have recognized the increase of salt solubility in small pores with respect to the bulk solubility through a NMR investigation of model materials and  $\text{Na}_2\text{SO}_4$  and  $\text{Na}_2\text{CO}_3$  salts. This variation of solubility may be a direct consequence of the existence of crystallization pressure which would be greater and cause the increase of solubility in smaller pores ([Rijniers, 2004](#); [Rijniers et al., 2005](#)).

[Bary \(2008\)](#) has proposed a coupled chemo-mechanical modeling to investigate damage of cement paste subjected to sulfates through an extension of poroelasticity to account for crystallization pressure. The model predicts well the damage evolution. [Bary et al. \(2014\)](#) estimated that the crystallization pressure of ettringite must be equal to several thousands of MPa to retrieve the magnitude of expansion observed experimentally, in spite of explicitly considering damage after crack initiation, even though the way how he introduced damage in his constitutive equations could be discussed. To better predict the expansion, he had to take into account the macroscopic bulk strain calculated from the volume fraction of precipitated ettringite. It suggests that the expansion of cementitious materials depends not only on the magnitude of crystallization pressure but also on the amount of crystal formed, in the spirit of [Coussy \(2006\)](#), who proposed that the macroscopic stress induced by crystallization is related to the product of the crystallization pressure with the volume fraction of the pore volume occupied by the crystal. [Basista \(2008\)](#); [Bary et al. \(2014\)](#); [Feng et al. \(2015\)](#) have used a similar hypothesis regarding volume change resulting from ettringite formation to reproduce accurately the expansion measured experimentally. [Derluyn et al. \(2014\)](#) have further developed a theoretical model coupling various phenom-

ena such as heat, salt ion transport, crystallization, etc. to investigate the crystallization-induced damage of porous materials. By using poroelasticity and crystallization pressure theories, they defined an effective stress caused by salt crystallization that not only depends on the magnitude of crystallization pressure but also on the amount of salt crystals.

In summary, the existing results suggest that the crystallization-induced expansion of porous materials not only depends on the crystallization pressure (through the supersaturation) but also on other factors e.g., pore sizes, amount of crystal formed, etc. It seems that the crystallization within small pores of nanometric size is expected to be the main cause of expansion and damage of porous materials.

### 1.5.3 Alternative proposed mechanisms

Alternative hypotheses have been proposed to explain why salt causes mechanical deformation and damage:

1. Hydration pressure: [Mortensen \(1933\)](#) performed experiments related with hydration/dehydration of anhydrous crystal  $\text{Na}_2\text{SO}_4$  (molar volume equal to  $53 \text{ cm}^3/\text{mol}$ ) and mirabilite  $\text{Na}_2\text{SO}_4 \cdot 10 \text{ H}_2\text{O}$  (molar volume equal to  $220 \text{ cm}^3/\text{mol}$ ). The material was subjected to regular day/night relative humidity cycles. He proposed a hypothesis according to which hydration was the cause of damage ([Mortensen, 1933](#)). However, [Flatt \(2002a\)](#) has pointed out that the crystal could not magically transform from one state to another more hydrated without a process of dissolution and recrystallization. He has therefore opposed to the idea of hydration pressure which has been considered to be a sub-set of crystallization pressure ([Rodriguez-Navarro, 1999](#)).
2. Differential thermal expansion: This hypothesis is based on the difference in thermal expansion between salts and solid matrix which could induce sufficiently highly heterogeneous deformation and damage the material ([Goudie and Viles, 1997](#)). However, it could not explain crystallization-induced damage at constant temperature, which is the case of sulfate attacks in cementitious materials (see Sec. [1.2.2](#)).

3. In case of sulfate attacks, [Polivka \(1973\)](#) suggested that the increase in solid volume leads to the expansion of cementitious materials. However, there is a lack of evidence to link expansion directly to the amount of ettringite ([Taylor et al., 2001](#)). Furthermore, [Kunther et al. \(2013\)](#) did not find a correlation between expansion and variation of solid volume. They suggested that the increase of solid volume could not cause the expansion of cementitious materials.

Salt damage of porous media deals with complex physical, mechanical, chemical, etc. processes ([Doehne, 2002](#)). Despite numerous research works over the past decade ([Doehne and Clifford, 2010](#)), the salt-induced damage of porous media is still poorly understood. Unanswered questions remain, such as: what is the driving force of salt crystallization that can lead to damage ([Désarnaud, 2009](#))?; what is the role of pore size?; what role plays the amount of crystal formed?

## 1.6 Motivations and objectives

In this context, the investigation of the mechanism of swelling of porous solids (e.g., stones, bricks, soils, cement-based materials) induced by crystallization of salt is necessary to bring out efficient solutions (or design new materials) to limit salt damage ([EC, 1996](#); [EU, 2009](#)). Cement-based materials are recognized as more complex than stones, because of their complex microstructure and reactive matrix that can evolve over time and in function of the pore fluid ([Garboczi and Bentz, 1998](#); [Ye et al., 2002](#); [Taylor, 1998](#)). Due to these features, studying the crystallization-induced expansion of cementitious materials is a challenge. The present work aims at better understanding how the salt-crystallization induces an expansion of cement-based materials in presence of sulfate ions. This knowledge may contribute to finding out a solution to ‘sulfate attacks’ issues, which are known to be a major concern for concrete durability. Moreover, a contribution of this thesis can shed some light on the subject of crystallization-induced swelling of porous solids in general.

The mechanism of expansion of cement-based materials in presence of sulfate ions is still not understood. The main issues with the usual experimental procedure of expansion testing are the duration of the test, and the difficulty to relate expansion with mineralogical evolutions because of the heterogeneous response of the sample. The following questions still deserve to be addressed:

1. In restrained conditions, can crystallization induce an ‘expansion stress’? Can we measure the stress development (termed ‘expansion stress’) preventing any expansion?
2. C-S-H represents a major solid phase of cementitious materials and has been expected to play a role in the expansion. But what is this role?
3. Salt crystallizing in pores of nanometric size (e.g., in the gel pores of C-S-H) is believed to be the main cause of expansion of cement-based materials (Scherer, 1999; Flatt, 2002b; Yu et al., 2013). Can ettringite crystals forming outside of C-S-H lead to an expansion?
4. Can gypsum contribute to an expansion?
5. Is a thermodynamic model relevant to predict the relationship between expansion (or expansion stress) and mineralogical evolution?
6. Is there any correlation between expansion and increase of solid volume?
7. How can we discriminate the potential contribution of gypsum to expansion from that of ettringite?

## 1.7 General strategy and thesis outline

To aim at answering the questions proposed in the section above, the investigation of the expansion of cementitious materials is carried out with original experiments on granular materials compacted into oedometric or isochoric

cells. The tested samples are manufactured by grinding  $C_3S$  pastes, regular Portland cement pastes, or mixtures of phases of which those pastes are made (e.g., monosulfoaluminate AFm or portlandite CH), and then compacting them in a cell to form 2-cm-high cylindrical specimens. In an oedometric cell, the sample is prevented from expanding radially, but is allowed to expand axially: we measure how injections of solutions induce an axial expansion. In an isochoric cell, the sample is prevented from expanding both radially and axially: we measure how injections of solutions induce the development of axial and radial stresses. One of the main objectives is to aim at correlating the measurements with evolutions of the mineralogy: those evolutions are predicted by thermodynamic modeling.

Chapter 2 is devoted to present the materials and methods used. We introduce the developed protocol for preparing samples and performing the experiments in oedometric and isochoric cells. The rationale for the choice of the various parameters of the developed protocol are discussed. We also present various methods of characterization of mineralogy and microstructure: X-ray fluorescence (XRF), thermogravimetric analysis (TGA), X-ray diffraction (XRD), aluminum nuclear magnetic resonance ( $^{27}\text{Al}$ -NMR) and scanning electron microscopy with X-ray analysis (SEM-EDS). We finally introduce the thermodynamic approach used for predicting the evolutions of mineralogy.

Chapter 3 is devoted to the investigation of the role of various parameters on crystallization-induced expansions: role of mineralogy, role of localization of monosulfoaluminate with respect to C-S-H, role of localization of ettringite with respect to C-S-H.

Chapter 4 investigates the role of the crystallization of gypsum on the expansion. To find out any potential correlation between expansion and gypsum formation, we use thermodynamic modeling in parallel with the expansion experiments.

Chapter 5 is devoted to the investigation of how an expansion stress is induced by crystallization of ettringite and gypsum in a sample in restrained conditions. This chapter is based on isochoric experiments. Experimental results, in conjunction with results from mineralogical and microstructural

## CHAPTER 1. INTRODUCTION

---

characterizations, make it possible to quantify the individual contribution of ettringite and gypsum to the development of an expansion stress.

Chapter 6 presents the conclusions and perspectives.

## Chapter 2

# Materials and methods

---

THIS CHAPTER presents the materials on which and the methods with which we characterized expansion or stresses induced by injection of sodium sulfate. The materials, obtained by hydration or by chemical synthesis, were first ground into powders with a maximum grain size equal to 300  $\mu\text{m}$ . The samples were manufactured by compacting the powders in cylindrical cells, in which the samples were then injected with solutions of sodium sulfate. Experiments were carried out either in an oedometer cell or in an isochoric cell. In oedometer testing, we measured the axial deformation of the sample under a constant applied axial stress, while radial deformations were prevented. In isochoric testing, we measured the axial and radial stresses, while axial and radial deformations were prevented. To better understand how crystallization induces expansion or stresses, mineralogical and microstructural characterizations were carried out before and after the injections of sodium sulfate. We present a method (termed ‘Combi’) used for characterization of phase assemblages, which is based on a combination of results obtained from X-ray fluorescence (XRF), Rietveld X-ray diffraction (XRD), thermogravimetric analysis (TGA), scanning electron microscopy with energy-dispersive X-ray spectroscopy (SEM-EDS), aluminum nuclear magnetic resonance ( $^{27}\text{Al-NMR}$ ). The rationale for the grinding and compacting protocols, as well as the rationale for the choice of a specific

*method of characterization of phase assemblage, are discussed. Finally, we introduce the experimental program followed in this thesis.*

---

**C**E CHAPITRE présente les matériaux sur lesquels et les méthodes avec lesquelles nous avons caractérisé l'expansion ou les contraintes induites par l'injection de sulfate de sodium. Les matériaux, obtenus par hydratation ou par synthèse chimique, ont d'abord été broyés en poudre d'une taille de grains maximale égale à 300  $\mu\text{m}$ . Les échantillons ont été manufacturés par compaction de poudre dans des cellules cylindriques, dans lesquelles les échantillons ont alors été injectés avec des solutions de sulfate de sodium. Les expériences ont été effectuées soit dans une cellule oedométrique, soit dans une cellule isochore. Dans les expériences oedométriques, nous avons mesuré la déformation axiale de l'échantillon sous une contrainte axiale constante, alors que les déformations radiales étaient empêchées. Dans les expériences isochores, nous avons mesuré les contraintes axiale et radiale, alors que les déformations axiale et radiale étaient empêchées. Afin de mieux comprendre comment la cristallisation induit expansion ou des contraintes, des caractérisations minéralogiques et microstructurales ont été réalisées avant et après les injections de sulfate de sodium. Nous présentons une méthode (que nous appelons méthode 'Combi') utilisée pour la caractérisation des assemblages de phases, qui est basée sur une combinaison de résultats obtenus à partir de spectrométrie fluorescence des rayons X (FX), diffractométrie des rayons X (DRX), analyse thermogravimétrique (ATG), microscopie électronique à balayage avec spectroscopie à rayons X à dispersion d'énergie (MEB-EDS), résonance magnétique nucléaire de l'aluminium ( $^{27}\text{Al}$ -RMN). Le raisonnement ayant conduit aux protocoles de broyage et de compactage, ainsi que le raisonnement ayant conduit au choix d'une méthode spécifique de caractérisation de l'assemblage de phases, sont discutés. Enfin, nous présentons le programme expérimental suivi au cours de cette thèse.

---

## 2.1 Materials

In this work, we studied samples obtained by compaction of ground cementitious materials or of the phases of which they are constituted. Before testing, the preparation of the samples consisted of 3 main steps, including: synthesis of the materials, grinding (which, for some samples, was used to mix various materials), and compaction of the resulting powders (see Fig. 2.1). This section aims at presenting the developed protocol of how to manufacture the compacted samples.

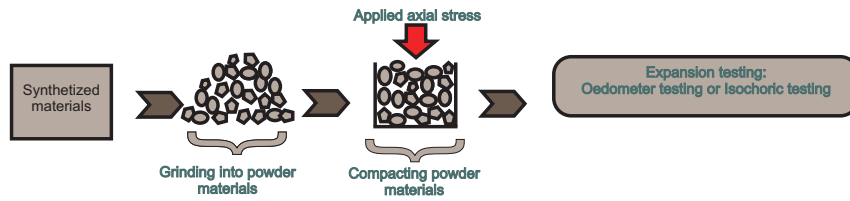


Figure 2.1: Schematics of the experimental process.

### 2.1.1 Ingredients

The ingredients used in the present works include:

- Ordinary Portland cement (noted OPC) paste
- $C_3S$  paste
- Monosulfoaluminate
- Portlandite
- Fontainebleau sand
- Limestone

The clinker used for the preparation of the ordinary Portland cement paste was a commercial CEM I provided by Lafarge and coming from the

Composition from XRF		Composition from XRD	
Component	Mass fraction, %	Phase	Mass fraction, %
SiO <sub>2</sub>	20.21	Alite	66.34
Al <sub>2</sub> O <sub>3</sub>	5.47	Belite	13.64
Fe <sub>2</sub> O <sub>3</sub>	1.9	Ferrite	4.7
CaO	68.85	Aluminate	10.18
MgO	1.09	Calcite	0.44
K <sub>2</sub> O	0.33	Gypsum	2.36
Na <sub>2</sub> O	0.2		
TiO <sub>2</sub>	0.19		
Loss on ignition	1.63		

Table 2.1: Chemical composition of the Ordinary Portland cement clinker used, in mass percent. XRF and XRD stand for X-ray fluorescence and X-ray diffraction, respectively.

Le Havre cement factory. Its chemical composition was obtained by X-ray fluorescence and is given in Tab. 2.1.

Portlandite and limestone (i.e., calcium carbonate) were purchased from Sigma-Aldrich and Omya SAS, respectively. According to the manufacturers, the purity of the portlandite and of the calcium carbonate was greater than 95% and 99%, respectively. The Fontainebleau sand was purchased from SIBELCO, its maximum grain size was inferior to 300  $\mu\text{m}$ .

The clinker used for the preparation of the C<sub>3</sub>S pastes was manufactured at Lafarge Centre de Recherche by heating a mixture of reagent-grade calcium carbonate CaCO<sub>3</sub> and silica SiO<sub>2</sub> at 1000°C during at least 4 hours (to decarbonate the mixture) and then at 1620°C during 3 days. The mixture was prepared at a molar ratio of calcium carbonate to silica of 3 to 1, which is the stoichiometry of the reaction of the formation of clinker, as observed in the following equation:



where the upward arrow indicates carbon dioxide gas CO<sub>2</sub> production. According to the results obtained by X-ray diffraction, the manufactured C<sub>3</sub>S clinker was quite pure, as indicated in Tab. 2.2 show.

Phase	Chemical composition	C <sub>3</sub> S clinker	C <sub>3</sub> A
C <sub>3</sub> S triclinic	3 CaO · SiO <sub>2</sub>	SP	-
C <sub>3</sub> S monoclinic	3 CaO · SiO <sub>2</sub>	SP	-
C <sub>2</sub> S	2 CaO · SiO <sub>2</sub>	PP	-
C <sub>3</sub> A	3 CaO · Al <sub>2</sub> O <sub>3</sub>	-	SP
Periclase	MgO	PP	-
Portlandite	Ca(OH) <sub>2</sub>	-	PP

Table 2.2: Mineralogical composition of C<sub>3</sub>S clinker and C<sub>3</sub>A clinker used, estimated by qualitative XRD. ‘SP’ stands for ‘strong probability’, ‘PP’ stands for ‘possible phases or suggested phases’, and ‘-’ stands for ‘not detected’.

Monosulfoaluminate was manufactured according to the following reaction:



by using reagent-grade tricalcium aluminate (noted C<sub>3</sub>A in cement chemistry notation) and gypsum (noted C\$H<sub>2</sub> in cement chemistry notation). Tricalcium aluminate C<sub>3</sub>A was quite pure, as results in Tab. 2.2 show. Tricalcium aluminate and gypsum were mixed in stoichiometric proportions, i.e., following Eq. (2.2), in a molar ratio of tricalcium aluminate to gypsum of 1 to 1. The solid mixture was then mixed with decarbonated water (noted H in cement chemistry notation) at a water-to-binder mass ratio of 20. The substance was stirred regularly at a constant temperature of 80°C during 3 weeks and then dried by freeze-drying. Results obtained by X-ray diffraction showed that the mass fraction of monosulfoaluminate in the material prepared according to this protocol was greater than 85%, the remaining 15% being partly composed of portlandite.

The OPC paste and the C<sub>3</sub>S paste were prepared with a water-to-binder mass ratio of 1 and conserved in plastic containers. Then, those plastic containers were rotated regularly to avoid sedimentation. After 1 month, we started curing the material for 90 days in saturated lime water at 20°C. Characterization of the solid phase obtained by X-ray diffraction showed that the hydration degree of both the OPC pastes and C<sub>3</sub>S pastes was greater than

96%.

### 2.1.2 Grinding and mixing of ingredients

After curing, the OPC paste and the  $C_3S$  paste were dried by vacuum drying and ground into a powder with a maximum grain size of  $300\ \mu\text{m}$ <sup>1</sup>. Each grinding was performed with 200 g of material in a ball mill for at least 3 hours at ambient temperature. The ball mill is described in Fig. 2.2. A typical grain size distribution is displayed in Fig. 2.3. Monosulfoaluminate AFm was ground with the same protocol. No grinding was necessary for portlandite or calcite, as they were already ground by the manufacturer.



Figure 2.2: Ball mill used for the present work, consisting in a motor, a ceramic container, and ceramic balls.

Some materials used to prepare the tested samples were obtained by mixing several ingredients. To obtain a homogeneous mixture, the protocol of mixing consisted of 2 steps: manual mixing and mechanical mixing. First, the ingredients to be mixed were put together into a plastic container. The plastic container was manually agitated for at least 15 minutes. Then, each mixture was placed into a different container, and all containers were agitated mechanically for 5 hours, as described in Fig. 2.4.

### 2.1.3 Materials preparation

We prepared 8 materials from the ingredients introduced in Sec. 2.1.1:

---

<sup>1</sup>The rationale for the choice of such maximum grain size will be presented in Sec. 2.2.3.

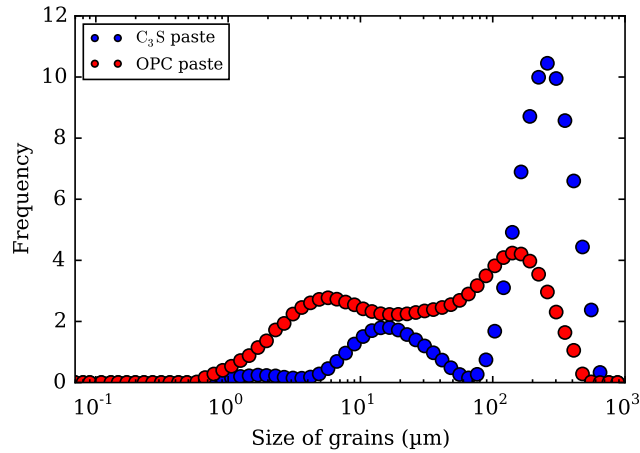


Figure 2.3: Grain size distribution of ground  $C_3S$  paste and ground OPC paste.

- 1 material obtained by hydrating the OPC clinker (those samples are labeled ‘OPC’).
- 1 material obtained by hydrating the  $C_3S$  clinker (those samples are labeled ‘C3S’).
- 1 material obtained by mixing a ground hydrated  $C_3S$  paste with a given amount of Fontainebleau sand which represented 40% of the mass of the mixture (those samples are labeled ‘C3S-sand’).
- 1 material obtained by hydrating the  $C_3S$  clinker mixed with a given amount of monosulfoaluminate, chosen such that the mass of monosulfoaluminate was equal to 8% of the mass of the hydrated paste (those samples are labeled ‘C3S-AFm8-b’).
- 1 material obtained by mixing the ground hydrated  $C_3S$  paste with the ground hydrated material ‘C3S-AFm8-b’ such that the final mass of monosulfoaluminate was equal to 3.83% of the mass of the mixture after the mixing (those samples are labeled ‘C3S-AFm4-b’).
- 1 material obtained by mixing the ground hydrated  $C_3S$  paste with the ground hydrated material ‘C3S-AFm8-b’ such that the final mass of

monosulfoaluminate was equal to 2% of the mass of the mixture after the mixing (those samples are labeled ‘C3S-AFm2-b’).

- 1 material obtained by mixing a ground hydrated  $C_3S$  paste with a given amount of monosulfoaluminate which represented 8% of the mass of the mixture (those samples are labeled ‘C3S-AFm8-a’).
- 1 material obtained by mixing a ground hydrated  $C_3S$  paste with a given amount of monosulfoaluminate which represented 3.83% of the mass of the mixture (those samples are labeled ‘C3S-AFm4-a’).
- 1 material obtained by mixing portlandite with an amount of monosulfoaluminate which represented 3.83% of the mass of the mixture (those samples are labeled ‘CH-AFm4’).

Calcite was added to materials ‘CH-AFm4’, ‘C3S-AFm4-a’, and ‘C3S-AFm8-a’ to decrease the mass fraction of CH in those samples and make it closer to the mass fraction of CH in materials ‘OPC’ and ‘C3S’. The phase composition of the 8 materials was obtained by XRD and is given in Tab. 2.3. In this table, Mc stands for monocarboaluminate, whose chemical formula is  $(CaO)_4(Al_2O_3)(CO_2)(H_2O)_{11}$ .

Materials	CH	C-S-H	Afwillite	AFm	AFt	CaCO <sub>3</sub>	Mc	C <sub>2</sub> S	C <sub>3</sub> S
OPC	25	57	0	8	0	5	3	2	0
C3S	25	64	0	0	0	7	0	2	2
CH-AFm4	20	0	0	3	0	77	0	0	0
C3S-AFm4-a	33	39	0	4	0	23	0	1	0
C3S-AFm8-a	22	50	0	7	0	21	0	1	0
C3S-AFm2-b <sup>(e)</sup>	26	60	2	2	0	7	0	3	0
C3S-AFm4-b	37	43	5	4	0	10	0	1	0
C3S-AFm8-b	29	48	8	8	0	6	0	1	0

Table 2.3: Phase assemblage of the various materials prepared, as obtained by X-ray diffraction, in mass percentage. (e) For material C3S-AFm2-b, the mineralogical composition was not obtained by XRD but was estimated from a combination of the mineralogical composition of materials ‘C3S-AFm8-b’ and ‘C3S’. Other methods than XRD for determining the phase assemblage will be discussed in Sec. 2.5. Notation: Mc stands for monocarboaluminate.

For each prepared material, when necessary, grinding and/or mixing were performed according to the protocol described in Sec. 2.1.2. Materials OPC, C3S, C3S-AFm8-b were ground. For materials C3S-AFm4-a and C3S-AFm8-a, we mixed monosulfoaluminate and calcite with the ground C3S paste. Materials C3S-AFm4-b and C3S-AFm2-b were manufactured by mixing ground C3S-AFm8-b and ground C3S paste. Material CH-AFm4 was prepared by mixing portlandite, monosulfoaluminate, and calcite, with no grinding involved.

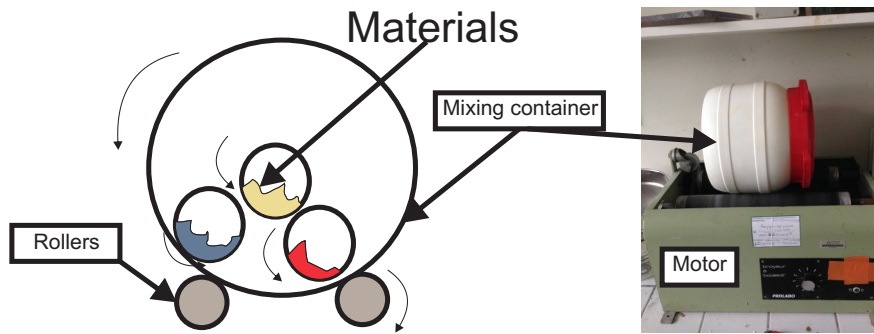


Figure 2.4: Schematics of mixing and machine used for mixing.

The solid phase density of the various prepared materials was measured by helium pycnometry and is given in Tab. 2.4. We measured the density of material OPC also by liquid pycnometry with demineralized water. The density of material OPC obtained with this latter method was equal to  $2.25 \text{ g/cm}^3$ , which is very close to the value determined by helium pycnometry. This results suggests that liquid pycnometry can be used to determine the solid phase density of ground hydrated cementitious materials.

## 2.2 Compaction and testing

Our experimental work aimed at measuring the expansion of and stress development in cement-based materials subjected to sulfate attacks. The samples we used were manufactured by compacting the powder materials presented in Sec. 2.1.3 into an oedometer cell or an isochoric cell. Both cells are made of a metallic hollow cylinder, so that compaction of the powder directly into those

Material	Density of solid phase, g/cm <sup>3</sup>
OPC	2.24
C3S	2.00
C3S-sand	2.61
CH-AFm4	2.58
C3S-AFm4-a	2.08
C3S-AFm8-a	2.06
C3S-AFm4-b	2.11
C3S-AFm8-b	2.24

Table 2.4: Solid phase density of the prepared powders, as measured by helium pycnometry.

cells yielded cylindrical samples. The mass of each sample was 18.09 g. The parameters of the protocol of compaction were chosen such that the samples remained quite permeable (the rationale for the choice of those parameters is described in details in Sec. 2.2.3).

The expansion or the stress development was induced by injecting a solution of sodium sulfate through the samples, still inside their oedometer or isochoric cell. As a reference or just to saturate the samples, the samples were also injected with pure water. In the oedometer cell, we measured the axial deformation of the sample under a constant axial stress, while preventing any radial deformation. In the isochoric cell, we measured both the radial and axial stresses applied by the sample on the cell induced by the injection of solution, while any radial or axial strain of the sample was prevented.

We prepared the solution of sodium sulfate from sodium sulfate decahydrate (i.e., mirabilite) purchased from Sigma-Aldrich, whose purity was larger than 99%. We used sulfate solutions with various concentrations ranging from 3 mM to 1190 mM.

### 2.2.1 Compaction and testing in oedometric cell

A schematic of an oedometer cell and a picture of an oedometer setup are displayed in Fig. 2.5. The inner diameter of the cell was 38 mm. Here, the loading frame applied a constant axial stress and the axial deformation

was measured over time with an electronic comparator whose accuracy was  $1\ \mu\text{m}$ . The cell was designed such that fluid could be injected throughout the sample, from its bottom to its top surface.

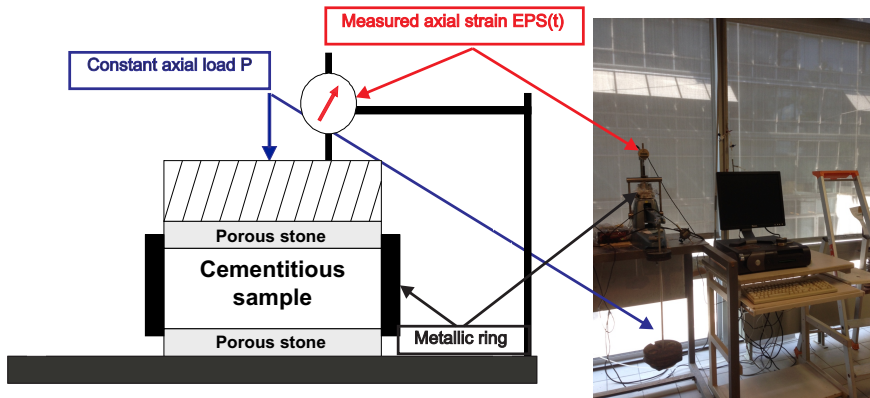


Figure 2.5: Schematics of an oedometer cell and pictures of the oedometer setup.

The height of the various samples ranged from 10.80 mm to 19.26 mm. The compaction process started by placing a given amount of ground material into the cell, as described in Fig. 2.6. Then, a mechanical axial stress of 88 kPa was applied and the sample was flushed (upwards) with demineralized water to saturate it: saturation induced swelling, probably as a consequence of the imbibition of C-S-H. We waited until this swelling slowed down significantly, which required more than 7 days, at which we obtain an estimation of the maximum swelling rate at which we consider equilibrium is reached. We then compacted the sample with an axial stress of 2 MPa. After compaction, the applied stress was decreased from 2 MPa to 0.88 MPa. Then, the sample was injected with demineralized water again.

Figure 2.7 displays the typical loading profile and strain evolution of a sample during compaction: although a significant creep was observed under a stress of 2 MPa, no more creep was observed after unloading. For soils, each loading step induces a time varying deformation due to a variation of porosity, which is called consolidation. Primary consolidation is related to a dissipation of the excess pore pressure induced by the mechanical loading. The secondary consolidation which may be caused by creep takes place after the primary

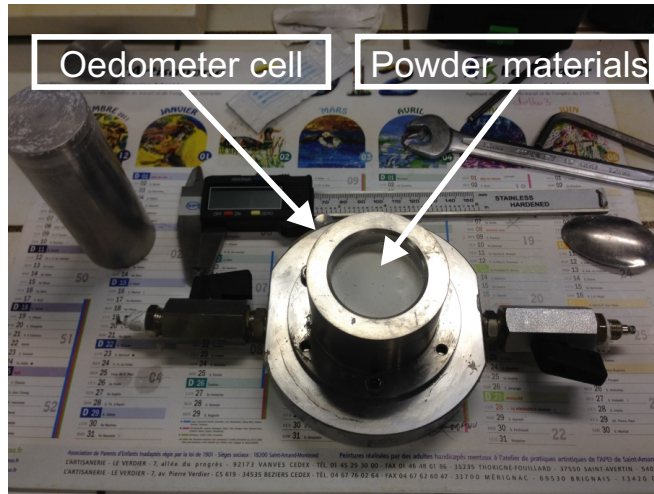


Figure 2.6: Powder materials placed into the oedometer cell. The powder was compacted manually before being compacted mechanically with the loading frame.

consolidation. Based on consolidation curves, we determined the swelling index  $C_s$  and the oedometric modulus  $E_{oed}$  of the sample under a mechanical load of 880 kPa from the deformations at the end of primary consolidation, as described in [Germaine \(2009\)](#). The swelling index  $C_s$  characterizes the magnitude of the increase in volume strain induced by an unloading with respect to a given stress state, while the oedometric modulus  $E_{oed}$  reflects the strain variation induced by an axial stress variation with respect to a given stress. A typical consolidation curve (here the one of material OPC) is displayed in [Fig. 2.8](#). The consolidation curves of the other prepared materials are given in [Appendix A.1](#). The physical and mechanical properties of all materials and samples tested in the oedometer cells can be found in [Tab. 3.2](#) and [4.2](#).

Before injection of the sulfate solution, the permeability of the sample was measured with an injection of demineralized water. For the various samples, this permeability ranged from about  $10^{-16}$  m<sup>2</sup> to about  $10^{-15}$  m<sup>2</sup>, which is 100 to 1000 times greater than the permeability of ordinary cementitious materials ([Powers, 1958](#)). Such high permeability is a direct consequence of the fact that the samples were obtained by compaction of a powder. The

## 2.2. COMPACTION AND TESTING

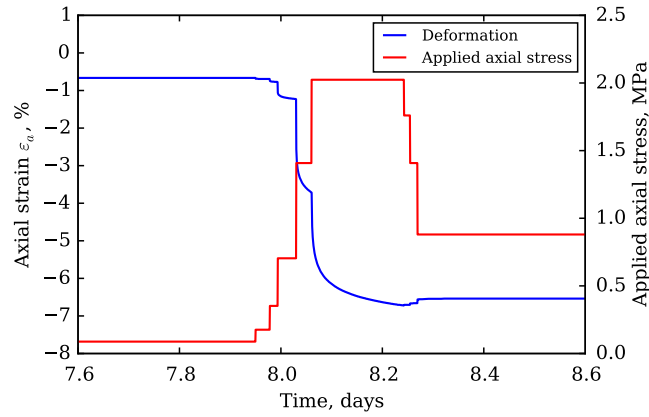


Figure 2.7: Load profile and resulting strain evolution of sample OPC during compaction into an oedometer cell.

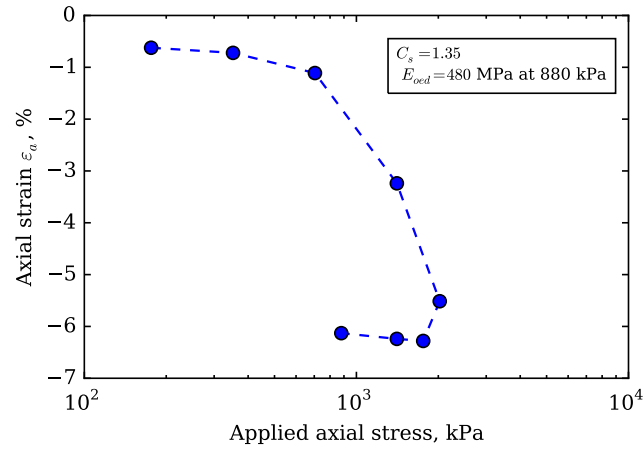


Figure 2.8: Compression curve (i.e., mechanical response during compaction into an oedometer cell) of the compacted powder material OPC.

pore size distribution was characterized by mercury intrusion porosimetry (MIP). For various materials prepared by oedometer compaction, their pore size distribution is displayed in Fig. 2.9.

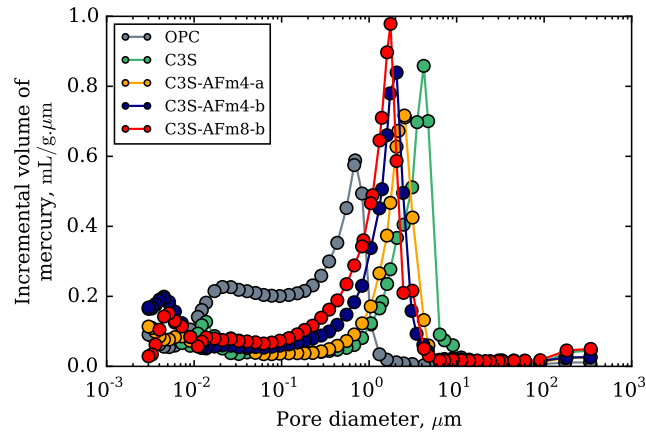


Figure 2.9: Pore size distribution of various powder materials compacted into the oedometer cell, as obtained by mercury intrusion porosimetry.

The test itself consisted in injecting the solution of sodium sulfate from the bottom toward the top of sample. For all tests but a few ones (see Tab. 2.17), the axial stress applied during the test was 0.88 MPa.

## 2.2.2 Compaction and testing in isochoric cell

A schematic of an isochoric cell and a photograph of the isochoric setup are displayed in Fig. 2.10.

In the isochoric cell, the deformation of the sample was prevented in both axial and radial directions (etymologically, ‘isochoric’ means ‘at constant volume’), while the radial stress and axial stress applied by the sample on the wall of the cell were measured with a pressure transducer and a force sensor, respectively, as indicated in Fig. 2.10. The pressure transducer (models PS-50KDM2, PS-50KGM2 and PS-70KDM2) and force sensor (model 1210AF-10KN) were purchased from ‘KYOWA electronic instruments’ and ‘Interface’, respectively.

## 2.2. COMPACTION AND TESTING

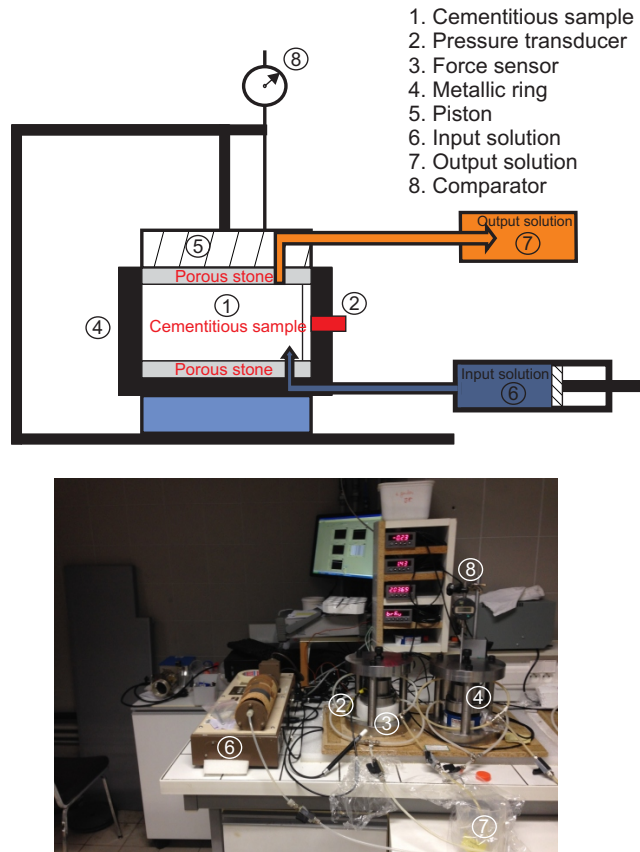


Figure 2.10: Schematic of an isochoric cell and photograph of the isochoric setting. Isochoric setup: Injection of sulfate solution performed by a standard pressure volume controller, axial and radial stresses measured by a pressure transducer and a force sensor, respectively, height of the sample controlled during compaction with an electronic comparator, data recorded with a computer.

For compaction of the samples dedicated to testing in the isochoric cells, the powder materials were compacted directly inside the isochoric cell into cylindrical samples with a diameter of 38 mm. The protocol of compaction into the isochoric cells consisted first, like for the compaction into the oedometric cells (see Sec. 2.2.1) in applying a slight axial stress of 88 kPa, flushing the sample with demineralized water, and letting it swell until an equilibrium was reached. Then we increased the axial stress to 2 MPa in several steps over a few hours, before decreasing it to 0.88 MPa. Compaction induced variations of height of the sample, which were measured with an electronic comparator following the top cap, as indicated in Fig. 2.10. Figure 2.11 displays an evolution of stresses during compaction. In-between increases of the axial stress up to 2 MPa, we observed relaxation of both radial and axial stresses over time. However, no more relaxation was observed after unloading down to 0.88 MPa. In addition, the radial stress that resulted from the compaction was significantly lower than the axial stress, both at the maximum load of 2 MPa and after unloading down to 0.88 MPa. If the sample were linear isotropic elastic, the ratio between radial and axial stresses should be equal to  $\nu/(1 - \nu)$ , where  $\nu$  is the Poisson's ratio. Here Fig. 2.11 shows that the ratio between radial and axial stresses was around 0.25, which would translate into a Poisson's ratio  $\nu = 0.2$ , which is a realistic value for cementitious materials.

After unloading, the sample was flushed again with demineralized water to measure its permeability. We also measured the bulk modulus at 880 kPa, which was obtained from variations of mean stress and volume strain, this latter being determined from the measurement of height variations of the sample. The physical and mechanical properties of the various samples tested in the isochoric cells can be found in Tab. 5.1.

The test itself consisted in injecting the solution of sodium sulfate from the bottom toward the top of sample. Before the first injection, the axial stress applied during the test was 0.88 MPa. For each injection of sulfate solution, the output solution was collected from the isochoric cell, as indicated in Fig. 2.10. Thanks to this possibility, we could determine, on top of the concentration of the input solution, the concentration of the output solution.

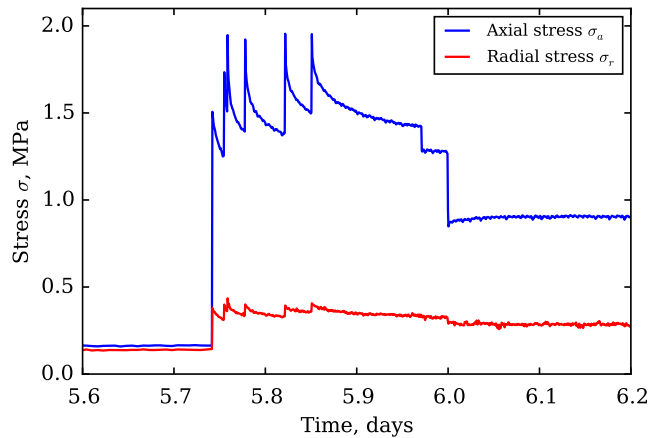


Figure 2.11: Stresses during compaction of powder material OPC into an isochoric cell.

How the concentrations were measured is described in Sec. 2.2.4.

### 2.2.3 Rationale for grinding and compaction protocol

During the protocol to manufacture the samples, we could choose the maximum size of the grains after grinding and the axial stress at which compaction was performed. This section details how those 2 parameters were chosen. When choosing those parameters, we aimed at obtaining samples that could be flushed ‘quickly’ with the sodium sulfate solution, i.e., with a characteristic time that would be smaller than the characteristic times of all other phenomena involved in the experiment. By doing so, we aimed at obtaining a homogeneous response of the sample to the injection. To allow for a ‘quick’ flushing, the sample should remain as permeable as possible. In the same time, the axial stress at which compaction was performed should remain significantly larger than the pressure at which the sodium sulfate solution was injected, to avoid any irreversible deformation of the sample induced by the flow of fluid.

We studied the relationship between permeability and compaction stress for powder material OPC ground down to a maximum grain size of 63  $\mu\text{m}$ . An incremental consolidation test was carried out with this material in the

oedometer cell to determine its intrinsic permeability as a function of the applied stress, as described in [Germaine \(2009\)](#). In such test, the coefficient of consolidation is determined from the compression curve. Based on this coefficient of consolidation, the hydraulic conductivity is determined with:

$$k_{v,j} = c_{v,j} \times \rho_w \times g \times \frac{\varepsilon_{s,j} - \varepsilon_{100,j}}{100 \times (\sigma_{a,j} - \sigma_{a,j-1})} \quad (2.3)$$

where  $k_{v,j}$  stands for the hydraulic conductivity (m/s) for load increment  $j$ ,  $c_{v,j}$  stands for the coefficient of consolidation for load increment  $j$  (m<sup>2</sup>/s),  $\rho_w$  stands for the mass density of water (kg/m<sup>3</sup>),  $g = 9.81$  m/s<sup>2</sup> stands for the gravitational acceleration,  $\varepsilon_{s,j}$  stands for the strain at the beginning of the consolidation for load increment  $j$  (-),  $\varepsilon_{100,j}$  stands for the strain at the end of consolidation for load increment  $j$  (-),  $\sigma_{a,j}$  and  $\sigma_{a,j-1}$  stand for the applied axial stress (Pa) for load increments  $j$  and  $j - 1$ , respectively. The intrinsic permeability was then determined from the hydraulic conductivity:

$$\kappa_{v,j} = \frac{k_j \times \rho_w \times g}{\eta_w} \quad (2.4)$$

where  $\kappa_j$  stands for the intrinsic permeability for load increment  $j$  (m<sup>2</sup>),  $\eta_w$  stands for the dynamic viscosity of water (Pa.s).

The measured permeability as a function of the compaction stress is displayed in [Fig. 2.12](#). The results shows that a greater applied axial stress led to a lower intrinsic permeability. Under 50 MPa of compaction stress, the intrinsic permeability was around  $2.3 \times 10^{-20}$  m<sup>2</sup>: with such permeability, to flush twice the pore volume of the sample with a typical pressure of injection of 500 kPa would require more than 700 days, which is much too slow. Even under a compaction stress of 6 MPa, the intrinsic permeability was around  $1.3 \times 10^{-18}$  m<sup>2</sup>, so that flushing of the sample would still require about 180 hours, which is still too long. Therefore, to obtain as high a permeability as possible, while keeping the compaction stress significantly larger than the targeted pressure of injection of 500 kPa, we chose a compaction stress of 2 MPa, and aimed at playing with the maximum grain size to maximize the permeability of the manufactured samples.

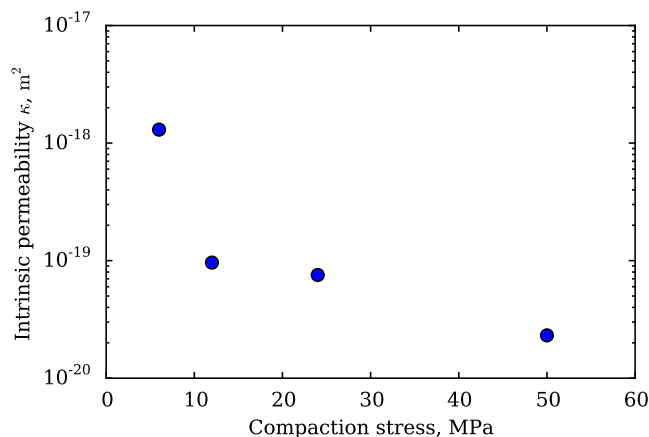


Figure 2.12: Permeability of material OPC versus the stress of compaction.

To determine an appropriate maximum grain size, we tested 2 samples, both compacted at 2 MPa, but manufactured from powder material OPC with 2 different maximum grain sizes: 300  $\mu\text{m}$  and 63  $\mu\text{m}$ . We did not measure their tensile strength. The intrinsic permeability of those samples was determined from a steady state injection of water. The results given in Tab. 2.5 show that the permeability of the sample with a maximum grain size of 300  $\mu\text{m}$  was 20 times higher than the permeability of the sample with a maximum grain size of 63  $\mu\text{m}$ . Flushing twice the porous volume of those samples with water at pressure of injection of 500 kPa would require 13 hours for the latter, but only about 40 minutes for the former. Therefore, we chose to grind the materials such that the maximum grain size was 300  $\mu\text{m}$ .

Material	Permeability $\kappa$ , $10^{-16}$ m <sup>2</sup>	Stress of compaction $\sigma_a$ , MPa	Max grain size $\mu\text{m}$	Porosity $\phi$ , %
OPC	3.75	2	300	60.5
OPC	$1.7 \times 10^{-1}$	2	63	54

Table 2.5: Properties of the tested samples. The porosity  $\phi$  is the porosity of the sample after compaction, but before injection.

In summary, the samples were manufactured by compacting the powder materials whose maximum grain size was equal to 300  $\mu\text{m}$ . The compaction

was carried out with an axial stress equal to 2 MPa. The permeability of the samples obtained with such protocol of compaction was on the order of  $10^{-16}$  m<sup>2</sup> (see Tab. 3.2 and 5.1), i.e., was about 100 times higher than the permeability of ordinary cement paste. With such samples, we could expect that flushing twice the pore volume of the samples with the sodium sulfate solution would take less than 1 hour.

### 2.2.4 Measurement of sulfate concentrations

In the isochoric cells, the concentration in sulfate of both the input and the output solutions was measured. In the oedometric cells, only the concentration in sulfate of the input solution was measured.

Sulfate concentrations were measured with a photometer from Hanna-France. The upper limit of the equipment is 150 mg/L and its accuracy is 1 mg/L $\pm$ 5% of the reading. To measure concentration which were higher than this upper limit, we had to dilute the solution to characterize with demineralized water. The uncertainty on the measured sulfate concentrations was calculated from:

$$|\Delta C_0| = C_0 \times \left( \left| \frac{\Delta C_1}{C_1} \right| + \left| \frac{\Delta V_1}{V_1} \right| + \left| \frac{\Delta V_0}{V_0} \right| \right) \quad (2.5)$$

where  $\Delta C_1/C_1$  stands for the uncertainty of the photometer, while  $\Delta V_1/V_1$  and  $\Delta V_0/V_0$  stand for the uncertainty on the volumes of solution before and after dilution, respectively. The values of those various uncertainties are given in Tab. 2.6.

Origin of error	Nature of error	Uncertainty	
Photometer	Measurement	$\frac{\Delta C_1}{C_1}$	$\frac{0.01 \text{ (mM)}}{C_1} + 5\%$
Container of original solution	Instrument	$\frac{\Delta V_0}{V_0}$	$\frac{0.2 \text{ (mm}^3\text{)}}{V_0} + 0.15\%$
Container of diluted solution	Instrument	$\frac{\Delta V_1}{V_1}$	$\frac{0.2 \text{ (mm}^3\text{)}}{V_1} + 0.15\%$

Table 2.6: Sources of uncertainties in the measurement of the concentrations in sulfates.

For experiments in isochoric cells, the sulfate concentration of both the input and the output solutions was measured with such protocol. During each injection of solution throughout the sample, the output solution was collected into a test tube. This solution was then filtered with a filter paper to remove any solid particle. The sulfate concentration of the output solution was measured right after collection and filtering, to avoid any potential delayed precipitation that would modify the sulfate concentration of solution, even though, according to our observations, the sulfate concentration of the output solution was the same right after the injection and a few days later.

Measurements of concentration by photometry were compared with measurements performed with 2 other usual methods: ionic chromatography and inductively coupled plasma atomic emission spectroscopy. Results of the comparison are displayed in Fig. 2.13: the comparison yields a good agreement between the various techniques, which shows that photometry is, for our study, a reliable method to measure sulfate concentrations. We measured the sulfate concentration of almost all solutions by photometry and the uncertainties were estimated by using Eq. (2.5).

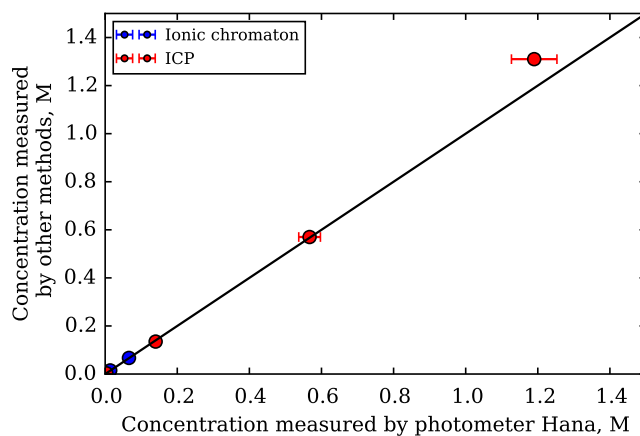


Figure 2.13: Sulfate concentrations measured by photometry, in comparison with concentrations measured with ion chromatography (noted ‘Ionic chromatation’) and inductively coupled plasma atomic emission spectroscopy (noted ‘ICP’).

## 2.3 Methods for characterization of phase assemblage and microstructure

In parallel to the measurement of the expansion or of the stresses induced by the injection of sulfates, we performed also a microstructural analysis of the samples and a characterization of their phase assemblage. The objective of such characterizations was to better understand the mineralogical or microstructural evolutions over the injections, and their correlation with the evolution of expansions or stresses. For this characterization of phase assemblage and microstructure, we used various methods: X-ray fluorescence (XRF), Rietveld X-ray diffraction (XRD), thermal gravity analysis (TGA),  $^{27}\text{Al}$  nuclear magnetic resonance (NMR), scanning electron microscopy with back-scattered electrons (SEM-EDS). All phase assemblages will be provided in terms of mass fractions.

Characterization was performed on the samples after testing, i.e., after all injections of sulfate solution. In parallel, we also manufactured reference samples, which were ground and compacted according to the procedure described in Sec. 2.2. However, those reference samples were only flushed with demineralized water, not with the solution of sodium sulfate: those reference samples are therefore representative of the tested samples, but before they were injected with the solution of sodium sulfate. A detailed list of which characterization was performed on which sample will be provided in Sec. 2.6.2.

To characterize a phase assemblage, various methods and experimental techniques are available. Here, in Secs. 2.3.1, 2.3.2, and 2.4.1, we present various experimental or thermodynamic methods that can provide information on the phase assemblage. The method which we eventually use in this thesis to characterize phase assemblages is described in Sec. 2.3.3: this new method, which we call method ‘Combi’, is based on a combination of results from XRF, XRD, TGA and  $^{27}\text{Al}$ -NMR. The rationale of design of such a method, together with a comparison with other methods, is given in Sec. 2.5.

### 2.3.1 Characterization of aluminate phases by $^{27}\text{Al}$ -NMR

For some materials (e.g., OPC, C3S-AFm8-b and C3S-AFm4-b), characterization or quantification of crystal AFt or AFm with XRD or TGA was expected to be difficult, as those phases could potentially be located in the vicinity of or inside C-S-H (Taylor, 1998). In contrast,  $^{27}\text{Al}$ -NMR is considered to be a powerful technique to characterize aluminates phases (e.g., calcium aluminate, ettringite, monosulfoaluminate) (Skibsted et al., 1993; Skibsted, 1997; Poulsen et al., 2009). Here, we performed  $^{27}\text{Al}$  magic-angle spinning nuclear magnetic resonance (MAS-NMR) experiments, at 208.5 MHz on a 18.8 T spectrometer equipped with a 3.2 mm probehead operating at a spinning frequency of 22 kHz. The record was carried out with 1  $\mu\text{s}$  pulse length (15° pulse angle), 0.5 s recycle delay and 2048 transients. We obtained the relative proportions between the different sites by simulating the spectra with the ‘dmfit software1’, as described in Massiot et al. (2002), and the results are given with an uncertainty of  $\pm 1\%$ . The  $^{27}\text{Al}$ -NMR characterizations presented and used for quantification of the aluminate phases in this thesis were carried out and analyzed at Laboratory ‘Laboratoire de Spectrochimie Infrarouge et Raman (LASIR)’, Lille University of Science and Technology, France, by Grégory Tricot. Other  $^{27}\text{Al}$ -NMR characterizations, performed at Department of Chemistry, Aarhus University, Denmark, can be found in Append. A.2.

The typical results of  $^{27}\text{Al}$ -NMR characterizations given by Lille University of Science and Technology, France are displayed in Tab. 2.7 in which there are 6 aluminate phases: ‘CAH/TAH’, ‘AFm’, ‘AFt’, ‘Al(V)’, ‘C-A-S-H’ and ‘Unknown’, which stands for third aluminate hydrate phase, monosulfoaluminate, ettringite, five-coordinated aluminum, calcium silicate hydrate (C-S-H) incorporating aluminum and ‘unknown aluminate phase’. There is a lack of knowledge for ‘Al(V)’ and ‘Unknown’ aluminate phases. In practice, we simplified the assemblage of aluminate phases by assimilating ‘CAH/TAH’, ‘Al(V)’ and ‘Unknown’ to  $\text{C}_3\text{AH}_6$ . This leads to 4 aluminate phases: AFm, AFt,  $\text{C}_3\text{AH}_6$  and C-A-S-H, whose quantities can be computed with the following equations:

$$n_{\text{AFt}} = f_{\text{AFt}} \times n_{\text{Al}_2\text{O}_3} \quad (2.6)$$

$$n_{\text{AFm}} = f_{\text{AFm}} \times n_{\text{Al}_2\text{O}_3} \quad (2.7)$$

$$n_{\text{C}_3\text{AH}_6} = (1 - f_{\text{AFt}} - f_{\text{AFm}} - f_{\text{C-A-S-H}}) \times n_{\text{Al}_2\text{O}_3} \quad (2.8)$$

where  $f_{\text{AFm}}$ ,  $f_{\text{AFt}}$  and  $f_{\text{C-A-S-H}}$  stand for the mole fraction of AFm, AFt and C-A-S-H (i.e., of calcium silicate hydrates that include alumina) with regard to the total mole amount  $n_{\text{Al}_2\text{O}_3}$  of alumina, respectively.  $^{27}\text{Al}$ -NMR provides those mole fractions, while the total mole amount  $n_{\text{Al}_2\text{O}_3}$  of alumina can be obtained with XRF. In contrast, the amount of C-A-S-H cannot be determined by using only results from XRF and  $^{27}\text{Al}$ -NMR characterizations, because the molar mass of C-A-S-H is not known (see more details in Sec. 2.3.3).

An example of the distribution of aluminate phases in various samples before injection of sulfates is given in Tab. 2.7. In this table, OPC(1), OPC(2) and OPC(3) stand for 3 different samples prepared with material OPC.

Materials	Phases distribution of $\text{Al}_2\text{O}_3$ , Molar (%)					
	CAH/TAH	AFm	AFt	Al(V)	C-A-S-H	Unknown
OPC(1)	21	47	7	6	19	-
OPC(2)	18	50	7	6	19	-
OPC(3)	17	52	7	6	18	-
C3S-AFm8-b	6	42	8	6	19	19
C3S-AFm4-b	9	40	22	7	17	5
C3S-AFm8-a	4	68	28	-	-	-
CH-AFm4	0	76	24	0	0	-

Table 2.7: Distribution of  $\text{Al}_2\text{O}_3$  in various materials before injection of sulfates, characterized by  $^{27}\text{Al}$ -NMR. Notations: ‘CAH/TAH’, ‘AFm’, ‘AFt’, ‘Al(V)’ and ‘C-A-S-H’ stand for third aluminate hydrate phase, monosulfoaluminate, ettringite, five-coordinated aluminum and calcium silicate hydrate (C-S-H) incorporating aluminium.

### 2.3.2 Other analytical methods: XRF, XRD, TGA, SEM

After testing (i.e., after injection of the solution of sodium sulfate) or flushing with water (for the reference samples), each sample was immersed in acetone and vacuum-dried to stop all chemical reactions. Immersion in acetone lasted for 1 day for samples unexposed to sulfates, and for a few weeks for samples exposed to sulfates (since the permeability of those latter was lower than the one of the former). Vacuum-drying lasted for about 3 days. After drying, the samples were ground into powder materials such that the maximum grain size was 63  $\mu\text{m}$ . Then, on each sample we performed X-ray fluorescence (XRF), Rietveld X-ray diffraction (XRD) and thermal gravity analysis (TGA): XRF was used to determine the chemical composition of the samples, while XRD and TGA were used to determine their mineralogical composition.

X-ray diffraction (XRD) analysis was performed with a Philips X'Pert Pro and X'Celerator detector. The  $2\theta$ -ranges scanned from  $5^\circ$  to  $65^\circ$  with a scan speed of  $0.016^\circ/\text{min}$ .

Thermogravimetric analysis was performed by using an ATG SETARAM 92-16 AMPP-0058 from  $30^\circ\text{C}$  to  $1000^\circ\text{C}$ , with a heating rate of  $10^\circ\text{C}/\text{min}$ .

In addition, sections of samples were observed by scanning electron microscopy (SEM) combined with image analysis treatments of digital images (Meulenyzer and Chen, 2013). The sections were cut parallel to the axial direction of the samples, impregnated with resin, polished and coated with a conductive layer of carbon. The SEM observations were performed with back-scattered electrons and energy dispersive X-ray analysis in a Philips scanning electron microscope.

All XRF, XRD, TGA, and SEM characterizations were carried out at Lafarge Centre de Recherche, Saint-Quentin Fallavier, France.

### 2.3.3 New method of characterization of phase assemblage based on a combination of results from XRF, XRD, TGA and $^{27}\text{Al}$ -NMR

In this section, we propose a new method (which we call method ‘Combi’) to determine the phase assemblage of our materials, which we will use throughout the thesis. This method ‘Combi’ is based on results obtained with XRF, XRD, TGA and  $^{27}\text{Al}$ -NMR:

- According to results given by XRF and  $^{27}\text{Al}$ -NMR characterizations, the amounts of the various aluminate phases (i.e., AFm, AFt,  $\text{C}_3\text{AH}_6$ ) are obtained by using Eqs. (2.6), (2.7) and (2.8) (see Sec. 2.3.1).
- The amounts of portlandite and calcite are determined with TGA.
- The amounts of the other crystalline phases are determined with XRD.
- The amount of solid attributed to none of the previously mentioned phases is considered to be C-S-H or C-A-S-H, where C-A-S-H stands for calcium silicate hydrates that include alumina (Rossen, 2014; Hopital, 2014). Distinguishing C-S-H from C-A-S-H is difficult, so that we will refer to those phases together as to the C-(A)-S-H phase or the C-(A)-S-H gel.

As will be discussed in Sec. 2.5.1, we observed some carbonation of our samples, which occurred after testing. This issue (i.e, carbonation) probably occurs during the preparation of the samples for the post-testing characterization. For samples characterized before exposure to sulfates, the amount of calcite initially added to the mixture is known (see Tab. 2.3): subtracting this amount from the total amount of calcite measured with TGA yields the amount of calcite produced by carbonation of C-(A)-S-H which probably occurred in a very dry environment (see more detail in Sec. 2.5.1). This mass  $m_{\text{C}\bar{\text{c}}}$  of calcite produced by carbonation of C-(A)-S-H is considered to have replaced a mass  $m_{\text{C}\bar{\text{c}}}M_{\text{CaO}}/M_{\text{CaCO}_3}$  of C-(A)-S-H (noted  $m_{\text{C}\bar{\text{c}}}^{\text{CASH}(0)}$ ) in the phase assemblage before carbonation, where  $M_{\text{CaO}}$  and  $M_{\text{CaCO}_3}$  are the

molar masses of CaO and CaCO<sub>3</sub>, respectively. Therefore, to obtain the phase assemblage of the sample before carbonation, which we believe is the phase assemblage that was exposed to sulfates, the mass  $m_{C\bar{c}}$  of calcite must be replaced by a mass  $m_{C\bar{c}}M_{CaO}/M_{CaCO_3}$  of C-(A)-S-H (noted  $m_{C\bar{c}}^{CASH(1)}$ ). For samples characterized after exposure to sulfates, we assume that the mass of calcite produced by carbonation of C-(A)-S-H is the same as the one in the corresponding sample before exposure to sulfates (i.e.,  $m_{C\bar{c}}^{CASH(1)} = m_{C\bar{c}}^{CASH(0)}$ ).

To convert the phase assemblages (expressed in mass fraction) into a chemical composition, the molar mass of the various phases must be known. The molar mass of C-(A)-S-H depends on the ratios CaO/SiO<sub>2</sub>, Al<sub>2</sub>O<sub>3</sub>/SiO<sub>2</sub>, and H<sub>2</sub>O/SiO<sub>2</sub>. Those values are chosen such that the chemical composition calculated from the phase assemblage is as close as possible to the one obtained with XRF. All values used, for all samples before and after exposure, are provided in Sec. 2.5.1: we will see in that section that all those values are realistic.

The justification and validation of this method will be discussed further in Sec. 2.5.

## 2.4 Thermodynamic modeling

In this thesis, thermodynamic modeling was carried out by using CHESS (Chemical Equilibrium of Species and Surfaces), which was developed by J. van der Lee, Centre d'Informatique and Géologique, Ecole des Mines Paris-Tech (Lee, 1998), with the database Cemdata14 of cement-based materials obtained from Lafarge Centre de Recherche (Lothenbach and Winnefeld, 2006; Damidot et al., 2011; Matschei et al., 2007). CHESS is a model of chemical speciation computing the equilibrium state of aqueous systems. Here, this thermodynamic modeling is carried out at 20°C by using the Truncated-Davies models for correction of activity.

CHESS is also able to determine the saturation index  $SI$  of various crystals (e.g., ettringite and gypsum) with the following expression:

$$SI = \log(IAP/K) \quad (2.9)$$

where  $IAP$  and  $K$  stand for the ion activity product and the equilibrium constant, respectively. The saturation index is a useful quantity to determine whether the solution is saturated ( $SI=0$ ), undersaturated ( $SI<0$ ), or supersaturated ( $SI>0$ ) with respect to the given crystal. In practice CHESS was mainly used at equilibrium, so that the saturation index was either zero or negative. In some cases, when we wanted to estimate the maximal saturation index with of a given phase, we ran the calculation while disabling the precipitation of the phase of interest. The calculation assumes that the saturation index of a given crystal would be maximal before the precipitation of crystal and the solution is in thermodynamic equilibrium with other phases (see more details in [Flatt et al. \(2006\)](#); [Kunther et al. \(2013\)](#)).

### 2.4.1 Thermodynamic calculations of phase assemblage

In this section, we present a method to calculate a phase assemblage, based on a combination of XRF data and thermodynamic calculations. This method of calculating the phase assemblage will be referred to as the method ‘XRF + CHESS’. Indeed, on top of the standard methods used for characterization of the mineralogy such as XRD or TGA, we also determined the chemical composition of the samples by XRF (the methods for those various techniques were described in Sec. 2.3.2). Based on the chemical composition (i.e, the amounts of  $\text{CaO}$ ,  $\text{SO}_3$ ,  $\text{Al}_2\text{O}_3$ ,  $\text{Fe}_2\text{O}_3$ , and  $\text{SiO}_2$ ), we will show how the phase assemblage can also be figured out by using thermodynamic calculations.

To facilitate the thermodynamic calculations with the oxide components, a first step consists in determining the data that needs to be input into the thermodynamic calculation. To do so, we estimated the amounts of  $\text{C}_3\text{AH}_6$ ,  $\text{CH}$ ,  $\text{C}\text{S}\text{H}_2$ ,  $\text{Fe}(\text{OH})_3$  and  $\text{C-S-H}$  from the XRF measurements by using the following equations:

$$n_{\text{C}\text{S}\text{H}_2} = n_{\text{SO}_3} \tag{2.10}$$

$$n_{\text{C}_3\text{AH}_6} = n_{\text{Al}_2\text{O}_3} \tag{2.11}$$

$$n_{\text{Fe}(\text{OH})_3} = n_{\text{Fe}_2\text{O}_3} \times 2 \tag{2.12}$$

$$n_{\text{C-S-H}} = n_{\text{SiO}_2} \quad (2.13)$$

$$n_{\text{CH}} = n_{\text{CaO}} - n_{\text{SO}_3} - 3 \times n_{\text{Al}_2\text{O}_3} - 1.6 \times n_{\text{SiO}_2} - n_{\text{CaCO}_3} \quad (2.14)$$

where  $n_X$  stands for the molar amount of compound X. Those amounts were input in the thermodynamic calculation, and CHESS then determined the phase assemblage that ensured thermodynamic equilibrium.

In this method, we assumed that the hydration degree of the materials was equal to 100%. Eq. (2.14) is obtained by assuming that the ratio Ca/Si of C-S-H is equal to 1.6. Also, the amount of  $\text{CaCO}_3$  displayed in Eq. (2.14) was considered to be equal to all calcium carbonate phases detected by XRD (i.e., calcite, vaterite, and so on).

Predictions of the phase assemblage of a sample can be performed very quickly with CHESS. However, beside this advantage, thermodynamic calculations with CHESS present an important drawback: the database does not include C-A-S-H.

### 2.4.2 Thermodynamic modeling of evolution of phase assemblage

In this thesis, we will aim at linking, over the injections of sodium sulfate solutions, expansion or variations of stresses with evolutions of the phase assemblage. Since an experimental characterization of the phase assemblage could not be realized during the injections experiments as this characterization involves a variety of destructive techniques (see Sec. 2.3.3), evolutions of phase assemblage over the injections need to be estimated. In this section, we describe how we estimated those evolutions. To validate the approach on a hydrated cement paste (material OPC) injected in a repeated manner with a solution of sodium sulfate, we compare, at the end of the experiment, the predicted phase assemblage with the one measured experimentally.

Estimations of the evolutions of the phase assemblage over the injection process are carried out with the software CHESS. The initial phase assemblage input into CHESS is the one obtained with the method ‘Combi’ (see Sec. 2.3.3). The mineralogical evolution is calculated with CHESS by flush-

ing this initial phase assemblage with a solution of sodium sulfate. Flushing is a process consisting in removing one part of the mother solution (i.e., the solution in thermodynamic equilibrium with the actual solid phases) and replacing it with the flush solution (here the sulfate solution): once this replacement is performed, CHESS determines the new phase assemblage in thermodynamic equilibrium. We assume that the solution of sodium sulfate is in equilibrium with the carbon dioxide present in the atmosphere. The fugacity of  $\text{CO}_2$  introduced for that purpose is equal to  $4 \times 10^{-4}$  atm, as the impact of sodium sulfate on the fugacity of carbon dioxide is negligible at the sulfate concentrations considered (Huet, 2005; Jödecke et al., 2015).

In terms of input data for the thermodynamic model, we assume for all samples that the unhydrated phases (e.g.,  $\text{C}_3\text{S}$ ,  $\text{C}_2\text{S}$ ) and the ettringite present in the initial phase assemblage (on average on all samples, about 7% of all  $\text{Al}_2\text{O}_3$  was located in ettringite) do not react with the flush solution. Indeed, since the various pastes have already been hydrated for 3 months, assuming that no additional hydration takes place during the experiment seems to be a reasonable assumption. In addition, in the thermodynamic model, C-(A)-S-H is replaced with C-S-H, due to the lack of thermodynamic data for C-(A)-S-H. We assume that the fraction of aluminates present in the C-(A)-S-H phase (on average on all samples, about 20% of all  $\text{Al}_2\text{O}_3$  was located in C-(A)-S-H, see Tab. A.1) is not available for further chemical reactions (Hopital, 2014).

We now consider the specific case of a sample made with material OPC (i.e., a hydrated cement paste made with ordinary Portland cement) and injected repeatedly with a sodium sulfate solution with a concentration equal to 66 mM. According to results obtained by  $^{27}\text{Al}$ -NMR displayed in Tab. 2.14, for this sample, after exposure, about 80% of all  $\text{Al}_2\text{O}_3$  was located in ettringite. The fact that about 20% of all  $\text{Al}_2\text{O}_3$  did not end up in ettringite supports the assumption that aluminates in C-(A)-S-H are inert.

The predicted evolutions of phase assemblage over the injections of sulfate are displayed in Fig. 2.14. Based on the total amount of sulfate injected through this sample, the final phase assemblage was predicted: this prediction is compared in Fig. 2.15 with the phase assemblage measured after the

experiment. In Fig. 2.16, the chemical composition predicted with the thermodynamic model at the end of experiment is compared with the one actually measured. Those two figures (Fig. 2.14 and 2.16) show that the thermodynamic model can predict quite accurately the phase assemblage and chemical composition of this sample. This conclusion suggests that the duration of the injections is sufficiently long to consider that a hypothesis of thermodynamic equilibrium over the injections is reasonable. This suggestion will in fact be widely supported in Chap. 4 and 5. Therefore, thermodynamic modeling through CHESSE proves to be a reliable tool to estimate the evolutions of the phase assemblages over the injection process.

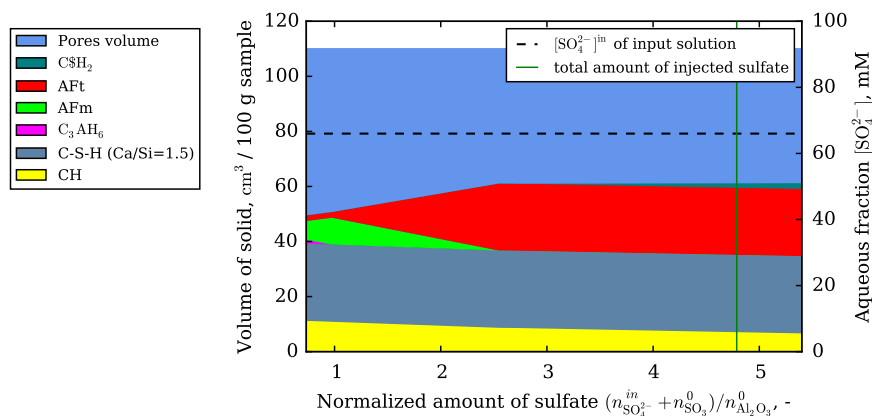


Figure 2.14: Thermodynamic modeling of the evolution of the phase assemblage of material OPC upon exposure to a solution of sodium sulfate with a concentration equal to 66 mM.

However, the predicted evolutions of phase assemblages with CHESSE displayed in Fig. 2.14 could not predict accurately the amount of calcium carbonate formed in the sample material. In fact, CHESSE predicted almost no formation of calcium carbonate, which shows that the amount of carbon dioxide injected with the solution through the sample is too small to explain production of calcite (i.e., carbonation), from what we conclude that carbonation did not occur during the experiment.

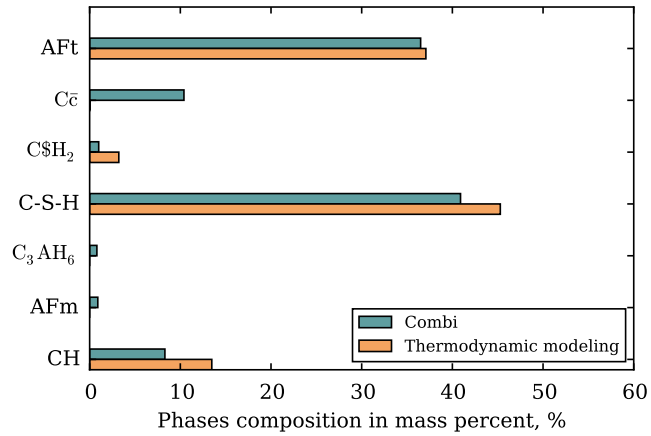


Figure 2.15: Phase assemblage of material OPC after exposure to a solution of sodium sulfate with a concentration equal to 66 mM, as predicted with thermodynamic modeling and measured with the method ‘Combi’.

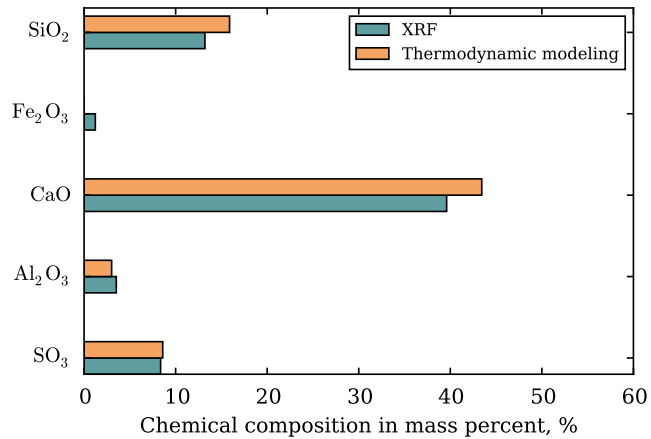


Figure 2.16: Chemical composition of material OPC after exposure to a solution of sodium sulfate with a concentration equal to 66 mM, as predicted with thermodynamic modeling and measured with the method XRF.

## 2.5 Comparison between methods for characterizing phase assemblage

We will compare 3 methods that can be used for the characterization of the phase assemblage of various materials, which are:

- XRD quantitative characterizations (noted as ‘XRD’).
- Thermodynamic calculations based on the chemical composition determined by XRF (noted as ‘CHESS+XRF’). This method was presented in Sec. 2.4.1.
- The method that we named ‘Combi’, which is based on a combination of results from XRF, XRD, TGA and  $^{27}\text{Al}$ -NMR, and was presented in Sec. 2.3.3.

Before doing so, in Sec. 2.5.1, we will justify and validate the method ‘Combi’, which will therefore serve as a reference. The aim of the comparison will be to determine, on various samples before or after exposure to sulfates, whether XRD or the method ‘CHESS+XRF’ can be used to determine accurate phase assemblages. The phase assemblage of all samples, before and after exposure to sulfates, can be found in Appendix. A.3. The term ‘Initial phase assemblage’ that we will use later refers to the phase assemblage of the samples before injection of sulfates, but after flushing with demineralized water.

### 2.5.1 Method ‘Combi’: justification and validation

As explained in Sec. 2.3.3, the method ‘Combi’ includes a correction for the post-testing carbonation of the samples. This section is dedicated to scrutinize this carbonation and justify how we corrected for it in the characterization of the phase assemblage.

On the various samples considered, when considering for the C-(A)-S-H phase a Ca/Si mole ratio equal to 1.5 and an Al/Si mole ratio equal to 0.03, we calculated the phase assemblages from the method ‘Combi’ but

in which we introduced no correction for carbonation. We converted those uncorrected phase assemblages into elemental compositions. When doing so and comparing these elemental compositions with the ones measured with XRF, consistently, we observed that the amount of CaO was overestimated (see Fig. 2.17 for the specific example of sample OPC). Likewise, for the predicted amount of CaO to correspond to the one measured with XRF, we needed to consider that the Ca/Si mole ratio in the C-(A)-S-H phase was around 1.2, which is unrealistically low. We believe that this discrepancy is due to carbonation of C-S-H.

	CH	C-S-H	Afwillite	AFm	AFt	CaCO <sub>3</sub>	Mc	C <sub>2</sub> S	C <sub>3</sub> S
After grinding <sup>a</sup>	22	69	0	3	0	1	0	1	2
After flushing with water	25	57	0	8	0	5	3	2	0

Table 2.8: Phase assemblage of material OPC, after grinding, and after flushing with water.

<sup>a</sup>before flushing with water

Carbonation may have occurred before testing, during testing, or after testing. It is likely that the observed carbonation did not occur during testing, as the detailed thermodynamic analysis performed in Sec. 2.4.2 shows that the amounts of carbon dioxide brought to the sample by the injected solution (in equilibrium with carbon dioxide from the atmosphere) is much too small to explain the extent of carbonation observed. Also, an XRD analysis of material OPC after its grinding but before its use for testing is provided in Tab. 2.8, which shows that the material placed in the cells was not carbonated. Table 2.8 also shows that, when having compacted the same material OPC, flushed it with water, and dried it to perform characterization, some carbonation was observed, as the mass fraction of calcite increased from 1% to 5%. A comparison of the two phase assemblages displayed in this table shows that this carbonation therefore occurs after experiment and this may result from the step of sample preparation for all post-testing characterizations. We also infer that under such conditions, carbonation occurred in C-S-H, not in CH. This observation is surprising (although not unique

## 2.5. COMPARISON BETWEEN METHODS FOR CHARACTERIZING PHASE ASSEMBLAGE

(Drouet, 2011)), as thermodynamic calculations show that, usually, carbonation should consume all CH before consuming C-S-H. A tentative explanation is the following: when vacuum-drying the samples before all experimental characterizations, drying may have been insufficient, water may have remained in C-(A)-S-H, which would have favored its carbonation. Based on this explanation, we considered that, during testing, C-(A)-S-H was not carbonated (i.e., its carbonation occurred after testing), hence the correction for carbonation introduced in the method ‘Combi’ (see Sec. 2.3.3).

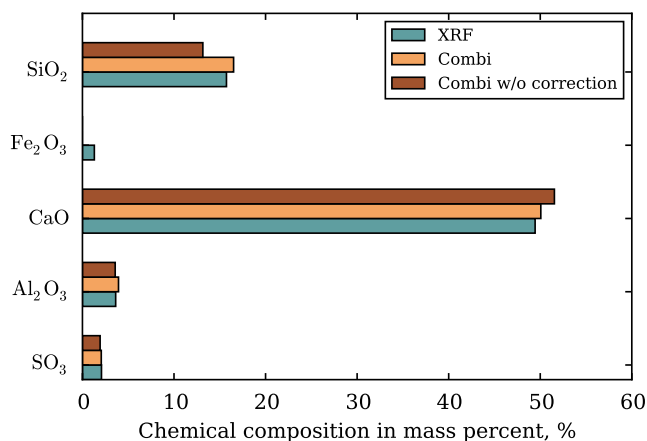


Figure 2.17: Elemental composition of sample OPC obtained with XRF, with the method ‘Combi’ (which includes a correction for carbonation), and with a method ‘Combi’ in which no correction for carbonation would be used.

Figure 2.15 displays the phase assemblage of the same material OPC, but after exposure to sulfates. On this figure, the phase assemblage is either directly measured, or predicted through thermodynamic modeling (see Sec. 2.4.2). In this latter, the prediction uses as an input the phase assemblage before exposure to sulfates. The comparison between the two phase assemblages shows that, in-between the moment when the sample started being exposed to sulfates and the moment when the sample was characterized, both CH and C-(A)-S-H were partly carbonated. For samples characterized after exposure to sulfates, we assume that the mass of calcite produced by carbonation of C-(A)-S-H is the same as the one in the corresponding sample before exposure to sulfates. In contrast, we introduce no correction for post-

testing carbonation of CH: the rationale for such choice was that, at the time when we fixed the protocol to perform the calculations of phase assemblages, the XRD results obtained after grinding and displayed in Tab. 2.8 were not available, so that we did not know whether carbonation of CH had occurred before or after testing.

The phase assemblages obtained with the method ‘Combi’ (which includes a correction for carbonation) are validated against the XRF data. To convert the phase assemblages (expressed in mass fraction) into a chemical composition, the molar mass of the various phases must be known. The molar mass of C-(A)-S-H depends on the ratios  $\text{CaO}/\text{SiO}_2$ ,  $\text{Al}_2\text{O}_3/\text{SiO}_2$ , and  $\text{H}_2\text{O}/\text{SiO}_2$ . Those values are chosen such that the chemical composition calculated from the phase assemblage is as close as possible to the one obtained with XRF. Table 2.9 provides those ratios, for samples before exposure to sulfates. One observes that all Ca/Si ratios are comprised between 1.5 and 1.6, which are realistic values. For all those samples, the back-calculated ratio  $\text{H}_2\text{O}/\text{SiO}_2$  is equal to 3, which is also realistic. With those realistic ratios, the phase assemblages yield an elemental composition that is in very good agreement with the one obtained with XRF (see Fig. 2.17 for the specific case of material OPC, and Sec. 2.5.2 to 2.5.5 for other samples). For samples after exposure to sulfate solutions, values of those ratios are given in Tab. 2.10.

Note that Tab. 2.9 also provides the ratios  $\text{CaO}/\text{SiO}_2$  and  $\text{Al}_2\text{O}_3/\text{SiO}_2$  of the C-(A)-S-H gel obtained with SEM-EDS, which is a technique that is regularly used for that purpose. But Tab. 2.9 also provides the ratio  $\text{Al}_2\text{O}_3/\text{SiO}_2$  of the C-(A)-S-H gel (noted as  $\left(\frac{\text{Al}_2\text{O}_3}{\text{SiO}_2}\right)_{\text{CASH}}$ ), as determined also from results obtained by  $^{27}\text{Al}$ -NMR and XRF, as follows:

$$\left(\frac{\text{Al}_2\text{O}_3}{\text{SiO}_2}\right)_{\text{CASH}} = \frac{f_{\text{C-A-S-H}} \times f_{\text{Al}_2\text{O}_3} \times M_{\text{SiO}_2}}{f_{\text{SiO}_2} \times M_{\text{Al}_2\text{O}_3}} \quad (2.15)$$

where  $f_{\text{C-A-S-H}}$  stands for the molar fraction of C-A-S-H (obtained with  $^{27}\text{Al}$ -NMR), and where  $f_X$  and  $M_X$  stand for mass fraction (obtained with XRF) and molar mass of oxide X. The ratios  $\text{CaO}/\text{SiO}_2$  and  $\text{Al}_2\text{O}_3/\text{SiO}_2$  obtained for the C-(A)-S-H gel with the method ‘Combi’ compare very well with those ratios measured otherwise, but for the 3 OPC materials, for which the ratio

## 2.5. COMPARISON BETWEEN METHODS FOR CHARACTERIZING PHASE ASSEMBLAGE

Ca/Si of the C-(A)-S-H gel obtained from SEM-EDS was slightly larger than the ratio used for the method ‘Combi’. This higher ratio Ca/Si may be due to the existence of nano crystals of CH intimately mixed with C-S-H (Chen et al., 2010).

Finally, Tab. 2.9 also provides the density  $\rho_{C(A)SH}$  that must be attributed to the C-(A)-S-H phase to retrieve the phase density of the solid phase measured by pycnometry: all those densities lie in the range [1.83-2.85] g/cm<sup>3</sup> that is found in the literature for C-(A)-S-H (Jennings, 2008; Pinson et al., 2015).

Material	CaO/SiO <sub>2</sub>		Al <sub>2</sub> O <sub>3</sub> /SiO <sub>2</sub>			$\rho_{C(A)SH}$ , g/cm <sup>3</sup>
	‘Combi’	SEM-EDS	‘Combi’	SEM-EDS	<sup>27</sup> Al-NMR	
OPC(1)	1.5	1.9	0.03	0.03	0.02	2.3
OPC(2)	1.5	1.9	0.03	0.03	0.03	2.3
OPC(3)	1.5	1.9	0.03	0.03	0.03	2.3
C3S	1.5	N/A	0.0	N/A	N/A	2.6
C3S-sand <sup>(e1)</sup>	1.5	1.8	0.0	0.0	N/A	2.1
CH-AFm4	0.0	N/A	0.0	N/A	N/A	N/A
C3S-AFm4-a	1.5	1.5	0.0	0.0	0.0	2.3
C3S-AFm8-a	1.5	N/A	0.0	N/A	0.01	1.9
C3S-AFm2-b <sup>(e2)</sup>	1.6	N/A	0.01	N/A	N/A	2.3
C3S-AFm4-b	1.6	1.5	0.02	0.02	0.02	2.1
C3S-AFm8-b	1.6	1.6	0.02	0.02	0.02	2.3

Table 2.9: Ratios CaO/SiO<sub>2</sub>, Al<sub>2</sub>O<sub>3</sub>/SiO<sub>2</sub>, H<sub>2</sub>O/SiO<sub>2</sub> and density  $\rho_{C(A)SH}$  of the C-(A)-S-H gel for all materials before exposure to sulfates. ‘Combi’ indicates the ratios that must be considered for the C-(A)-S-H gel for the chemical composition calculated from the phase assemblages measured with the method ‘Combi’ to be close to the one measured with XRF. ‘SEM-EDS’ and ‘<sup>27</sup>Al-NMR’ indicate the ratios measured with SEM-EDS and <sup>27</sup>Al-NMR combined with XRF, respectively. The density of C-(A)-S-H  $\rho_{C(A)SH}$  is the one back-calculated from the phase assemblages given in Tab. 2.16 to retrieve the density of the solid phase given in Tab. 2.4.

In conclusion, the proposed method ‘Combi’, which includes a correction for post-testing carbonation, yields phase assemblages which are consistent with other experimental results, such as chemical composition, density of C-

Test reference	CaO/SiO <sub>2</sub>	Al <sub>2</sub> O <sub>3</sub> /SiO <sub>2</sub>	H <sub>2</sub> O/SiO <sub>2</sub>
OPC-3	1.2	0.01	3.0
OPC-3-66	1.5	0.01	3.0
OPC-66	1.5	0.01	3.0
OPC-1190	1.2	0.01	5.0
OPC-140(O)	1.5	0.02	3.0
OPC-315(O)	1.5	0.02	3.0
OPC-540(O)	1.5	0.01	3.0
OPC-1190(O)	1.5	0.02	3.0
CH-AFm4	0.0	0.0	0.0
C3S-AFm4-a-66	1.5	0.0	3.0
C3S-AFm4-a-1190	1.5	0.0	4.0
C3S-AFm8-a	1.5	0.0	3.0
C3S-AFm4-b	1.6	0.02	3.0
C3S-AFm8-b	1.6	0.02	3.0

Table 2.10: Ratios CaO/SiO<sub>2</sub>, Al<sub>2</sub>O<sub>3</sub>/SiO<sub>2</sub>, H<sub>2</sub>O/SiO<sub>2</sub> considered for the C-(A)-S-H gel for the chemical composition calculated from the phase assemblages measured with the method ‘Combi’ to be close to the one measured with XRF, for samples after exposure to sulfates. Values are provided only for the tests after which the characterization was sufficiently thorough to apply the method ‘Combi’.

## 2.5. COMPARISON BETWEEN METHODS FOR CHARACTERIZING PHASE ASSEMBLAGE

---

(A)-S-H, or ratio Ca/Si of C-(A)-S-H. We will use this method ‘Combi’ to measure phase assemblages throughout the thesis.

### 2.5.2 Characterization of initial phase assemblage of samples CH-AFm4, C3S-AFm4-a, and C3S-AFm8-a

Samples CH-AFm4, C3S-AFm4-a and C3S-AFm8-a were manufactured by mixing well-known synthesized phases. In samples C3S-AFm4-a and C3S-AFm8-a, aluminum phases were added after hydration of the C3S, so that aluminum had no chance to be located within the C-S-H gel. The calculated initial phase assemblages of those materials are given in Tab. 2.11.

The application of the method ‘Combi’ to sample CH-AFm4 needed to be slightly adapted. Indeed, we recall that, with the method ‘Combi’, once the mass of all phases but C-S-H is determined, the remaining mass of solid in the sample is considered to be C-S-H (see Sec. 2.3.3). For sample CH-AFm4, this method cannot be directly used, as the sample contains no C-S-H. Therefore, for this sample, after quantification of the mass of CH, AFm, AFt, and  $C_3AH_6$ , the remaining mass of solid in the sample was considered to be calcite. The phase assemblage thus determined was quite identical to the one obtained with XRD. The chemical composition obtained from the phase assemblage thus determined was quite similar to the chemical composition obtained with XRF, as shown in Fig. 2.18.

Table 2.11 shows that the amounts of CH and C-S-H predicted with the method ‘XRF+CHESS’ are consistent with the ones obtained with XRD and with the method ‘Combi’ for sample CH-AFm4-a, but inconsistent for samples C3S-AFm4-a and C3S-AFm8-a. For those latter two samples, with respect to the other 2 methods, the method ‘XRF+CHESS’ significantly underestimated the amount of CH.

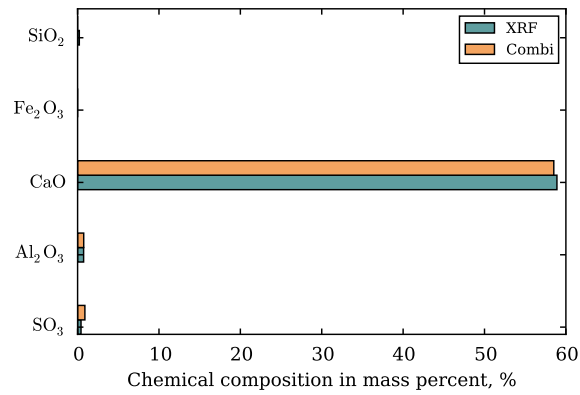
For the 3 samples considered in this section, the amount of AFm determined with XRD was comparable to the one determined with the method ‘Combi’, while the method ‘XRF+CHESS’ underestimated the amount of AFm and overestimated the amount of monocarboaluminate, noted Mc and whose chemical formula is  $(CaO)_4(Al_2O_3)(CO_2)(H_2O)_{11}$ . This observation

Material	Phase	Methods used			
		XRD	XRF+CHESS	TGA	Combi
CH-AFm4-a	CH	20	17.3	19	19
	C-S-H	0	0.7	N/A	0
	AFm	3	0.0	N/A	3.4
	Mc	0	3.1	N/A	0
	AFt	0	2.2	N/A	2.2
	C $\bar{c}$	77	76.7	77	75.4
	C <sub>3</sub> AH <sub>6</sub>	0	0.0	N/A	0
C3S-AFm4-a	CH	33	22.2	32	35
	C-S-H	39	49.5	N/A	49
	AFm	4	0.0	N/A	4
	Mc	0	3.5	N/A	0
	AFt	0	2.5	N/A	0
	C $\bar{c}$	23	22.3	21	11
	C <sub>3</sub> AH <sub>6</sub>	0	0.0	N/A	0
C <sub>2</sub> S	1	0.0	N/A	1	
C3S-AFm8-a	CH	22	11.7	22	22.7
	C-S-H	50	56.0	N/A	53.3
	AFm	7	0.0	N/A	6.8
	Mc	0	6.9	N/A	0.0
	AFt	0	5.0	N/A	5.7
	C $\bar{c}$	21	20.3	17	10.3
	C <sub>3</sub> AH <sub>6</sub>	0	0.0	N/A	0.2
C <sub>2</sub> S	1	0.0	N/A	1.0	

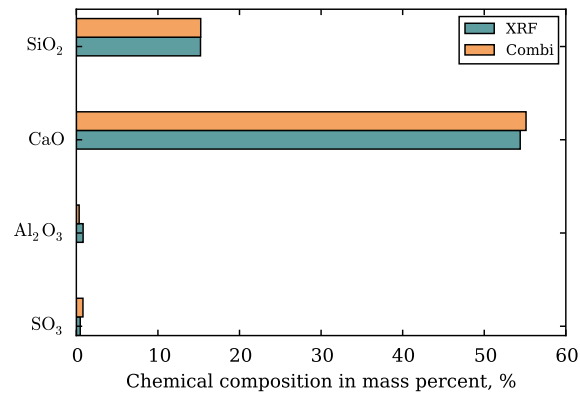
Table 2.11: Initial phase assemblage of samples CH-AFm4, C3S-AFm4-a, and C3S-AFm8-a, obtained with various methods.

## 2.5. COMPARISON BETWEEN METHODS FOR CHARACTERIZING PHASE ASSEMBLAGE

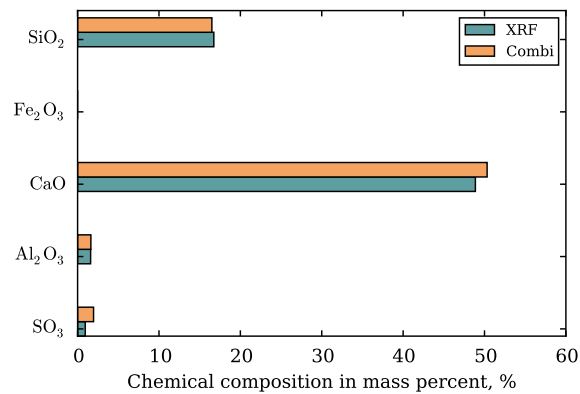
---



(a)



(b)



(c)

Figure 2.18: Chemical compositions calculated from the phase assemblage obtained with the method 'Combi' and measured with XRF: samples (a) CH-AFm4, (b) C3S-AFm4-a and (c) C3S-AFm8-a.

shows that XRD can yield quantitative measurement of the amount of AFm, when AFm is not intimately mixed with C-S-H (which, here, is a consequence of the fact that AFm was added after hydration of the paste). In contrast, the method XRD could not detect ettringite, while  $^{27}\text{Al}$ -NMR, on which the method ‘Combi’ is based, shows that there was ettringite in samples CH-AFm4-a and C3S-AFm8-a.

### 2.5.3 Characterization of initial phase assemblage of samples C3S-AFm4-b and C3S-AFm8-b

The phase assemblage of samples C3S-AFm4-b and C3S-AFm8-b, calculated with the various methods considered, is given in Tab. 2.12. The amounts of aluminate phases obtained with XRD differed from the ones obtained with the method ‘Combi’. This difference may be due to the fact that, in those samples, some AFm or AFt could be located in the vicinity or inside C-(A)-S-H, which might make it hard to detect with XRD.

Based on the phase assemblage obtained with the method ‘Combi’, we determined the chemical composition of the samples. These chemical compositions, together with the ones obtained with XRF, are displayed in Fig. 2.19. The chemical compositions back-calculated from the method ‘Combi’ were quite comparable to the ones obtained with XRF.

As was the case in Sec. 2.5.2, XRD and the method ‘XRF+CHESS’ significantly misestimated the amounts of CH or C-(A)-S-H and XRD did not detect any ettringite in the samples, while there was some and the method ‘XRF+CHESS’ overestimated that amount and the amount of Mc. The method ‘XRF+CHESS’ also significantly underestimated the amounts of AFm, while that amount was quite well measured with XRD.

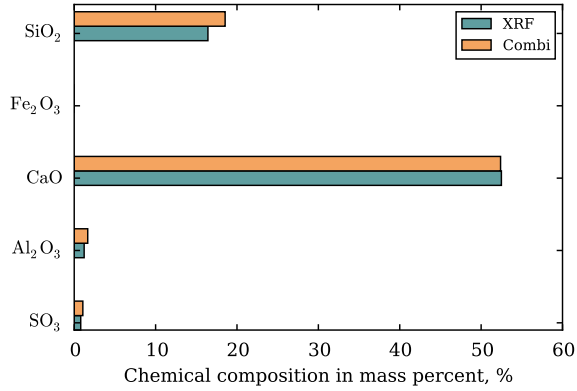
### 2.5.4 Characterization of initial phase assemblage of samples OPC

The chemical composition of samples OPC(1), OPC(2), and OPC(3) were determined with XRF: the results are displayed in Fig. 2.20. Those 3 OPC

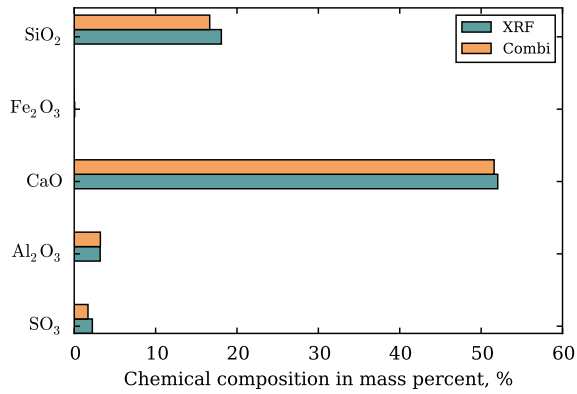
2.5. COMPARISON BETWEEN METHODS FOR CHARACTERIZING  
PHASE ASSEMBLAGE

Material	Phase	Methods used			
		XRD	XRF+CHESS	TGA	Combi
C3S-AFm4-b	CH	37	26.5	28	29.2
	C-(A)-S-H	43	54.8	N/A	62.3
	Afwillite	5	0.0	N/A	0.0
	AFm	4	0.0	N/A	3.1
	Mc	0	5.0	N/A	0.0
	AFt	0	4.3	N/A	3.4
	C $\bar{c}$	10	9.3	9.0	0.0
	C <sub>3</sub> AH <sub>6</sub>	0	0.0	N/A	0.9
	C <sub>3</sub> FH <sub>6</sub>	0	0.0	N/A	0.0
C <sub>3</sub> S	1	0.0	N/A	1.0	
C3S-AFm8-b	CH	29	18.3	27	27.7
	C-(A)-S-H	48	55.5	N/A	55.8
	Afwillite	8	0.0	N/A	0.0
	AFm	8	0.0	N/A	8.4
	Mc	0	11.7	N/A	0.0
	AFt	0	10.9	N/A	3.2
	C $\bar{c}$	6	3.6	6	0.0
	C <sub>3</sub> AH <sub>6</sub>	0	0.0	N/A	3.8
	C <sub>3</sub> FH <sub>6</sub>	0	0.0	N/A	0.0
C <sub>3</sub> S	1	0.0	N/A	1.0	

Table 2.12: Initial phase assemblage of samples C3S-AFm4-b and C3S-AFm8-b, obtained with various methods.



(a)



(b)

Figure 2.19: Chemical compositions calculated from the phase assemblage obtained with the method 'Combi' and measured with XRF: samples (a) C3-AFm4-b and (b) C3S-AFm8-b.

## 2.5. COMPARISON BETWEEN METHODS FOR CHARACTERIZING PHASE ASSEMBLAGE

samples were ground and compacted at 3 different moments, but all with the protocol presented in Sec. 2.2. The chemical compositions of the 3 samples were almost identical, which confirms the reproducibility of the protocol developed to manufacture the samples. The initial phase assemblages of the 3 OPC samples obtained with the various methods are given in Tab. 2.13.

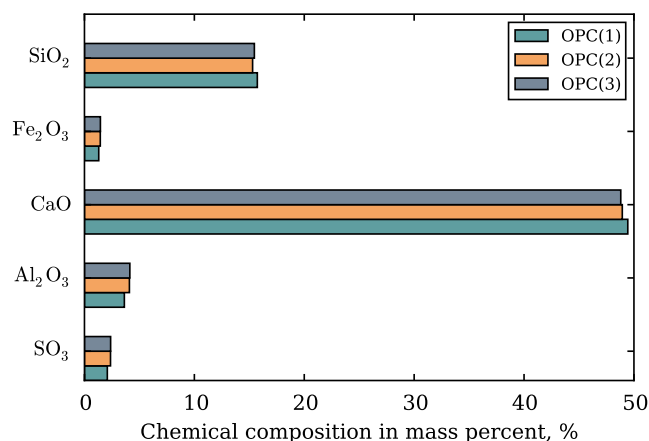


Figure 2.20: Chemical compositions of 3 OPC samples, measured with XRF.

As results in Fig. 2.21 and in Tab. 2.7 show, in the OPC samples here considered, we observed experimentally a mixture of C-S-H with alumina. From SEM-EDS measurements, the average Ca/Si and Al/Si (equal to  $2\text{Al}_2\text{O}_3/\text{SiO}_2$ ) ratios of the C-(A)-S-H gel were 1.9 and  $2 \times 0.03 = 0.06$ , respectively, while those ratios, based on the phase assemblage obtained with the method ‘Combi’, were 1.5 and 0.03, respectively (see Tab. 2.9). The difference in ratio Ca/Si may be due to the existence of nanocrystals of CH intimately mixed with C-(A)-S-H (Chen et al., 2010), and that would be included in the C-(A)-S-H gel for SEM-EDS measurements.

Based on the phase assemblages obtained with the method ‘Combi’, we determined also the chemical composition of the samples: Figure 2.22 shows that the chemical compositions back-calculated from the method ‘Combi’ were quite comparable to the ones obtained with XRF.

XRD correctly measured the amounts of CH in the samples but over-estimated very significantly the amounts of C-(A)-S-H. As was the case

Material	Phase	Methods used			
		XRD	XRF+CHESS	TGA	Combi
OPC(1)	CH	24	13.8	25	26.6
	C-(A)-S-H	60	50.9	N/A	54.1
	AFm	7	0.0	N/A	11.1
	Mc	0	15.1	N/A	0.0
	AFt	0	10.7	N/A	3.1
	C $\bar{c}$	8	4.5	14	0.0
	C <sub>3</sub> AH <sub>6</sub>	0	0.0	N/A	3.8
	Fe–Mc	0	5.0	N/A	0.0
	C <sub>2</sub> S	1	0.0	N/A	1.1
OPC(2)	CH	24	10.6	23	24.3
	C-(A)-S-H	57	49.0	N/A	54.0
	AFm	8	0.0	N/A	13.2
	Mc	0	16.8	N/A	0.0
	AFt	0	12.2	N/A	3.7
	C $\bar{c}$	8	5.9	12	0.0
	Vaterite	2	0.0	N/A	0.0
	C <sub>3</sub> AH <sub>6</sub>	0	0.0	N/A	3.8
	Fe–Mc	0	5.5	N/A	0.0
C <sub>2</sub> S	1	0.0	N/A	1.1	
OPC(3)	CH	25	14.0	24	25.0
	C-(A)-S-H	57	51.0	N/A	52.9
	AFm	8	0.0	N/A	13.6
	Mc	3	15.3	N/A	0.0
	AFt	0	12.6	N/A	3.7
	C $\bar{c}$	5	1.4	9	0.0
	C <sub>3</sub> AH <sub>6</sub>	0	0.0	N/A	3.7
	Fe–Mc	0	5.7	N/A	0.0
	C <sub>2</sub> S	2	0.0	N/A	1.0

Table 2.13: Initial phase assemblage of 3 OPC samples, obtained by various methods of characterization. Notation: Fe–Mc stands for Fe-monocarboaluminate.

## 2.5. COMPARISON BETWEEN METHODS FOR CHARACTERIZING PHASE ASSEMBLAGE

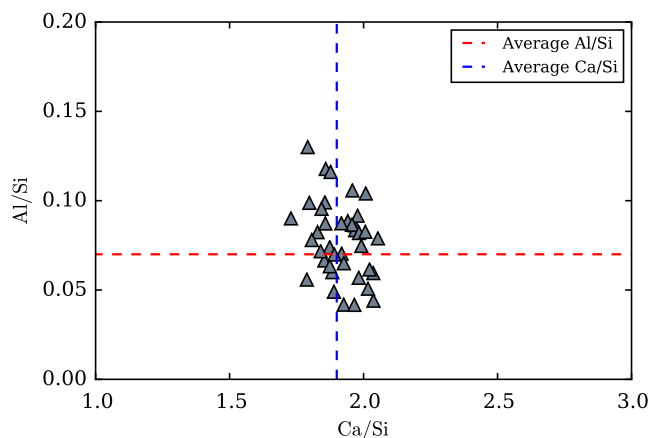


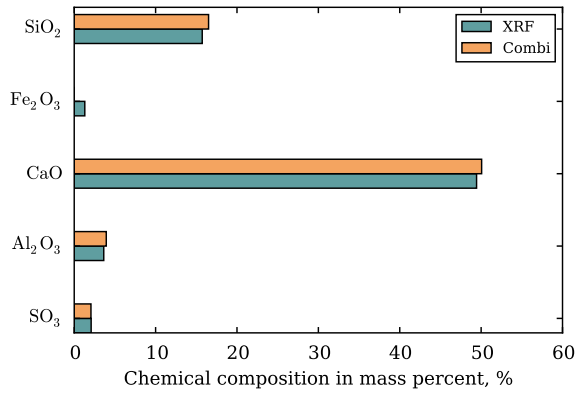
Figure 2.21: SEM-EDS measurement of the Ca/Si and Al/Si ratio of the C-(A)-S-H in material OPC flushed with water only.

in Sec. 2.5.2, the method ‘XRF+CHESS’ significantly underestimated the amount of CH and of C-(A)-S-H. Here, both XRD and the method ‘XRF+CHESS’ underestimated the amount of AFm. Again, XRD could not detect ettringite in the samples, while there was some and the method ‘XRF+CHESS’ overestimated this amount.

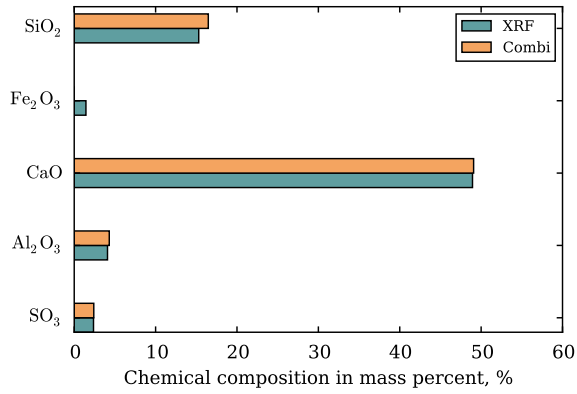
### 2.5.5 Characterization of phase assemblage of samples after exposure to sulfates

On samples after testing, i.e., after having performed the injections of sodium sulfate solution, the chemical and mineralogical characterizations were also performed by using XRF, XRD, TGA and  $^{27}\text{Al}$ -NMR. In this section, we present and discuss the phase assemblage of samples C3S-AFm8-a, C3S-AFm8-b, and OPC, after exposure to a sodium sulfate solution of concentration of 66 mM, obtained with the various methods introduced at the beginning of Sec. 2.3.

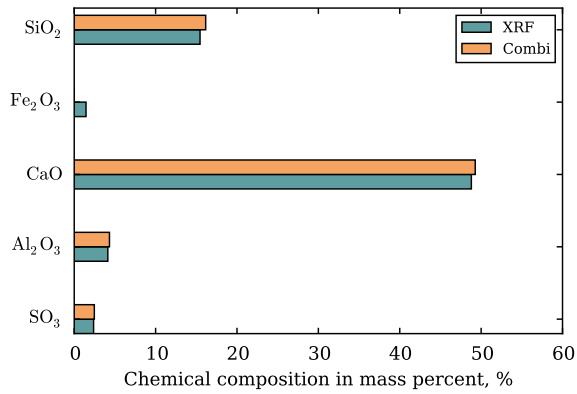
Results of characterizations of aluminates phases obtained by  $^{27}\text{Al}$ -NMR are shown in Tab. 2.14. The phase assemblage of the 3 materials, obtained with the methods ‘XRD’, ‘XRF+CHESS’, and ‘Combi’, is given in Tab. 2.15. We note that the amount of ettringite obtained with the method ‘Combi’ was



(a)



(b)



(c)

Figure 2.22: Chemical compositions calculated from the phase assemblage obtained with the method 'Combi' and measured with XRF: samples (a) OPC(1), (b) OPC(2), and (c) OPC(3).

## 2.5. COMPARISON BETWEEN METHODS FOR CHARACTERIZING PHASE ASSEMBLAGE

close to the one obtained with XRD for sample C3S-AFm8-a, which is a sample for which, after the injection of sulfates, we observed no ettringite within the C-S-H gel, as Fig. 2.23 shows. Said otherwise, for materials in which ettringite is not intimately mixed with the C-S-H gel, the amount of ettringite can be determined accurately with XRD. In Sec. 2.5.2, the same type of conclusion was drawn, for the characterization of the amount of AFm in samples C3S-AFm4-a and C3S-AFm8-a after injection of sulfate. These observations suggest that the amount of an aluminate phase such as monosulfoaluminate or ettringite can be accurately determined with XRD, if the aluminate phase is not intimately mixed with the C-S-H gel, may it be before or after exposure to sulfates.

Materials	Distribution of aluminate phases, Molar (%)					
	CAH/TAH	AFm	AFt	Al(V)	C-A-S-H	Unknown
OPC	2	4	81	4	9	-
C3S-AFm8-b	1	1	90	1	7	-
C3S-AFm8-a	5	5	80	3	7	-

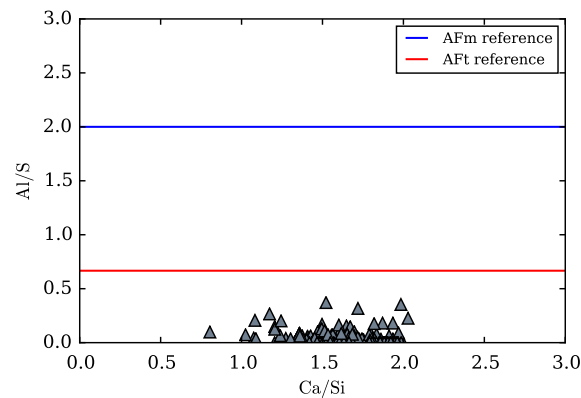
Table 2.14: Distribution of aluminate phases in samples after exposure to a sodium sulfate solution with a concentration equal to 66 mM, characterized with  $^{27}\text{Al}$ -NMR.

The chemical compositions are displayed in Fig. 2.24. For samples C3S-AFm8-a and C3S-AFm8-b (see Fig. 2.24 (a) and (b)), XRD and the method ‘Combi’ yielded chemical compositions which were in equally good agreement with the chemical composition obtained with XRF. In contrast, for sample OPC (see Fig. 2.24 (c)), XRD yielded poorer chemical compositions than the method ‘Combi’ (again, with respect to the chemical composition obtained with XRF). The results also confirm that the method ‘Combi’ can yield a chemical composition that is comparable to the one obtained with XRF. We note however that the mass fraction of  $\text{SO}_3$  obtained with the method ‘Combi’ was slightly lower than the one obtained with XRF: such discrepancy may be due to an underestimation of gypsum with XRD. This underestimation of the amount of gypsum is one limitation of the method ‘Combi’, will be discussed in more details in Chap. 4.

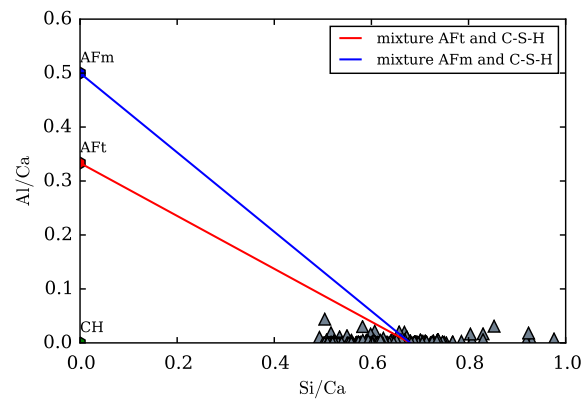
Material	Phase	Methods used			
		XRD	XRF+CHESS	TGA	Combi
C3S-AFm8-a	CH	25	18.5	25	26.5
	C-(A)-S-H	32	34.6	N/A	43.6
	AFm	0	0.0	N/A	0.4
	AFt	13	17.0	N/A	12.7
	C $\bar{c}$	28	28.5	25	12.7
	C <sub>3</sub> AH <sub>6</sub>	0	0.0	N/A	0.4
	C\$H <sub>2</sub>	0	1.5	N/A	0.0
	C <sub>2</sub> S	2	0.0	N/A	2.1
C3S-AFm8-b	CH	17	11.3	18	18.3
	C-(A)-S-H	37	47.1	N/A	47.9
	Afwillite	10	0.0	16	0.0
	AFm	0	0.0	N/A	0.2
	AFt	27	32.4	N/A	28.5
	C $\bar{c}$	8	8.3	8	3.8
	C <sub>3</sub> AH <sub>6</sub>	0	0.0	N/A	0.2
	C\$H <sub>2</sub>	0	0.8	N/A	0.0
OPC	C <sub>2</sub> S	1	0.0	N/A	1.0
	CH	5	0.2	8	8.3
	C-(A)-S-H	61	42.5	N/A	39.9
	AFm	0	0.0	N/A	0.9
	Mc	1	0.0	N/A	1.0
	AFt	21	42.7	N/A	36.5
	Fe-AFt	0	0.0	N/A	0.0
	C $\bar{c}$	10	9.9	19	10.4
Fe-Mc	0	4.8	N/A	0.0	
C\$H <sub>2</sub>	1	0.0	N/A	1.0	
C <sub>2</sub> S	1	0.0	N/A	1.0	

Table 2.15: Phase assemblage of samples C3S-AFm8-a, C3S-AFm8-b, and OPC, after exposure to a sodium sulfate solution with a concentration equal to 66 mM, obtained with various methods of characterization.

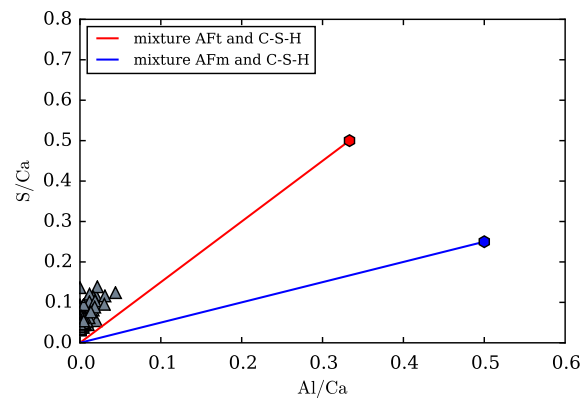
## 2.5. COMPARISON BETWEEN METHODS FOR CHARACTERIZING PHASE ASSEMBLAGE



(a)

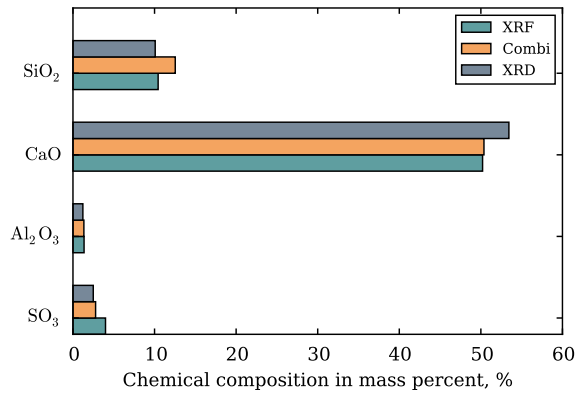


(b)

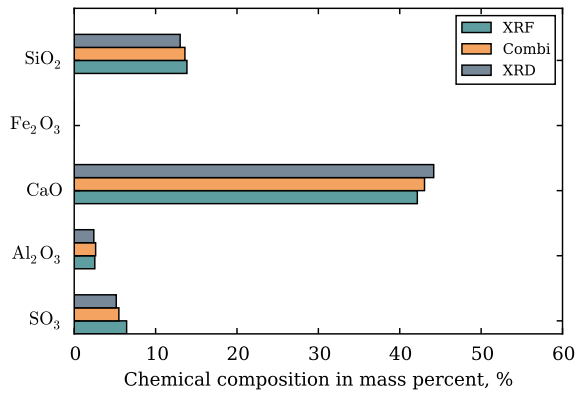


(c)

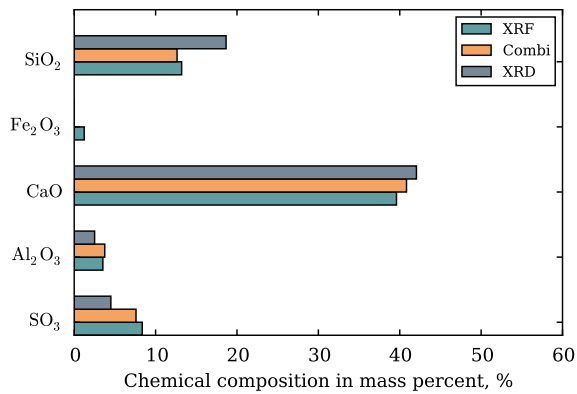
Figure 2.23: SEM-EDS measurements performed on the C-(A)-S-H gel of sample C3S-AFm8-a after exposure to a sodium sulfate solution with a concentration equal to 66 mM: (a) ratio Al/S vs ratio Ca/Si, (b) ratio Al/Ca vs ratio Si/Ca, (c) ratio S/Ca vs ratio Al/Ca. We observed no AFt in the C-(A)-S-H gel.



(a)



(b)



(c)

Figure 2.24: Chemical compositions obtained from phase assemblage determined with the method ‘Combi’, with XRD, and with XRF, for samples (a) C3S-AFm8-a, (b) C3S-AFm8-b and (c) OPC. It is noted that the chemical composition calculated from the method ‘XRD’ is labeled as XRD in this figure.

## 2.5. COMPARISON BETWEEN METHODS FOR CHARACTERIZING PHASE ASSEMBLAGE

---

On the samples here considered, XRD once again measured the amounts of CH quite accurately. But it overestimated very significantly the amounts of C-(A)-S-H in sample OPC, and underestimated this amount in samples C3S-AFm-8a and C3S-AFm-8b. Also, again, the method ‘XRF+CHESS’ underestimated the amount of CH. But, on samples C3S-AFm-8b and OPC, this method predicted reasonably well the amount of C-(A)-S-H (maybe by chance). Both XRD and the method ‘XRF+CHESS’ correctly concluded that there was no more AFm in the samples exposed to sulfates. The amount of AFt was quite well measured with XRD in samples C3S-AFm-8a and C3S-AFm-8b, but strongly underestimated in sample OPC. The amount of AFt was reasonably well predicted with the method ‘XRF+CHESS’ in samples C3S-AFm-8a and C3S-AFm-8b, but not in sample OPC.

### 2.5.6 Conclusion on the comparison between various methods for characterization of phase assemblage

In Sec. 2.5.2 to 2.5.5, various methods were applied for the characterization of the phase assemblage of various samples, before or after exposure to sulfates. For all samples, the chemical composition calculated from the method ‘Combi’ was in good agreement with the one obtained with XRF, further confirming the validity of the method, already discussed in Sec. 2.5.1.

The phase assemblages obtained with the method ‘XRF+CHESS’ were not consistent with the method ‘Combi’. This method ‘XRF+CHESS’ always underestimated the amount of CH and AFm, mostly tended to overestimate the amounts of AFt and Mc. Sometimes, the method predicted reasonably well the amount of C-(A)-S-H, but sometimes it overestimated this amount. A reason for the discrepancy is that C-A-S-H is not implemented in CHESS, only C-S-H. Another reason for this discrepancy could be that the use of CHESS, which performs calculations at thermodynamic equilibrium, implies assuming that the sample is in contact with liquid water, while the experimental techniques used for characterization of the phase assemblage were applied to dried samples. In any case, given the observed discrepancies, the method ‘XRF+CHESS’ is not recommended for characterization of phase

assemblage: this conclusion is unfortunate, since, in terms of experimental characterization, this method only required performing XRF.

Chemical compositions back-calculated from phase assemblages obtained with the various methods were compared with the XRF data, considered as a reference. In this comparison, after exposure to sulfates, XRD performed as well as the method ‘Combi’ for samples C3S-AFm4-a and C3S-AFm8-b. In contrast, XRD performed worse than the method ‘Combi’ for sample OPC. In fact, the phase assemblages obtained with XRD compared reasonably well with those obtained with the method ‘Combi’, for samples CH-AFm4, C3S-AFm4-a, C3S-AFm8-a, and C3S-AFm8-b, close to carbonation. At least for the first 3 samples, in which aluminates were added to the sample after any potential hydration, this relatively good agreement can be explained by the fact that AFm or AFt was not located in or near the C-(A)-S-H gel. In contrast, for samples C3S-AFm8-b and OPC, in which AFm was present in the mixture before its hydration (thus leading to AFm or AFt being probably located in or near the C-(A)-S-H gel), XRD yielded poor phase assemblages.

Of all methods considered here, the method ‘Combi’ is the one that yields the most accurate phase assemblages. However, this method has some drawbacks: its use requires heavy experimental characterization and significant interpretation, and the method may underestimate the quantity of gypsum, obtained by XRD. An issue specific to this study was carbonation, which probably occurred after testing, when we prepared the samples for experimental characterization: this carbonation complicated the interpretation of the characterization data.

In spite of the drawbacks just mentioned, in this thesis, we apply the method ‘Combi’ to characterize the phase assemblage of all materials, before or after exposure to sulfates.

## 2.6 Experimental program

### 2.6.1 List of materials

For this thesis, we manufactured 9 different types of materials. A paste made with ordinary Portland cement (noted OPC) was manufactured 3 times to verify the reproducibility of the process. The list of all materials manufactured, together with their phase assemblage, is given in Tab. 2.16. These phase assemblages were obtained with the method ‘Combi’ described in Sec. 2.3.3.

Materials	CH	C-(A)-S-H	Quartz	AFm	AFt	CaCO <sub>3</sub>	C <sub>3</sub> AH <sub>6</sub>	C <sub>2</sub> S
OPC(1)	26.6	54.1	0.0	11.1	3.1	0.0	3.8	1.1
OPC(2)	24.3	54.0	0.0	13.2	3.7	0.0	3.8	1.1
OPC(3)	25.0	52.9	0.0	13.6	3.7	0.0	3.7	1.0
C3S	26.0	72.0	0.0	0.0	0.0	0.0	0.0	2.0
C3S-sand <sup>(e1)</sup>	15.0	43.0	40.0	0.0	0.0	0.0	0.0	2.0
CH-AFm4	19.0	0.0	0.0	3.4	2.2	75.4	0.0	0.0
C3S-AFm4-a	35	49	0	4	0	11	0	1
C3S-AFm8-a	22.7	53.3	0.0	6.8	5.7	10.3	0.0	1.0
C3S-AFm2-b <sup>(e2)</sup>	26.0	60.0	2.0	2.0	0.0	7.0	0.0	3.0
C3S-AFm4-b	29.2	62.3	0.0	3.1	3.4	0.0	0.9	1.0
C3S-AFm8-b	27.7	55.8	0.0	8.4	3.2	0.0	3.8	1.0

Table 2.16: Phase assemblage of all materials manufactured in this thesis, as obtained with the method ‘Combi’, in mass percentage. (e1) For material C3S-sand, the phase assemblage was not measured: the material was considered as a mixture of material C3S with sand (considered as pure quartz). (e2) For material C3S-AFm2-b, the phase assemblage was not measured: the material was considered as a mixture of ‘C3S-AFm8-b’ with material C3S.

### 2.6.2 List of experiments

As will be described in the following chapters, the various manufactured materials will be submitted to a variety of injections of sodium sulfate solutions. We used sulfate solutions with various concentrations: 3 mM, 66 mM, 140 mM, 315 mM, 540 mM, and 1190 mM. Experiments were performed in an oedometer cell or in an isochoric cell. The exhaustive list of all experiments performed in this thesis is given in Tab. 2.17 and 2.18.

To create a reference, some samples were only injected with demineralized water: those reference tests are indicated with a ‘0’ in the column displaying the concentration of the injected solution.

During experiments in oedometric conditions, the applied axial stress was constant over time. For almost all tests, this axial stress was 0.88 MPa: only for experiments OPC(0.52) and OPC(1.14) was this axial stress equal to 0.52 MPa and 1.14 MPa, respectively.

Most  $^{27}\text{Al}$ -NMR characterizations were performed at ‘[Laboratoire de Spectrochimie Infrarouge et Raman \(LASIR\)](#)’, Lille University of Science and Technology, France. A few were performed at [Department of Chemistry](#), Aarhus University, Denmark: in Tab. 2.17 and 2.18, those latter ones are indicated with an asterisk (\*).

The results of the experimental program will be given and discussed in the next chapters.

## 2.7 Summary

In this chapter, we presented the materials and methods used in this thesis. The manufactured materials are listed in Tab. 2.16. The originality of the prepared samples is that they are obtained by grinding and compaction of those materials into cylindrical specimens. The permeability of those specimens is about 100 times larger than the permeability of usual cement pastes, so that the specimens could be flushed with a sodium sulfate solution in less than 1 hour.

Experiments are performed into oedometer cells or into isochoric cells. In the oedometer cell (described in Sec. 2.2.1), we measured the axial deformation of the sample under a constant axial stress, while preventing any radial deformation. In the isochoric cell (described in Sec. 2.2.2), we measured both the radial and axial stresses applied by the sample on the cell after injection of solution, when any radial or axial strain of the sample was prevented. A feature of the isochoric cells we developed is that all solution flushed throughout the sample can be recovered: thus, from the measurements of concentrations and volumes of injected and output solutions, the

Label of test	Material	Type of cell	$[\text{SO}_4^{2-}]$ , mM	Methods of characterization
CH-AFm4-Ref	CH-AFm4	O	0	XRF, XRD, TGA, $^{27}\text{Al-NMR}$
CH-AFm4	CH-AFm4	O	66	XRF, XRD, TGA, $^{27}\text{Al-NMR}$
C3S-Ref	C3S	O	0	XRF, XRD, TGA, MIP
C3S-sand-Ref	C3S	O	0	XRF SEM-EDS
C3S-sand	C3S	O	1190	XRF SEM-EDS
C3S-66-1190	C3S	O	$\begin{matrix} 66 \\ 1190 \end{matrix}$	XRF, XRD, TGA
C3S-AFm4-a-Ref	C3S-AFm4-a	O	0	XRF, XRD, TGA, SEM-EDS, MIP
C3S-AFm4-a or C3S-AFm4-a-66	C3S-AFm4-a	O	66	XRF, XRD, TGA, SEM-EDS, MIP
C3S-AFm4-a-66-1190	C3S-AFm4-a	O	$\begin{matrix} 66 \\ 1190 \end{matrix}$	XRF, XRD, TGA
C3S-AFm8-a-Ref	C3S-AFm8-a	O	0	XRF, XRD, TGA, $^{27}\text{Al-NMR}$ , MIP
C3S-AFm8-a	C3S-AFm8-a	O	66	XRF, XRD, TGA, $^{27}\text{Al-NMR}$ , SEM-EDS
C3S-AFm2-b	C3S-AFm2-b	O	66	XRF, XRD, TGA, $^{27}\text{Al-NMR}^*$
C3S-AFm4-b-Ref	C3S-AFm4-b	O	0	XRF, XRD, TGA, $^{27}\text{Al-NMR}$ , MIP
C3S-AFm4-b	C3S-AFm4-b	O	66	XRF, XRD, TGA, $^{27}\text{Al-NMR}$
C3S-AFm8-b-Ref	C3S-AFm8-b	O	0	XRF, XRD, TGA, $^{27}\text{Al-NMR}$ , SEM-EDS, MIP
C3S-AFm8-b	C3S-AFm8-b	O	66	XRF, XRD, TGA, $^{27}\text{Al-NMR}$ , SEM-EDS

Table 2.17: First part of list of experiments carried-out in this thesis. Regarding the type of cell, ‘O’ stands for oedometer testing and ‘I’ stands for isochoric testing. The numbers displayed in column ‘ $[\text{SO}_4^{2-}]$ , mM’ are the concentration in sulfate of the solution or of the solutions that were injected: ‘0’ means that only demineralized water was injected in the sample.

CHAPTER 2. MATERIALS AND METHODS

Label of test	Material	Type of cell	$[\text{SO}_4^{2-}]$ , mM	Methods of characterization
OPC-Ref(O)	OPC	O	0	XRF, XRD, TGA, MIP, $^{27}\text{Al}$ -NMR, SEM-EDS
OPC-66(O)	OPC	O	66	XRF, XRD, TGA, MIP, $^{27}\text{Al}$ -NMR, SEM-EDS
OPC-66-1(O)	OPC	O	66	XRF, XRD, TGA, $^{27}\text{Al}$ -NMR
OPC-66-water(O)	OPC	O	66 0	N/A
OPC(0.52)	OPC	O	0	N/A
OPC(0.88)	OPC	O	66	$^{27}\text{Al}$ -NMR
OPC(1.14)	OPC	O	66	N/A
OPC-140(O)	OPC	O	140	XRF, XRD, TGA, $^{27}\text{Al}$ -NMR(*)
OPC-315(O)	OPC	O	315	XRF, XRD, TGA, $^{27}\text{Al}$ -NMR
OPC-540(O)	OPC	O	540	XRF, XRD, TGA, $^{27}\text{Al}$ -NMR(*)
OPC-1190(O)	OPC	O	1190	XRF, XRD, TGA, $^{27}\text{Al}$ -NMR
OPC-Ref(I)	OPC	I	0	XRF, XRD, TGA, $^{27}\text{Al}$ -NMR
OPC-3	OPC	I	3	XRF, XRD, TGA, $^{27}\text{Al}$ -NMR, SEM-EDS
OPC-3-66	OPC	I	3 66	XRF, XRD, TGA, $^{27}\text{Al}$ -NMR, SEM-EDS
OPC-66	OPC	I	66	XRF, XRD, TGA, $^{27}\text{Al}$ -NMR, SEM-EDS
OPC-1190	OPC	I	1190	XRF, XRD, TGA, $^{27}\text{Al}$ -NMR
OPC-315-1190	OPC	I	315 1190	XRF, XRD, TGA, $^{27}\text{Al}$ -NMR
OPC-I(0.52) <sup>a</sup>	OPC	I	66	N/A

Table 2.18: Second part of list of experiments carried-out in this thesis. Regarding the type of cell, ‘O’ stands for oedometer testing and ‘I’ stands for isochoric testing. The numbers displayed in column ‘ $[\text{SO}_4^{2-}]$ , mM’ are the concentration in sulfate of the solution or of the solutions that were injected: ‘0’ means that only demineralized water was injected in the sample.

<sup>a</sup> the initial axial stress was equal to 0.52 MPa

amount of sulfate remaining in the sample over the experiments could be determined.

The samples will be injected with 1 or several sodium sulfate solutions with various concentrations. The list of all experiments performed is given in Tab. 2.17 and in Tab. 2.18.

After each experiment, the microstructure and the mineralogy of the sample are characterized. In parallel of each experiment, a reference sample is manufactured, that is not exposed to sulfates, and is therefore believed to be representative of its companion sample before exposure to sulfates. The microstructure and the mineralogy of this reference sample are also characterized. Based on a combination of the results from XRF, XRD, TGA, and  $^{27}\text{Al}$ -NMR, a new method of characterization of phase assemblage is proposed: this is the method called ‘Combi’ introduced in Sec. 2.3.3. Evolutions of the phase assemblage over the injection process are predicted through thermodynamic modeling with the chemical speciation software CHESS.

In addition, from the work performed in this chapter, some conclusions can be drawn in terms of methodology for samples characterization. In particular, the comparison between various methods to characterize the phase assemblages (see Sec. 2.5) suggests that the amount of aluminate phases (e.g., monosulfoaluminate and ettringite), and consequently the whole phase assemblage, can be reasonably well determined with XRD, if the aluminate phase is not intimately mixed with the C-(A)-S-H gel. Therefore, for samples for which AFm was added to the sample after any potential hydration (as is the case, e.g., for samples CH-AFm4, C3S-AFm4-a, and C3S-AFm8-a), XRD could provide phase assemblages, at a lower cost than the method ‘Combi’. In contrast, in almost all cases, the method ‘XRF+ CHESS’ yielded poor phase assemblages and is therefore not recommended.



## Chapter 3

# Oedometric study of kinetics and role of mineralogy and microstructure

---

THIS CHAPTER aims at investigating qualitatively the role of several mineralogical and microstructural features (e.g., role of location of ettringite precipitation, presence of C-S-H, or initial amount of AFm) on the expansion of cementitious materials, by using the original testing protocol in oedometric cells, which has been described in Chap. 2. We recall that the hydrated material was ground into particles and then compacted into the oedometer cell, in which the axial strain is measured under a constant axial stress and the radial strain is prevented. The materials used in this study are CH-AFm<sub>4</sub>, C3S-AFm<sub>4</sub>-a, C3S-AFm<sub>8</sub>-a, C3S-AFm<sub>4</sub>-b, C3S-AFm<sub>8</sub>-b, and OPC. By working with such granular compacted samples which are highly permeable, we can flush the pore volume of the sample with a sodium sulfate solution in a few dozen of minutes. By using SEM-EDS, we check that such fast injection makes it possible to obtain a homogeneous crystallization throughout the sample. We also show that the expansion starts right after the injection of solution and stops after a few days or weeks. This feature is a

### CHAPTER 3. OEDOMETRIC STUDY OF KINETICS AND ROLE OF MINERALOGY AND MICROSTRUCTURE

---

*significant difference with respect to usual experiments in which the expansion progresses over months or even years. In addition, we also find that, in our compacted ground samples (which present a lower tensile strength than regular cement pastes), pockets of ettringite (i.e., large crystals of ettringite) can lead to an expansion, and that the presence of C-S-H seems not to be necessary to observe an expansion. These observations raise questions about the expansion mechanism in cement-based materials subjected to sulfate attacks.*

---

**C**E CHAPITRE vise à étudier qualitativement le rôle de plusieurs caractéristiques minéralogiques et microstructurales (par exemple, le rôle de la localisation d'ettringite, de la présence de C-S-H, de la quantité initiale de AFm) sur l'expansion des matériaux cimentaires en utilisant le protocole original qui a été décrit dans le Chap. 2. Nous rappelons que le matériau hydraté a été broyé en particules et ensuite compacté dans la cellule oedométrique, dans laquelle la déformation axiale est mesurée sous une contrainte axiale constante et la déformation radiale est empêchée. Les matériaux utilisés dans cette étude sont CH-AFm4, C3S-AFm4-a, C3S-AFm8-a, C3S-AFm4-b, C3S-AFm8-b et OPC. En travaillant avec de tels échantillons granulaires compactés qui sont très perméables, on peut laver le volume poreux de l'échantillon avec une solution de sulfate de sodium en quelques dizaines de minutes. En utilisant la technique SEM-EDS (voir Sec. 2.3), nous vérifions que cette injection rapide permet d'obtenir une cristallisation homogène à travers l'échantillon. Nous avons également montré que l'expansion peut être observée très rapidement, c'est-à-dire juste après l'injection de solution : cette caractéristique est une différence significative par rapport aux essais courants, dans lesquels l'expansion progresse pendant plusieurs mois ou des années. En outre, nous avons également constaté que, dans nos matériaux compactés (qui présentent une résistance en traction plus faible que celles de pâtes de ciment classiques), les amas de cristaux d'ettringite (gros cristaux d'ettringite) peuvent conduire à une expansion et que la présence de C-S-H ne semble pas être nécessaire pour observer une expansion. Ces observations soulèvent des

---

*questions sur le mécanisme d'expansion des matériaux cimentaires soumis à des attaques sulfatiques.*

---

### 3.1 Introduction

As discussed in Chap. 1, sulfate attacks, e.g., external sulfate attacks due to the ingress of sulfate ions from the surroundings into the material, can damage cementitious materials significantly, with typical occurrences such as expansion, spalling, or cracking. The interaction between the reactive matrix of cementitious materials and sulfate ions can lead to the crystallization of ettringite and/or gypsum. The expansion has been mostly attributed to the formation of confined crystals of ettringite (e.g., within the C-S-H gel) (Schmidt et al., 2009; Lothenbach et al., 2010; Yu et al., 2013; Kunther et al., 2013; Bary et al., 2014). According to recent literature (Lothenbach et al., 2010; Yu et al., 2013; Bary et al., 2014; Yu et al., 2015), C-S-H has been expected to be the phase in which the ettringite leading to expansion crystallizes. In addition, Kunther et al. (2015) suggested that a greater ratio of Ca/Si for C-S-H in cement-based materials can lead to a greater expansion. It seems that the presence of C-S-H is a key feature to the potential expansion of cementitious materials and that the contribution of pockets of ettringite (i.e., of large crystals of ettringite outside the C-S-H gel) is negligible (Yu et al., 2013; Kunther et al., 2015). It is noted that the role of the formation of gypsum on the expansion is still poorly understood (see Sec. 1.2.2 for more details). Regarding laboratory experiments, there exist considerable difficulties in studying the expansion mechanism of cement-based materials subjected to external sulfate attacks, because of a variety of limitations in the usual experimental procedure: the expansion of cementitious materials usually progresses over months or even years, and the evolution of the various phases is heterogeneous throughout the material, which leads to a heterogeneous mineralogical formation associated with a complex thermo-chemical equilibria (see Sec. 1.2.1 for more details).

In the present chapter, we aim at answering questions regarding the role of several mineralogical or microstructural features on the expansion of cement-based materials by using an original experimental protocol which has been described in Chap. 2. The originality of the developed protocol lies in the fact that we work with hydrated cementitious materials ground and recompacted

and that the expansion is induced by an injection of sodium sulfate solution. We performed experiments with a series of model materials with various microstructural and mineralogical features to investigate the impact of those features on the expansion of cementitious materials. The results obtained in this study are discussed and used to draw conclusions.

## 3.2 Materials and methods

This section introduces the experimental protocol and setup.

In this chapter, we tested 6 types of samples: an ordinary Portland cement (noted OPC) paste, a  $C_3S$  paste mixed with two amounts of monosulfoaluminate added either before or after hydration, and a mixture of portlandite with monosulfoaluminate. The 6 types of samples are labeled: OPC, CH-AFm4, C3S-AFm4-a, C3S-AFm8-a, C3S-AFm4-b, and C3S-AFm8-b. The phase composition of the 6 materials before testing is displayed in Tab. 2.3. The phase assemblage of the samples before testing (i.e., before the injection of solution) as well as after testing (i.e., after the injection of solution), as obtained by XRD, is given in Tab. 3.1. The same phase assemblages, but obtained with the method ‘Combi’ introduced in Sec. 2.3.3, are given in Chap. 2.

Each sample was obtained by compaction into an oedometric cell (as presented in Sec. 2.2.1) of the powder materials prepared by using the process of manufacturing described in Sec. 2.1. We presented the schematic and working principle of the oedometer cell in Sec. 2.2.1. We recall that in an oedometric cell, any lateral deformation is prevented by a metallic ring; in contrast, an axial stress can be applied to the sample and the axial deformation can be measured. Here, the cell diameter was 38 mm. The properties of all tested samples are displayed in Tab. 3.2. The mass  $m^0$  of each sample before injection of water and testing was  $m^0 = 18.09$  g. In Tab. 3.2, no information on the tensile strength of the samples is provided, as we did not measure it. However, the tensile strength of the compacted ground samples used in this study is expected to be significantly lower than that of intact cementitious materials.

CHAPTER 3. OEDOMETRIC STUDY OF KINETICS AND ROLE OF MINERALOGY AND MICROSTRUCTURE

Materials	CH	C-S-H	Afwillite	AFm	AFt	CaCO <sub>3</sub>	Mc	C <sub>2</sub> S	C\$H <sub>2</sub>
Before testing									
OPC	25	57	0	8	0	5	3	2	0
CH-AFm4	20	0	0	3	0	77	0	0	0
C3S-AFm4-a	33	39	0	4	0	23	0	1	0
C3S-AFm8-a	22	50	0	7	0	21	0	1	0
C3S-AFm4-b	37	43	5	4	0	10	0	1	0
C3S-AFm8-b	29	48	8	8	0	6	0	1	0
After testing									
OPC	10	55	0	0	22	8	3	2	0
CH-AFm4	15	0	0	0	6	79	0	0	0
C3S-AFm4-a	29	48	0	0	7	16	0	0	0
C3S-AFm8-a	25	32	0	0	13	28	0	2	0
C3S-AFm4-b	28	42	5	0	14	8	0	2	0
C3S-AFm8-b	17	37	10	0	27	8	0	1	0

Table 3.1: Phase composition of the various samples before and after the experiments, obtained by X-ray diffraction, in mass percentage, with an accuracy of measurement of  $\pm 2\%$ .

Material	Permeability $\kappa, 10^{-16} \text{ m}^2$	Swelling index $C_s, 10^{-2}$	Oedometric modulus $E_{oed}, \text{ MPa}$	Porosity $\phi, \%$
OPC	3.75	1.35	480	60.5
CH-AFm4	18.57	1.50	270	41.58
C3S-AFm4-a	16.17	0.95	400	39.18
C3S-AFm8-a	16.38	0.99	518	39.53
C3S-AFm4-b	13.70	0.88	500	54.53
C3S-AFm8-b	6.47	1.32	440	65.76

Table 3.2: Properties of the tested samples. The porosity  $\phi$  is the porosity of the sample after compaction, but before injection.

The expansion was induced by injecting a solution of sodium sulfate through the samples, directly in the oedometer cell. In this chapter, all samples were injected with sodium sulfate solutions with a concentration equal to 66 mM. Generally, each injection consisted in injecting 36 mL of solution, which represented at least twice the pore volume for all samples: thus, with each injection, 2.38 mmol of sulfate were brought to the sample. Injections were repeated until when, roughly, a new injection would induce no more significant expansion. After testing (i.e., after the injections of the solution of sodium sulfate), each of the 6 samples was immersed in acetone for at least one week and vacuum-dried to stop all chemical reactions. Then, on each sample we performed X-ray diffraction fluorescence (XRF), X-ray diffraction Rietveld (XRD) and thermal gravity analysis (TGA), as described in Sec. 2.3. We recall that we also manufactured reference samples (see Sec. 2.2.1), which were only flushed with demineralized water: the analysis of those samples yielded the phase assemblage of the samples before testing.

In addition, sections of samples OPC, C3S-AFm4-a, C3S-AFm8-a and C3S-AFm8-b were observed by scanning electron microscopy (SEM) and analyzed by EDS X-ray spectroscopy.

### 3.3 Results and discussion

Figure 3.1 displays the evolution of deformation with time for the 6 tested samples, i.e.: OPC, C3S-AFm4-a, C3S-AFm8-a, C3S-AFm4-b, C3S-AFm8-b, and CH-AFm4. The reference height of the sample used to calculate the axial strains was the height of the sample right before the first injection of solution. The reference time was chosen as the time at the beginning of the first injection of solution.

The results of the reference experiments (i.e., for which the samples were flushed with demineralized water only) can be found in App. B.

CHAPTER 3. OEDOMETRIC STUDY OF KINETICS AND ROLE OF MINERALOGY AND MICROSTRUCTURE

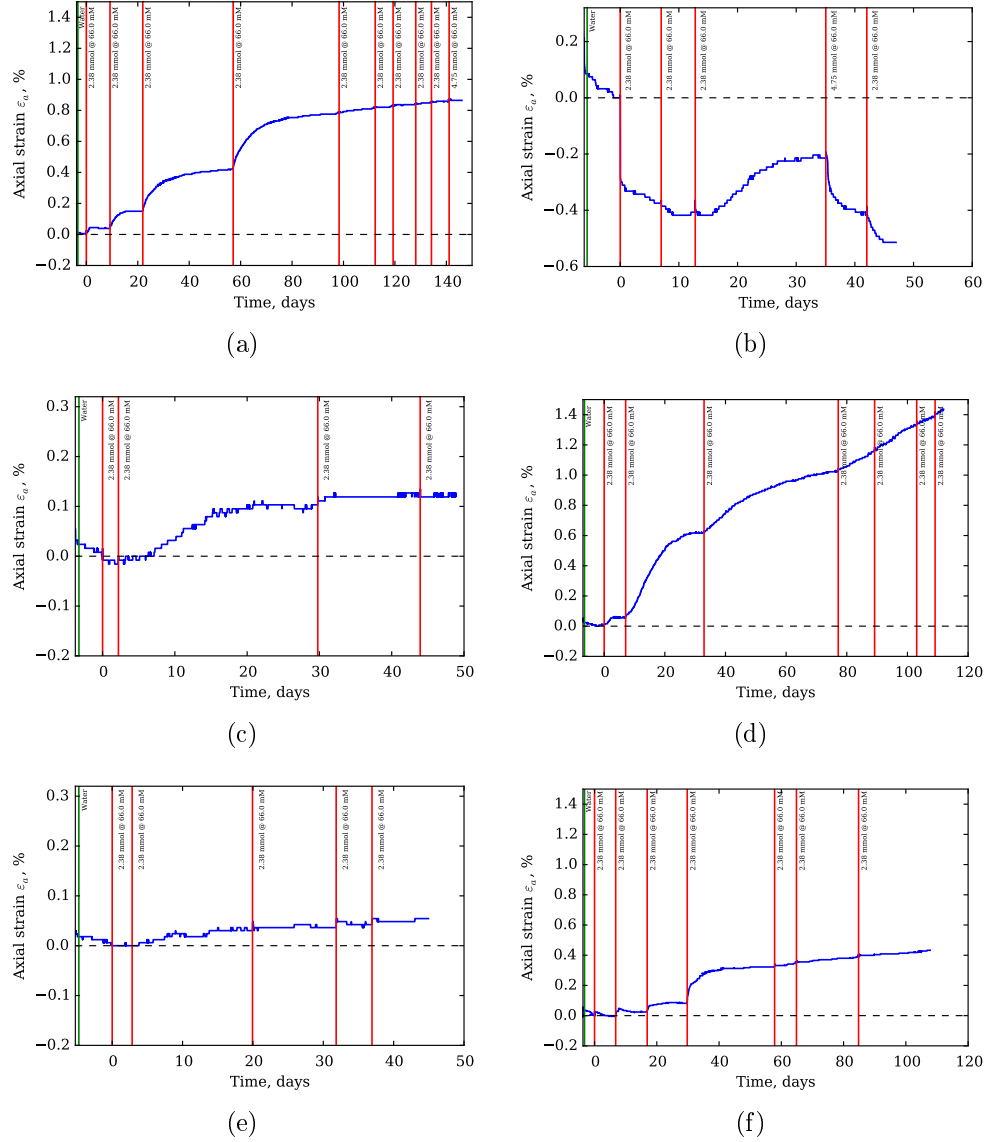


Figure 3.1: Evolution of deformation induced by injections of water or sodium sulfate solution into samples: (a) OPC, (b) CH-AFm4, (c) C3S-AFm4-a, (d) C3S-AFm8-a, (e) C3S-AFm4-b, and (f) C3S-AFm8-b. The injection of water is displayed with a green vertical line. Each injection of solution is displayed with a red vertical line, on which is indicated the concentration of the injected solution and the amount of injected sulfate.

### 3.3.1 Qualitative description of test on sample OPC

Figure 3.1 (a) displays the evolution of deformation with time for sample OPC, together with the profile of injection of water and sulfate solution. The injection of water is displayed with a green vertical line. Each injection of solution is displayed with a red vertical line, on which is indicated the concentration of the injected solution and the amount of injected sulfate.

During the injection of water, we observed a slight expansion of the sample material, which is a poroelastic effect induced by the pressure of injection of 500 kPa. After the injection of water, we observed no expansion of the sample but a slight subsidence, which may be due to creep. Interestingly, creep was no longer observed right after the first injection of solution. Such phenomenon was also observed in other materials containing C-S-H, i.e.: C3S-AFm8-b, C3S-AFm8-a, C3S-AFm4-b, and C3S-AFm4-a.

Some days after the injection with water, the sample was flushed with a sodium sulfate solution at the same injection pressure equal to 500 kPa. The injection was repeated several times. Each injection induced an expansion, but in various amounts: the expansion was more significant with the second, third and fourth injections, than with the other ones. After the first injection, the strain exceeded significantly the typical elastic limit of intact cementitious materials, which is around 1%, so that the sample is expected to be damaged and hence more easy to expand for the second, third and fourth injections. For all injections, we could observe expansion very quickly: the expansion started right after the injection of solution. Furthermore, for what concerns the first 4 injections of solution, one observes that, after the injection, the expansion reached an asymptotic value in just a few days or few weeks. After the 5<sup>th</sup> injection of solution (which was carried-out at day 58), the expansion went on increasing slowly, maybe as a consequence of too short a period between consecutive injections.

After the experiment, the mineral composition of the sample was investigated by XRD and SEM-EDS. According to XRD, as shown in Tab. 3.1, a significant amount of AFt was detected, while no gypsum was detected. Results obtained by SEM-EDS, which are displayed in Fig. 3.2, confirm an

### CHAPTER 3. OEDOMETRIC STUDY OF KINETICS AND ROLE OF MINERALOGY AND MICROSTRUCTURE

---

important amount of AFt and show that there was a little bit of gypsum in the material, but less than 2% (in mass fraction): this amount of gypsum may have been below the capacity of XRD detection. The formation of ettringite and gypsum within cementitious materials subjected to sulfate solutions was also recognized in other works (Mehta, 1983; Gollop and Taylor, 1992; Schmidt et al., 2009; Yu et al., 2013; Müllauer et al., 2013). In the case of external sulfate attacks, ettringite is known to be a product causing expansion, while the role of crystallization of gypsum on the expansion of cement-based materials is still poorly understood (see Sec. 1.2.2).

Figure 3.2 shows that the mineral distribution over the sample's height ( $\sim 18$  mm) was quite homogeneous. One should note however that this figure displays only a fraction of the height of sample ( $\sim 13$  mm): as a consequence of the preparation of the sample, we could not image the whole height of the sample. The zone of investigation displayed in Fig. 3.2 is located at about mid-height. The homogeneity of the distribution of phases throughout the height of the sample was also confirmed in another sample flushed only a few times with the solution, such that only about 2 thirds of the amount of AFm initially present in the sample was consumed (see more details in App. D). This homogeneity is not fully understood and in fact quite surprising: indeed, as will be seen later, the concentration of the injected solution varies significantly across the height of the sample, in particular during the first injections. The observed homogeneity of phases might be due to phase redistributions or sulfate diffusion after the injection.

In a typical work on sulfate attacks by Yu et al. (2013), an expansion could be measured after 120 days only, and, even after 300 days, the deformation continued increasing and had not stabilized. In our present work, expansion was observed right after the injection and got stabilized after a few days or weeks. Therefore, the fact that, when macroscopic samples are immersed in a sulfate solution, expansions can only be observed after several dozens of days, is not a consequence of any slow kinetics of the chemical reactions at stake: it is likely that, in such experiments, the rate-limiting factor is the diffusion of the sulfate ions into the material. Also, with the developed protocol, we could obtain a homogeneous crystallization throughout the sample, which is

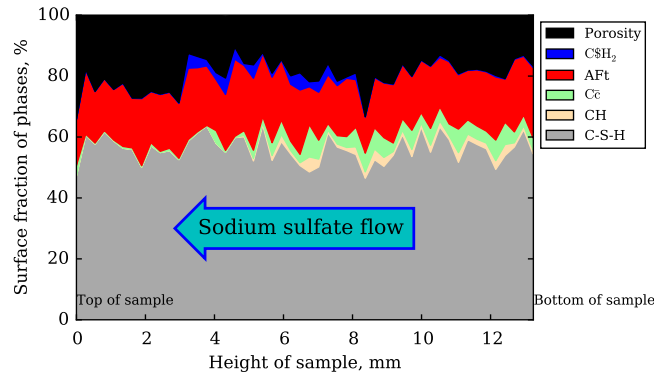


Figure 3.2: Phase composition of sample OPC throughout the height of the sample. Surface fractions were determined by SEM-EDS.

a second significant difference with respect to classical experiments, in which usual cementitious samples are immersed in a sulfate solution, and for which sulfate ingress by diffusion induces significant gradients and heterogeneities throughout the sample.

### 3.3.2 On the necessity of the presence of C-S-H to observe an expansion

The results displayed in Fig. 3.1 can be represented in a time-independent manner, by plotting the axial strain versus the cumulative amount of sulfates injected through the sample. This time-independent manner of representing the data is displayed in Fig. 3.3. On this figure, the strain displayed for the  $n^{th}$  injection of solution is the strain right before the  $(n + 1)^{th}$  injection. The response to the injections of sulfates varied from sample to sample, probably as a consequence of their variety of mineralogy, pore size distribution, and (unmeasured) tensile strength.

For all samples that contained C-S-H (i.e., samples OPC, C3S-AFm8-b, C3S-AFm8-a, C3S-AFm4-b, and C3S-AFm4-a), after the second injection of solution, only expansion was observed. In particular, swelling was also observed for samples C3S-AFm8-a and C3S-AFm4-a, to which AFm was added after hydration, and could therefore not be located inside the C-S-H gel: For

CHAPTER 3. OEDOMETRIC STUDY OF KINETICS AND ROLE OF MINERALOGY AND MICROSTRUCTURE

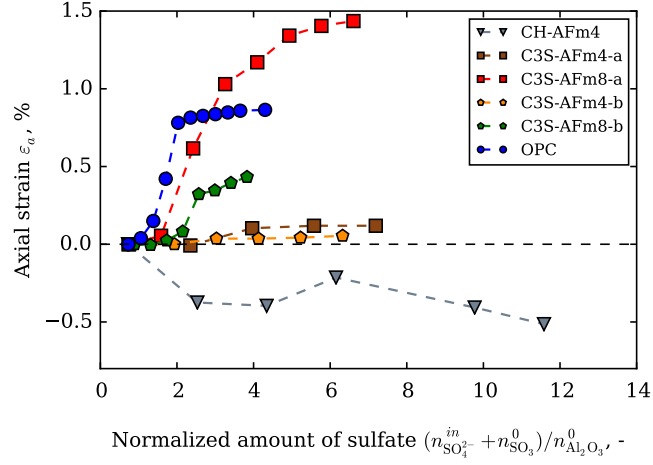


Figure 3.3: Axial strain versus the normalized amount of sulfate injected.  $n_{\text{SO}_4^{2-}}^{\text{in}}$  stands for the amount of injected sulfate (expressed in mmol),  $n_{\text{SO}_3}^0$  and  $n_{\text{Al}_2\text{O}_3}^0$  stand for the initial amounts of  $\text{SO}_3$  and  $\text{Al}_2\text{O}_3$  (expressed in mmol), respectively, as obtained from XRF.

crystallization-induced expansions to be observed, the AFm initially present in the material did not need to be intimately mixed with the C-S-H gel. Said otherwise, ettringite crystallizing in macro pores, not necessarily in C-S-H gel, can induce expansion in ground compacted materials.

In contrast, for sample CH-AFm4, which does not contain any C-S-H, for most injections, the sample shrank. However, swelling was observed for one injection (i.e., for the 3<sup>rd</sup> injection), and the amount of this swelling was comparable to the incremental swelling observed on materials that contained C-S-H. Based on such observation, we consider that this swelling was significant, which proves that swelling can occur in materials that contain no C-S-H. Said otherwise, ettringite crystallizing in macropores, not necessarily in C-S-H, can induce expansion in ground compacted materials.

The measured strains can result from a competition between a variety of phenomena: crystallization of gypsum and/or ettringite (which induces a swelling), dissolution of portlandite (which, intuitively, should induce a contraction), and creep (which induces a contraction). For sample CH-AFm4, the contraction induced by dissolution of portlandite is expected to lead to a

more significant contraction than for all other samples in this study, since, in sample CH-AFm4, the matrix was made of portlandite, while, in the other samples, the matrix was made of C-S-H. Also, as can be observed on Fig. 3.1 (b), the sample CH-AFm4 was more susceptible to creep than the other samples, probably as a consequence of the fact that its matrix was made of portlandite crystals in contact with each other, while the matrix of the other samples was made of C-S-H, which is more amorphous and less soluble compared with CH. Those observations can explain why sample CH-AFm4 mostly shrank: for each injection of solution but the third one, dissolution-induced and creep-induced shrinkage overcame any crystallization-induced expansion. Only after the third injection of solution was the crystallization-induced expansion sufficiently large to overcome any dissolution-induced or creep-induced shrinkage.

### 3.3.3 Correlation between expansion and various compositional factors

Expansion might be caused by precipitation of ettringite or gypsum, which, as Eqs. (1.1) and (1.2) show, both result from a reaction involving sulfate. From a thermodynamic point of view, over the injection process, first ettringite should precipitate, and then gypsum. In the experiments considered in this chapter, we injected a sufficient amount of sulfate in order for most swelling potential to have been exhausted (see Fig. 3.3): it is likely that, at the end of the experiment, most of the ettringite that could precipitate had precipitated. Also, we recall that the amount of precipitated gypsum was negligible in all samples (see Tab. 3.1). In this section, we aim at verifying how expansion is correlated with the initial amount of AFm in the sample, the final amount of sulfur trioxide  $\text{SO}_3$  in the sample, and the final amount of ettringite in the sample.

Figure 3.4 (a) displays the final expansion, i.e., the axial strain at the end of the experiment, versus the initial mass fraction of AFm obtained by XRD on the reference samples (which are representative of the samples before injection). We compare samples C3S-AFm4-b and C3S-AFm8-b which, apart

### CHAPTER 3. OEDOMETRIC STUDY OF KINETICS AND ROLE OF MINERALOGY AND MICROSTRUCTURE

---

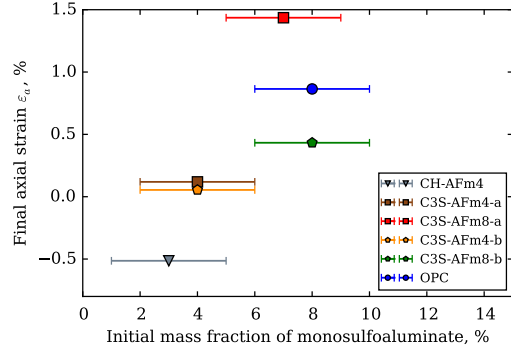
from the amount of AFm added before hydration, are identical: we observe that, for those two samples, expansion increased with the initial amount of AFm. The same correlation is observed for samples C3S-AFm4-a and C3S-AFm8-a, which, also, apart from the amount of AFm added after hydration, are identical.

We look at how expansion is correlated with the normalized mass  $m_{\text{SO}_3}^1/m^0$  of sulfur trioxide in the sample at the end of the experiment,  $m^0$  being the initial mass of the sample. Figure 3.4 (b) displays the final expansion versus this normalized mass. Comparing again sample C3S-AFm4-b with sample C3S-AFm8-b, and sample C3S-AFm4-a with sample C3S-AFm8-a, we observe that the expansion is positively correlated with the normalized mass  $m_{\text{SO}_3}^1/m^0$  of sulfur trioxide in the sample at the end of the experiment.

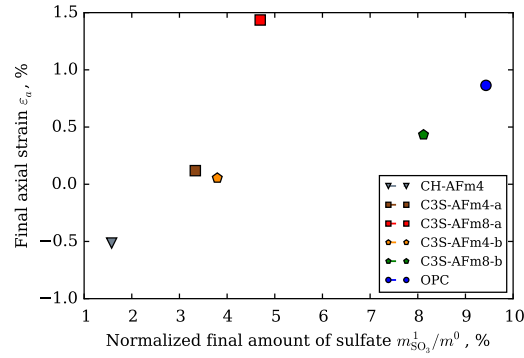
We finally look at how expansion is correlated with the normalized mass  $m_{\text{AFt}}^1/m^0$  of ettringite that has precipitated in the sample. We calculate this normalized mass with  $m_{\text{AFt}}^1/m^0 = f_{\text{AFt}}^1 \times f_{\text{Al}_2\text{O}_3}^0 / f_{\text{Al}_2\text{O}_3}^1$ , where  $f_{\text{AFt}}^1$  is the mass fraction of AFt in the sample after testing (measured by XRD), and where  $f_{\text{Al}_2\text{O}_3}^0$  and  $f_{\text{Al}_2\text{O}_3}^1$  are the mass fraction of  $\text{Al}_2\text{O}_3$  in the sample before and after testing (measured by XRF). Note that the ratio  $f_{\text{Al}_2\text{O}_3}^0 / f_{\text{Al}_2\text{O}_3}^1$  is in fact used to calculate the ratio of the mass of the sample after testing to the mass of the sample before testing, as aluminate ions concentration in the pore solution is very low (Taylor, 1998). The expansion versus this normalized mass of ettringite is displayed in Fig. 3.4 (c). Comparing again sample C3S-AFm4-b with sample C3S-AFm8-b, and sample C3S-AFm4-a with sample C3S-AFm8-a, we observe that the expansion is positively correlated with the normalized mass of precipitated ettringite.

In conclusion, the magnitude of expansion of the cement-based materials was positively correlated with the amount of AFm present initially in the sample, and with the amount of sulfur trioxide present in the sample after the experiment, and with the amount of AFt that precipitated during the experiment.

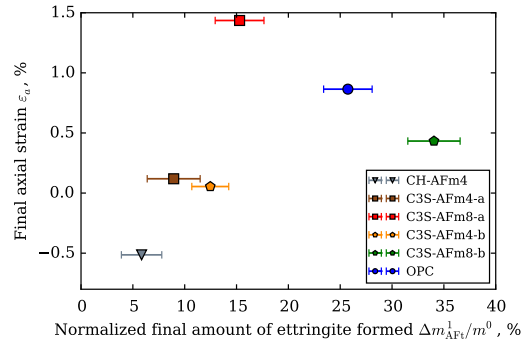
### 3.3. RESULTS AND DISCUSSION



(a)



(b)



(c)

Figure 3.4: Final axial strain of the various tested samples versus: (a) the initial mass fraction of AFm in the sample (measured by XRD), (b) the final mass  $m_{\text{SO}_3}^1$  of sulfur trioxide in the sample normalized by the initial mass  $m^0$  of the sample before testing, (c) the final mass  $m_{\text{AFt}}^1$  of AFt in the sample normalized by the mass  $m^0$  of the sample before testing.

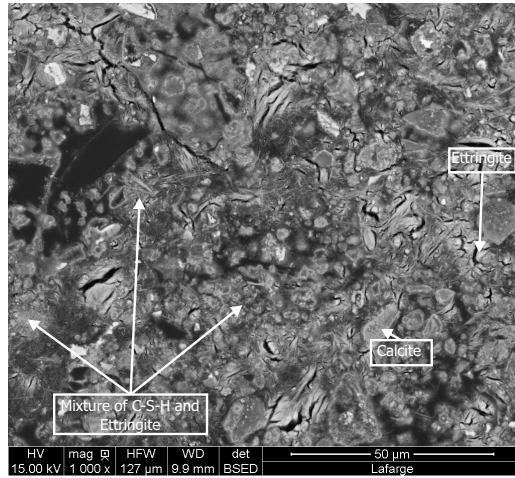
### 3.3.4 Location of AFt leading to expansion

This section is focused on the location of the ettringite that leads to expansion, in samples OPC and C3S-AFm4-a, which were designed to represent different relative locations of ettringite with respect to C-S-H gel.

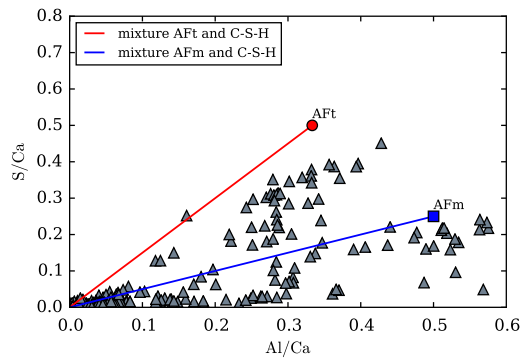
By using the SEM-EDS technique described in Sec. 2.3, we examined mineralogical and microstructural features of sample OPC before and after testing: the results are displayed in Fig. 3.5. Before testing (i.e., before the injection of sulfates), the sample contains a mixture of C-S-H with fine monosulfoaluminate, as can be inferred from the cloud of points locating on the tie lines of AFm in Fig. 3.5 (b). Such mixture has also been observed in other works (see, e.g., [Gollop and Taylor \(1992\)](#); [Yu et al. \(2013\)](#)). After exposure to sulfates, those monosulfoaluminate transformed into ettringite, as indicated by the cloud of points locating on the tie lines of AFt in Fig. 3.5 (c). A representative mixture of C-S-H with ettringite is displayed in Fig. 3.5 (a). Equivalent features are observed for sample C3S-AFm8-b (see App. B). According to the crystallization pressure theory ([Scherer, 1999, 2004](#); [Flatt and Scherer, 2008](#)), the growth of crystals in a confined space (i.e., of ettringite into the C-S-H gel porosity) is expected to exert a significant pressure on the pore wall. Therefore, the expansion of cementitious materials subjected to sulfate attacks is mostly attributed to such small crystals of ettringite that are located within the C-S-H gel ([Yu et al., 2013](#); [Bary et al., 2014](#); [Kunther et al., 2015](#)).

Concerning sample C3S-AFm4-a after testing (i.e., after injection of sulfates), one can observe on Fig. 3.6 (a) that some macroscopic pockets of ettringite are located outside the C-S-H gel. Results obtained by SEM-EDS and displayed in Fig. 3.6 (b) indicate that those macroscopic pockets of ettringite are made of pure ettringite (with  $S/Ca=1/2$  and  $Al/Ca=1/3$ ). Furthermore, still after testing, the mineral composition of the C-S-H gel was also obtained by SEM-EDS: the results, displayed in Fig. 3.6 (c), show a cloud of points with an average ratio  $Ca/Si$  estimated to about 1.6 and a ratio  $Al/S$  close to zero, i.e., lower than the value for AFt which should be equal to 0.67. From those results, we can infer that, in this sample, the C-

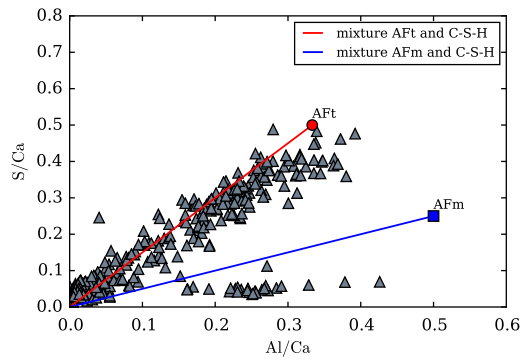
### 3.3. RESULTS AND DISCUSSION



(a)



(b)



(c)

Figure 3.5: SEM-EDS results on sample OPC: (a) Typical microstructure of the sample after testing (which shows some mixture of C-S-H with AFt), (b) Ratio Al/Ca versus ratio S/Ca at various locations in the sample before testing, (c) Ratio Al/Ca versus ratio S/Ca at various locations in the sample after testing.

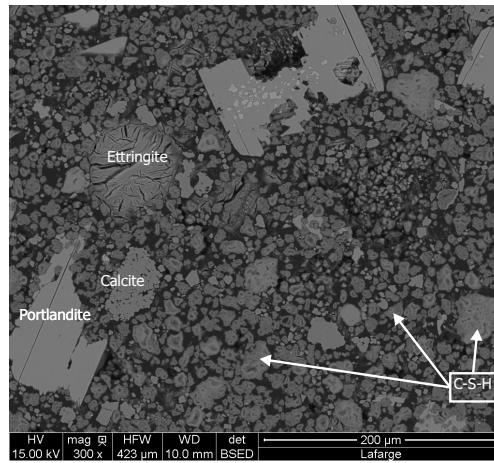
S-H gel contained no ettringite, but only adsorbed sulfate. In addition, we observed (see Fig. 3.6 (a)) that the entry radius of a significant number of pores around the pocket of ettringite was greater than 1  $\mu\text{m}$ : such observation is not consistent with the concept of ettringite crystals precipitating in a highly supersaturated environment and remaining confined in pores with pore entry radiuses smaller than 100 nm (as proposed, e.g., in Steiger (2005b); Bizzozero et al. (2014); Bizzozero (2014)). We observed similar features for sample C3S-AFm8-a, for which the final expansion was the highest among all studied samples. For this sample, the microstructural and mineralogical investigation can be found in Chap. 4.

These results show that, following an injection of sulfates, ettringite pockets which precipitated outside the C-S-H gel can lead to an expansion of our ground compacted materials. This conclusion however is limited to our samples, whose tensile strength must be significantly lower than that of intact cementitious materials. Whether pockets of ettringite can induce an expansion in intact cementitious materials remains an open question.

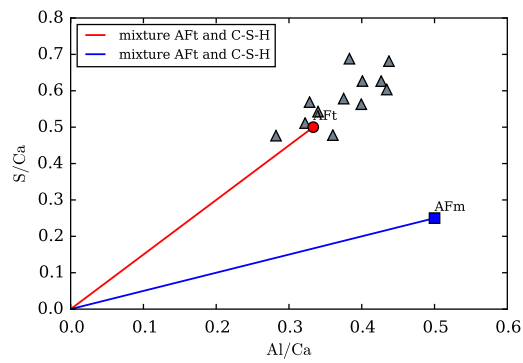
### 3.4 Conclusions

The conclusions drawn from this study are the following:

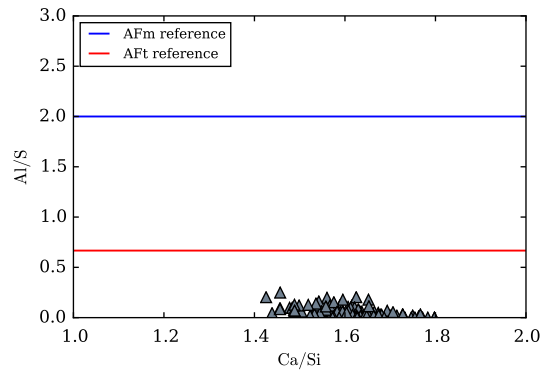
1. By working with samples obtained by compaction of powder and injected with sulfate solutions, the expansion induced by sulfate attacks could be observed much faster than with classical experiments in which usual cementitious samples are immersed in a sulfate solution: the pore volume of our samples could be flushed in less than 1 hour, expansions started right after the injection and were stabilized after a few days.
2. Postmortem analyses showed that, with the protocol we developed, crystallization of ettringite occurred quite homogeneously in the sample. This is a second significant difference with classical experiments in which cementitious samples are usually immersed in a sulfate solution, and for which sulfate ingress by diffusion induces significant gradients



(a)



(b)



(c)

Figure 3.6: SEM-EDS results on sample C3S-AFm4-a: (a) Typical pocket of AFt located outside the C-S-H gel, (b) Ratio Al/Ca versus ratio S/Ca in the pocket of AFt, (c) Ratio Ca/Si versus ratio Al/S in the C-S-H gel.

### CHAPTER 3. OEDOMETRIC STUDY OF KINETICS AND ROLE OF MINERALOGY AND MICROSTRUCTURE

---

and heterogeneities throughout the sample. The reason for this homogeneity remains unclear.

3. The reactions involved in the process are not the rate-limiting factor of the classical experiments in which cementitious samples are immersed in a sulfate solution, and for which expansions are only observed after several dozens of days. It is likely that, in such experiments, the rate-limiting factor is the diffusion of the sulfate ions into the material.
4. In our samples (i.e., ground compacted cementitious materials), strains resulted from a competition between crystallization-induced expansion, dissolution-induced shrinkage, and creep-induced shrinkage. In all samples that contained C-S-H, each injection of sodium sulfate solution induced an expansion. In the sample with no C-S-H, one injection of sulfate solution induced a swelling: therefore, the presence of C-S-H was not necessary to observe an expansion induced by crystallization of ettringite. Whether, in absence of C-S-H, a sample with a tensile strength closer to that of an intact cementitious material would swell after an injection of sulfates remains an open question.
5. For crystallization-induced expansions of the present material to be observed, the AFm initially present in the material did not need to be intimately mixed with the C-S-H gel. Again, whether such a conclusion would hold for intact cementitious materials remains an open question.
6. Ettringite crystallizing outside the C-S-H gel could induce an expansion in our samples, but whether the same conclusion would be reached for intact cementitious materials is unclear.
7. For samples containing C-S-H, the final expansion was positively correlated with the amount of AFm initially present in the sample and, logically, with the amount of ettringite formed.

On top of these concluding remarks, some questions have arisen or remain unanswered, which must be investigated to better understand the mechanism through which an injection of sulfates induces an expansion in cementitious

materials. One of these questions concerns the role played by gypsum crystallization, which shall be investigated and discussed in the following chapters.

Note that, as a perspective to the work performed in this chapter, it would be of high interest to determine which of the conclusions drawn here would still hold for intact cementitious samples rather than for ground compacted ones.

CHAPTER 3. OEDOMETRIC STUDY OF KINETICS AND ROLE OF  
MINERALOGY AND MICROSTRUCTURE

---

## Chapter 4

# Oedometric study of the role of gypsum crystallization in expansion

---

THIS CHAPTER presents an investigation of the role of crystallization of gypsum on the expansion of cementitious materials. We performed an oedometric study with the materials C3S-sand, C3S-AFm4-a, and C3S-AFm8-a. The testing samples were manufactured by compacting powder materials. The mineralogy and microstructure of the various tested samples were investigated before and after testing by using X-ray fluorescence (XRF), Rietveld X-ray diffraction (XRD), thermogravimetric analysis (TGA), scanning electron microscopy with EDS X-ray (SEM-EDS),  $^{27}\text{Al}$ -NMR nuclear magnetic resonance. Beside these experimental characterizations, we also investigated the mineralogical evolution over the experiment, and its relation with the evolution of strains, by using thermodynamic modeling. The final mineralogy obtained with thermodynamic modeling was in good agreement with the one characterized experimentally. The results obtained in this study show that, in our compacted ground samples (which present a lower tensile strength than regular cement pastes), gypsum can lead to expansion and that

## CHAPTER 4. OEDOMETRIC STUDY OF THE ROLE OF GYPSUM CRYSTALLIZATION IN EXPANSION

---

*a greater amount of gypsum formed within the material causes a larger expansion. In addition, we show that the magnitude of expansion is an increasing function of the volume of crystals formed (i.e., ettringite and gypsum) within material. We also identify a threshold amount of those crystals that needs to be formed before one can observe an axial expansion.*

---

**C**E CHAPITRE présente une étude du rôle de la cristallisation du gypse dans le gonflement des matériaux cimentaires. Nous avons effectué des tests oedométriques avec les matériaux modèles tels que C3S-sand, C3S-AFm4-a et C3S-AFm8-a. Les échantillons d'essai ont été fabriqués par compactage de matériaux en poudre selon le processus décrit dans le Chap. 2. La minéralogie et la microstructure des échantillons ont été étudiées avant et après l'expérience en utilisant la spectrométrie de fluorescence des rayons X (FX), la diffractométrie de rayons X (DRX), l'analyse thermogravimétrique (ATG), la microscopie électronique à balayage avec rayons X EDS (MEB-EDS), la résonance magnétique nucléaire de l'aluminium (RMN  $^{27}\text{Al}$ ). Outre ces caractérisations expérimentales, nous avons étudié également l'évolution minéralogique liée à l'évolution de la déformation mesurée en utilisant la modélisation thermodynamique et la base de données Cemdata14. Les minéralogies obtenues par la modélisation thermodynamique ont été également revues et montrent un bon accord avec les caractérisations expérimentales. Les résultats obtenus montrent que, dans nos matériaux broyés compactés (qui présentent une résistance en traction plus faible que celle de pâtes de ciment classiques), le gypse peut conduire à une expansion et qu'une plus grande quantité de gypse formée dans le matériau cause une expansion plus grande. En outre, nous montrons que l'ampleur de l'expansion est une fonction croissante du volume de cristal formé dans le matériau. Nous avons également mis en évidence l'existence d'une quantité critique de ces cristaux formés au-delà de laquelle nous pouvons observer l'expansion axiale.

---

## 4.1 Introduction

In case of external sulfate attacks, upon the diffusive ingress of sulfate ions through the porosity of the material, chemical reactions occur, which lead to the crystallization of gypsum and ettringite within the material. These formations are normally associated with an expansion and a damage of the material (Marchand and Odler, 2002). The expansion of cementitious materials is attributed mostly to the crystallization of ettringite (see Sec. 1.2.2). In particular, the crystallization of ettringite within the C-S-H gel is believed to be the primary cause of expansion (Yu et al., 2013; Kunther et al., 2015). In contrast, the role of the crystallization of gypsum on the expansion is still poorly understood with some considering that gypsum cannot induce any expansion (see, e.g., (Scrivener, 2012; Yu et al., 2013)), while others consider that gypsum can potentially induce an expansion (see, e.g., (Tian and Cohen, 2000; Gartner, 2009; Müllauer et al., 2013)).

The main objective of the present chapter is to better understand the role of gypsum on the expansion of cementitious material, in particular relatively to the role of ettringite. Our strategy to reach this goal is to correlate the strain evolution to the mineralogical evolution of the studied samples. To do so, we tested materials C3S-sand, C3S-AFm4-a, and C3S-AFm8-a (described in Chapter. 2). With these 3 materials, we performed various expansion experiments in oedometric cells, by injecting sodium sulfate solutions with a variety of injection profiles and a variety of concentrations ranging from 66 mM to 1190 mM. C3S pastes were chosen rather than OPC pastes, because their mineralogical and microstructural features are expected to be simpler than the ones of OPC pastes. Also, by adding relatively small amounts of AFm to the materials (with respect to the amount of AFm in OPC pastes), we could expect the crystallization of relatively small amounts of AFt. Noting that, upon injections of sulfates, in the early stage AFt precipitates while in the late stage gypsum precipitates, we injected large amounts of sulfates to favor crystallization of gypsum.

We used various techniques such as X-ray fluorescence (XRF), X-ray diffraction (XRD), thermogravimetric analysis (TGA), scanning electron mi-

## CHAPTER 4. OEDOMETRIC STUDY OF THE ROLE OF GYPSUM CRYSTALLIZATION IN EXPANSION

---

croscopy with EDS X-ray (SEM-EDS),  $^{27}\text{Al}$ -NMR nuclear magnetic resonance to study the mineralogical and microstructural changes of those materials before and after testing. In parallel, the prediction of the mineralogical evolution in those samples was carried-out by using thermodynamic modeling (see Sec. 2.4.2). To validate this modeling approach, the results obtained by thermodynamic modeling were compared with the phase assemblage and chemical composition measured after testing. Based on the predictions from thermodynamic modeling, we study how the expansion was correlated to the crystallization of ettringite and gypsum. Although experiments on C3S pastes are at the core of this chapter, in a final section, we present additional oedometric expansion experiments performed on OPC pastes and show that the results on those pastes are consistent with the conclusions drawn from the experiments on the C3S pastes.

### 4.2 Materials and methods

In the study performed in this chapter, again, the samples were prepared by compacting powder materials with the manufacture process described in Sec. 2.1. We studied 3 types of material: C3S-sand, C3S-AFm4-a, and C3S-AFm8-a, which are described in Sec. 2.1.3. The composition of samples made with C3S as a clinker is expected to be significantly simpler than the composition of samples made with ordinary Portland cement clinker.

On those 3 materials, a total of 4 experiments was performed. In each experiment, the sample was injected repeatedly with a sodium sulfate solution. On sample C3S-AFm4-a, 2 experiments were performed: in one experiment the concentration of the sodium sulfate solution was 66 mM only (this experiment is labeled as ‘C3S-AFm4-a-66’), and in the other one the concentration was 66 mM for some injections and 1190 mM for others (this experiment is labeled as ‘C3S-AFm4-a-66-1190’). On sample C3S-sand, the concentration of the solution was 1190 mM: this experiment is labeled as ‘C3S-sand’. On sample C3S-AFm8-a, the concentration of the solution was 66 mM: this experiment is labeled as ‘C3S-AFm8-a’.

The mineralogical composition of all samples, obtained with the method

‘Combi’ (see Sec. 2.5) for all samples but C3S-sand, is displayed in Tab. 4.1. The ratios  $\text{CaO}/\text{SiO}_2$ ,  $\text{H}_2\text{O}/\text{SiO}_2/\text{SiO}_2$  of the C-S-H gel in these samples can be found in Tab. 2.9 and 2.10.

Materials	CH	C-S-H	Quartz	AFm	AFt	CaCO <sub>3</sub>	C <sub>2</sub> S	C\$H <sub>2</sub>
Before testing								
C3S	26	72	0	0	0	0	2	0
C3S-sand <sup>(e)</sup>	15	43	40	0	0	0	2	0
C3S-AFm4-a-66	35	49	0	4	0	11	1	0
C3S-AFm4-a-66-1190	35	49	0	4	0	11	1	0
C3S-AFm8-a	23	53	0	7	6	10	1	0
After testing								
C3S-sand	N/A	N/A	N/A	N/A	N/A	N/A	N/A	N/A
C3S-AFm4-a-66	30	52	0	0	7	11	0	0
C3S-AFm4-a-66-1190	25	52	0	0	7	13	1	2
C3S-AFm8-a	27	44	0	0	14	13	2	0

Table 4.1: Mass percentage of the various phases in the various samples, before and after the experiment, as obtained with the method Combi. <sup>(e)</sup> For sample C3S-sand, we performed no XRD, or TGA, may it be before or after testing: the displayed values are obtained by a combination of the phase assemblage of the C<sub>3</sub>S paste and of Fontainebleau sand, assumed as pure quartz.

The expansion testings were carried-out in an oedometric cell, which is described in Sec. 2.2.1. We recall that, in oedometer testing, radial deformations are prevented and axial deformations are measured, while a constant axial stress is applied to the sample. The diameter of all samples was 38 mm, their initial mass was 18.09 g. The physical properties of all tested samples are given in Tab. 4.2. The large permeability obtained, in particular for sample C3S-sand, is indicative of large pores and/or of a large porosity. Thermodynamic modeling was carried out by using CHESS software (Chemical Equilibrium of Species and Surfaces), which was described in Sec. 2.4.2.

After testing, each of the 4 samples was immersed in acetone and vacuum-dried to stop all chemical reactions. Then, on each sample we performed X-ray fluorescence (XRF), Rietveld X-ray diffraction (XRD) and thermal gravity analysis (TGA). In addition, sections of samples ‘C3S-sand’, ‘C3S-AFm4-a-66’, and ‘C3S-AFm8-a’ were observed by scanning electron microscopy

CHAPTER 4. OEDOMETRIC STUDY OF THE ROLE OF GYPSUM  
CRYSTALLIZATION IN EXPANSION

Experiment	Initial permeability $\kappa, 10^{-15} \text{ m}^2$	Swelling index $C_s, 10^{-2}$	Oedometric modulus $E_{oed}, \text{ MPa}$	Porosity $\phi, \%$
C3S-sand	14.72	1.19	440	59.55
C3S-AFm4-a-66	1.62	0.95	400	39.18
C3S-AFm4-a-66-1190	0.82	1.10	440	38.19
C3S-AFm8-a	1.64	0.99	518	39.53

Table 4.2: Properties of the tested samples. The porosity  $\phi$  is the porosity of the sample after compaction, but before injection of sodium sulfate solution.

(SEM) and analyzed by EDS X-ray (see Sec. 2.3). We also performed a characterization of aluminate phases by using  $^{27}\text{Al}$ -NMR (nuclear magnetic resonance) on sample C3S-AFm8-a: this characterization was carried out at laboratory ‘Laboratoire de Spectrochimie Infrarouge et Raman’ (LASIR), Lille University, France .

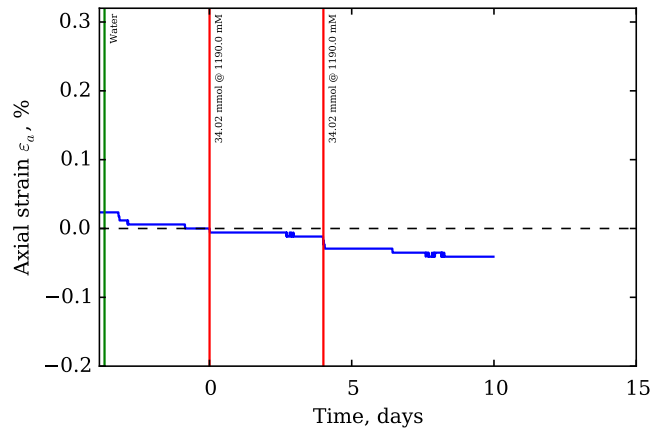
### 4.3 Results

On each of the 4 samples described in Sec. 4.2, we performed an expansion experiment, in which expansion was induced by injections of sodium sulfate. Figure 4.1 displays the evolution of the axial strain of those samples over time, together with the profile of injection. The injection of water is displayed with a green vertical line, each injection of solution is displayed with a red vertical line, on which is indicated the concentration of the injected solution and the amount of injected sulfate. To obtain the strain evolution, the reference time was chosen as the time at the beginning of the first injection of solution, and the reference height of the sample used to calculate the axial strains was the height of the sample right before the first injection of solution.

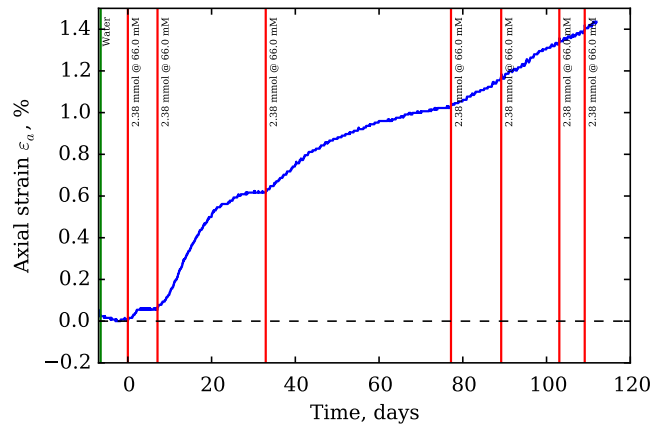
#### 4.3.1 Qualitative description of evolution of strains

The evolution of the axial strains, together with the profiles of injection, are displayed in Fig. 4.1.

For all experiments performed, during the injection of either water or so-



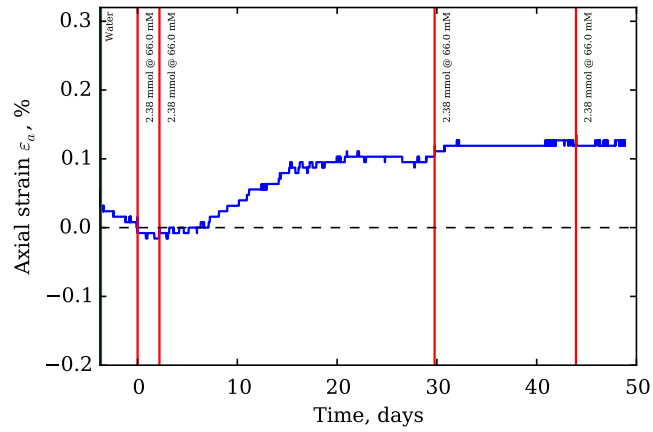
(a)



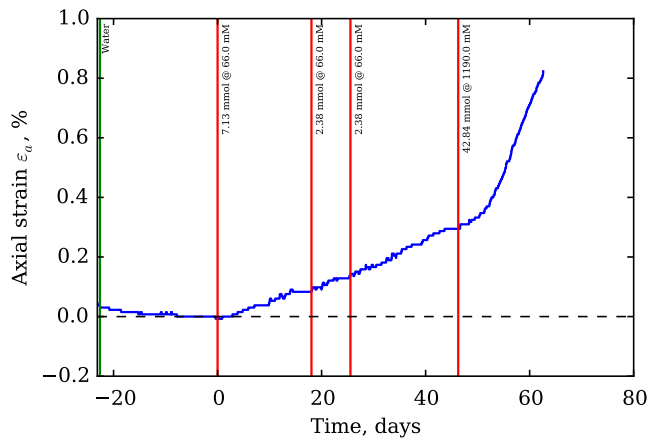
(b)

CHAPTER 4. OEDOMETRIC STUDY OF THE ROLE OF GYPSUM  
CRYSTALLIZATION IN EXPANSION

---



(c)



(d)

Figure 4.1: Evolution of axial strain over experiment (a) C3S-sand, (b) C3S-AFm8-a, (c) C3S-AFm4-a-66, and (d) C3S-AFm4-a-66-1190.

lution, a slight and transient increase of axial strain was observed, which is a classical poroelastic effect induced by the transient increase of pore pressure. After the injection of water, for all samples we observed a slight shrinkage of the material, which may be due to creep.

For sample C3S-sand, no expansion was observed, after none of the two injections of solution at 1190 mM. The evolution of strain after those injections was similar to the one observed after the injection of water (see Fig. 4.1 (a)).

For samples C3S-AFm4-a-66, C3S-AFm4-a-66-1190, and C3S-AFm8-a, the injections of solution induced expansions, and more injections induced a larger expansion. For some injections, we did not wait long enough before performing the subsequent injection or stopping the experiment: this is the case for the last 4 injections in sample C3S-AFm8-a and for the last 2 injections in sample C3S-AFm4-a-66-1190.

We now focus on samples C3S-AFm4-a-66 and C3S-AFm4-a-66-1190. Those two samples were prepared with the same material and manufactured following an identical procedure. Their mechanical and physical properties were quite similar, as results given in Tab. 4.2 show: we can assume that the samples used in those two experiments were similar before the injection of solution. The total amount of sulfate injected into sample C3S-AFm4-a-66 (i.e., 9.52 mmol) was injected into sample C3S-AFm4-a-66-1190 after 2 injections: interestingly, after those 2 injections, the expansion of sample C3S-AFm4-a-66-1190 was somewhat similar to the one of sample C3S-AFm4-a-66 at the end of the experiment. In contrast, for sample C3S-AFm4-a-66-1190, the last 2 injections significantly increased the expansion. We note that the last injection, in which the largest amount of sulfates (i.e., 42.84 mmol) was injected at the largest concentration (i.e., 1190 mM), induced an expansion that had not stabilized by the end of the experiment: if we had waited longer, the expansion that could have been induced by this injection would probably have been significantly larger than the one measured at the end of the experiment.

A deeper mineralogical and microstructural investigation, presented in the sections below, will allow us to better understand the reasons for the various expansions observed on the various samples.

### 4.3.2 Predictions of evolution of mineralogy with thermodynamic modeling

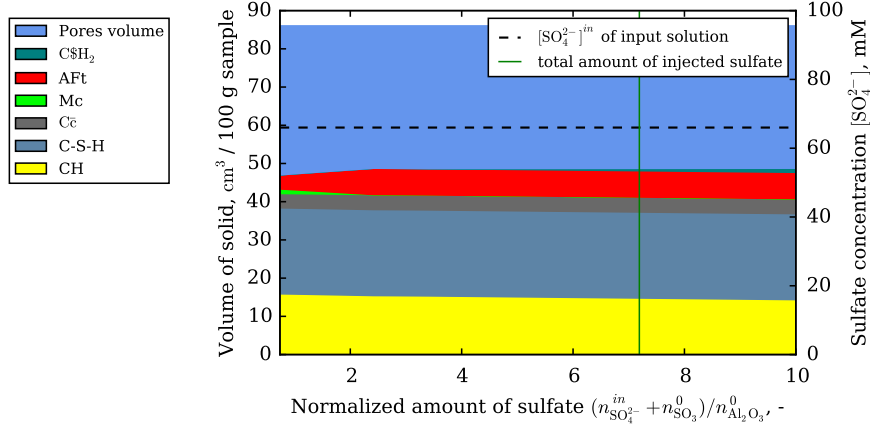
The mineralogical evolution of the various samples over the injection process, as predicted with CHESS (see Sec. 2.4.2), is displayed in Fig. 4.2 and 4.3. We recall that, for all samples, the initial phase assemblage input into CHESS was the one obtained with the method ‘Combi’. The ratio  $\text{CaO}/\text{SiO}_2$  of C-S-H introduced for thermodynamic modeling was the one displayed in Tab. 2.9.

One observes in Fig. 4.2 and 4.3 the following for samples C3S-AFm4-a-66, C3S-AFm4-a-66-1190, and C3S-AFm8-a: in the early stage of the injection process, AFt must have crystallized until all AFm was consumed (note that, here, AFm is in fact under the form of monocarboaluminate (noted Mc) because of the initial presence of calcium carbonate  $\text{CaCO}_3$  in the material), while, in the late stage of the injection process, gypsum must have crystallized. In contrast, for sample C3S-sand, only gypsum crystallized, as the sample contained no AFm. Therefore, over all 4 samples, from 80% to 100% of the injected sulfates must have been used for crystallization of gypsum rather than of ettringite. A summary of what phase must have crystallized in what sample is given in Tab. 4.3.

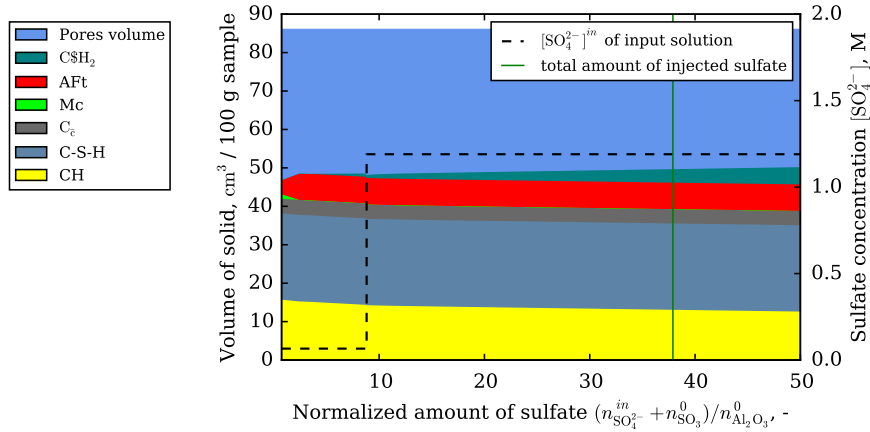
Tested samples	Ettringite			Gypsum		
	XRD	SEM-EDS	Model	XRD	SEM-EDS	Model
C3S-sand	N/A	-	-	N/A	+	+
C3S-AFm4-a-66	+	+	+	-	-	+
C3S-AFm4-a-66-1190	+	N/A	+	+	N/A	++
C3S-AFm8-a	++	+	++	-	+	+

Table 4.3: Qualitative mineralogical and microstructural analysis of the various samples. ‘XRD’, ‘SEM-EDS’ and ‘Model’ stand for Rietveld X-ray diffraction, scanning electron microscopy (SEM) and analysis by EDS X-ray and thermodynamic modeling respectively. ‘-’, ‘+’ and ‘++’ stand for ‘not detected’, ‘detected with a light presence’ and ‘detected with a significant presence’.

The phase assemblage of each sample after testing, as predicted by thermodynamic modeling, is displayed in Fig. 4.4, together with the phase assemblage after testing measured with the method ‘Combi’. Both phase assem-



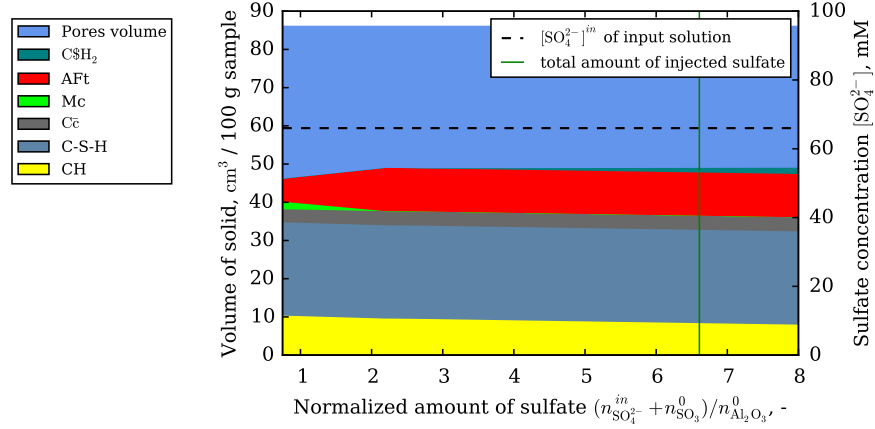
(a)



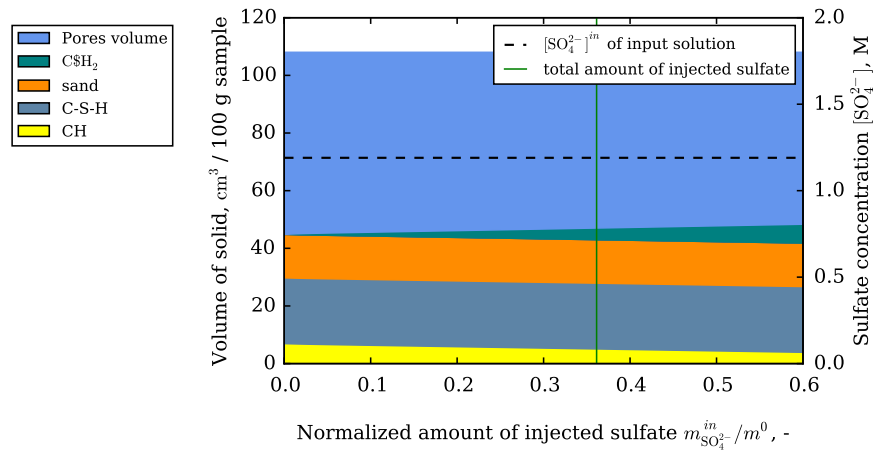
(b)

Figure 4.2: Evolution of phase assemblage predicted by thermodynamic modeling and profiles of injections for samples (a) C3S-AFm4-a-66 and (b) C3S-AFm4-a-66-1190.  $n_{\text{SO}_4^{2-}}^{\text{in}}$  stands for the amount of injected sulfate (mmol), while  $n_{\text{SO}_3}^0$  and  $n_{\text{Al}_2\text{O}_3}^0$  stand for the initial amounts of sulfate and aluminates in the sample, respectively (mmol).

CHAPTER 4. OEDOMETRIC STUDY OF THE ROLE OF GYPSUM  
CRYSTALLIZATION IN EXPANSION



(a)



(b)

Figure 4.3: Evolution of phase assemblage predicted by thermodynamic modeling and profiles of injections for samples: (a) C3S-AFm8-a and (b) C3S-sand.  $n_{SO_4^{2-}}^{in}$  stands for the amount of injected sulfate (mmol), while  $n_{SO_3}^0$  and  $n_{Al_2O_3}^0$  stand for the initial amounts of sulfate and aluminate in the sample, respectively (mmol).

blages compare reasonably well, except for the fact that the mass of gypsum in the various samples, as predicted by thermodynamic modeling, was greater than the mass of gypsum estimated with the method ‘Combi’. The method ‘Combi’ underestimated the amount of gypsum in these samples after testing, in particular for sample C3S-AFm4-a-66-1190 for which a significant amount of gypsum must have precipitated.

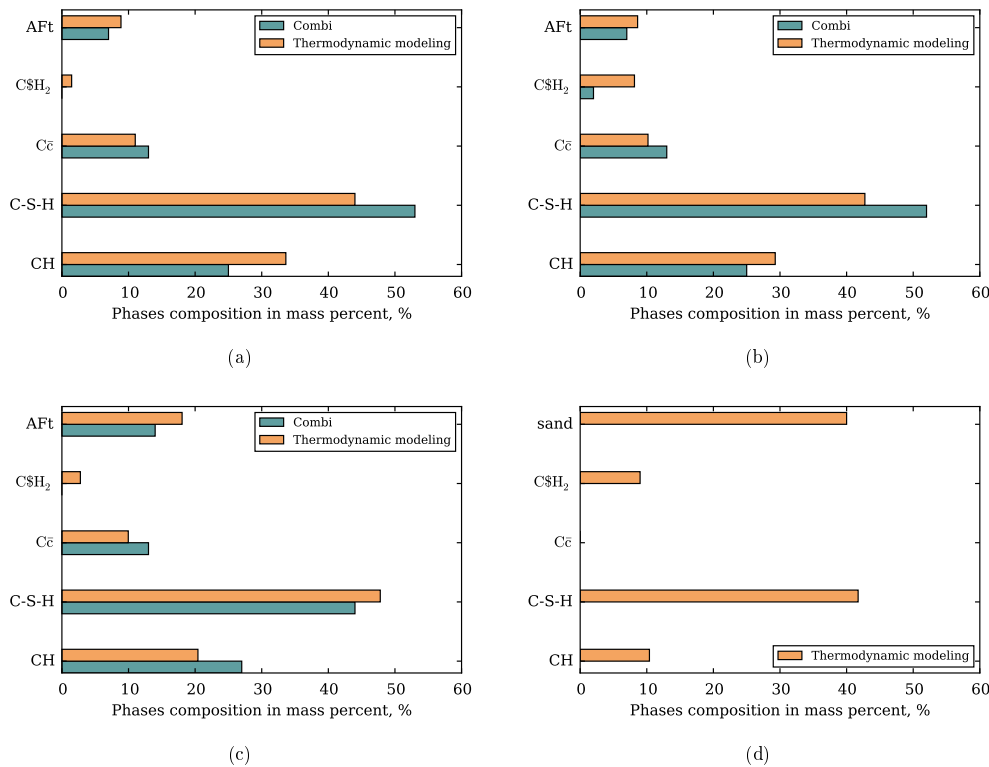


Figure 4.4: Phase assemblage after testing, obtained with thermodynamic modeling and with the method ‘Combi’, for samples (a) C3S-AFm4-a-66, (b) C3S-AFm4-a-66-1190, (c) C3S-AFm8-a, and (d) C3S-sand. Note that, for sample C3S-sand, the experimental characterization was not sufficient to apply the method ‘Combi’.

The chemical composition of the samples after testing, as obtained from thermodynamic modeling, is displayed in Fig. 4.5 together with the one measured with XRF. Some slight discrepancies can be observed, whose reasons were already discussed in Sec. 2.5: carbonation during the characterization

CHAPTER 4. OEDOMETRIC STUDY OF THE ROLE OF GYPSUM  
CRYSTALLIZATION IN EXPANSION

process (see Sec. 2.5.1), disregard of kinetics effects, disregard of unhydrated phases (e.g.,  $C_2S$  or  $C_3S$ ), or difference in hydric states (i.e., the experimental characterizations were performed on dried samples while the thermodynamic modeling was performed for a saturated sample). In spite of those slight differences, the chemical composition predicted by thermodynamic modeling was in good agreement with the chemical composition measured by XRF. In particular, the amount of sulfates present in the sample after testing was correctly predicted by thermodynamic modeling. From this comparison, we infer that, after each injection, thermodynamical modeling with CHES is a reliable tool to predict the phase assemblage.

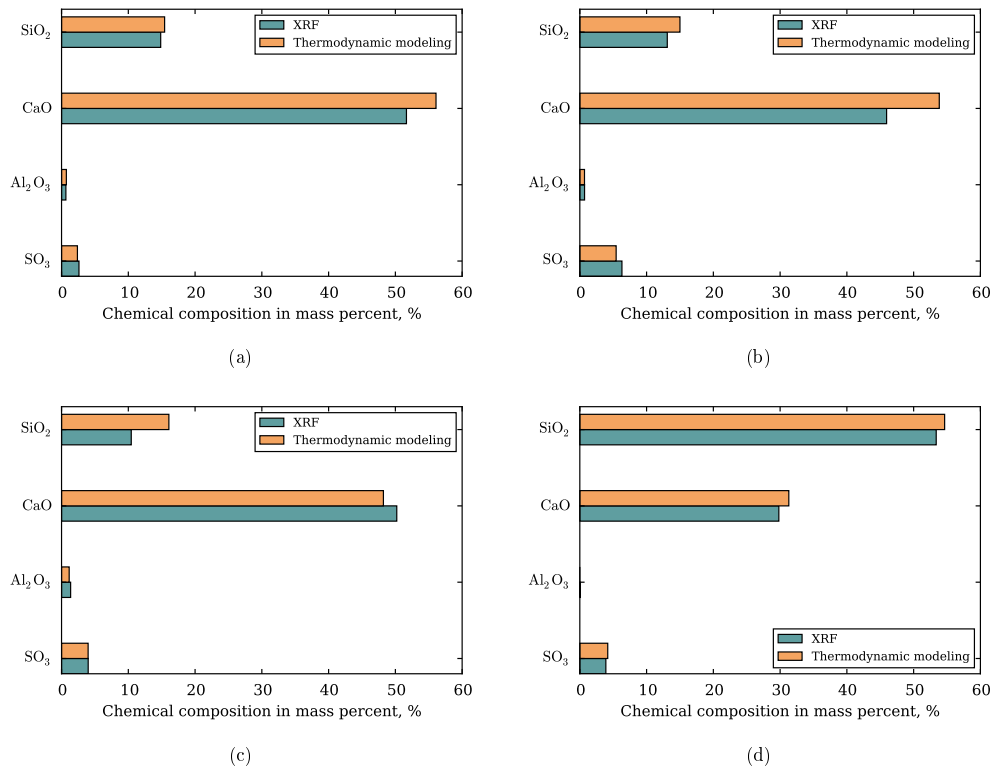


Figure 4.5: Chemical composition after testing, obtained with thermodynamic modeling and XRF, for samples (a) C3S-AFm4-a-66, (b) C3S-AFm4-a-66-1190, (c) C3S-AFm8-a, and (d) C3S-sand.

### 4.3.3 Observation of initial and final mineralogy and microstructure

We performed SEM observations of the reference sample C3S-AFm4-a, which had only been flushed with demineralized water and should therefore have been representative of sample C3S-AFm4-a before injections of sulfate. A typical microstructure is displayed in Fig. 4.6. This figure shows that the AFm platelets are located outside the C-S-H gel. The typical size of those AFm platelets is estimated to be lower than 50  $\mu\text{m}$ .

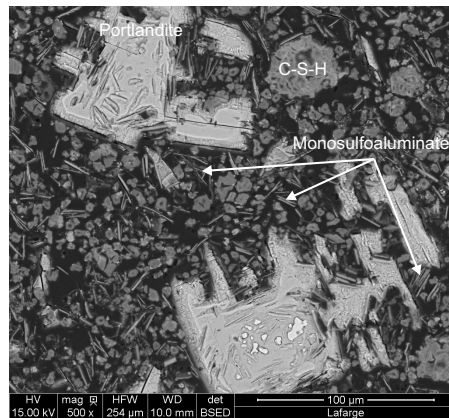


Figure 4.6: A typical microstructure of sample C3S-AFm4-a before testing, showing the co-existence of AFm platelets with C-S-H gel and CH.

Pockets of ettringite were observed in samples C3S-AFm4-a-66 and C3S-AFm8-a after testing (i.e., after the injection of sulfate solution), as displayed in Fig. 4.7. These pockets of ettringite were located outside the C-S-H gel and showed a typically rounded morphology, instead of the flat morphology of the monosulfoaluminate observed in the material before testing. It is interesting to note that the typical size of those pockets of ettringite is much greater than the typical size of the AFm platelets before testing (showed in Fig. 4.6), which was lower than 50  $\mu\text{m}$ . This observation suggests that the pockets of ettringite occupied more space than the monosulfoaluminate in the material before testing.

In samples C3S-sand and C3S-AFm8-a, a significant presence of gypsum precipitated, as can be observed by SEM in Fig. 4.8. In contrast,

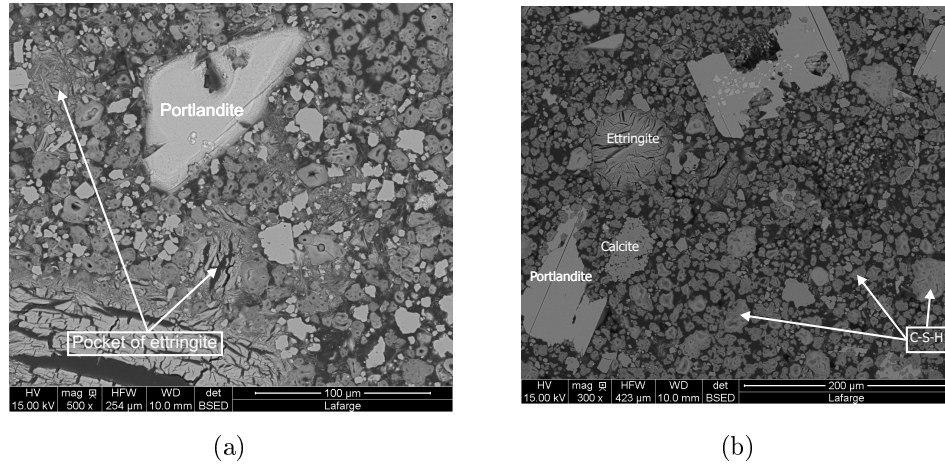


Figure 4.7: Pockets of ettringite observed by SEM in samples (a) C3S-AFm8-a and (b) C3S-AFm4-a-66.

gypsum could not be observed in sample C3S-AFm4-a-66 with SEM, although thermodynamic modeling showed that this sample contained some (see Sec. 4.3.2), but probably in too small an amount. Sample C3S-AFm4-a-66-1190 was not imaged with SEM. Although SEM pictures show that gypsum precipitated at least in samples C3S-sand and C3S-AFm8-a, according to results given in Tab. 4.1, no gypsum (or very little gypsum) was present in those materials after testing: this discrepancy is a further confirmation that XRD (and hence the method ‘Combi’, which uses XRD to determine the amount of gypsum) underestimates the amount of gypsum in the materials we studied (see Sec. 2.5 for potential reasons for this discrepancy), as is visible in Tab. 4.3. Such underestimation is likely to be due to the drying protocol used in the present work, that could have dehydrated gypsum in the material (Mantellato et al., 2015).

We also performed a mineralogical analysis of sample C3S-sand by using SEM-EDS. Results shown in Fig. 4.9 display various atomic ratios such as Si/Ca, S/Ca and Al/Ca, measured on the whole sample: as obviously expected from the absence of AFm in the sample before testing, the sample after testing contained no AFt. In this sample, the presence of gypsum is shown by points with ratio S/Ca close to 1.0. Figure 4.9 (b) shows that the

C-S-H gel contained adsorbed sulfate.

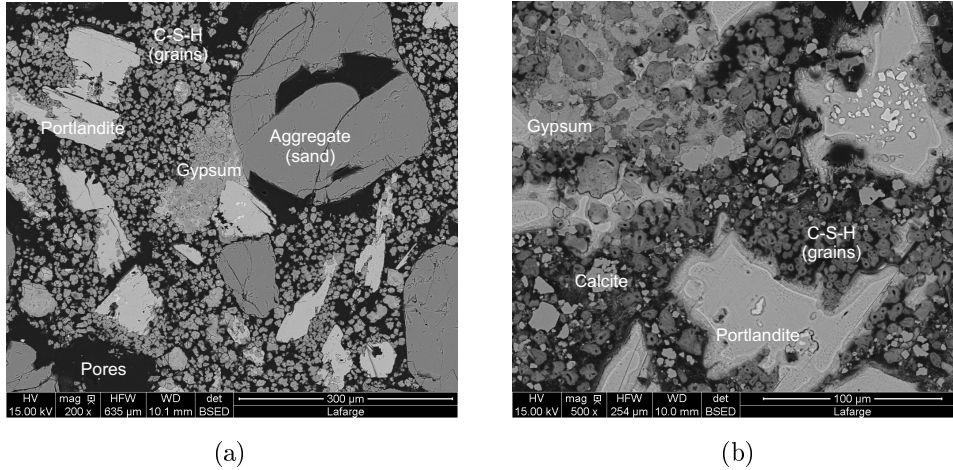


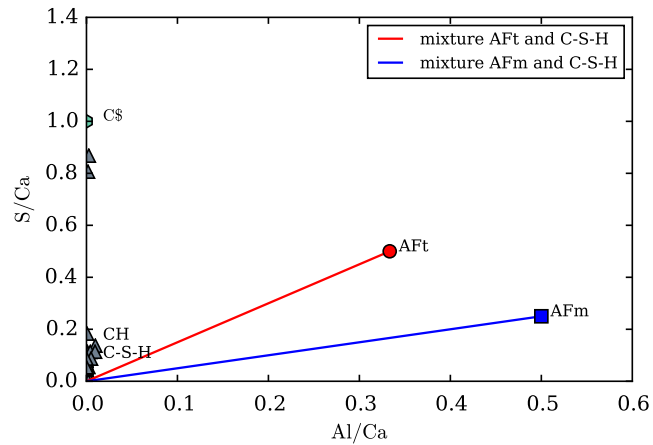
Figure 4.8: Formation of gypsum observed by SEM in samples (a) C3S-sand and (b) C3S-AFm8-a.

The phase assemblage of the various materials obtained with the method ‘Combi’ is given in Tab. 4.1. Based on those phase assemblages, we also determined the chemical composition of the various samples before testing (see Fig. 4.10) and after testing (see Fig. 4.11). Note that, for experiment C3S-sand, no reference sample was made, and on the sample after testing, we performed no TGA or XRD, so that we could not apply the method ‘Combi’ to this sample. Globally, the chemical composition of all samples obtained from the method ‘Combi’ was in quite good agreement with the method XRF, except for the fact that the back-calculated mass fraction of  $\text{SO}_3$  was consistently lower than the one obtained with XRF, as a consequence of the underestimation of gypsum. The error on the mass fraction of  $\text{SO}_3$  was greater for the samples in which the amount of gypsum that precipitated was greater.

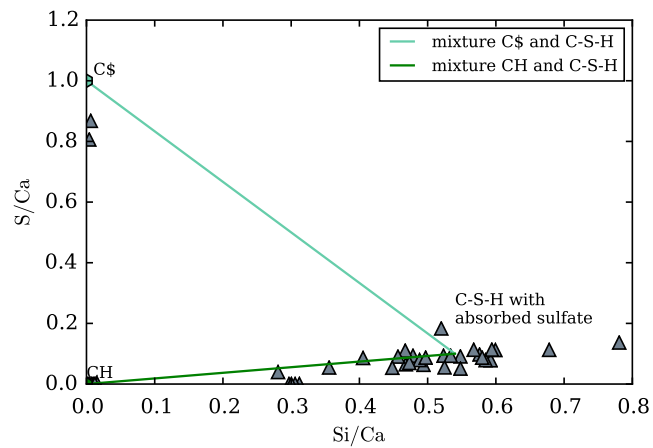
The rest of this section is dedicated to sample C3S-AFM8-a. For this sample after testing, we examined the mineralogical composition of the C-S-H gel, as displayed in Fig. 4.12. This figure shows that the average ratio Ca/Si of the C-S-H gel in that sample was equal to about 1.6, and that no point was located on the references corresponding to ettringite or monosul-

CHAPTER 4. OEDOMETRIC STUDY OF THE ROLE OF GYPSUM  
CRYSTALLIZATION IN EXPANSION

---



(a)



(b)

Figure 4.9: SEM-EDS measurements on sample C3S-sand: (a) Ratio  $Al/Ca$  versus ratio  $S/Ca$ , (b) Ratio  $Si/Ca$  versus ratio  $S/Ca$ .

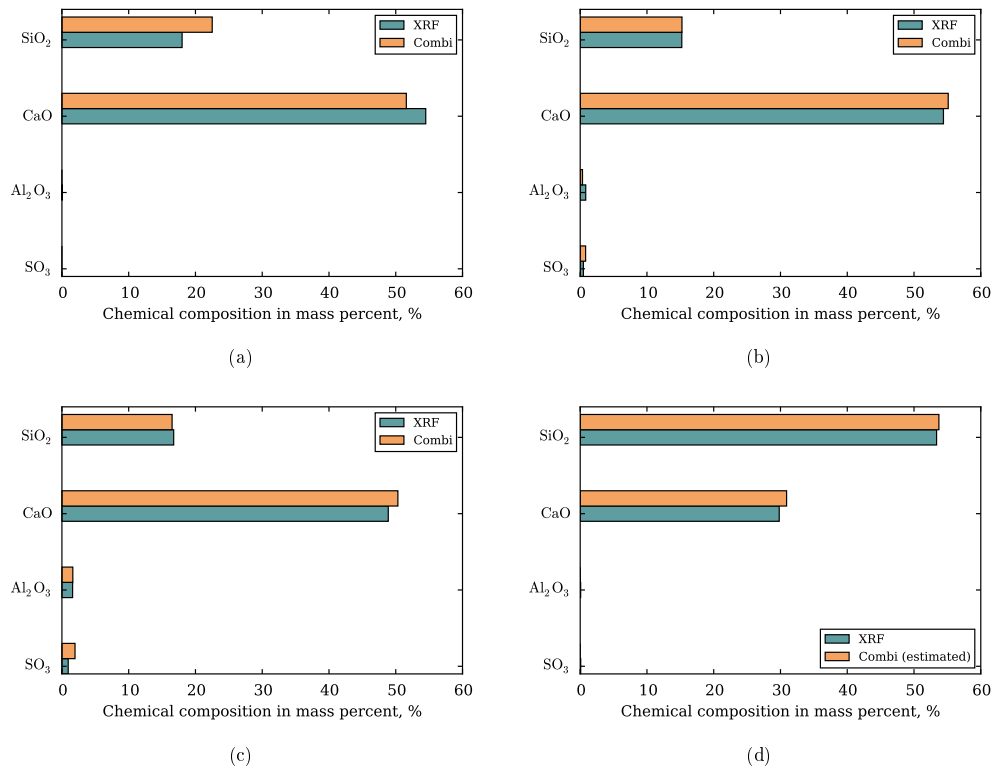
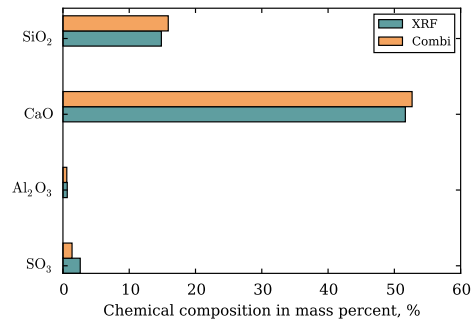


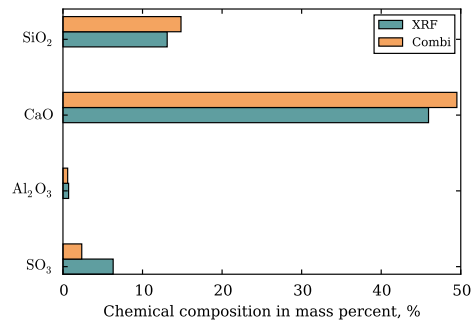
Figure 4.10: Chemical composition before testing, back-calculated from the phase assemblage given in Tab. 4.1 or measured with XRF, for samples (a) C3S, (b) C3S-AFm4-a-66 or C3S-AFm4-a-66-1190, and (c) C3S-AFm8-a and (d) C3S-sand.

CHAPTER 4. OEDOMETRIC STUDY OF THE ROLE OF GYPSUM  
CRYSTALLIZATION IN EXPANSION

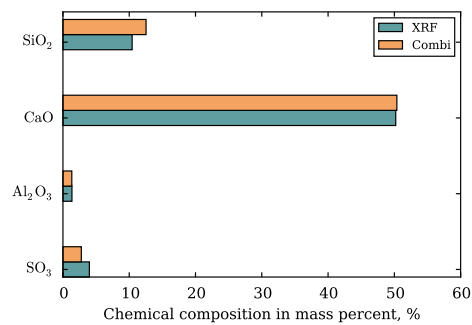
---



(a)



(b)



(c)

Figure 4.11: Chemical composition after testing, back-calculated from the phase assemblage given in Tab. 4.1 or measured with XRF, for samples (a) C3S-AFm4-a-66, (b) C3S-AFm4-a-66-1190 and (c) C3S-AFm8-a.

foaluminate. With such results, we infer that no ettringite precipitated in the C-S-H gel during the experiment C3S-AFm8-a, although this sample expanded significantly (i.e., the axial expansion reached 1.43%). Given that the amount of gypsum that precipitated in this sample was small, we infer that, for this sample, pockets of ettringite contributed to the expansion. This fact was also observed for sample C3S-AFm4-a-66 in Chap. 3.

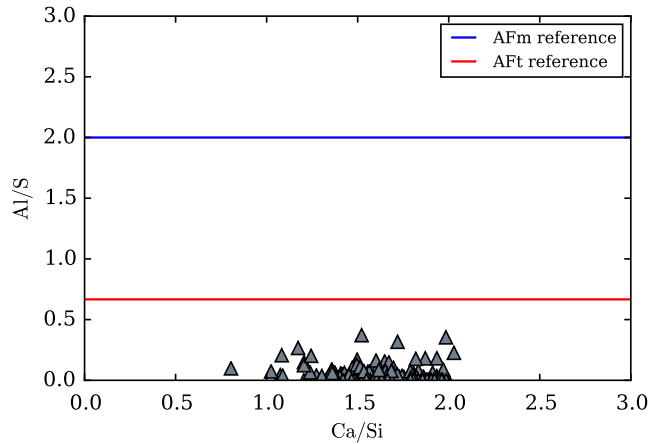


Figure 4.12: SEM-EDS measurement on the C-S-H gel of sample C3S-AFm8-a after testing: Ratio Ca/Si versus ratio Al/S. We observed no AFt in the C-S-H gel of this sample.

On sample C3S-AFm8-a again, results provided by  $^{27}\text{Al}$ -NMR and XRD characterization are given in Tab. 4.4, which shows that almost all monosulfoaluminate reacted during the experiment to form ettringite.  $^{27}\text{Al}$ -NMR identified a small amount of  $\text{C}_3\text{AH}_6$  that XRD could not detect, both before and after the experiment. We note that the phase distribution in aluminates obtained with XRD was quite similar to the one obtained with  $^{27}\text{Al}$ -NMR, probably as a consequence of the fact that monosulfoaluminate and ettringite were located outside the C-S-H gel, as discussed in Sec. 2.5.

CHAPTER 4. OEDOMETRIC STUDY OF THE ROLE OF GYPSUM  
CRYSTALLIZATION IN EXPANSION

Phases in mass percent, %	$C_3AH_6$		AFm		AFt	
	NMR	XRD	NMR	XRD	NMR	XRD
Before testing	0.2	0.0	6.8	7	5.7	0.0
After testing	0.4	0.0	0.4	0.0	12.7	13

Table 4.4: Aluminate phases in sample C3S-AFm8-a, provided by  $^{27}\text{Al}$ -NMR and by XRD.

## 4.4 Discussion

This section is devoted to identifying the role of gypsum crystallization with respect to the role of ettringite crystallization on the expansion.

The results displayed in Fig. 4.1 can be represented in a time-independent manner, by plotting the axial strain versus the cumulative amount of sulfates injected through the sample. This time-independent manner of representing the data is displayed in Fig. 4.13. On this figure, the strain displayed for the  $n^{\text{th}}$  injection of solution is the strain right before the  $(n + 1)^{\text{th}}$  injection. As mentioned in Sec. 4.3.1, after some injections we waited long enough in order for the strain to be stabilized (those data points are indicated as ‘equilibrium strains’), while, for other injections, we did not wait long enough (those data points are indicated as ‘non-equilibrium strains’). When the strain was not stabilized, the system was not in thermodynamic equilibrium.

Figure 4.13 shows that a greater amount of injected sulfate led to a larger expansion, in samples that contained AFm initially (i.e., C3S-AFm4-a-66, C3S-AFm4-a-66-1190 and C3S-AFm8-a). In contrast, for sample C3S-sand, we observed a slight subsidence after each injection of sulfate solution.

Figure 4.14 displays the strain over time of a sample OPC-66-water which has been flushed successively with a sulfate solution and with water. After both injections of solution, we observed an expansion that started right after the injection, and the strain got stabilized after a few days. The sample was then flushed with two injections of water: we observed no shrinkage after those injections of water, although those injections of water should have removed any supersaturation that may have remained in the sample. Said otherwise, the expansion strain induced by the injections of solution is irre-

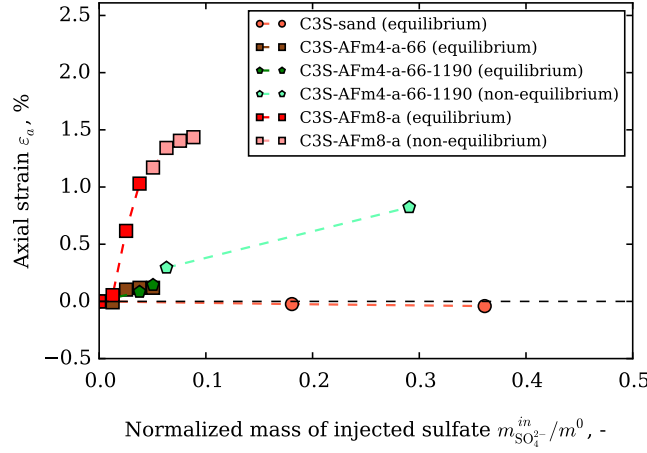


Figure 4.13: Evolution of deformation versus the normalized mass  $m_{SO_4^{2-}}^{in}/m^0$  of injected sulfate where  $m_{SO_4^{2-}}^{in}$  stands for the mass of injected sulfate (g) and  $m^0$  stands for the initial mass of the sample (g).

versible. Based on such observations, it is possible that, after any injection of solution, once the expansion has stabilized, the sample has reached its thermodynamic equilibrium and there is no more supersaturation in the material. With such interpretation, the supersaturation (and hence the crystallization pressure) would only be a transient phenomenon: but this transient crystallization pressure would be sufficiently large to deform the sample irreversibly. In the present works, we correlate those irreversible strains to the mineralogy and microstructure changes induced by the injections of solution.

#### 4.4.1 Comparison between experiments C3S-AFm4-a-66 and C3S-AFm4-a-66-1190

As already explained in Sec. 4.3.1, comparing experiments C3S-AFm4-a-66 and C3S-AFm4-a-66-1190 seems interesting, as the samples in those 2 experiments were identical before testing. Only did the profiles of injection differ: for experiment C3S-AFm4-a-66 the sample was only subjected to injections with a solution at 66 mM, while for experiment C3S-AFm4-a-66-1190 the sample was subjected to 3 injections with a solution at 66 mM and to 1

CHAPTER 4. OEDOMETRIC STUDY OF THE ROLE OF GYPSUM CRYSTALLIZATION IN EXPANSION

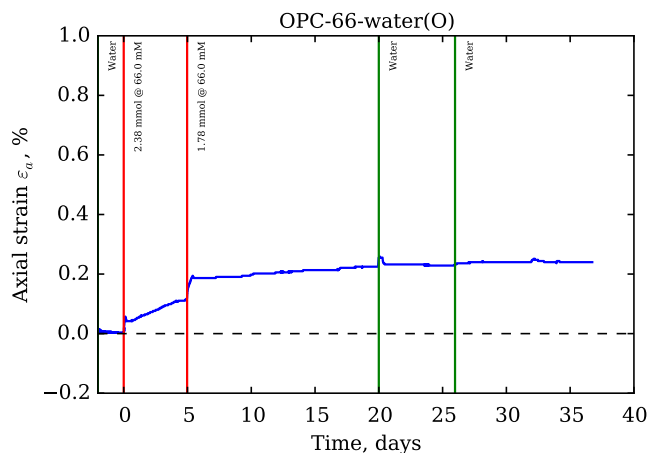


Figure 4.14: Evolution of axial strain over experiment OPC-66-water.

injection with a solution at 1190 mM.

Figure 4.13 shows that, for those 2 experiments, identical normalized amounts  $m_{\text{SO}_4^{2-}}^{\text{in}}/m^0$  (values comprised between 0.03 and 0.05) of injected sulfates led to identical axial strains (axial deformation  $\varepsilon_a$  close to 0.12%), thus proving the repeatability of the procedure. A greater amount of sulfate injected into sample C3S-AFm4-a-66-1190 led to a final expansion that was larger than the final expansion of sample C3S-AFm4-a-66. Note that, for sample C3S-AFm4-a-66-1190, the strains resulting from the last two injections are “non-equilibrium strains” and therefore underestimate the expansion that would have been measured if we had waited longer after each of those 2 injections.

Table 4.5 provides, for those 2 samples, the final expansion, the cumulative normalized amount  $n_{\text{SO}_3}/n_{\text{Al}_2\text{O}_3}$  of injected sulfate, and the normalized mass  $m_{\text{C}_2\text{SH}_2}^1/m^0$  of gypsum formed. All those parameters were greater for sample C3S-AFm4-a-66-1190 than for sample C3S-AFm4-a-66. This table also provides the normalized mass of ettringite formed in those two samples, which was similar. Again, note that the amounts of ettringite or gypsum obtained with the method ‘Combi’ differ from the ones obtained with thermodynamic modeling, as already discussed in Sec. 4.3.2 and 4.3.3.

The larger final strain of sample C3S-AFm4-a-66-1190 with respect to

Samples	Final axial strain, %	$n_{\text{SO}_3}/n_{\text{Al}_2\text{O}_3}$ , -	$m_{\text{AFt}}^1/m^0$ , %		$m_{\text{C\$H}_2}^1/m^0$ , %	
			Combi	Model	Combi	Model
C3S-AFm4-a-66	0.12	5.11	8.94	10.22	0.0	1.68
C3S-AFm4-a-66-1190	0.82	11.32	8.18	10.22	2.34	9.66

Table 4.5: Comparison of various parameters for experiments C3S-AFm4-a-66 and C3S-AFm4-a-66-1190: final axial strain, normalized final amount  $n_{\text{SO}_3}/n_{\text{Al}_2\text{O}_3}$  of sulfate in sample, normalized mass  $m_{\text{AFt}}^1/m^0$  of ettringite formed and normalized mass  $m_{\text{C\$H}_2}^1/m^0$  of gypsum formed. ‘Combi’ and ‘Model’ stand for results obtained with the method ‘Combi’ and with thermodynamic modeling, respectively.

sample C3S-AFm4-a-66 cannot be explained by a difference in the amount of ettringite formed, as this amount is identical in both experiments. Also, although the concentration of the last solution injected into sample C3S-AFm4-a-66-1190 (i.e., 1190 mM) was much greater than the concentration of the solutions injected into sample C3S-AFm4-a-66 (i.e., 66 mM), CHESS calculations show that injections of a solution at either 66 mM or 1190 mM lead to a saturation index (see Eq. (2.9)) with respect to ettringite equal to 7.19<sup>1</sup>. This value is not significantly different from 6.48 (Kunther et al., 2013), i.e., the maximal saturation index with respect to ettringite which is estimated from the solubility product of ettringite and the concentration of the solution in equilibrium with AFm and C\\$H<sub>2</sub> (Flatt and Scherer, 2008). The fact that this difference is small can be explained by the fact that, when gypsum forms, the saturation index with respect to ettringite is limited by the solubility of gypsum (Flatt and Scherer, 2008; Kunther et al., 2013). Therefore, the greater expansion of sample C3S-AFm4-a-66-1190 with respect to sample C3S-AFm4-a-66 cannot be explained by a difference in supersaturation: a last possible explanation is that this greater expansion must be a direct consequence of the greater amount of gypsum formed in the former. Such explanation does not negate the role of crystallization pressure in the expansion phenomenon: in any case, the crystallization pressure is at the origin

<sup>1</sup>the precipitation of gypsum is assumed in those calculations. Without this assumption, the injections of solution at 1190 mM lead to a maximal SI with respect to ettringite equal to 8.77 which is not significantly larger than the one resulting from injections of solution at 66 mM equal to 7.75.

of the phenomenon, as an irreversible expansion will only be observed if this crystallization pressure is sufficiently large to plastify the sample.

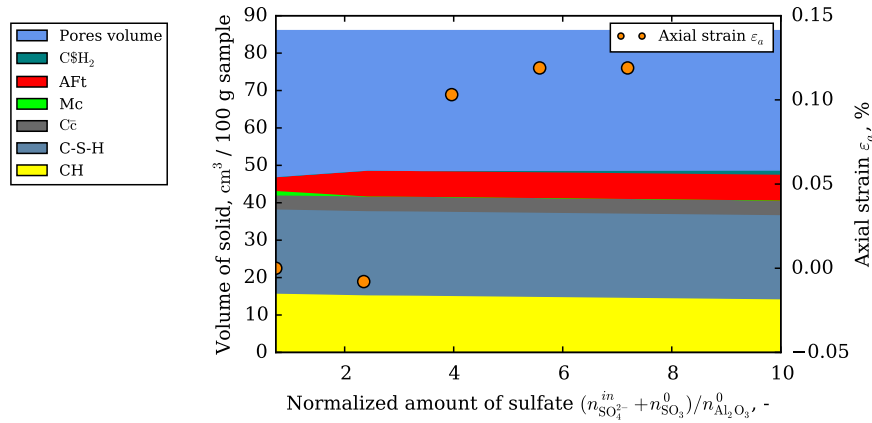
In conclusion, the comparison between experiments C3S-AFm4-a-66-1190 and C3S-AFm4-a-66 shows that gypsum crystallization must contribute to the irreversible expansion of our ground compacted samples. The fact that gypsum contributes to this expansion may be a consequence of the relatively low tensile strength of our materials, which would make it possible for the developed crystallization pressure to plastify the material.

#### 4.4.2 Respective roles of ettringite and gypsum on expansion

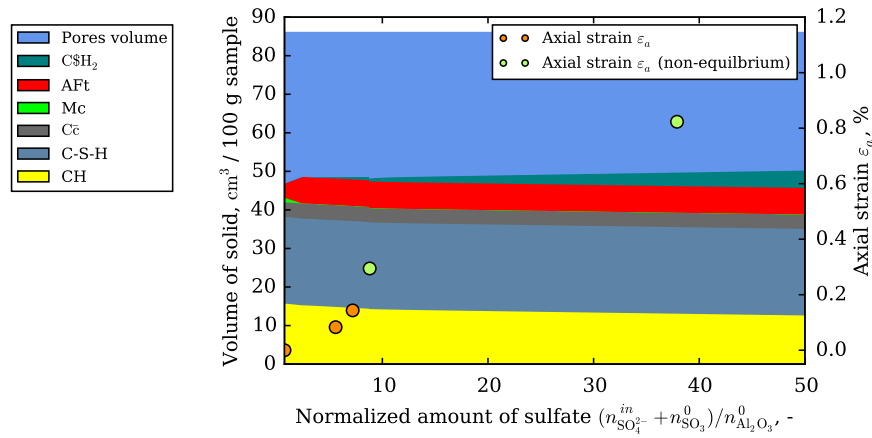
Results displayed in Fig. 4.15 and 4.16 show the evolutions of the strain and of the mineralogy in function of the normalized amount of injected sulfate. We observe that, after all injections having led to a precipitation of ettringite, we waited long enough in order for the strain to reach its equilibrium value (displayed with orange symbols in Fig. 4.15 and 4.16). In contrast, we observe that, after most injections having led to the precipitation of gypsum, we did not wait long enough in order for the strain to reach its equilibrium value (displayed with green symbols in Fig. 4.15 and 4.16). Therefore, the measured gypsum-induced expansions were probably underestimated.

Results displayed in Fig. 4.17 (a) show that the formation of ettringite led to an expansion for samples C3S-AFm4-a-66, C3S-AFm4-a-66-1190, and C3S-AFm8-a. Looking more closely at the first two injections of solution in sample C3S-AFm8-a, we found that a greater amount of ettringite formed led to a larger expansion. The vertical asymptotes visible in Fig. 4.17 (a) indicate that, in the late stage of the experiments, injections still induced an expansion, but with no additional formation of ettringite. Said otherwise, this expansion in the late stage of the experiments could not be attributed to the formation of ettringite.

Figures 4.15 and 4.16 show that, once the sulfates reacted with all mono-carboaluminate, gypsum started precipitating. Therefore, the vertical asymptotes visible in Fig. 4.17 (a) can be explained by the fact that a formation



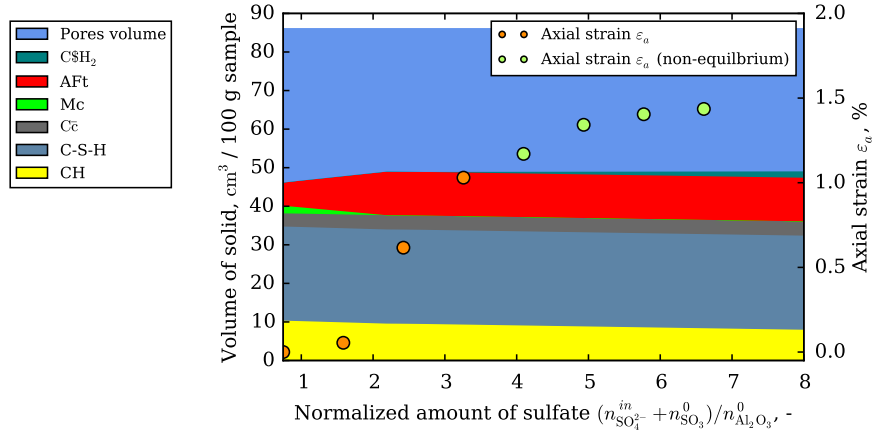
(a)



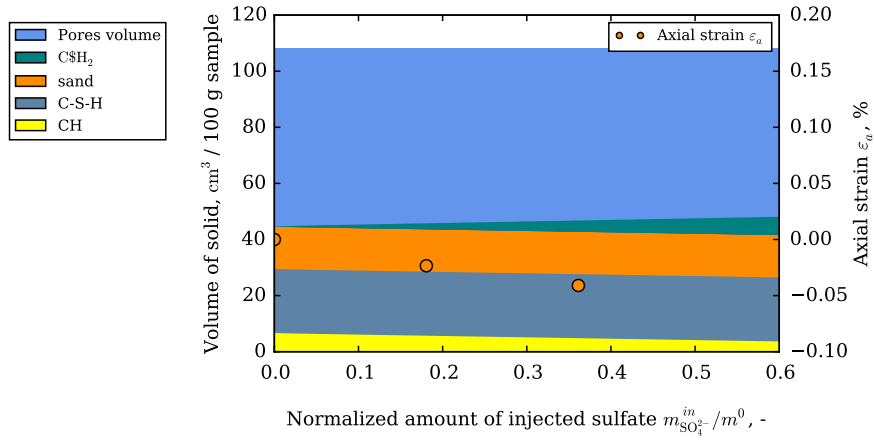
(b)

Figure 4.15: Evolution of phase assemblage and expansion for samples (a) C3S-AFm4-a-66 and (b) C3S-AFm4-a-66-1190.  $n_{SO_4^{2-}}^{in}$  stands for the amount of injected sulfate (mmol), while  $n_{SO_3}^0$  and  $n_{Al_2O_3}^0$  stand for the initial amounts of sulfate and of aluminate in the sample, respectively (mmol).

CHAPTER 4. OEDOMETRIC STUDY OF THE ROLE OF GYPSUM  
CRYSTALLIZATION IN EXPANSION



(a)



(b)

Figure 4.16: Evolution of phase assemblage and expansion for samples (a) C3S-AFm8-a and (b) C3S-sand.  $n_{SO_4^{2-}}^{in}$  stands for the amount of injected sulfate (mmol), while  $n_{SO_3}^0$  and  $n_{Al_2O_3}^0$  stand for the initial amounts of sulfate and of aluminate in the sample, respectively (mmol).

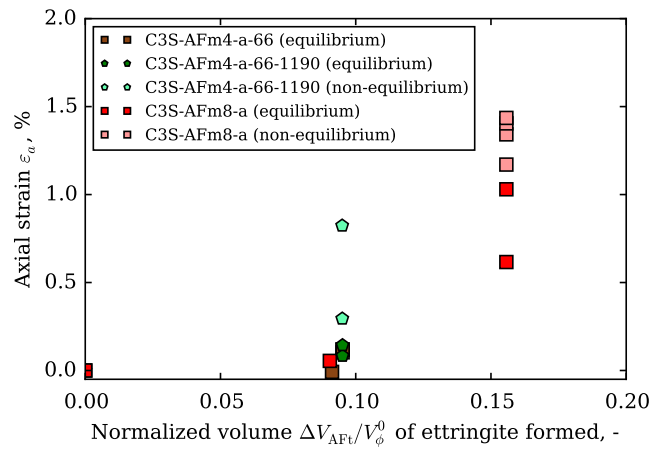
of gypsum could induce an expansion. Such mechanism is confirmed by Fig. 4.17 (b), which shows that, in the late stage of the experiments, the expansion increased with the formation of gypsum. This figure also shows that the greater residual expansion of sample C3S-AFm4-a-66-1190 with respect to sample C3S-AFm4-a-66 is a direct consequence of a greater amount of gypsum formed in the former sample than in the latter. These observations confirm that gypsum can induce an expansion (as already mentioned in Sec. 4.4.1), and show that a greater amount of gypsum formed leads to a larger expansion.

We also note that those samples are expected to be damaged during the late stage of the experiment, during which the strain exceeded significantly the typical elastic limit of cementitious materials i.e., 0.1%, so that relatively little stress is needed to cause further expansion. Whether gypsum crystallization can exceed the local strength and lead to an expansion in intact cementitious materials remains an open question.

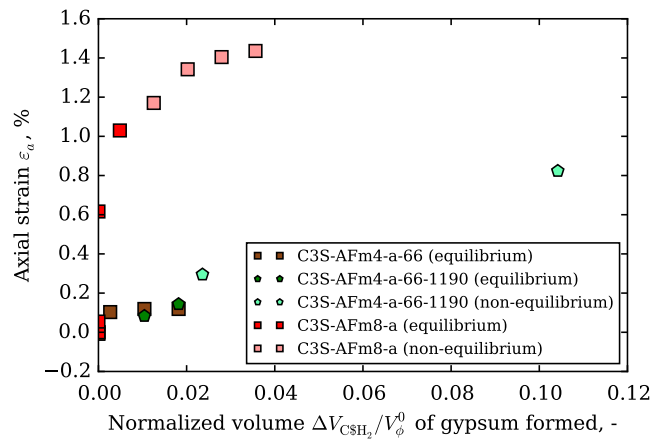
### 4.4.3 Combined roles of ettringite and gypsum in expansion

Figure 4.18 displays the expansion versus the normalized sum  $(V_{\text{AFt}} + V_{\text{C}\$H_2})/V_{\phi}^0$  of the volume  $V_{\text{AFt}}$  of ettringite and  $V_{\text{C}\$H_2}$  of gypsum formed, where  $V_{\phi}^0$  is the initial pore volume. This figure shows that all data points end up on a unique curve, but the one corresponding to the last injection of experiment C3S-AFm4-a-66-1190, for which we know that the measured strain may have been significantly underestimated the value that one would have measured if one would have waited long enough after this final injection (see Fig. 4.1 (d)). The superimposition is clear in particular for experiments C3S-AFm4-a-66 and C3S-AFm4-a-66-1190. This alignment along a master curve shows that the magnitude of axial expansion depends mostly on the volume of precipitated crystals (i.e., ettringite and gypsum) rather than on the profile of injection of solution. We note also that the residual expansion was an increasing function of this volume. We observe no direct effect of supersaturation on such master-curve (see more details in Sec. 4.5).

CHAPTER 4. OEDOMETRIC STUDY OF THE ROLE OF GYPSUM  
CRYSTALLIZATION IN EXPANSION



(a)



(b)

Figure 4.17: Expansion versus the formed volume of (a) Ettringite and (b) Gypsum.  $V_{AFt}$  and  $V_{CSH_2}$  stand for the volumes of ettringite and of gypsum formed, respectively.  $V_\phi^0$  stands for the initial pore volume .

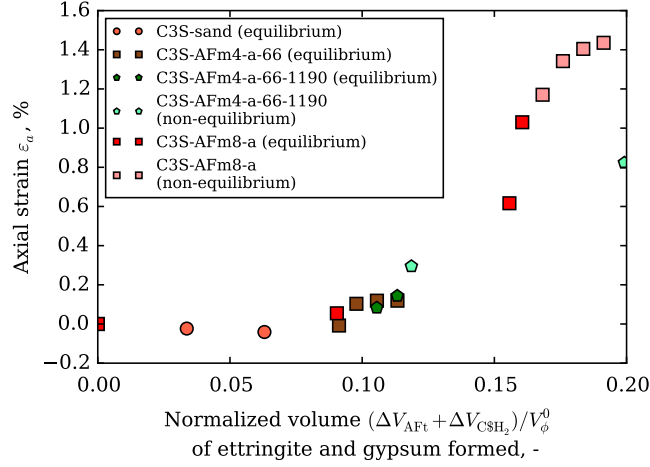


Figure 4.18: Strain evolution versus the normalized combined volume of ettringite and gypsum formed, for all oedometric experiments on C3S pastes.  $V_{AFt}$  and  $V_{C\text{\$}H_2}$  stand for the volumes of ettringite and gypsum formed, respectively;  $V_\phi^0$  stands for the initial pore volume.

An interesting observation is that expansion was not observed at the lowest volumes of crystallized ettringite and gypsum: the expansion started becoming significant only when the ratio  $(V_{AFt} + V_{C\text{\$}H_2})/V_\phi^0$  became greater than 0.1, i.e., when ettringite and gypsum occupied together 10% of the initial pore volume. Hence, there appears to be a threshold volume of crystal formed (here, 10% of the initial porosity) below which no axial expansion is observed. We propose next several hypotheses that could explain why a threshold volume is observed.

As displayed schematically in Fig. 4.19, the first hypothesis is that the pore space must be filled enough so that the grown crystal can exert a pressure (the so-called ‘crystallization pressure’) on the pore wall and thus lead to a deformation of the pore as well as to an expansion of the porous solid (Flatt, 2002b; Scherer, 2004). The results displayed in Tab. 4.2 and in Fig. 4.8 suggest that sample C3S-sand has more large pores than other samples. Therefore, more amount crystals formed is needed to fill enough those large pores before exerting ‘crystallization pressure’ on pore wall. The second hypothesis concerns the fact that the intergranular pore space must be filled by

## CHAPTER 4. OEDOMETRIC STUDY OF THE ROLE OF GYPSUM CRYSTALLIZATION IN EXPANSION

---

those crystals (i.e., ettringite and gypsum) before precipitating into intra-granular pore space and causing expansion. A third hypothesis relies on the anisotropy of the state of stresses in the material. Indeed, due to the oedometric compaction performed to prepare the sample (see Sec. 2.2.1), before injections, the radial stress must have been lower than the axial stress: such anisotropy of the initial stresses will be confirmed in Chap. 5. The existence of a threshold volume to observe an axial expansion may be due to the fact that crystals could prefer growing (and pushing) firstly in the direction of lower stress (i.e., here, in the radial direction) before growing (and pushing) in the other directions. This hypothesis will be discussed in more detail in Sec. 5.3.2, based on results obtained in isochoric cells, with which we can have a better understanding of the anisotropy of stresses, as both radial and axial stresses are measured with these cells. Finally, a last explanation for which a threshold volume is observed is that the moment when this threshold volume is observed would in fact correspond to the moment when the sample would start being significantly damaged.

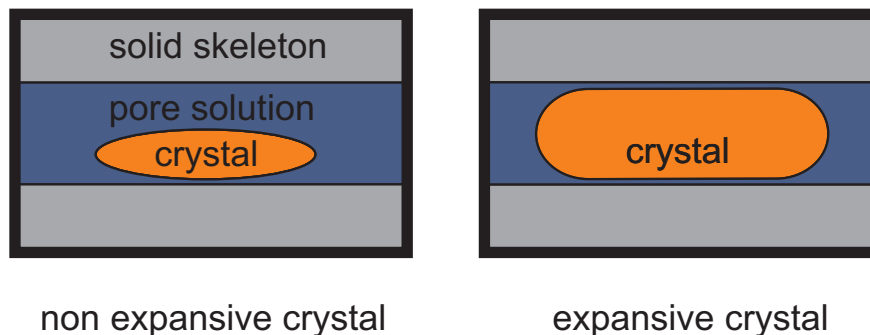


Figure 4.19: Schematics of crystallization in pore: the pore space must be filled enough before the growth of crystal can exert a pressure on the pore wall (Flatt, 2002b; Scherer, 2004).

Results displayed in Fig. 4.1 and 4.13 show that no axial expansion was observed in experiment C3S-sand, which may seem quite surprising, as a significant amount of sulfate was injected in the sample: over the experiment, we injected about 68 mmol of sulfates into sample C3S-sand and the sam-

ple did not swell, while we injected only 17 mmol of sulfates into sample C3S-AFm-8a, which swelled significantly. However, Fig. 4.3 (b) shows that the large quantity of sulfates injected into sample C3S-sand translated into the precipitation of gypsum that eventually occupied only about 6% of the initial porosity: this value is below the threshold volume identified in this section, which can explain why sample C3S-sand did not swell. The first reason why so little volume of crystals precipitated in this sample is that part of the injected sulfates in fact exited the sample with the output solution: the thermodynamic modeling shows that, out of the 68 mmol injected during experiment C3S-sand, only 28 mmol remained (noted  $n_{\text{SO}_4^{2-}}^{\text{re}}$ ) in the sample, the rest having been flushed with the output solution. The second reason is that the initial pore volume  $V_\phi^0$  of sample C3S-sand is much greater than the one of remaining samples. The third reason is that sample C3S-sand contained no AFm: consequently, all injected sulfate induced the precipitation of gypsum only, whose molar volume  $\overline{V}_{\text{CSH}_2}$  (i.e., about 75 cm<sup>3</sup>/mol (Lothenbach and Winnefeld, 2006; Matschei, 2007)) is much smaller than the one of ettringite  $\overline{V}_{\text{AFt}}$  (i.e., about 708 cm<sup>3</sup>/mol (Lothenbach and Winnefeld, 2006; Matschei, 2007))), which is why the volume of crystal formed (equal to  $\overline{V}_{\text{CSH}_2} \times n_{\text{SO}_4^{2-}}^{\text{re}}/V_\phi^0$ ) in C3S-sand is much smaller than in other samples containing AFm.

In summary, the axial expansion seems to be governed by the combined volume of ettringite and gypsum crystals formed in the material, rather than by the profile of injection of the solution. The axial expansion was an increasing function of this combined volume, but started departing from zero only when this combined volume reached a threshold value, which here was equal to about 10% of the initial pore volume.

## 4.5 Results on OPC samples

This chapter was up to now only dedicated to experiments performed on C3S pastes. In the present section, we present oedometric experiments that we performed on OPC pastes. We will show that the features observed in this chapter for the C3S pastes were also observed for the OPC pastes. Only the

## CHAPTER 4. OEDOMETRIC STUDY OF THE ROLE OF GYPSUM CRYSTALLIZATION IN EXPANSION

---

main results are presented in this section: the full set of data is provided in App. C.

All experiments were performed with the material OPC described in Tab. 2.16. We performed 5 experiments with the oedometric cells, in which the sample was injected 1 or several times with a solution of sodium sulfate at the following concentrations: 66, 140, 315, 540, 1190 mM. Those 5 experiments are labeled OPC-66(O) to OPC-1190(O) (see Tab. 2.18). The expansion measured over time during the various experiments is displayed in Fig. 4.20. For all injections and for all samples, we waited long enough before ending the test or performing the next injection in order for the expansion to have roughly stabilized.

By thermodynamic modeling again, we determined the mineralogical evolution of the various samples, based on the profile of injection of sulfate solution displayed in Fig. 4.20. The evolutions of the phase assemblage, superimposed with the measured strains, are displayed in Fig. 4.21 for experiments OPC-66(O) and OPC-140(O). Evolutions of phase assemblage for the other 3 experiments are provided in Appendix (see Fig. C.1). In case OPC-66(O), we introduced a corrective parameter  $\alpha$  ( $\alpha=0.8$ ) as defined in Eq. (5.1) and (5.2) to retrieve the chemical and mineralogical compositions given by experimental results (i.e., XRF and Combi). The corrective parameter  $\alpha$  is equal to 1 for the remaining samples (i.e., OPC-140(O), OPC-315(O), OPC-540(O) and OPC-1190(O)). As was the case with the C3S pastes mixed with AFm, in the early stage of the injection process AFt precipitated, while gypsum precipitated or may have precipitated in a latter stage. A greater amount of injected sulfate led not only to a greater amount of ettringite and gypsum formed but also a greater magnitude of expansion. The final phase assemblage and chemical composition for all samples are provided in Appendix (see Fig. C.2 and C.3, respectively).

Figure 4.21 displays results for experiment OPC-66(O). As was the case for the experiments with the C3S paste, in the early stage of the experiment crystallization of ettringite induced an expansion, while in the late stage of the experiment crystallization of gypsum induced an expansion. However, in oedometric tests, we do not have access to experimental data to detect

## 4.5. RESULTS ON OPC SAMPLES

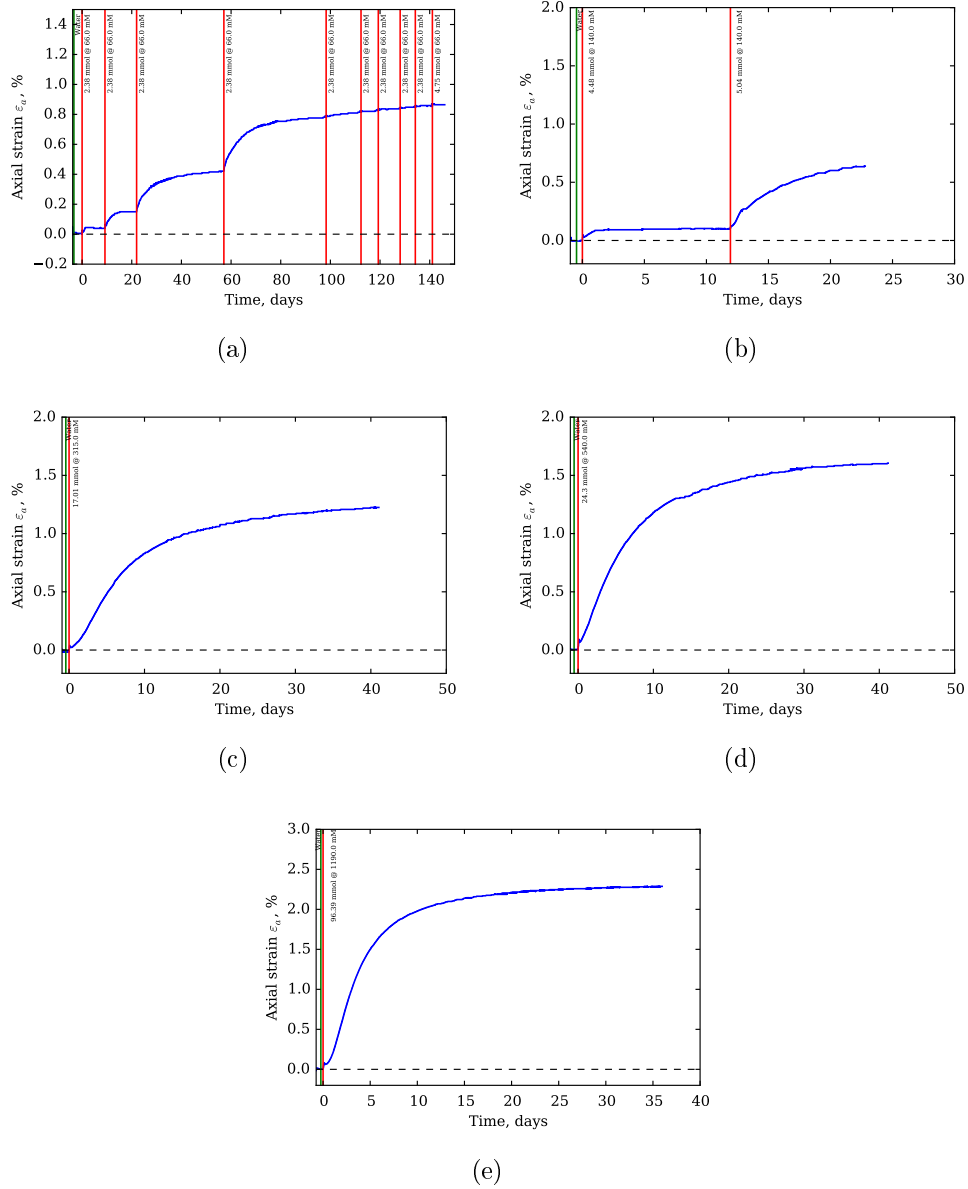
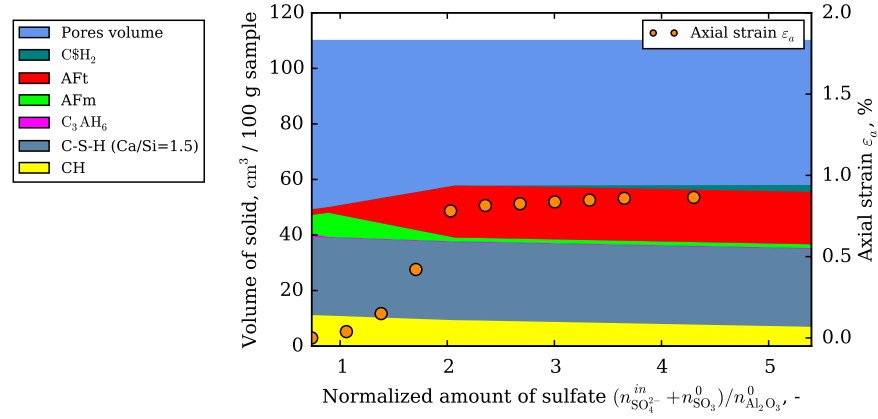
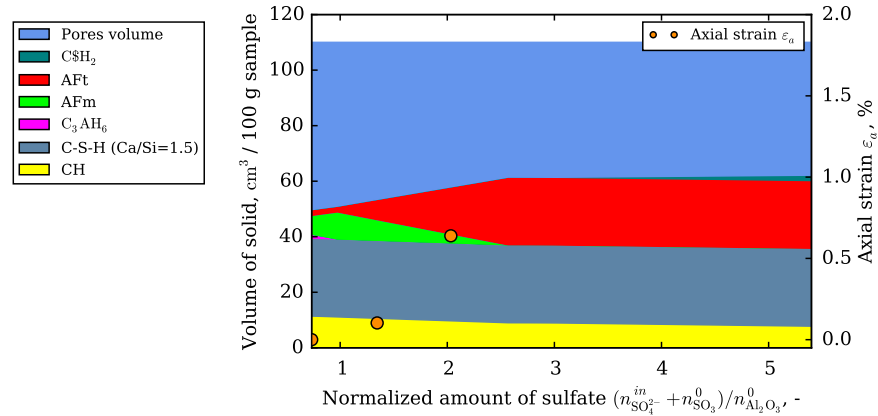


Figure 4.20: Evolution of axial strain over experiment (a) OPC-66(O), (b) OPC-140(O), (c) OPC-315(O), (d) OPC-540(O), and (e) OPC-1190(O).

CHAPTER 4. OEDOMETRIC STUDY OF THE ROLE OF GYPSUM  
CRYSTALLIZATION IN EXPANSION



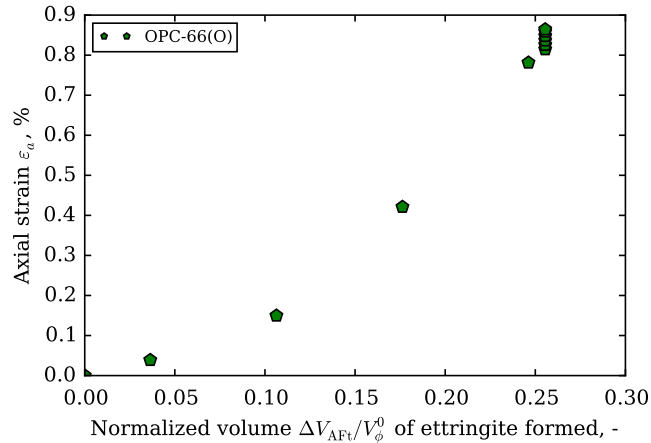
(a)



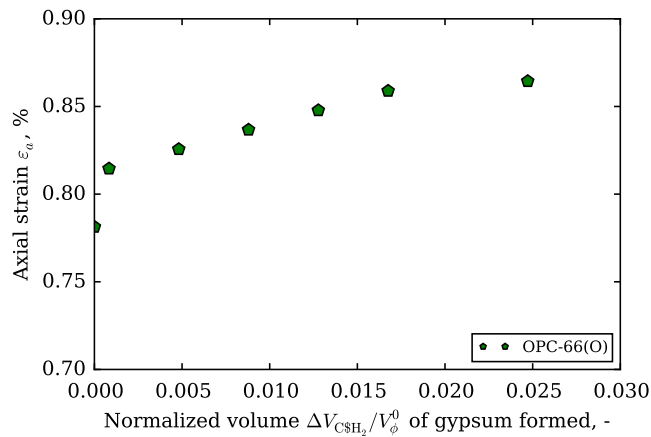
(b)

Figure 4.21: Evolution of phase assemblage and expansion for experiments (a) OPC-66(O) ( $\alpha=0.8$ ) and (b) OPC-140(O) ( $\alpha=1.0$ ), where  $\alpha$  is defined in Eq. (5.1) and (5.2).  $n_{SO_4^{2-}}^{in}$  stands for the amount of injected sulfate (mmol), while  $n_{SO_3}^0$  and  $n_{Al_2O_3}^0$  stand for the initial amounts of sulfate and of aluminate in the sample, respectively (mmol).

distinctly the moment when gypsum starts precipitating. This issue will be resolved with isochoric tests (see more details in Chap. 5) .



(a)



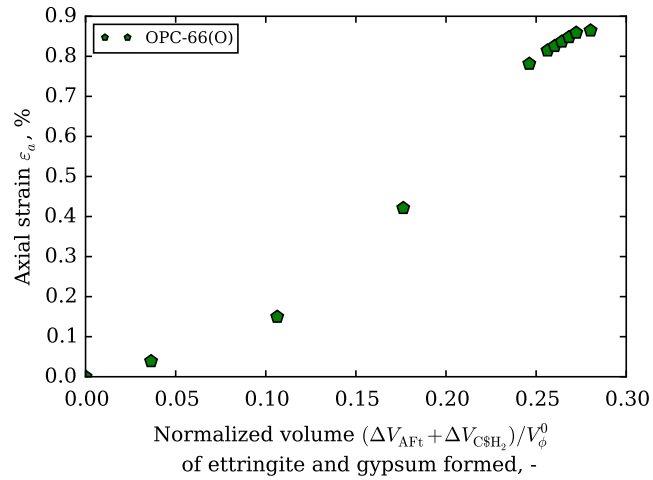
(b)

Finally, Fig. 4.22 shows that, again, the expansion seemed to depend in a unique manner on the volume occupied by both the ettringite and gypsum formed, although not necessarily in a linear way. Also, a threshold volume is observed, from which the expansion departed from zero: in contrast to what was observed with the C3S pastes, for the OPC pastes here considered, this threshold value was around 0.03.

To explain the data displayed in Figs. 4.18 and 4.22 the following ex-

CHAPTER 4. OEDOMETRIC STUDY OF THE ROLE OF GYPSUM  
CRYSTALLIZATION IN EXPANSION

---



(c)

Figure 4.21: Evolution of strains versus the formed amount of ettringite and/or gypsum for experiment OPC-66(O).  $V_{AFt}$  and  $V_{C\$H_2}$  stand for the volumes of ettringite and of gypsum formed, respectively.  $V_\phi^0$  stands for the initial pore volume.

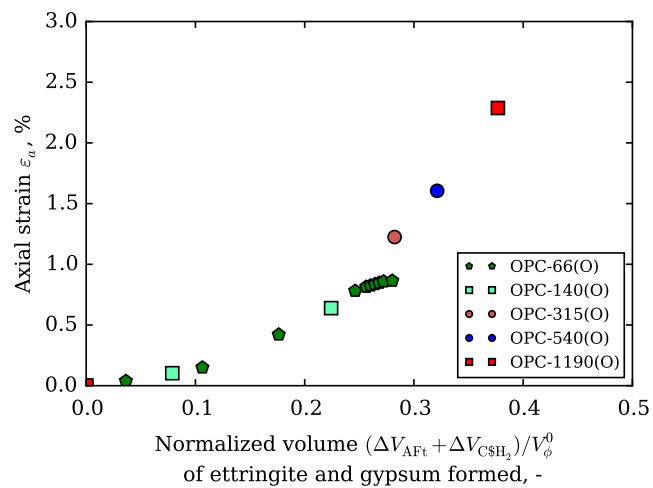


Figure 4.22: Strain evolution versus the normalized combined volume ettringite and gypsum formed, for all oedometric experiments on OPC pastes.  $V_{AFt}$  and  $V_{C\$H_2}$  stand for the volumes of ettringite and gypsum formed, respectively;  $V_\phi^0$  stands for the initial pore volume.

pansion mechanism is envisioned: after each injection of solution, the pore solution becomes highly supersaturated with respect to a crystal (e.g., ettringite, gypsum); this supersaturation induces a crystallization pressure that is sufficiently large to deform the material plastically; the crystal growth consumes the supersaturation while deforming the material; the deformation becomes stabilized once thermodynamic equilibrium is reached, at which moment any supersaturation has vanished. In such expansion mechanism, expansion partly remains, even in absence of any supersaturation, because the solid was plastically deformed. Such mechanism is consistent with an expansion strain correlated with the volume of crystals formed, as results displayed in Figs. 4.18 and 4.22 show. We note that the measured expansions are much greater than the typical elastic limit of cementitious material (i.e., around 0.1 %): it is likely that the samples have been damaged during the experiment. Such damage could at least partly induce the nonlinearity of the relationship between expansion strain and volume of crystal formed.

## 4.6 Conclusions

The results obtained in this chapter confirm some results obtained in the previous chapters with regards to methodology:

- XRD is able to determine reasonably accurately the amount of aluminate phases in the samples when those aluminate phases are added after hydration (as is the case for samples C3S-AFm4-a and C3S-AFm8-a).
- XRD (and hence the method ‘Combi’) consistently underestimated the amount of gypsum in our samples, probably because the drying protocol employed dehydrated the gypsum, as explained in (Mantellato et al., 2015).
- Thermodynamic modeling makes it possible to predict quite accurately the mineralogical evolutions in function of the amount of injected sulfate.

## CHAPTER 4. OEDOMETRIC STUDY OF THE ROLE OF GYPSUM CRYSTALLIZATION IN EXPANSION

---

In this chapter, we presented a series of expansion experiments in oedometric cells, during which we injected sodium sulfate solutions with a variety of injection profiles and a variety of concentrations. Most of the chapter was dedicated to experiments based on C3S pastes, but we also presented experiments performed with OPC paste. The strategy of analysis of the data was to correlate the strain evolution to the mineralogical evolution of the studied samples, this mineralogical evolution being obtained by thermodynamic modeling. The conclusions drawn are the following:

- For our compacted ground materials, pockets of ettringite formed outside of the C-S-H gel can lead to an expansion, and a greater amount of ettringite crystals (including large ettringite crystals) formed leads to a larger expansion. This conclusion is in agreement with the concluding remarks of Chap. 3 but is again limited to our compacted ground materials.
- For our ground compacted materials again, precipitation of gypsum can lead to an expansion and a greater amount of gypsum formed leads to a larger expansion. Whether such conclusion remains valid in an intact cementitious material is an open question.
- The amount of sulfate remaining in the sample seems to be a key factor governing the magnitude of expansion (see Sec. 4.4.1 and 4.4.3).
- The residual expansion (i.e., crystallization induced plastic deformation) seems to depend on the volume of ettringite and gypsum formed rather than on the profile of injection of solution. The residual expansion is an increasing function of the volume of those crystals (i.e., ettringite and gypsum) formed. Even in absence of any supersaturation (i.e., after flushing with water), the expansion strain remains: the transient crystallization pressure must have been sufficiently strong to plastify the material.
- An expansion is observed only after a threshold combined volume of ettringite and gypsum is formed. The existence of this threshold can

explain why, during experiment C3S-sand, no expansion was observed: the volume of gypsum formed in this sample (which contained no AFm and therefore in which no ettringite was formed) was below the threshold. The existence of such a threshold volume may be due to the fact that crystals need first to fill a given fraction of the pores before being able to induce an expansion, or may be due to the initial anisotropy of the state of stresses in the oedometer cells.

Those concluding remarks make it possible to better understand the role of gypsum formation in the expansion of compacted ground materials. However, the role of gypsum formation in the expansion of significantly stronger intact cementitious materials (whose physical and mechanical properties differ significantly from the material used in this study) still remains an open question. Beside those concluding remarks, several questions remain unanswered or deserve to be more thoroughly studied, e.g.: the role of the amount of sulfate remaining in the sample on the expansion (since this amount seems to be a key parameter), the relationship between magnitude of expansion and amount of ettringite and gypsum (fully answering this question was impeded by the fact that, for most injections that induced formation of gypsum, we did not wait long enough to reach equilibrium), the reason why a threshold value is observed, below which no expansion is observed.

To further shed light on those questions, in the next chapter, we will use isochoric cells, for which there are 2 main advantages with respect to the oedometric cells used in the present chapter. The first advantage is that, in the isochoric cells, all output solution can be recovered, such that we can directly infer from experimental measurements the amount of sulfate remaining in the sample. The second advantage is that, in contrast to the oedometric cells in which only one axial quantity was measured (i.e., the axial expansion), the isochoric cells make it possible to measure not only one axial quantity (i.e., the axial stress), but also one radial quantity (i.e., the radial stress).

CHAPTER 4. OEDOMETRIC STUDY OF THE ROLE OF GYPSUM  
CRYSTALLIZATION IN EXPANSION

---

## Chapter 5

# Isochoric study of factors governing expansion stress

---

THIS CHAPTER presents a study of the factors governing the development of expansion stresses. We performed an experimental program consisting in measuring expansion stresses in isochoric cells. The expansion stresses were induced by injecting sodium sulfate solutions throughout samples made by compaction of ground hydrated cement-based powders. In the isochoric cells we developed, one can measure the axial and radial stresses exerted by the sample on the cell walls, while the volume of the sample is kept constant. Over the injections, we also measured the sulfate concentration of the output solution exiting from the sample. These measurements allowed us to determine the amount of sulfate remaining in the sample. We performed thermodynamic modeling with the program CHESS to determine the evolutions of the phase assemblage with regard to the amount of sulfate injected through or remaining in the sample. In addition, we also performed mineralogical and microstructural characterizations, by using the method ‘Combi’ based on results from X-ray fluorescence (XRF), X-ray diffraction (XRD), thermogravimetric analysis (TGA), scanning electron microscopy with EDS

## CHAPTER 5. ISOCHORIC STUDY OF FACTORS GOVERNING EXPANSION STRESS

---

*X-ray (SEM-EDS),  $^{27}\text{Al}$ -NMR nuclear magnetic resonance. The results obtained by thermodynamic modeling were in good agreement with the experimental characterizations. Also, the thermodynamic modeling could predict accurately the evolutions of the sulfate concentration of the output solution, which depends on the formation of ettringite and gypsum. We then discuss the relationship between the evolutions of expansion stress and the evolutions of the phase assemblage. These results allow us to find out what the main factors are that govern the development of an expansion stress in compacted ground cementitious materials.*

---

**C**E CHAPITRE présente une étude des facteurs gouvernant le développement de contraintes de gonflement. Nous avons réalisé une campagne expérimentale consistant à mesurer les contraintes de gonflement dans des cellules isochores. Les contraintes de gonflement étaient induites par l'injection de solutions de sulfate de sodium à travers des échantillons obtenus par compaction de poudres issues du broyage de matériaux cimentaires hydratés. Dans les cellules isochores que nous avons développées, il est possible de mesurer les contraintes axiale et radiale exercées par l'échantillon sur les parois de la cellule, pendant que le volume de l'échantillon est maintenu constant. Au cours des injections, nous avons également mesuré la concentration en sulfates de la solution sortant de l'échantillon. Ces mesures nous ont permis de déterminer la quantité de sulfates restés dans l'échantillon. Nous avons mené des analyses thermodynamiques avec le logiciel CHESS afin de déterminer les évolutions de l'assemblage de phases en fonction de la quantité de sulfates injectés ou restant dans l'échantillon. Nous avons par ailleurs réalisé des caractérisations minéralogiques et microstructurales, en utilisant la méthode 'Combi' basée sur les résultats de spectrométrie de fluorescence des rayons X (FX), diffractométrie de rayons X (DRX), l'analyse thermogravimétrique (ATG), la microscopie électronique à balayage avec EDX rayons X (MEB-EDS), RMN  $^{27}\text{Al}$  la résonance magnétique nucléaire de l'aluminium  $^{27}\text{Al}$ . Les résultats obtenus par la modélisation thermodynamique ont été en

---

*bon accord avec les résultats expérimentaux. De plus, la modélisation thermodynamique a pu prédire de façon précise les évolutions de la concentration en sulfates de la solution en sortie d'échantillon, concentration qui dépend de la formation d'ettringite et de gypse. Nous avons ensuite discuté la relation entre les évolutions des contraintes de gonflement and les évolutions de l'assemblage de phase. Ces résultats nous ont permis d'identifier les principaux facteurs gouvernant le développement de contraintes de gonflements dans les matériaux cimentaires broyés et recompactés.*

---

## 5.1 Introduction

In this chapter, rather than focusing on the expansions induced by injections of sulfates, we focus on the stresses that develop in a sample which is prevented from deforming, when this sample is injected with sulfates: the stresses which thus arise (i.e., the stresses that the sample thus applies on the wall of the system preventing its expansion) are referred to as “expansion stresses”.

Regarding those expansion stresses, we aim at answering questions, some of which being quite similar to the ones that we aimed at answering regarding the expansion measured in oedometric cells in the previous chapters:

- If the deformation of cementitious sample is prevented, upon crystallization of ettringite and gypsum, do we observe a development of expansion stresses?
- What are the main factors controlling those expansion stresses? In particular, what is the role of the sulfate concentration of the injected solution?
- What are the respective contributions of ettringite and gypsum to the development of those expansion stresses?

To answer these questions, we performed original experiments on cement-based materials compacted into isochoric cells which, once closed, prevent any deformation of the sample. The development of expansion stresses was induced by injections of sodium sulfate solutions. A salient feature of our cells is that they allow the measurement of an expansion stress in both the axial direction and the radial direction. Another salient feature is that our cells make it possible to collect all solution exiting from the sample during the injections. Therefore, we could determine the amounts of sulfate remaining in the samples after each injection, by measuring the sulfate concentrations of both the injected and the output solutions. In parallel, we predicted the mineralogical evolution with thermodynamic modeling and studied its correlation with the development of expansion stresses. Based on the results

obtained, conclusions are drawn, that make it possible to better understand how cement-based materials react mechanically to crystallization induced by sulfate attacks.

## 5.2 Materials and methods

In the study presented in this chapter, we tested 4 samples made with an Ordinary Portland Cement (material OPC introduced in Sec. 2.1), manufactured by compacting the powder obtained by grinding, following the process of manufacture described in Sec. 2.1. The tested samples and the label of the corresponding experiments are:

- 1 sample subjected to a sodium sulfate solution with a concentration of 3 mM (this sample and the corresponding experiment are labeled ‘OPC-3’).
- 1 sample subjected to a sodium sulfate solution with a concentration of 66 mM (this sample and the corresponding experiment are labeled ‘OPC-66’).
- 1 sample subjected to sodium sulfate solutions with concentrations of 3 and 66 mM (this sample and the corresponding experiment are labeled ‘OPC-3-66’).
- 1 sample subjected to a sodium sulfate solution with a concentration of 1190 mM (this sample and the corresponding experiment are labeled ‘OPC-1190’).

All 4 samples were prepared from the material OPC and compacted directly into the isochoric cell, as described in Sec. 2.2: all samples were cylinders with a diameter of 38 mm and a height of about 18 mm. Their initial mass was 18.09 g. Their physical properties are given in Tab. 5.1.

The measurements of expansion stresses were carried out in isochoric cells, already described in Sec. 2.2.2. We recall that, in an isochoric cell, all macroscopic deformations of the sample are prevented. Our isochoric

CHAPTER 5. ISOCHORIC STUDY OF FACTORS GOVERNING  
EXPANSION STRESS

Sample	Permeability $\kappa$ , $10^{-16}$ m <sup>2</sup>	Bulk modulus $K$ , MPa	Porosity $\phi$ , %
OPC-3	4.67	657	59.21
OPC-66	1.53	639	59.53
OPC-3-66	2.15	720	57.48
OPC-1190	9.05	684	58.68

Table 5.1: Properties of the tested samples. The porosity  $\phi$  and the permeability of the samples were obtained after compaction, but before injection of water. The bulk modulus is measured at 880 kPa

cells made it possible to measure both the radial and axial stresses over time. Expansion stresses were induced by flushing the samples upward with a sodium sulfate solution. The isochoric cells were designed such as to allow the recovery of all solution exiting the sample: after each injection of solution, we measured the volume and the sulfate concentration of the injected and output solutions, as described in Sec. 2.2 and 2.2.4. The experiments were carried out at  $20^\circ\text{C} \pm 1.5^\circ\text{C}$ .

After testing (i.e., after the injections of solutions of sodium sulfate), each of the 4 samples was immersed in acetone and vacuum-dried to stop all chemical reactions. Sections of samples OPC-3, OPC-3-66, and OPC-66 were observed by scanning electron microscopy (SEM) and analyzed by EDS X-ray. On all 4 samples, we also performed X-ray fluorescence (XRF), X-ray diffraction Rietveld (XRD), thermal gravimetry analysis (TGA), and <sup>27</sup>Al-NMR nuclear magnetic resonance: these characterizations are described in Sec. 2.3. The phase assemblage of those samples was obtained with the method we proposed (i.e., the method ‘Combi’ described in Sec. 2.3.3): the inputs required for the use of this method (e.g., ratios CaO/SiO<sub>2</sub>, Al<sub>2</sub>O<sub>3</sub>/SiO<sub>2</sub>, H<sub>2</sub>O/SiO<sub>2</sub> of the mixture C-(A)-S-H) before and after testing are given in Tab. 2.9 and 2.10 and the obtained phase assemblages are given in Tab. 5.2, where the label C-(A)-S-H stands for C-S-H, whether it contains Al<sub>2</sub>O<sub>3</sub> or not (see Sec. 2.3.3 for a discussion of the difficulty in distinguishing C-S-H from C-A-S-H).

The 4 tested samples were in fact prepared from 3 different batches, where, by batch, we mean the amount of powder prepared in one grinding: samples OPC-66 and OPC-1190 were compacted from OPC powder coming

5.2. MATERIALS AND METHODS

Composition	Materials			
Component Mass, %	OPC-3	OPC-3-66	OPC-66	OPC-1190
Before testing				
CH	26.6	24.3	25.0	25.0
C-(A)-S-H	54.1	54.0	52.9	52.9
AFm	11.1	13.2	13.6	13.6
AFt	3.1	3.7	3.7	3.7
C $\bar{c}$	0.0	0.0	0.0	0.0
C <sub>3</sub> AH <sub>6</sub>	3.8	3.8	3.7	3.7
C <sub>2</sub> S	1.1	1.1	1.0	1.0
After testing				
CH	0.0	0.0	8.3	7.2
C-(A)-S-H	42.2	48.4	40.9	54.2
AFm	7.3	1.2	0.9	0.7
AFt	23.7	42.0	36.5	29.7
C $\bar{c}$	23.3	6.3	10.4	5.1
C <sub>3</sub> AH <sub>6</sub>	1.4	0.0	0.8	1.1
C\$H <sub>2</sub>	N/A	1.0	1.0	2.0
C <sub>2</sub> S	2.1	1.0	1.0	0.0

Table 5.2: Phase assemblage of samples OPC-3, OPC-3-66, OPC-66, and OPC-1190, before and after testing.

## CHAPTER 5. ISOCHORIC STUDY OF FACTORS GOVERNING EXPANSION STRESS

---

from the same batch, i.e., obtained with a unique grinding. For each of the 3 batches, some ground powder was used to manufacture a reference sample, which was compacted according to the same procedure as for the tested samples (see Sec. 2.1). However, these 3 reference samples were only flushed with demineralized water, not with the solution of sodium sulfate: these reference samples should therefore have been representative of the tested samples, but before they were injected with the solution of sodium sulfate. In fact, the first reference sample must have been representative of sample OPC-3 before injection, the second reference sample should have been representative of sample OPC-3-66 before testing, and the third reference sample should have been representative of both samples OPC-66 and OPC-1190 before testing. Those 3 reference samples were immersed in acetone and vacuum-dried to stop all chemical reactions. Such drying protocol may dehydrate some crystal phases of the material (see more details in Chap. 4). Then, on those samples, we performed all experimental characterizations required to obtain the phase assemblage with our method ‘Combi’. In particular, the results of the characterization by  $^{27}\text{Al}$ -NMR are shown in Tab. 5.3. The measured phase assemblages before testing were already given in Tab. 2.13, as we used those 3 reference samples to justify the reproducibility of the manufacturing: these phase assemblages are recalled in Tab. 5.2, where they are referred to as the phase assemblages of the materials ‘before testing’.

For all samples before and after testing, based on the phase assemblages obtained with the method ‘Combi’ (see Tab. 5.1), the chemical composition (i.e., the amounts of  $\text{CaO}$ ,  $\text{Al}_2\text{O}_3$ ,  $\text{SiO}_2$ ,  $\text{SO}_3$ , and  $\text{Fe}_2\text{O}_3$ ) can be inferred: this composition, expressed for 100 g of sample, is displayed in Fig. 5.1 for the samples before testing and in Fig. 5.2 for the samples after testing. These results were compared with the chemical composition obtained with XRF. As Fig. 5.1 shows, for the samples before testing, the chemical composition inferred from the phase assemblages corresponded very well to the one obtained with XRF, which is consistent with the discussion in Sec. 2.5.4. For all samples after testing (i.e., after injection of sulfates), Fig. 5.2 shows that the chemical composition inferred from the phase assemblage was in very good agreement with the one obtained with XRF, but for sample OPC-1190:

## 5.2. MATERIALS AND METHODS

Materials	Phases distribution in Al <sub>2</sub> O <sub>3</sub> , Molar (%)				
	CAH/TAH	AFm	AFt	Al(V)	C-A-S-H
Before testing					
OPC-3	21	47	7	6	19
OPC-3-66	18	50	7	6	19
OPC-66	17	52	7	6	18
OPC-1190	17	52	7	6	18
After testing					
OPC-3	6	31	50	4	9
OPC-3-66	0	5	87	0	8
OPC-66	2	4	81	4	9
OPC-1190	7	5	79	3	6

Table 5.3: Distribution of aluminate phases Al<sub>2</sub>O<sub>3</sub> characterized by <sup>27</sup>Al-NMR, before and after testing, for samples OPC-3, OPC-3-66, OPC-66, and OPC-1190.

for this sample, the phase assemblage significantly underestimated the mass fraction of SO<sub>3</sub>, as a consequence of the underestimation of gypsum by XRD, an issue that has already been discussed in Sec. 4.3.2.

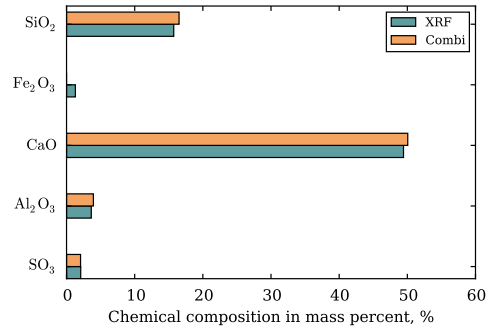
Furthermore, the parameters used for the characterization of phase assemblage, such as the ratios CaO/SiO<sub>2</sub>, Al<sub>2</sub>O<sub>3</sub>/SiO<sub>2</sub>, H<sub>2</sub>O/SiO<sub>2</sub> of the mixture C-(A)-S-H, which are displayed in Tab. 2.10, show a good agreement with the experimental results obtained from other methods such as SEM-EDS or <sup>27</sup>Al-NMR. Before and after testing, based on the measured phase assemblage, we back-calculated the density that we needed to assume for the C-(A)-S-H phase to retrieve the density of the solid phase measured by helium pycnometry: those densities are displayed in Tab. 5.4 and lie in the range [2.28, 2.76] g/cm<sup>3</sup>, which is consistent with the range of density of C-S-H [1.83, 2.85] g/cm<sup>3</sup> given by Jennings (2008).

	OPC-3	OPC-3-66	OPC-66	OPC-1190
Before testing	2.3	2.32	2.31	2.31
After testing	2.28	2.76	2.67	2.56

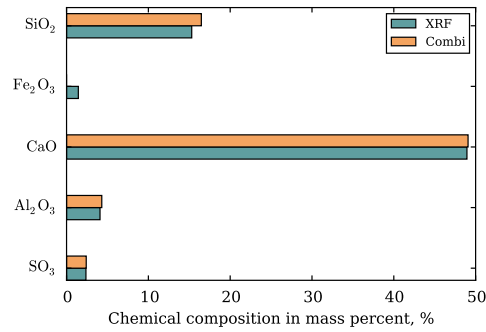
Table 5.4: Density  $\rho_{C(A)SH}$  (g/cm<sup>3</sup>) of C-(A)-S-H that needs to be chosen to retrieve the density of the solid phase measured by helium pycnometry.

## CHAPTER 5. ISOCHORIC STUDY OF FACTORS GOVERNING EXPANSION STRESS

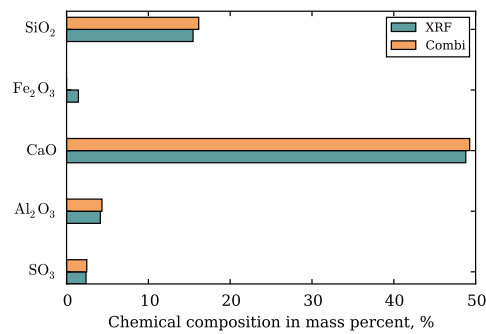
---



(a)



(b)



(c)

Figure 5.1: Chemical composition before testing, back-calculated from the phase assemblage given in Tab. 5.2, and determined by XRF: (a) OPC-3, (b) OPC-3-66, and (c) OPC 66. The material used for OPC-1190 was the same as for OPC-66.

## 5.2. MATERIALS AND METHODS

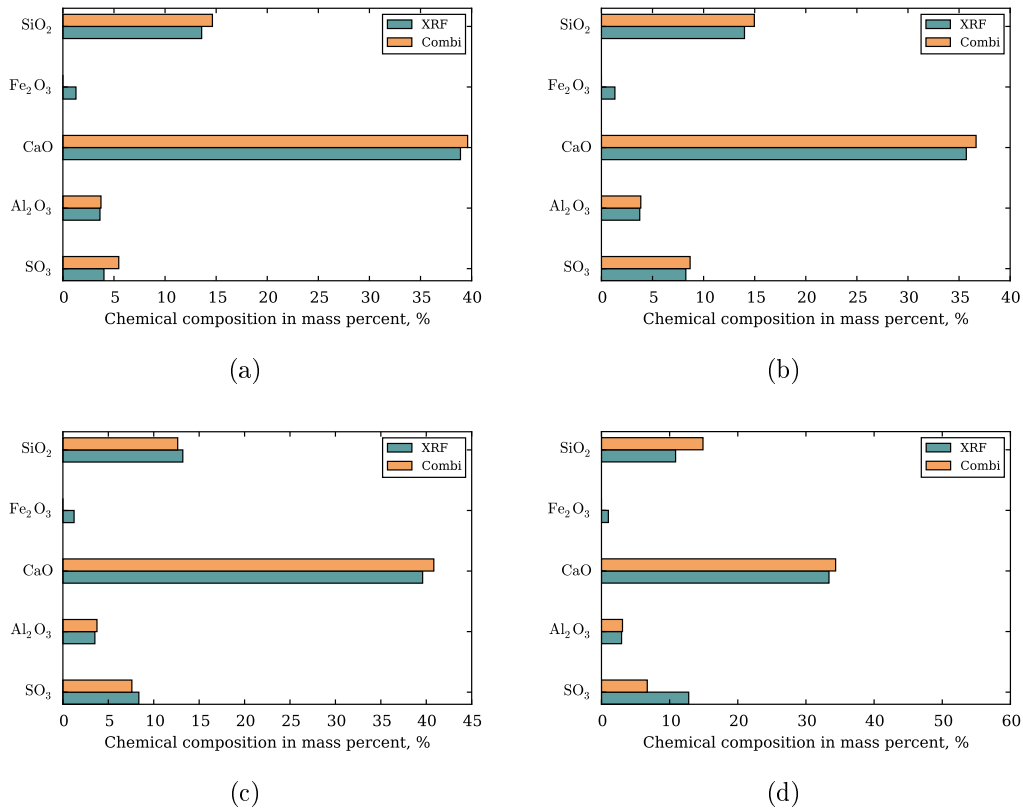


Figure 5.2: Chemical composition after testing, back-calculated from the phase assemblage given in Tab. 5.2, and determined by XRF: (a) OPC-3, (b) OPC-3-66 (c) OPC 66, and (d) OPC-1190.

## 5.3 Results and discussion

For the 4 tested samples, we measured the evolution of radial stress and axial stress over time. In parallel of each injection of sulfate solution, we measured the volume and concentration of the injected and output solutions. Based on such measurements, we determined the amount of sulfate remaining in the sample after each injection of solution. Additionally, we performed thermodynamic modeling to find out the relationship between stress development and formation of phases in the materials, in particular of ettringite and gypsum. In this section, those results are described and discussed.

### 5.3.1 Qualitative description of evolution of expansion stress

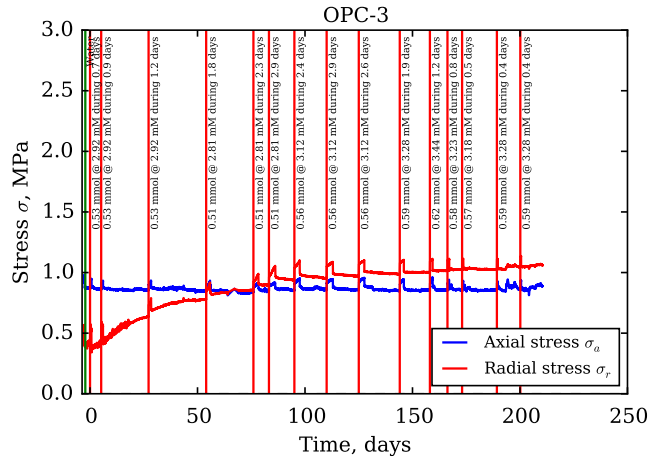
For the various experiments performed, the evolutions of the radial stress  $\sigma_r$  and of the axial stress  $\sigma_a$  are displayed in Fig. 5.3 and 5.4, and the evolutions of the mean stress  $\sigma = (2\sigma_r + \sigma_a)/3$  are displayed in Fig. 5.5 and 5.6.

In all experiments, during the duration of the injection (of either water or solution), one observes that both the radial and axial stresses, and hence the mean stress, increased by a few hundreds of kPa. Such increase is a classical poroelastic effect induced by the increase of fluid pressure in the porosity: the magnitude of this increase is consistent with the magnitude of the pressure of injection, which was 500 kPa.

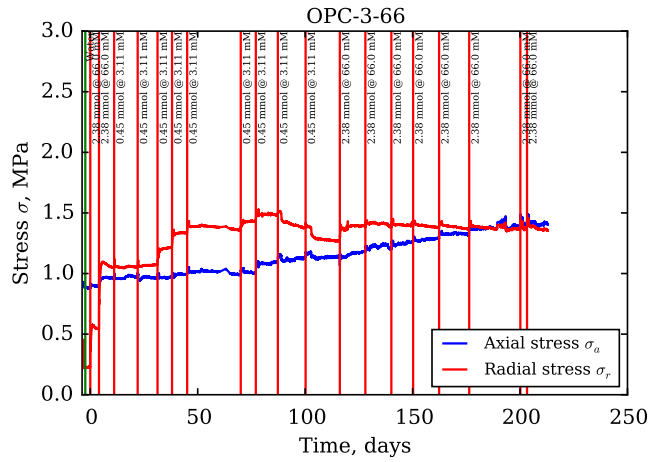
For all experiments, after the injection of water, both radial and axial stresses remained quite steady. The injections of solution led to a build-up of mean expansion stress, and more injections led to a larger expansion stress. The first injections led to a larger increase of expansion stress than the latter ones. That the expansion stress reaches a plateau is not clear: even the last injections of solution seem to lead to a slight increase in expansion stress.

After each injection of solution, the increase of expansion stress started right after the injection: actually, a close look at Fig. 5.5 (a) shows that the expansion stress started increasing even during the injection, when this injection lasted several days. How fast the expansion stress stabilized with

### 5.3. RESULTS AND DISCUSSION



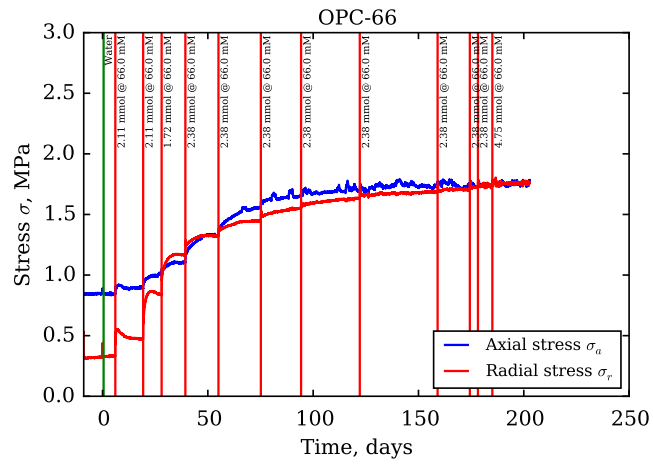
(a)



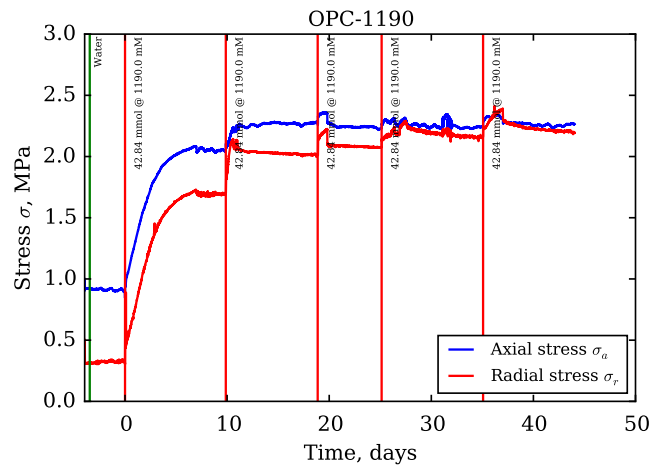
(b)

Figure 5.3: Evolution of stresses induced by injection of sodium sulfate solution for experiments (a) OPC-3 and (b) OPC-3-66.

CHAPTER 5. ISOCHORIC STUDY OF FACTORS GOVERNING EXPANSION STRESS



(a)

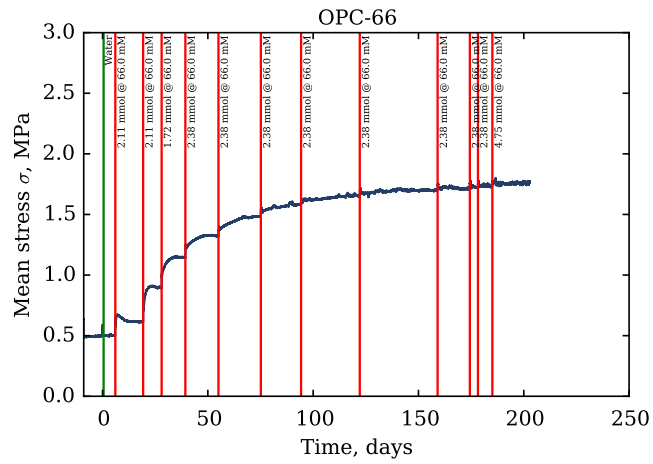


(b)

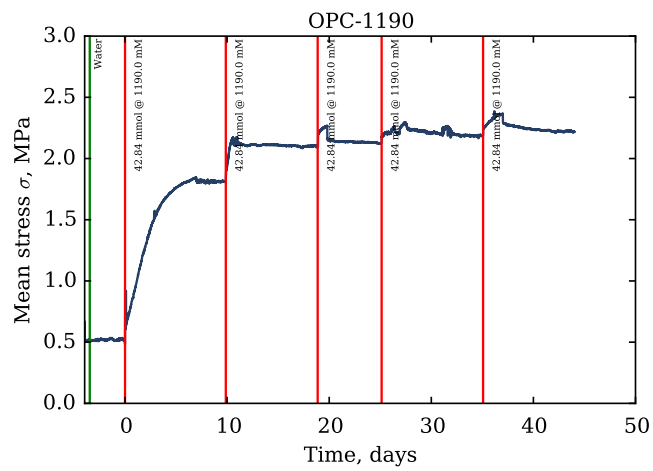
Figure 5.4: Evolution of stresses induced by injection of sodium sulfate solution for experiments (a) OPC-66 and (b) OPC-1190.



## CHAPTER 5. ISOCHORIC STUDY OF FACTORS GOVERNING EXPANSION STRESS



(a)



(b)

Figure 5.6: Evolution of mean stress induced by injection of sodium sulfate solution for experiments (a) OPC-66 and (b) OPC-1190.

time after the injection of solution depended significantly on the experiment: for sample OPC-1190, after each injection the stresses stabilized in a few days; for samples OPC-66 and OPC-3-66, the expansion stresses stabilized within a week after the first injections, but seemed not to stabilize after several weeks after the latter injections; for sample OPC-3, even after the first injection of solution, the expansion stresses seemed to have not stabilized even after a few weeks. Once those mean stresses get stabilized, we assume that the sample is no longer supersaturated and reached thermodynamic equilibrium (see Sec. 4.4).

Before the first injection of solution, for all samples, the axial stress was greater than the radial stress, as a consequence of the process of compaction (see Sec. 5.2). The first injections of solution led to a greater increase of radial stress than of axial stress, until radial and axial stresses roughly become equal; then the increases in radial and axial stresses became quite similar. At late stage, the stresses in sample OPC-66, OPC-1190, as results displayed in Fig. 5.4, were clearly greater than the typical tensile strength of intact cementitious materials about 1.7 MPa (Flatt and Scherer, 2008). In the extreme case of OPC-3, we actually observed only an increase of radial stress and no increase of axial stress (but during the injections of fluid themselves), so that, eventually, the radial stress even became greater than the axial stress. We will discuss in greater details those questions of stress anisotropy in Sec. 5.3.2.

Having a closer look at the evolution of the mean stress right after each of the first two injections into samples OPC-66 and OPC-3-66, the evolution was clearly nonmonotonic: the mean stress reached a maximum a few days after the injection, and then decreased back toward an asymptotic value. In contrast, for most other injections, once the injection was over, the stress increased quite monotonically with time.

The mean stress as a function of the normalized amount of sulfate injected in the sample is displayed in Fig. 5.7 and 5.8, where the normalized amount is defined as the sum of the molar amount of sulfate initially present in the sample with the molar amount of sulfate injected in the sample, divided by the molar amount of aluminates initially present in the sample.

## CHAPTER 5. ISOCHORIC STUDY OF FACTORS GOVERNING EXPANSION STRESS

---

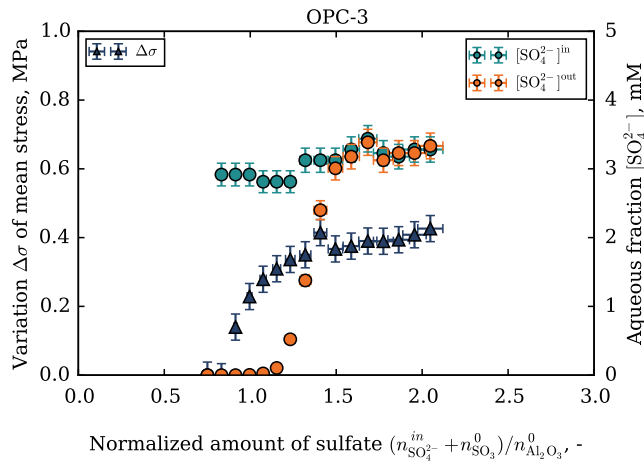
This figure shows that the increase of the expansion stress increased more with the amount of injected sulfate early in the experiment than late in the experiment. The magnitude of expansion stress at the end of the experiment was about 0.4 MPa for sample OPC-3, about 1 MPa for samples OPC-66 and OPC-3-66, and about 1.5 MPa for sample OPC-1190. Sorting each experiment according to the total amount of injected sulfate yields: OPC-3, OPC-66 and OPC-3-66, and OPC-1190. Sorting each experiment according to the maximum concentration of the injected solution yields also: OPC-3, OPC-66 and OPC-3-66, and OPC-1190. Therefore, it is unclear whether the magnitude of the final expansion stress is governed rather by the total amount of injected sulfate or by the concentration of those injected sulfates.

Only sample OPC-3-66 was subjected to injections of solutions at various concentrations. Figure 5.8 (b) shows that, after 2 injections at 66 mM, the first 8 injections at 3 mM led to an increase of expansion stress, but the last 2 injections at this latter concentration led to a decrease of expansion stress. During those first 8 injections, interestingly, we note that the rate of increase of the expansion stress with respect to the injected amount of sulfate was the same as during the injections at 66 mM. Part of the decrease observed over the last 2 injections at 3 mM was recovered over the subsequent injections at 66 mM.

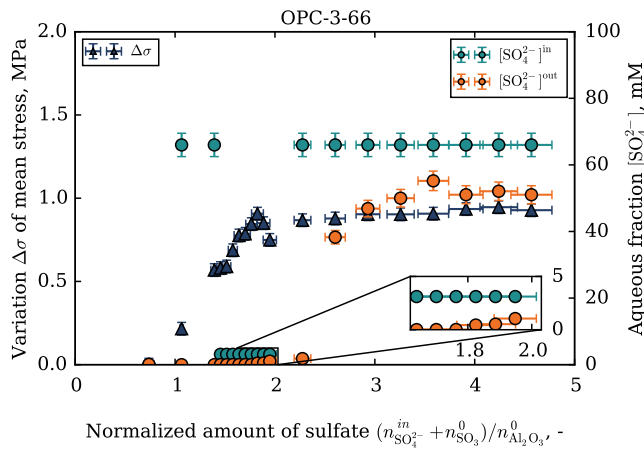
### 5.3.2 Evolution of anisotropy of stresses

Results in Figs. 5.9 and 5.10 display how the axial and radial stresses evolved with the injected amount of sulfates. Initially, the axial stress was greater than the radial stress, because the sample was prepared by axial compaction (see Sec. 2.2). For all samples, the total variation of radial stress along the experiment was greater than the total variation of axial stress.

For experiments OPC-66 and OPC-1190, in the early stage of the experiment the radial stress increased more than the axial stress, until the stresses became isotropic: then, the stresses remained isotropic, i.e., the evolutions of radial and axial stresses were identical. Over the experiment OPC-3, the axial stress remained constant, while the radial stress increased and even overshot



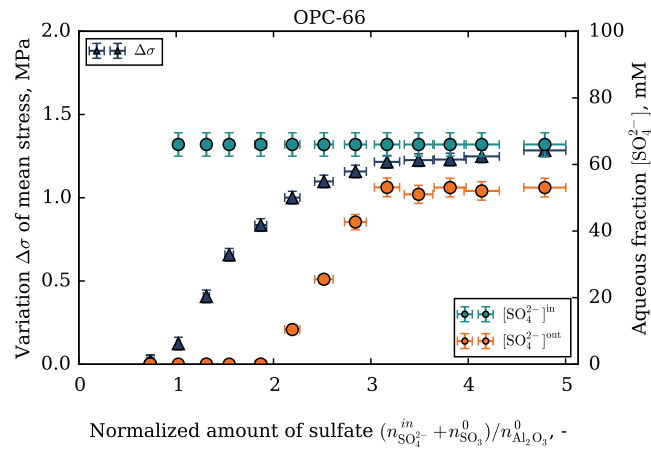
(a)



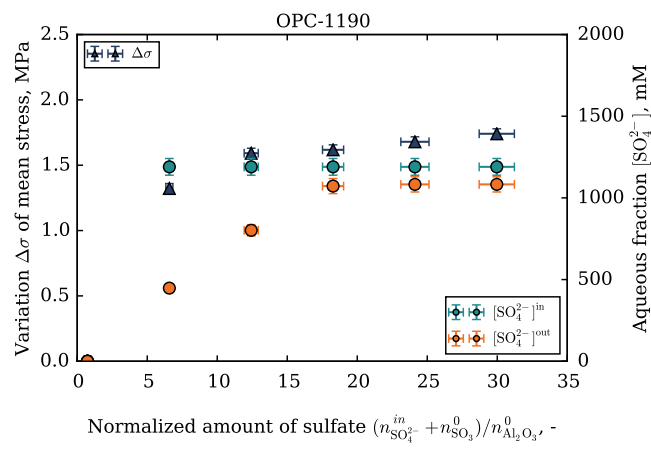
(b)

Figure 5.7: Variation of mean stress and aqueous fraction of the output solution versus the normalized amount of sulfate injected for experiments (a) OPC-3 and (b) OPC-3-66.

CHAPTER 5. ISOCHORIC STUDY OF FACTORS GOVERNING EXPANSION STRESS



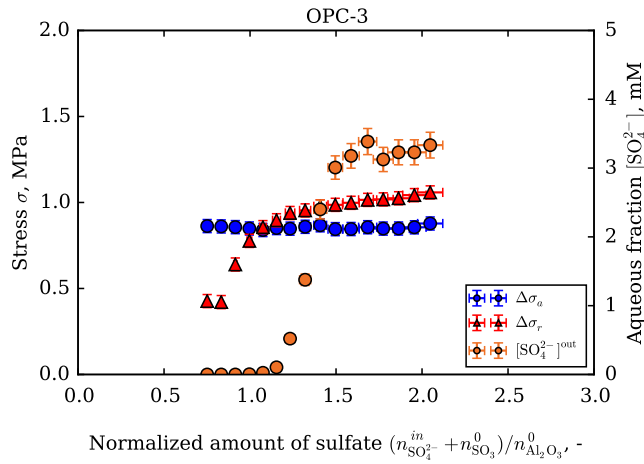
(a)



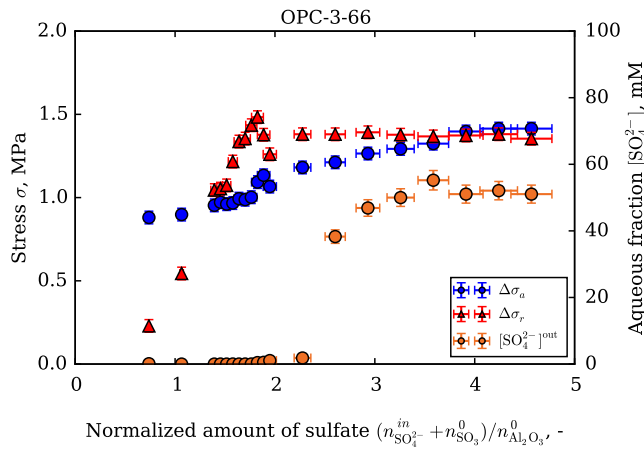
(b)

Figure 5.8: Variation of mean stress and aqueous fraction of the output solution versus the normalized amount of sulfate injected for experiments (a) OPC-66 and (b) OPC-1190.

### 5.3. RESULTS AND DISCUSSION



(a)

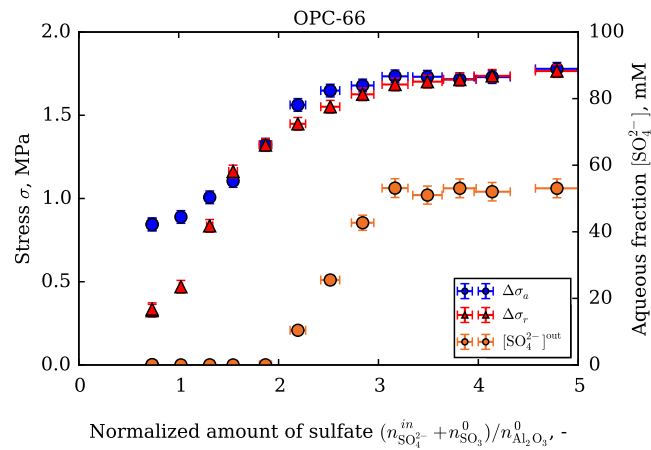


(b)

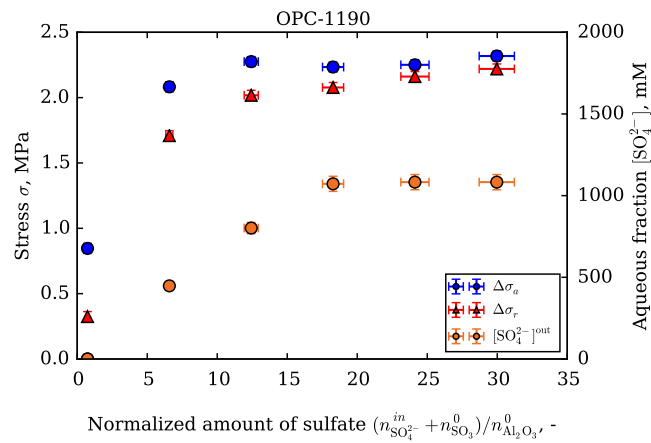
Figure 5.9: Variations of axial and radial stress versus the normalized amount of injected sulfate for experiments (a) OPC-3 and (b) OPC-3-66.

CHAPTER 5. ISOCHORIC STUDY OF FACTORS GOVERNING EXPANSION STRESS

the axial stress. For experiment OPC-3-66, the radial stress increased and overshoot the axial stress, but then stopped increasing: in consequence, one observes that, in the late stage of this experiment, the state of stresses also became isotropic. For all experiments but OPC-3, the state of stresses became isotropic roughly when the concentration of the output solution reached a plateau.



(a)



(b)

Figure 5.10: Variations of axial and radial stresses versus the normalized amount of injected sulfate for experiments (a) OPC-66 and (b) OPC-1190.

This isotropization of the stresses suggests that the forming crystals

preferred inducing an expansion stress in the direction that was the least stressed.

Actually, this suggestion could also explain the fact that, in oedometric testing, an axial expansion was observed only after a threshold volume of crystals had precipitated (see Sec. 4.4.3). Indeed, in oedometer testing also, because of the compaction needed to prepare the sample, the radial stress was initially lower than the axial stress. Therefore, upon their formation, the crystals may have preferred pushing first in the direction of the lower stress (i.e., in the radial direction) before pushing as well in the axial direction, hence yield a threshold volume of crystals formed below which no expansion could be observed.

### 5.3.3 Qualitative description of evolution of output concentration

Figures 5.7 and 5.8 display the concentration of the output solution with respect to the normalized amount of injected sulfate. For all 4 experiments, the trends are identical: early in the test, the output concentration was close to zero (i.e., the output concentration was much smaller than the concentration of the injected solution), and, late in the test, a plateau was observed with a non-zero magnitude.

The fact that, early in the stage, the output concentration was close to zero means that, during the first injections in the test, almost all sulfate remained in the sample. We infer from this observation that, for those injections, the characteristic time of capture of the sulfate ions by the solid matrix of the sample was much smaller than the characteristic time of transfer throughout the sample.

The magnitude of the plateau of the output concentration observed late in the stage depended on the concentration of the injected solution. When the concentration of the injected solution was 3 mM (see Fig. 5.7 (a)), the magnitude of this plateau was also 3 mM, i.e., late in the test, all sulfate entering the sample exited the sample. When this concentration was 66 mM (see Fig. 5.7 (b) and 5.8 (a)), the magnitude of this plateau was around 51 mM.

## CHAPTER 5. ISOCHORIC STUDY OF FACTORS GOVERNING EXPANSION STRESS

---

When this concentration was 1190 mM (see Fig. 5.8 (b)), the magnitude of this plateau was 1080 mM.

In Fig. 5.7 and 5.8, all values are displayed with respect to the normalized amount of injected sulfate. The normalized amount of injected sulfate at which the output concentration varied significantly depended on the concentration of the injected solution. When this concentration was 3 mM (see Fig. 5.7 (a)), variations of output concentration were observed when this normalized amount reached values comprised between 1.2 and 1.7. In contrast, when this concentration was 66 mM (see Fig. 5.7 (b) and 5.8 (a)), variations of output concentration were observed when this normalized amount reached values comprised between 1.8 and 3.2. For the experiment performed with injections at 1190 mM (see Fig. 5.8 (b)), variations of output concentration were observed at least when this normalized amount was in the range from 6 to 13.

Figures 5.7 and 5.8 also display the expansion stress induced by each injection: for each injection, the displayed expansion stress is in fact the expansion stress measured right before the following injection. For all experiments, as long as the output concentration was zero, the expansion stress increased linearly with the normalized amount of injected sulfates. In the range over which the output concentration varied significantly, the expansion stress increased less significantly with the normalized amount of injected sulfates than when the output concentration was zero. Once the output concentration reached its non-zero plateau, the subsequent increases in expansion stress were tiny but non negligible, in the sense that, injection after injection, the expansion stress did not quite reach a plateau, but went on increasing.

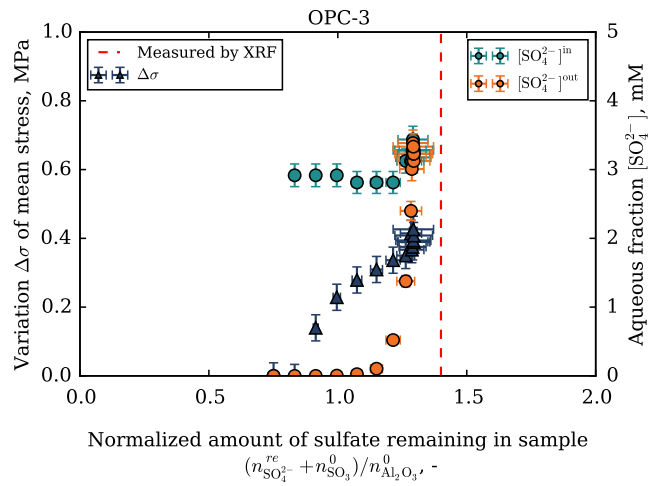
Such observations suggest that there exists a relationship between the expansion stress and the concentration in sulfates of the output solution. Based on thermodynamic modeling, we will shed some light on this relationship in Sec. 5.3.5. Before doing so, however, rather than aiming at correlating the measured expansion stresses with the amount of sulfates injected into the sample as was done in this section, we will aim at correlating those expansion stresses with the amount of sulfates remaining in the sample: such study will be the focus of the next section.

### 5.3.4 Role of amount of sulfate in sample

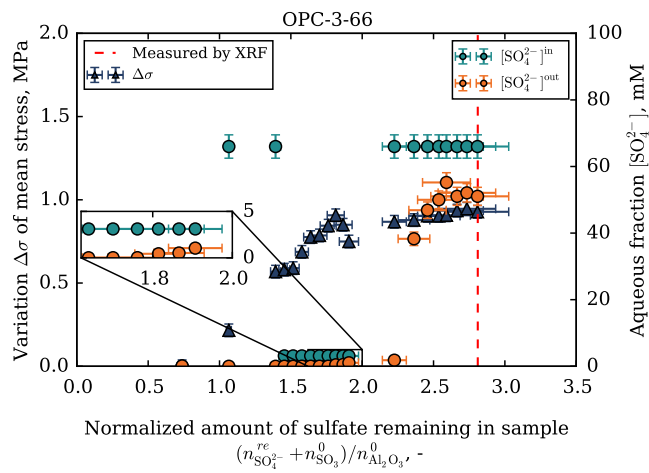
For each injection of sulfate solution, measurements of the volume of the injected solution and of the concentrations of the injected and output solutions allowed us to determine the amount of sulfate added to the sample by this injection, as  $V^{in} \times ([\text{SO}_4^{2-}]^{in} - [\text{SO}_4^{2-}]^{out})$ , where  $V^{in}$ ,  $[\text{SO}_4^{2-}]^{in}$ , and  $[\text{SO}_4^{2-}]^{out}$  stand for the volume of injected solution, the concentration in sulfate of the injected solution, and the concentration in sulfate of the output solution, respectively. By summation over the injections, we thus obtained, after each injection, the total molar amount  $n_{\text{SO}_4^{2-}}^{re}$  of sulfate added to the sample by the injections. Figures 5.11 and 5.12 display the expansion stress with respect to the normalized amount of sulfate remaining in the sample, which is defined as the sum of this molar amount  $n_{\text{SO}_4^{2-}}^{re}$  of sulfate added to the sample by the injections with the molar amount of sulfate initially present in the sample, divided by the molar amount of aluminates initially present in the sample.

At the end of each test, we measured the molar ratio  $n_{\text{SO}_3}/n_{\text{Al}_2\text{O}_3}$  of sulfates to aluminates by XRF: this measured ratio is indicated as red dashed lines in Figs. 5.11 and 5.12. For samples injected with solutions at 3 mM or 66 mM (see Figs. 5.11 and 5.12 (a)), the ratio determined by XRF was in very good agreement with the ratio predicted from the measurements of concentrations of the injected and output solutions. In contrast, for the sample injected with solutions at 1190 mM (see Fig. 5.12 (b)), the ratio determined by XRF was significantly lower than the ratio predicted from the measurements of concentrations of the injected and output solutions. The reason for this discrepancy is that the measurements of concentrations of the injected and output solutions takes into account not only the sulfates present within the solid matrix of the sample under the form of various sulfate phases (e.g., AFt, AFm, C $\text{S}\text{H}_2$ ), but also the sulfates dissolved in the pore fluid (i.e., in an aqueous form). For the experiments OPC-3, OPC-66, and OPC-3-66, the contribution of those sulfates from the pore solution was negligible. But, for sample OPC-1190, this contribution was non-negligible, which explains the difference of about 30% between the ratio measured by XRF and the one measured from the volumes and concentrations of injected and output

CHAPTER 5. ISOCHORIC STUDY OF FACTORS GOVERNING EXPANSION STRESS



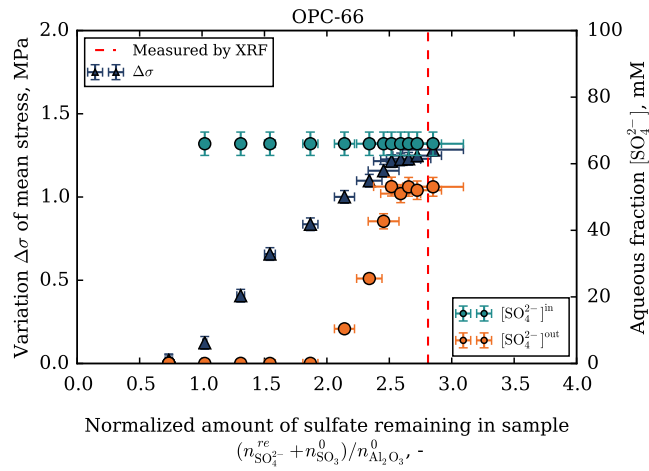
(a)



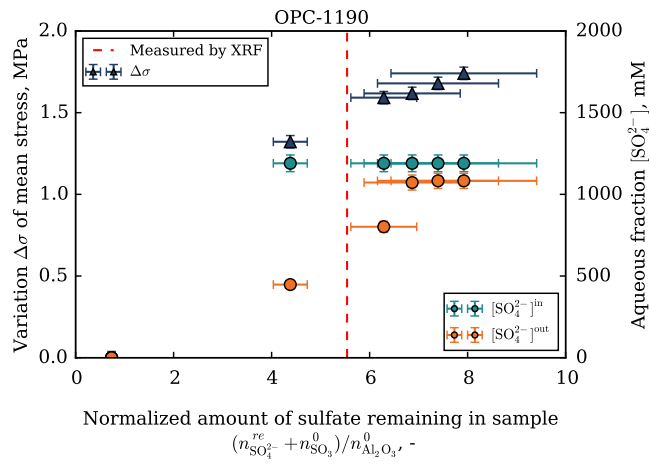
(b)

Figure 5.11: Variation of mean stress versus the normalized amount of sulfate remaining in the sample for experiments (a) OPC-3 and (b) OPC-3-66.

### 5.3. RESULTS AND DISCUSSION



(a)



(b)

Figure 5.12: Variation of mean stress versus the normalized amount of sulfate remaining in the sample for experiments (a) OPC-66 and (b) OPC-1190.

## CHAPTER 5. ISOCHORIC STUDY OF FACTORS GOVERNING EXPANSION STRESS

---

solutions.

Most features that were observed in Figs. 5.7 and 5.8 can also be observed in Figs. 5.11 and 5.12, although some differences can be noted. In particular, for sample OPC-3 (see Fig. 5.11 (a)), in the late stage of the test, vertical asymptotes are observed, which are a direct consequence of the fact that the output concentration was equal to the concentration of the injected solution, and therefore that no sulfate was added to the sample over the last injections. Also, more clearly than in Figs. 5.7 and 5.8, we observe on Figs. 5.11 and 5.12 that, even when the output concentration had reached a plateau in the late stage of any of the 4 experiments, the expansion stress never reached a plateau and went on increasing, injection after injection. We also note that, in this study, we focus only on the stage when the stresses reached a plateau, which we consider happened when all supersaturation vanished and thermodynamic equilibrium was reached, as discussed in Sec. 4.4.

How the mean stress evolved with the normalized amount of sulfate remaining in the sample is displayed for all samples in Fig. 5.13. We observe that, for all samples, the expansion stress increased with the normalized amount of sulfate remaining in the sample, and that this increase was a bilinear function, as indicated by the black and red dashed lines in the figure. Interestingly, the slope of those two dashed lines depended neither on the sulfate concentration of the injected solution, nor on the profile of injection (i.e., on the volumes of injected solution). Note that the ratio of the slopes of the black to red dashed lines is equal to about 9.0, which is close to  $708/75 = 9.4$ , which is the ratio of the molar volume of ettringite to the molar volume of gypsum. A comparison with the results displayed in Figs. 5.11 (b), 5.12 and 5.13 shows that, for samples OPC-3-66, OPC-66, and OPC-1190, the kink in the bilinear function displayed in Fig. 5.13 was observed for the injections over which the output concentration varied significantly. For sample OPC-3, no kink was observed on Fig. 5.13: the expansion stress was roughly a linear function of the amount of sulfate remaining in the sample.

Although the slope of the two linear portions of the bilinear relation displayed in Fig. 5.13 did not depend on the profile of injection, the intercept between those two linear portions did depend on the profile of injection:

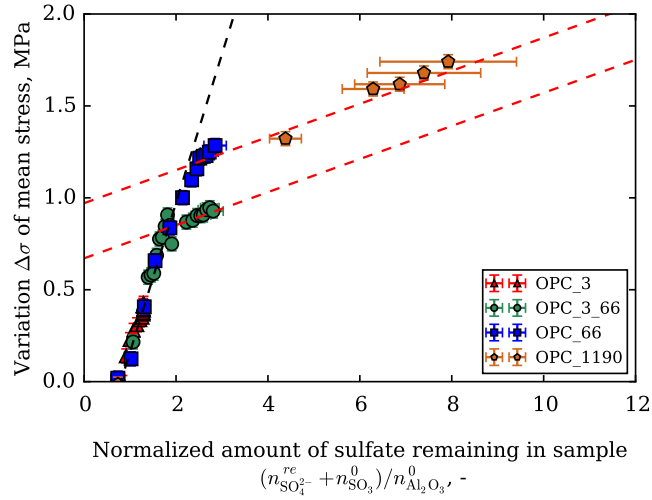


Figure 5.13: Variation of mean stress versus the normalized amount of sulfate remaining in the sample for experiments OPC-3, OPC-66, OPC-3-66, and OPC-1190.  $n_{\text{SO}_4}^{\text{re}}$  stands for the cumulated amount of sulfate remaining in sample,  $n_{\text{SO}_3}^0$  and  $n_{\text{Al}_2\text{O}_3}^0$  stand for the initial amounts of  $\text{SO}_3$  and  $\text{Al}_2\text{O}_3$  in the sample, respectively.

indeed, for sample OPC-3-66, the kink occurred at a normalized amount of remaining sulfate (and hence at an expansion stress) lower than for samples OPC-66 and OPC-1190. Such observation will be discussed more detail in Sec. 5.3.7.

In summary, we can conclude that the amount of sulfate remaining in the sample is an important factor governing the expansion stress: the expansion stress was recognized as a bilinear function of this amount, and the slope of the two linear portions was independent of the sulfate concentration or of the profile of injection of the solution. Also, the kink in how the expansion stress depended on the amount of sulfate remaining in the sample occurred when the sulfate concentration of the output solution varied significantly.

### 5.3.5 Evolution of phase assemblage and relationship with output sulfate concentration

In this section, we aim at explaining the magnitude of the output concentration observed in the early and late stages of the various experiments (see Section 5.3.3).

Following the method presented in Sec. 2.4.2, from the amount of sulfate injected in each sample, we calculated how the phase assemblage evolved upon sulfate injection. The initial phase assemblage of the various samples indicated in Tab. 5.2 was introduced as input data for the thermodynamic modeling. The results are displayed in Figs. 5.14 and 5.15. The thermodynamic calculations also provided the sulfate aqueous fraction of the solution in thermodynamic equilibrium with the predicted phase assemblage. This aqueous fraction, together with the measured concentration in sulfates of the output solution, is also displayed in Figs. 5.14 and 5.15.

One observes that the predicted sulfate aqueous concentrations are in very good agreement with the sulfate concentrations of the output solution, in the sense that the thermodynamic calculations predict the plateaus in sulfate concentrations observed at both the smallest and the largest amounts of injected sulfate considered. Also, the thermodynamic calculations correctly predict the magnitude of these plateaus. This observation makes it possible to conclude that, at both the smallest and the largest amounts of injected sulfates considered, the output solution was in equilibrium with the solid phases and, therefore that the thermodynamic modeling, performed under the hypothesis of thermodynamic equilibrium, will make it possible next to shed some light on the magnitude of those plateaus. In contrast, in the range of intermediate amounts of injected sulfates, over which the sulfate concentration of the output solution varies from one plateau to the other, the agreement is less satisfactory: the thermodynamic calculation predicts a much steeper variation of the sulfate concentration than is observed experimentally. One can conclude that, in this range, the hypothesis of thermodynamic equilibrium between the output solution and the solid phases of the sample is less reasonable.

### 5.3. RESULTS AND DISCUSSION

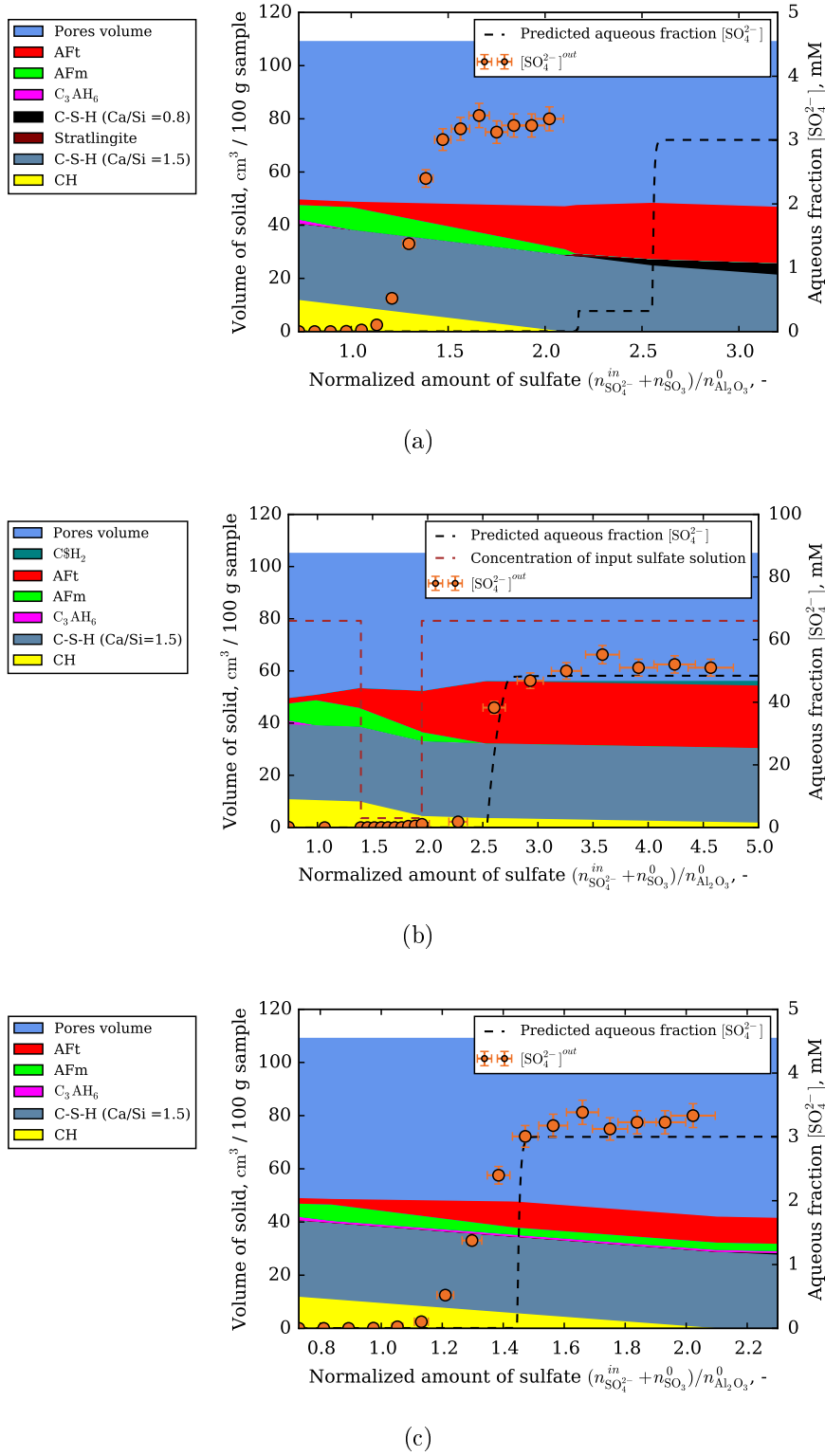
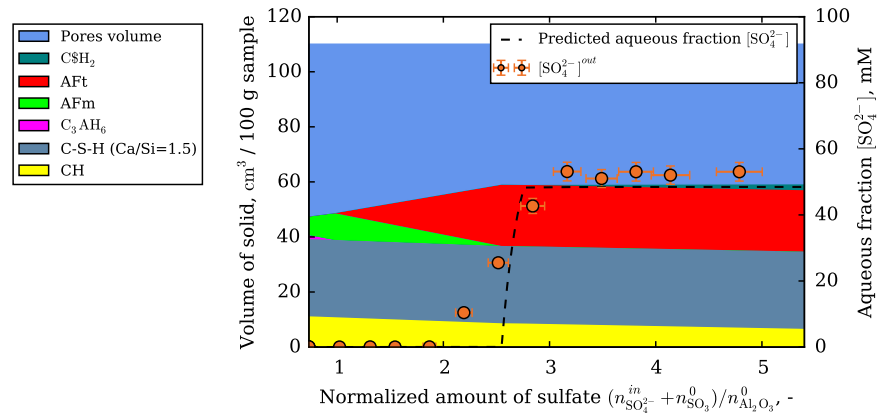
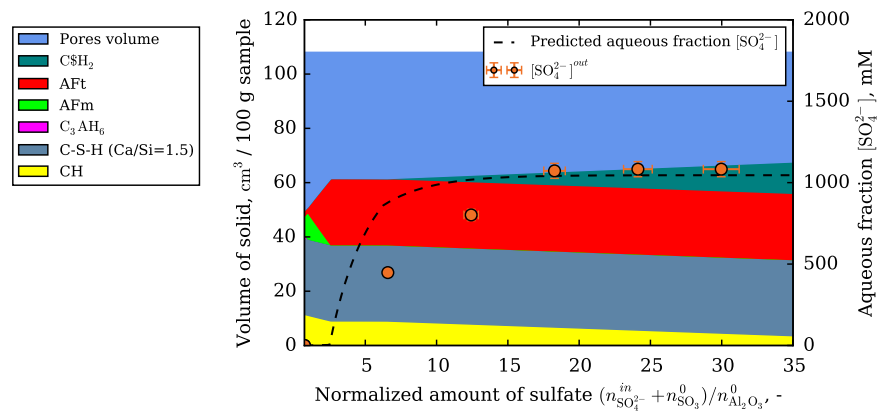


Figure 5.14: Evolution of phase assemblages and aqueous fractions of output solution for experiments (a) OPC-3 when assuming  $\alpha = 1$  (where  $\alpha$  is defined in Eq. (5.1) and (5.2)), (b) OPC-3-66, and (c) OPC-3 when assuming  $\alpha = 0.4$ .

CHAPTER 5. ISOCHORIC STUDY OF FACTORS GOVERNING EXPANSION STRESS



(a)



(b)

Figure 5.15: Evolution of phase assemblages and aqueous fractions of output solution for experiments (a) OPC-66 and (b) OPC-1190.

The thermodynamic calculations show that, for all experiments, the output concentration remained much smaller than the concentration of the injected solution until all AFm reacted. In fact, during this stage, the predicted sulfate aqueous concentration was inferior to 0.1 mM. The thermodynamic calculations also predicted that the concentration of the output solution in the late stage of the experiments depended on the concentration of the injected solution. For sample OPC-3, which was subjected to injections of solution at a concentration of 3 mM, the predicted sulfate aqueous fraction, once all AFm and stratlingite had reacted, was equal to 3 mM. No gypsum was created at any time during the experiment and, in this late stage, any injection of sulfate led to a consumption of C-S-H with a Ca/Si ratio of 1.5 and to a production of C-S-H with a Ca/Si ratio of 0.8, i.e., led to a decalcification of C-S-H. For samples OPC-3-66, OPC-66, and OPC-1190 which were subjected to injections of solution at a concentration of 66 mM (for samples OPC-3-66 and OPC-66) or of 1190 mM (for sample OPC-1190), the sulfate aqueous fraction reached a plateau of 48 mM (for samples OPC-3-66 and OPC-66) and of 1172 mM (for sample OPC-1190) once gypsum started being produced: in the late stage of those experiments, any injection of sulfate led to a consumption of portlandite and to a production of gypsum.

For all samples but OPC-3, the thermodynamic modeling predicted well the amount of injected sulfate at which the concentration of the output solution varied significantly. In contrast, for sample OPC-3, the thermodynamic modeling overestimated this amount, by a factor of about 2. A detailed study of this discrepancy will be performed in Sec. 5.3.6.

Table 5.5 provides the normalized amounts of aluminate phases (i.e., AFm, AFt and  $C_3A_6$ ) and of gypsum at the end of all experiments, as predicted from thermodynamic modeling. For comparison, this table also provides the amount of those same phases, as measured with the method ‘Combi’ after the experiments. For what concerns the aluminate phases (i.e., AFt, AFm,  $C_3AH_6$ ), thermodynamic predictions were in very good agreement with the experimental results. In contrast, the estimated amount of gypsum obtained from thermodynamic modeling was slightly greater than the measured one, at least for samples OPC-3-66 and OPC-66. In case of

## CHAPTER 5. ISOCHORIC STUDY OF FACTORS GOVERNING EXPANSION STRESS

sample OPC-1190, the thermodynamic modeling can also explain that the underestimation of the amount of  $\text{SO}_3$  given by method ‘Combi’, as shown in Fig. 5.2 (d), may be due to the underestimation of the amount of gypsum which was characterized experimentally by XRD, as already mentioned in Sec. 4.3.2.

Materials	$\text{C}_3\text{AH}_6$		AFm		AFt		$\text{C}\$\text{H}_2$	
	Model	Combi	Model	Combi	Model	Combi	Model	Combi
OPC-3	0.0	1.4	6.5	7.3	33.3	23.7	0.0	0.0
OPC-3-66	0.0	0.0	0.0	1.2	40.3	42.0	3.2	1.0
OPC-66	0.0	0.8	0.0	0.9	37.1	36.5	3.2	0.0
OPC-1190	0.0	1.1	0.0	0.7	33.4	29.7	17.0	2.1
OPC-3 ( $\alpha=0.4$ )	2.3	1.4	6.8	7.3	21.3	23.7	0.0	0.0

Table 5.5: Mass fraction of aluminate and sulfate phases, as predicted by thermodynamic modeling (label ‘Model’) and as characterized with the method ‘Combi’. The parameter  $\alpha$  is defined in Eq. (5.1) and (5.2).

Figure 5.16 displays the chemical composition of the samples after testing, as obtained from XRF measurements, and as predicted from thermodynamic modeling. For what concerns this chemical composition, for samples OPC-3-66, OPC-66, and OPC-1190, predictions from thermodynamic modeling are in good agreement with chemical composition from XRF, but for CaO and  $\text{SiO}_2$ . This difference may be due to the lack of data concerning the phase C-(A)-S-H used in this thermodynamic modeling, or it may also be due to the fact that the thermodynamic modeling did not capture the presence of the calcium carbonate formed within the materials (see Tab. 5.2), a problem already mentioned in Sec. 2.5.1. In addition, we note that, for sample OPC-3 only (see Fig. 5.14 (a)), the thermodynamic modeling significantly overestimated the amount of sulfate in the sample. A more detailed scrutiny of this sample is presented in the next section.

In the present work, we considered in our thermodynamic modeling that both solid and aqueous phases are at ambient pressure. But, during the isochoric experiments, the mean stress applied to the material was non-zero. To study the effect of any potential mechanical stress applied to the solid phases on the microstructure and mineralogy evolutions, we did the following: we assumed that all solid phases were under an identical pressure (i.e., volumet-

### 5.3. RESULTS AND DISCUSSION

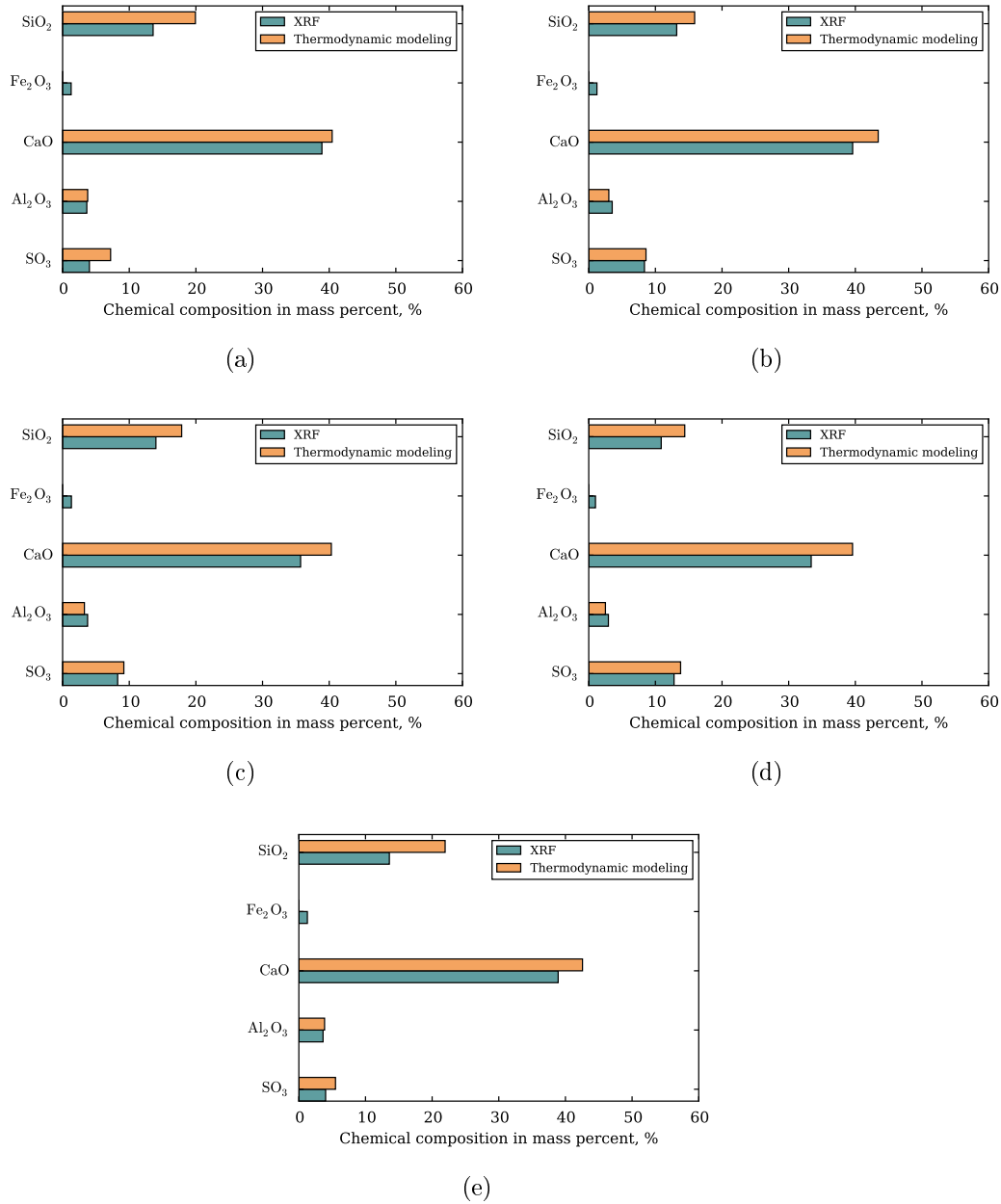


Figure 5.16: Chemical composition after testing, obtained with thermodynamic modeling and XRF for samples (a) OPC-3, (b) OPC-66, (c) OPC-3-66, (d) OPC-1190, and (e) OPC-3 when assuming  $\alpha = 0.4$  (where  $\alpha$  is defined in Eq. (5.1) and (5.2)).

ric stress) equal to the atmospheric pressure, to 1.5 MPa, or to 2.7 MPa, but that the aqueous phases remained at atmospheric pressure; the solubility of the various solid phases was modified through Eq. (1.6); the mineralogical evolution of sample OPC-66 was predicted by thermodynamic modeling with those modified solubilities. The results of those calculations are displayed in Fig. 5.17. The predicted aqueous fractions  $[\text{SO}_4^{2-}]$  are much less satisfactory when the solid phases are considered not at atmospheric pressure than when the solid phases are considered at atmospheric pressure: indeed, the output sulfate concentrations at early stage are significantly greater than zero, while the ones at late stage are significantly lower than the measured ones. Therefore, we conclude that, in our thermodynamic modeling, considering the effect of the mechanical stress on the solid phases is not essential and can even be detrimental to predict mineralogy and microstructure changes. A potential explanation for this conclusion is that equilibrium is not significantly affected by stresses in the bulk of the solid, but is affected by the normal stress at the solid-liquid interface (Sekerka and Cahn, 2004; Flatt et al., 2011): therefore, since in our present work the liquid pressure remains close to atmospheric pressure, one understands why performing thermodynamic modeling by considering that the solid phase remains at atmospheric pressure would be most appropriate. However, a better understanding of the consequences of mechanical stresses on microstructure and mineralogy evolutions in general remains an interesting topic for further studies.

### 5.3.6 Evolution of phase assemblage: the specific case of OPC-3

Mostly for sample OPC-3, the thermodynamic modeling could not predict correctly the evolution of the sulfate concentration of the output solution (see Fig. 5.14 (a)). In addition, the thermodynamic predictions overestimated the amount of sulfate (i.e.,  $\text{SO}_3$ ) within the material (see Fig. 5.16 (a)). Table 5.5 also shows that there was a significant difference between the mass fraction of AFt predicted with thermodynamic modeling and the measured one. In addition, as shown in Tab. 5.2, Tab. 5.3, the amount of ettringite formed in

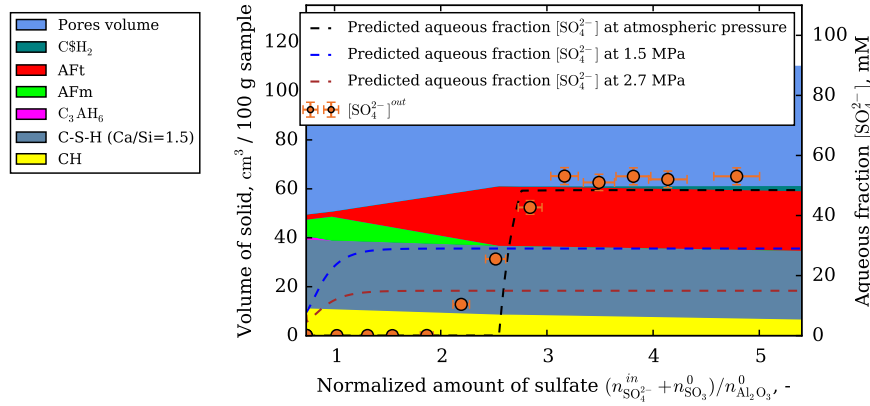


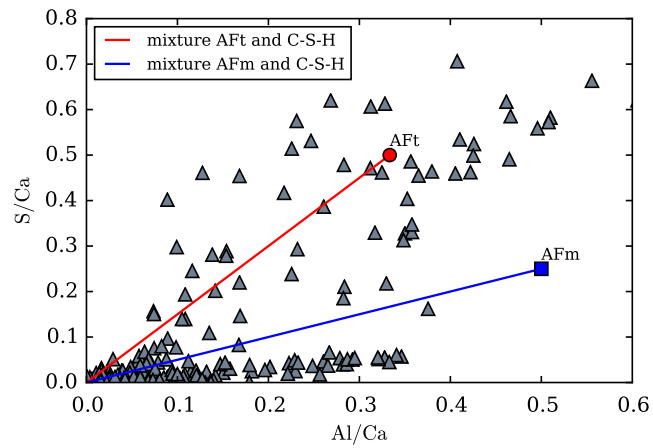
Figure 5.17: Evolution of aqueous fractions of output solution for experiment OPC-66 predicted by thermodynamic modeling with solid phases submitted to atmospheric pressure, 1.5 MPa and 2.7 MPa. The aqueous phases are at atmospheric pressure in those calculations. The evolution phase assemblage here displayed is the one predicted with calculations at atmospheric pressure.

sample OPC-3 was significantly lower than in samples OPC-3-66, OPC-66, and OPC-1190.

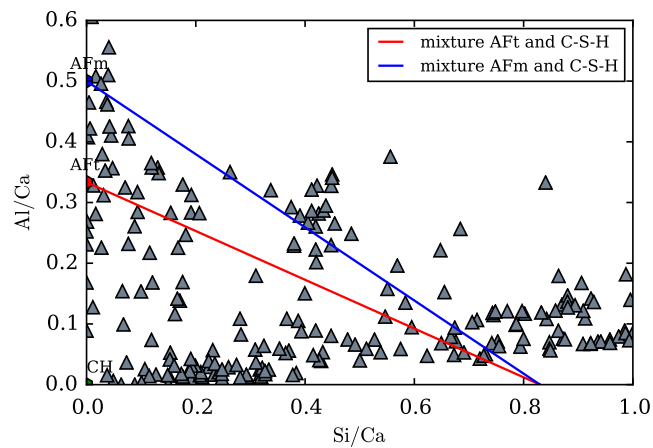
By using the SEM-EDS technique described in [Scrivener \(2004\)](#) on sample OPC-3 after testing, the results displayed in [Fig. 5.18](#) show numerous points located on the tie line AFm, from which we conclude that a significant amount of AFm remained in the sample, intermixed with C-S-H. Therefore, in this experiment for which the concentration of the injected solution was equal to 3 mM, only part of AFm reacted with the injected sulfate ions to form ettringite. In addition, the results displayed in [Fig. 5.18 \(b\)](#) show the existence of numerous points with ratio Si/Ca superior to 0.81 (i.e., ratio Ca/Si close to 1.23), which means that part of the C-(A)-S-H present in sample OPC-3 became decalcified. The existence of considerable mixtures of C-S-H and AFm after testing in the sample exposed to solution at 3 mM may be due to several reasons, such as: a lower concentration gradient could make diffusion of sulfates into the cement grains slower, or a lower concentration may not grant access to all the AFm. Regarding this latter point, indeed, CHES calculations show that the injections of a solution at 3 mM lead to a maximal saturation index SI (see [Eq. \(2.9\)](#)) with regard to ettringite equal

CHAPTER 5. ISOCHORIC STUDY OF FACTORS GOVERNING EXPANSION STRESS

to 5.67 which is lower than the one resulting from the injections of solution at 66 mM and at 1190 (maximal SI equal to 7.19<sup>1</sup>): that supersaturation (SI=5.67) may be not sufficient for the transformation into AFt of the AFm located in small pores such as the ones of the C-(A)-S-H gel (Scherer, 1999; Flatt, 2002b).



(a)



(b)

Figure 5.18: SEM-EDS analysis of sample OPC-3: (a) Ratio Al/Ca against to S/Ca and (b) Ratio Si/Ca against Al/Ca.

<sup>1</sup>the precipitation of gypsum is assumed in those calculations.

We now introduce a parameter  $\alpha$  defined as the molar fraction of  $C_3AH_6$  and AFm initially present in the sample that can react with the injected sulfates, i.e.:

$$n_{C_3AH_6}^{reactive} = \alpha n_{C_3AH_6}^{total} \quad (5.1)$$

$$n_{AFm}^{reactive} = \alpha n_{AFm}^{total} \quad (5.2)$$

where  $n_{C_3AH_6}^{reactive}$  and  $n_{AFm}^{reactive}$  stand for the reactive molar amount  $C_3AH_6$  and AFm, respectively;  $n_{C_3AH_6}^{total}$  and  $n_{AFm}^{total}$  stand for the total molar amount of  $C_3AH_6$  and AFm (which are determined by the method ‘Combi’), respectively. We assume that  $\alpha$  is equal to the fraction of AFm initially present in the material that can react with the injected sulfates, and that  $\alpha$  is also the fraction of  $C_3AH_6$  initially present in the material that can react with the injected sulfates. The remaining fraction of the aluminate phases (which represent a fraction  $1-\alpha$  of all aluminates initially present in the sample) were considered inert (i.e., unable to participate to chemical reactions) in the thermodynamic modeling.

For this sample OPC-3 after injection, in order for the mole fraction of ettringite within  $Al_2O_3$  predicted by thermodynamic modeling to be equal to the mole fraction of ettringite measured with  $^{27}Al$ -NMR, we needed to consider in the thermodynamic model that only 40% of the AFm and  $C_3AH_6$  initially present in sample OPC-3 was reactive. Therefore, for this sample, we repeated the thermodynamic predictions, by considering that only 40% of the AFm and  $C_3AH_6$  it contained initially could react, and that the remaining 60% were inert. In this case, the initial amounts of AFm and  $C_3AH_6$  used as input data of the thermodynamic model for 100 g of sample, instead of being equal to 11.1 g and 3.8 g, respectively, were considered to be equal to 4.4 g and 1.5 g, respectively. The results of these alternative predictions are displayed in Fig. 5.14 and Tab. 5.5. We observe that this alternative prediction is now in much better agreement with the experimental data, for all microstructural features considered: the predicted amounts of ettringite and sulfate  $SO_3$  in the sample after testing compared well with the experimental results; the

## CHAPTER 5. ISOCHORIC STUDY OF FACTORS GOVERNING EXPANSION STRESS

---

evolution of the aqueous fraction  $\text{SO}_4^{2-}$  correlated better with the measured evolution of the output sulfate concentration than if all aluminates were considered reactive. Therefore, it really seems that, in our OPC sample, when the concentration of the injected sulfate solution was as low as 3 mM, not all AFm was reactive. In contrast, when the concentration of the injected sulfate solution was greater than 3 mM (i.e., 66 mM or 1190 mM), we could consider that all AFm and  $\text{C}_3\text{AH}_6$  was reactive. From now on, the thermodynamic modeling will be performed by considering that, for sample OPC-3 (and for this sample only), only 40% of the AFm and  $\text{C}_3\text{AH}_6$  initially present was reactive. For the other samples (i.e., OPC-3-66, OPC-66 and OPC-1190), we will consider that all AFm and  $\text{C}_3\text{AH}_6$  can react.

In summary, the phase assemblage and chemical composition predicted from thermodynamic modeling showed a good agreement with the measured ones, but for sample OPC-3, for which we needed to consider that only part of the aluminates initially present in the sample was reactive. Also, thermodynamic modeling made it possible to retrieve the evolutions of the sulfate concentration of the output solution. These results suggest that the output solution is in thermodynamic equilibrium with the solid phases of the material. Furthermore, thermodynamic modeling makes it possible to relate the sulfate concentration of the output solution to the mineralogy of the sample and thus to relate the evolutions of the expansion stress to the mineralogical evolutions (and in particular to the formation of ettringite and gypsum). This is a significant progress in comparison with usual protocols of sulfate-induced expansion testing, in which, because of gradients induced by the propagation of a front, relating the expansion to a mineralogical evolution is not an easy task.

### 5.3.7 Role of formed solid phases

This section is dedicated to the study of how the development of expansion stresses is correlated with the precipitation of the various phases. Figures 5.19 and 5.20 display the evolutions of the phase assemblage and of the expansion stress for the various experiments. At first glance, the development

### 5.3. RESULTS AND DISCUSSION

of expansion stresses seems to occur mostly during the early stage of the experiment (i.e., when ettringite precipitates), and only slightly during the late stage of the experiment (i.e., when gypsum precipitates). For experiment OPC-1190, the development of expansion stress during the late stage of the experiment is slightly more visible than for the other experiments: in this experiment, more gypsum precipitated than in the other ones.

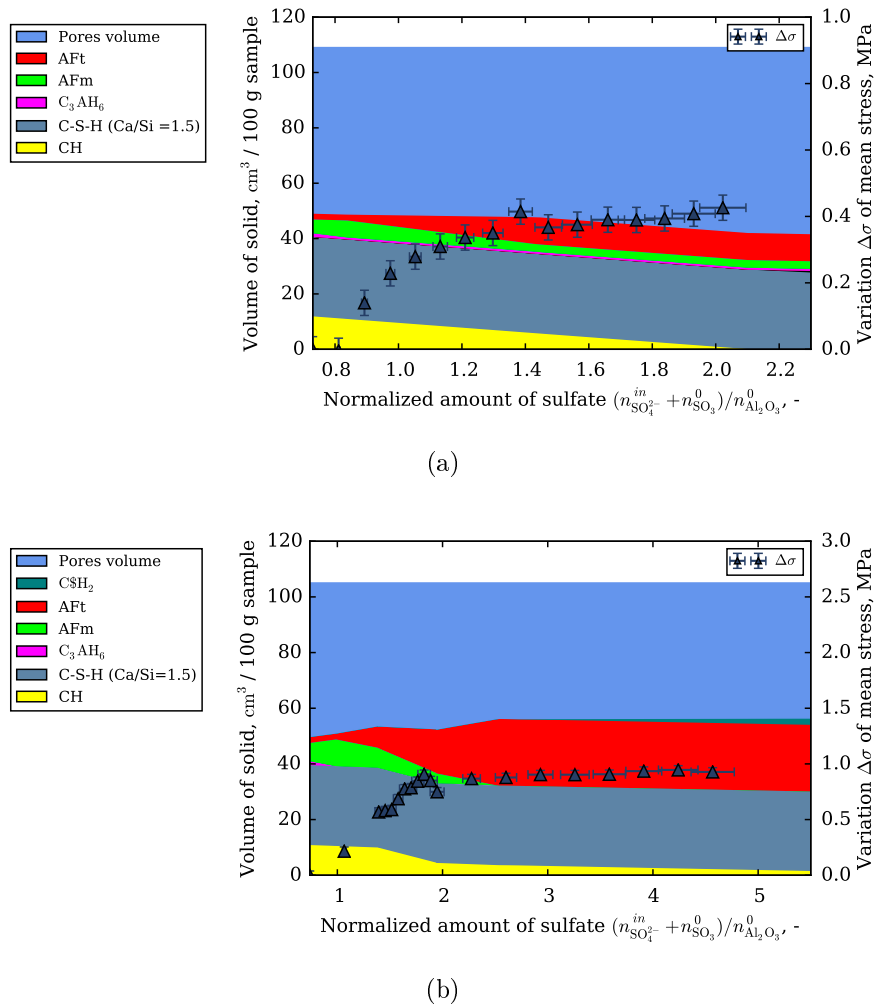
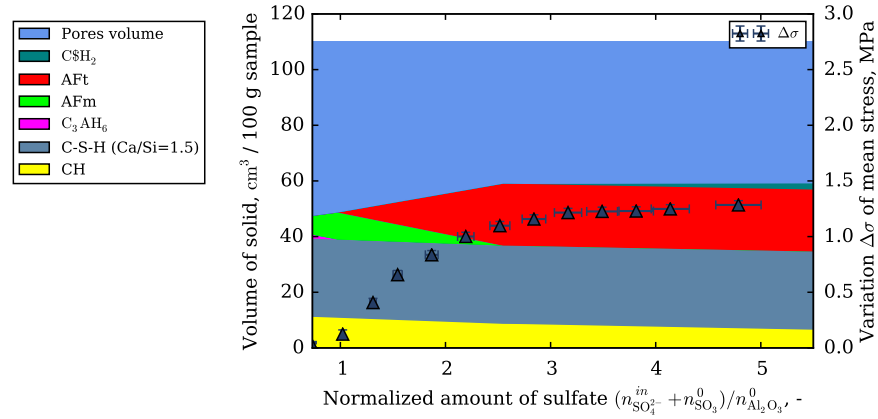


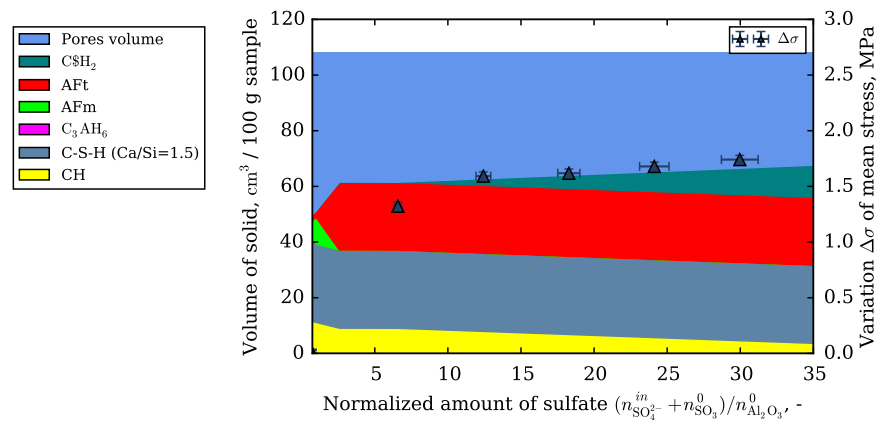
Figure 5.19: Evolution of phase assemblages and variation of mean stress for experiments (a) OPC-3 (when assuming  $\alpha=0.4$ ) and (b) OPC-3-66.

Based on the predicted phase assemblages displayed in Figs. 5.19 and 5.20 and on the knowledge of the density of all produced phases, we calculated

CHAPTER 5. ISOCHORIC STUDY OF FACTORS GOVERNING EXPANSION STRESS



(a)



(b)

Figure 5.20: Evolution of phase assemblages and variation of mean stress for experiments (a) OPC-66 and (b) OPC-1190.

how the total volume of the solid phases evolved upon injection. As shown in Fig. 5.21, for experiments OPC-66 and OPC-1190, the total volume of solid phases increased with the expansion stress. In contrast, for experiment OPC-3-66, the expansion stress did not evolve monotonically with the total volume of solid phases. And, even more surprisingly, for experiment OPC-3, when the expansion stress increased, the total volume of solid phases decreased mainly due to CH dissolution. Therefore, the development of expansion stresses cannot be explained by an increase of the total volume of solid phases.

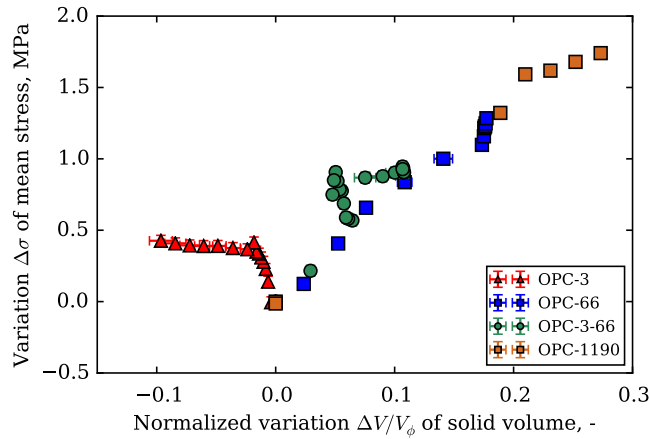


Figure 5.21: Variation of mean stress versus the normalized variation of solid volume, during experiments OPC-3, OPC-66, OPC-3-66, and OPC-1190.

How the expansion stress varied with the normalized amount of ettringite is displayed in Fig. 5.22 (a), in which the volume of ettringite formed was normalized with the initial volume of pores. In the early stage of all experiments, all data points became aligned on a same master curve, which was a line whose slope was 3.42 MPa. For experiments OPC-66 and OPC-1190, the data points started departing from this master curve when no more ettringite could be formed, thus the vertical alignment of the data points. In contrast, for experiment OPC-3-66, the data points started departing from the master curve at a moment while more ettringite could still precipitate: this departure occurred after the concentration of the injected solution was increased from 3 mM to 66 mM. Such observation may be explained by the

## CHAPTER 5. ISOCHORIC STUDY OF FACTORS GOVERNING EXPANSION STRESS

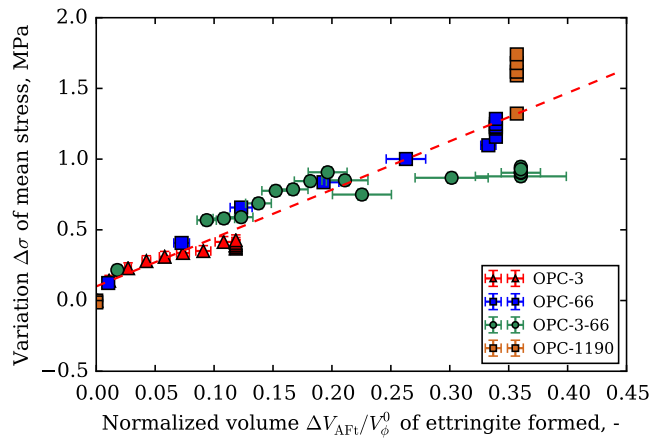
---

fact that some ettringite might form in space where CH dissolved. However, this phenomenon is not fully understood, but it is worth noting that this is the unique case where gypsum precipitates after almost of CH has been leached out.

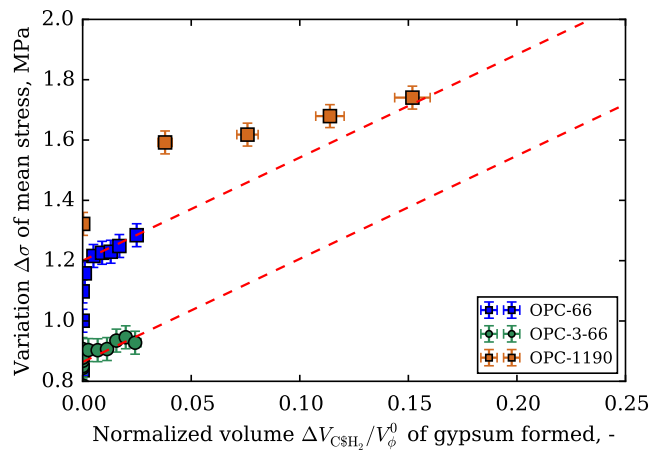
We performed an SEM-EDS analysis of the material OPC before testing (more precisely, of the reference sample OPC-66), and of the various OPC samples after testing. Figure 5.23, which displays the results obtained on material OPC before testing, shows a considerable amount of points located on the tie line AFm (blue line), which indicates the existence of an intimate mixture of AFm with the C-S-H gel. After testing, we could observe both pockets of ettringite (see Fig. 5.24 for an SEM picture of sample OPC-66) and an intimate mixture of ettringite with the C-S-H gel (see Fig. 5.25 for an SEM-EDS analysis of samples OPC-3-66 and OPC-66). Out of the ettringite having precipitated into the pockets or into the C-S-H gel, it is not possible to determine whether one kind or the other induced the development of the expansion stress.

In the late stage of the experiments OPC-66, OPC-3-66, and OPC-1190, even when all ettringite that could precipitate had precipitated, a development of the expansion stress was still observed (see the vertically aligned data points in the late stage of the experiments displayed in Fig. 5.22 (a)). Figure 5.22 (b) shows that this development could be explained by the precipitation of gypsum, since in the late stage of all experiments but of OPC-3 (during which no gypsum precipitated), the expansion stress increased quite linearly with the normalized volume of gypsum formed. Interestingly, the slope of this linear trend appears to be quite similar to the value determined for ettringite, i.e., 3.42 MPa. This similarity is confirmed by Fig. 5.22 (c), which displays the expansion stress versus the normalized combined volume of formed ettringite and gypsum: on this figure, but for experiment OPC-3-66, all data points appear to be quite aligned along a unique master line. In addition, gypsum started precipitating and inducing an expansion stress while the sample underwent a mean stress greater than 1.5 MPa (see Fig. 5.6): such observation makes it possible to conclude that gypsum could induce an expansion stress in a compacted ground material under a quite high stress.

### 5.3. RESULTS AND DISCUSSION



(a)



(b)

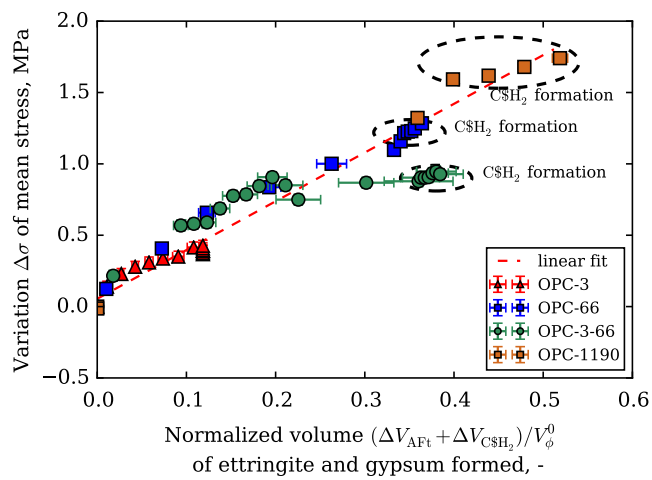


Figure 5.22: Variation of mean stress versus the normalized volume of (a) formed ettringite, (b) formed gypsum, and (c) formed ettringite and gypsum. On all figures, the slope of the dashed lines is 3.42 MPa.

CHAPTER 5. ISOCHORIC STUDY OF FACTORS GOVERNING EXPANSION STRESS

---

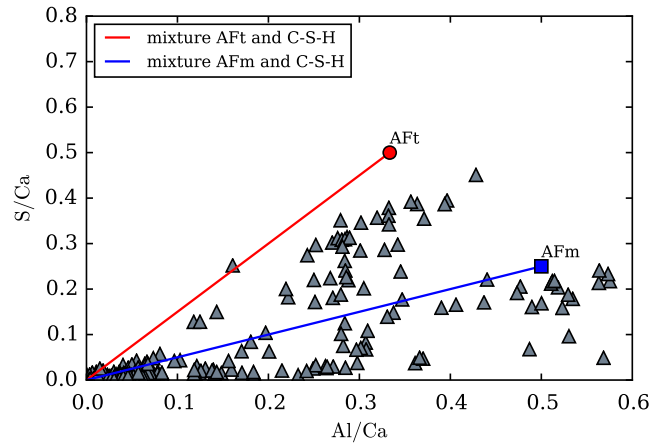


Figure 5.23: SEM-EDS analysis of material OPC before testing (i.e., before injection of solution). An intimate mixture of AFm with the C-S-H gel is observed in this material.

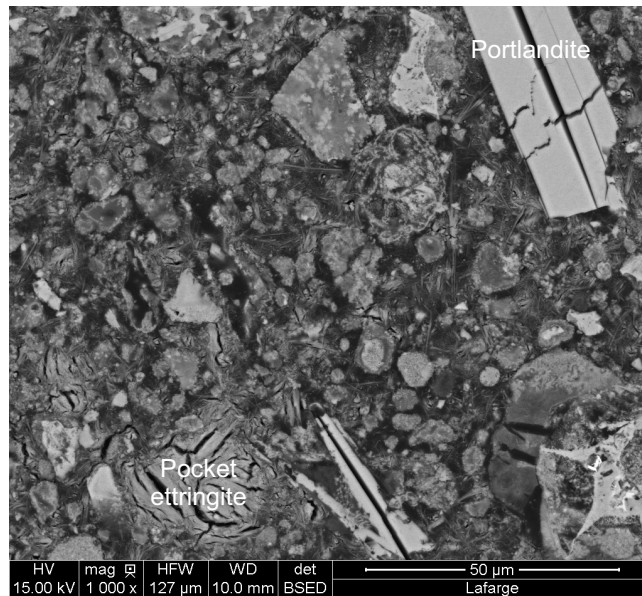
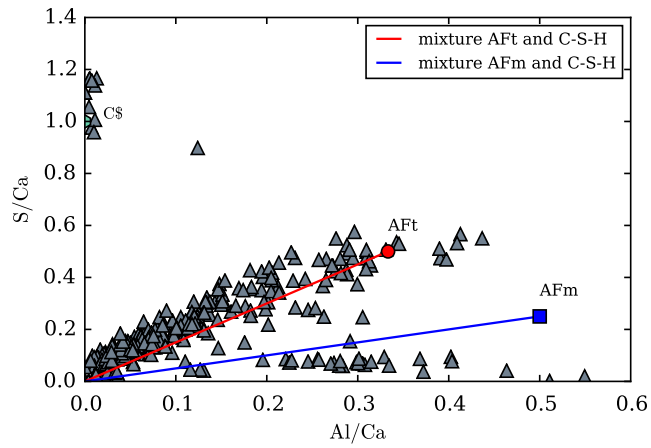
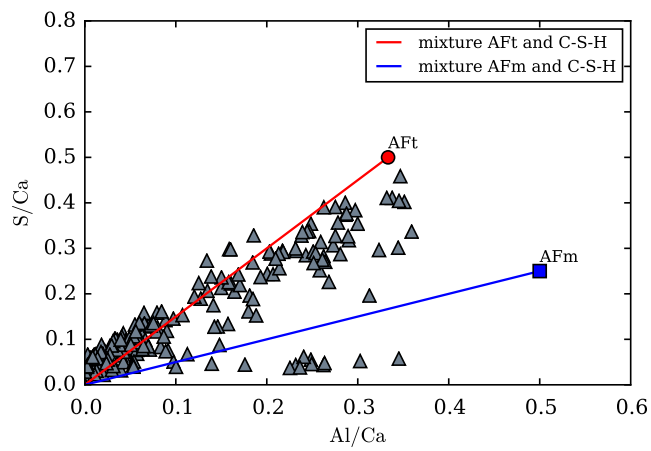


Figure 5.24: SEM picture of sample OPC-66 after testing (i.e., after injection of solution). Pockets of ettringite are observed.



(a)



(b)

Figure 5.25: SEM-EDS analysis of samples (a) OPC-3-66 and (b) OPC-66, after testing. An intimate mixture of AFt with the C-S-H gel is observed in these samples.

CHAPTER 5. ISOCHORIC STUDY OF FACTORS GOVERNING EXPANSION STRESS

We recall that, here, to remain consistent with what was done in the previous chapters, all thermodynamic calculations were performed by inputting into CHESS the injected amounts of sulfates. However, since in this chapter we measured the amounts of sulfates having remained in the sample, we could as well have used those amounts as inputs for the thermodynamic modeling: actually, doing so yields Fig. 5.26, on which the linear dependence of the expansion stress on the combined volume of ettringite and gypsum formed appears still more clearly than in Fig. 5.22 (c). In most cases, it appears that ettringite and gypsum both contribute to the development of expansion stress to a same extent, if this development is considered by unit volume of crystal formed.

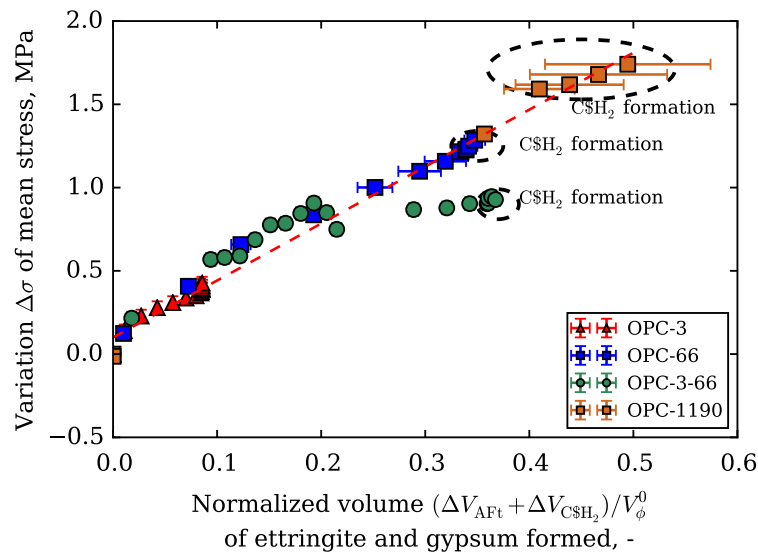


Figure 5.26: Variation of mean stress versus the normalized volume of formed ettringite and gypsum, where the evolutions of phase assemblage were calculated based on the measured amounts of sulfates remained in the sample. On all figures, the slope of the dashed lines is 3.42 MPa.

In summary, the fact that the expansion stress increases does not always mean that the total volume of solids in the sample increases: we show that, sometimes, this total volume decreased. We showed here that the expansion stress in our compacted ground material was a linear function of the vol-

umes of ettringite and gypsum formed. Therefore, the main factor governing expansion was the amount of sulfates remaining in the sample, not the concentration of the injected solution. The precipitation of a given volume of gypsum induced the same development of expansion stress as the precipitation of an identical volume of ettringite. However, how those crystals would induce an expansion stress in intact cementitious materials is still an open question.

## 5.4 Conclusions

The following conclusions can be drawn:

- The isochoric cells that we developed make it possible, while keeping the sample at constant volume, to measure both the axial and radial stresses exerted by the sample on the walls of the cell. Another salient feature of the cell is that all solution exiting from the sample can be collected, thus making it possible to determine the amount of sulfate remaining in the sample.
- In presence of sulfates, so-called expansion stresses are observed. The present experimental procedure allows us not only to observe those expansion stresses very quickly, but also to investigate how the evolutions of those expansion stresses are related to mineralogical evolutions (i.e., formation of ettringite and gypsum).
- Upon the consecutive injections and crystallizations, we observed that the stresses tended to become isotropic. In other words, the expansion stress increased more in the direction of lower stress (i.e., here, in the radial direction) than in the direction of higher stress.
- For the most part of the experiments, the output solution seems to be in thermodynamic equilibrium with the solid phases of the sample.
- The amount of sulfate remaining in the sample was shown to be an important factor governing the expansion of cementitious materials.

## CHAPTER 5. ISOCHORIC STUDY OF FACTORS GOVERNING EXPANSION STRESS

---

In our compacted ground material, the magnitude of the expansion stresses was an increasing and bilinear function of the amount of sulfate remaining in the sample. The ratio of those slopes (here equal to 9.0) is close to the one of molar volume of ettringite to the molar volume of gypsum.

- The development of expansion stresses cannot be explained by an increase in the total volume of the solid phases. Such explanation was one of the theories used to explain the expansion of unconstrained cement-based materials subjected to sulfate solution.
- In our compacted ground material, both ettringite and gypsum could induce an expansion stress. The recognition of the ability of gypsum to induce an expansion stress is consistent with the study performed in Chap. 4, in which we observed that, in oedometric conditions, gypsum could induce an expansion. But, again, whether such conclusion would hold in an intact cementitious material still remains an open question.
- In our compacted ground material, the expansion stress was a linear function of the volume of ettringite and gypsum formed. Both ettringite and gypsum contributed to the development of the expansion stress to a same extent, in the sense that the precipitation of a given volume of gypsum induced the same development of expansion stress as the precipitation of an identical volume of ettringite. Here again, whether the same conclusion could be reached for intact cementitious materials is unclear: how ettringite and gypsum crystals would induce an expansion stress in a significantly stronger material is still an open subject.

## Chapter 6

### Conclusions and perspectives

## 6.1 Conclusions

The main objective of this study was to better understand the mechanisms behind the crystallization-induced expansion of cementitious materials submitted to sulfate attacks. To reach this objective, we developed an original experimental procedure consisting in working with ground cementitious materials compacted directly into an oedometer cell or an isochoric cell. The expansion or expansion stress was induced by flushing the sample with a sodium sulfate solution. We applied a variety of injection profiles to samples with a variety of compositions and mineralogies.

In the oedometric experiments, we measured the axial expansion of the samples, submitted to a constant axial stress and prevented from deforming radially. In the isochoric experiments, we measured the evolutions of the radial and axial stresses (which we coined ‘expansion stresses’) when the sample was prevented from deforming macroscopically. With our isochoric cells, we could recover all solution flushed through the sample: thanks to this feature, by measuring the concentrations and volumes of the injected and output solutions, we could determine the amount of sulfate remaining in the sample after each injection.

In terms of mineralogical and microstructural characterizations, we proposed a new method that we coined method ‘Combi’, which is based on data from XRF, XRD, TGA, and  $^{27}\text{Al}$ -NMR. With such method, we characterized the phase assemblage of the samples before and after testing. The evolutions of mineralogy induced by the injections were predicted by using thermodynamic modeling. These predictions made it possible to correlate the development of expansions or expansion stresses with mineralogical evolutions.

The conclusions are manifold, but can mainly be gathered into two categories: conclusions on methodology and protocol, and conclusions on the mechanisms of expansion of cement-based materials in presence of sodium sulfates.

### 6.1.1 Conclusions on methodology and protocol

The first remarkable result is that, by working with compacted ground samples in oedometric cells, the expansions induced by sulfate attacks could be observed much faster than with classical experiments in which cementitious samples are immersed in a sulfate solution. Such result is a direct consequence of the high permeability of the manufactured samples: their pore volume could be flushed in less than 1 hour (at the beginning of the experiments), and expansions started right after (or even during) the injection.

We also designed a new type of experiment to characterize the mechanical reaction of cementitious materials to sulfate attacks: experiments in isochoric cells. In those cells, we can measure the evolution of stresses in both axial and radial directions, when the sample is prevented from deforming macroscopically. Such experiment differs significantly from classical experiments in which a strain is measured, not a stress. To the best of our knowledge, our experiments made it possible to obtain the first direct measurement of a stress (coined ‘expansion stress’) induced by sulfate attacks in compacted ground cementitious materials.

Postmortem analysis showed that, with the developed protocol, crystallization of ettringite occurred quite homogeneously in the sample. Such feature is another significant difference with classical experiments, for which sulfate ingress by diffusion induces significant gradients of concentration and mineralogy throughout the sample. However, this homogeneity is not fully understood, since, at least during the first injections, the concentration of the injected solution varied significantly across the height of the sample and was therefore heterogeneous: further study is needed to better understand how mineralogy and microstructure evolved within the sample over time. The observed homogeneity of phases might be due to phase redistributions or sulfate diffusion after the injection.

We also dedicated a significant effort to determine what the best method was to characterize the phase assemblage of our samples, before and after testing. The best method that we could figure out was the method that we coined method ‘Combi’, which is based on data from XRF, XRD, TGA, and

$^{27}\text{Al}$ -NMR. XRD consistently underestimated the amount of gypsum in our samples. Also, the amount of aluminate phases could be well determined by XRD when (and only when) the aluminate phases were not intimately mixed with the C-S-H gel.

Finally, we showed that thermodynamic modeling (here performed with CHESS) is a powerful tool to predict the evolutions of mineralogy resulting from injection of a sulfate solution.

### **6.1.2 Conclusions on mechanisms of expansion of cement-based materials in presence of sodium sulfates**

We showed that, in classical experiments, in which cementitious samples are immersed in a sulfate solution and for which expansions are only observed after several dozens of days, the reactions involved in the process are not the rate-limiting phenomenon. It is likely that, in such experiments, the rate-limiting phenomenon is the kinetics of transport (i.e., the diffusion of ions) throughout the sample, rather than the chemical reactions.

Strains result from a competition between crystallization-induced expansion, dissolution-induced shrinkage, and creep-induced shrinkage. In all samples that contained C-S-H, each injection of sodium sulfate solution induced an expansion. However, the presence of the C-S-H gel is not necessary to observe an expansion: a sample with no C-S-H swelled after an injection of solution, as a consequence of crystallization of ettringite.

In our compacted ground materials, the amount of sulfate remaining in the sample governs the expansion or the development of an expansion stress in cementitious materials subjected to sulfate attacks. The expansion stress is a monotonously increasing and bilinear function of the amount of sulfate remaining in the sample.

In isochoric testing, crystallization leads to an isotropic stress state after a certain amount of crystal is formed. Said otherwise, the expansion stress increases more in a less stressed direction than in a more stressed direction.

When ordinary cementitious materials are subjected to sodium sulfate solutions, first we observe crystallization of ettringite, and then crystalliza-

tion of gypsum. Both ettringite and gypsum can contribute to an expansion or to an expansion stress in our compacted ground materials.

For crystallization-induced expansions to be observed, the AFm initially present in the material does not need to be intimately mixed with C-S-H. Ettringite crystallizing outside C-S-H (i.e., pockets of ettringite) can induce an expansion or an expansion stress in our compacted ground materials.

Expansion cannot be merely explained by an increase in the total volume of the solid phase, although such theory is widespread in the literature. In fact, the expansion and expansion stress are affine or linear increasing functions of the combined volume of ettringite and gypsum formed. Said otherwise, in our compacted ground materials, ettringite and gypsum contribute equally to the phenomenon, in the sense that the crystallization of a given volume of gypsum induces the same ‘residual expansion’ or ‘residual expansion stress’ (see more details in Sec. 4.4) as the crystallization of an identical volume of ettringite.

In oedometric testing, we identified a threshold volume of crystal below which no axial expansion was observed. In isochoric testing, we observed no such threshold volume: the precipitation of any volume of ettringite or gypsum induced a mean expansion stress.

## 6.2 Perspectives

Perspectives can aim at alleviating some issues encountered, or at performing new developments.

The main issue we encountered in our study is that of carbonation, which occurred during the characterization of the samples. We can aim at getting rid of carbonation, or at better correcting for it when it happens. To limit carbonation, what could be done would be to dry the samples either by freezing-drying or at a temperature of 40°C under N<sub>2</sub> flow for 16 hours, and then storing them in desiccators to fully isolate them from the atmosphere: such drying protocol (Mantellato et al., 2015) is expected to better preserve the cement microstructure than the protocol used in the present study.

When carbonation occurred, for the characterization of the phase assem-

blage, the method ‘Combi’ could be improved by taking into account not only the carbonation of C-S-H, but also the carbonation of CH. For instance, we could use the following formulas to calculate the corrected amounts of CH and C-S-H:

$$m_{\text{CH}}^{\text{corrected}} = m_{\text{CH}}^0 + x m_{\text{C}\bar{\text{e}}}^0 \frac{M_{\text{Ca}(\text{OH})_2}}{M_{\text{CaCO}_3}} \quad (6.1)$$

$$m_{\text{C-(A)-S-H}}^{\text{corrected}} = m_{\text{C-(A)-S-H}}^0 + (1 - x) m_{\text{C}\bar{\text{e}}}^0 \frac{M_{\text{CaO}}}{M_{\text{CaCO}_3}} \quad (6.2)$$

where  $m_{\text{CH}}^{\text{corrected}}$  and  $m_{\text{C-(A)-S-H}}^{\text{corrected}}$  stand for the masses of CH and C-(A)-S-H after correction;  $m_{\text{CH}}^0$ ,  $m_{\text{C-(A)-S-H}}^0$ , and  $m_{\text{C}\bar{\text{e}}}^0$  stand for the masses of CH, C-(A)-S-H, and  $\text{C}\bar{\text{e}}$  before correction, respectively; the unknown parameter  $x$  lies in the range  $[0;1]$ ;  $M_{\text{X}}$  stands for the molar mass of compound X.

Thermodynamic modeling should be improved by taking into account the C-A-S-H gel: to do so, the thermodynamic properties of C-(A)-S-H must be known. But, to understand all experiments here performed, thermodynamic modeling (i.e., calculations performed by assuming thermodynamic equilibrium) may not be sufficient. In particular, when almost all AFm reacted, we observed that the thermodynamic model did not predict well how the concentration of the output solution varied: in such case, it may well be that capturing these evolutions would require the introduction of some kinetics (e.g., chemical reaction kinetics or kinetics of diffusion into particles).

In terms of future development, what is obviously needed is to find out expansion mechanisms that can explain all the phenomenology observed in the present study. Indeed, we gathered a significant amount of original data, obtained from experiments designed carefully, and analyzed thoroughly. We hope that this set of data will prove to be valuable food for thoughts and pave the way toward models (at the scale of representative elementary volume) of crystallization-induced expansions of cementitious materials that are more and more physically-based. An important step in this process is to assess what conclusions or mechanisms proposed in this manuscript remain valid for regular intact cementitious materials, whose strength is significantly larger than that of the compacted ground samples here tested.

# Appendix A

## Materials and Methods

### A.1 Behavior of the compacted powder materials

According to oedometer compaction described in Sec. [2.2.1](#), behavior of various material are displayed Fig. [A.1](#).

### A.2 Characterization of aluminate phases by $^{27}\text{Al}$ NMR

### A.3 Phase Assemblage

## APPENDIX A. MATERIALS AND METHODS

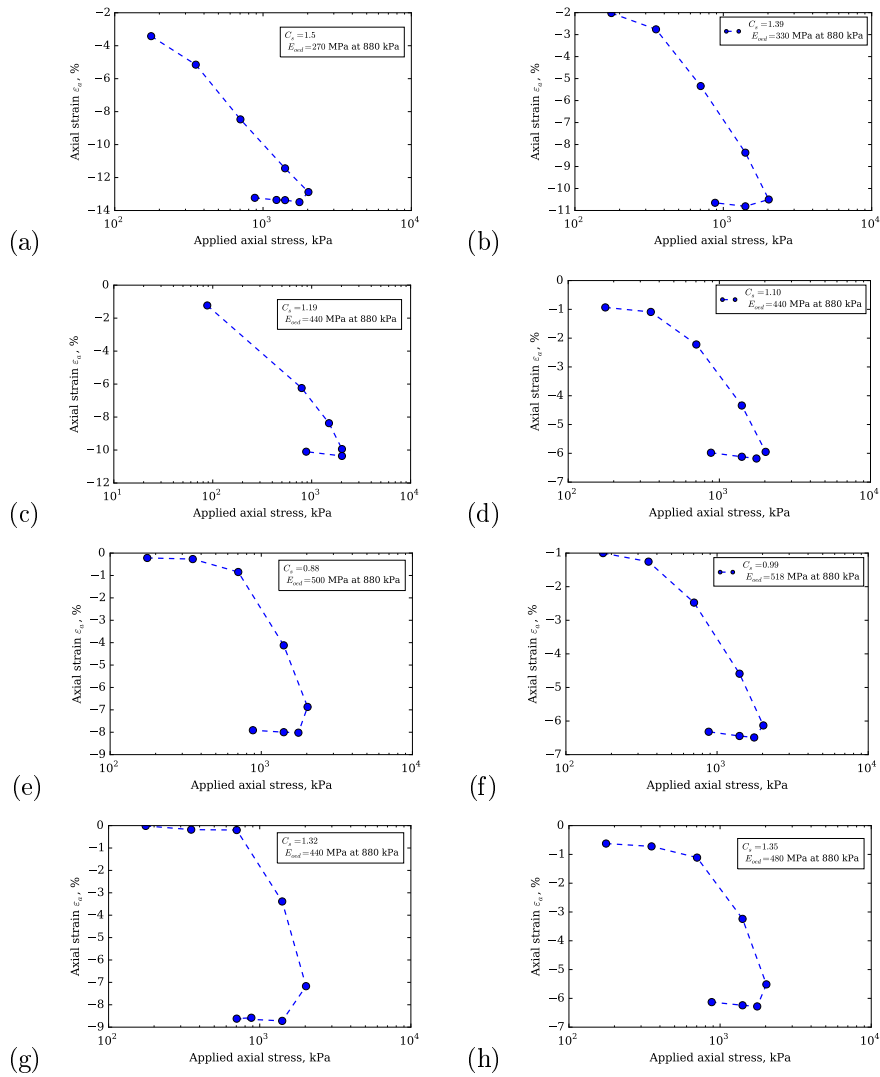


Figure A.1: Behavior of various material: (a) CH-AFm4, (b) C3S, (c) C3S-sand, (d) C3S-AFm4-a, (e) C3S-AFm4-b, (f) C3S-AFm8-a, (g) C3S-AFm8-b and (h) OPC.

### A.3. PHASE ASSEMBLAGE

Materials	Phases distribution in Al <sub>2</sub> O <sub>3</sub> , Molar (%)					
	CAH/TAH	AFm	AFt	Al(V)	C-A-S-H	Unknown
C3S-AFm8-b-Ref	6	42	8	6	19	19
C3S-AFm8-b	1	1	90	1	7	0
C3S-AFm4-b-Ref	9	40	22	7	17	5
C3S-AFm4-b	7	3	76	6	8	0
C3S-AFm2-b	10	7	70	7	9	0
C3S-AFm8-a-Ref	4	68	28	0	0	0
C3S-AFm8-a	5	5	80	3	7	0
CH-AFm4-Ref	0	76	24	0	0	0
CH-AFm4	1	5	90	2	2	0
OPC(1)	21	47	7	6	19	0
OPC(2)	18	50	7	6	19	0
OPC(3)	17	52	7	6	18	0
OPC-3	6	31	50	4	9	0
OPC-3-66	0	5	87	0	8	0
OPC-66	2	4	81	4	9	0
OPC-1190	7	5	79	3	6	0
OPC-315-1190	7	10	67	7	9	0
OPC-66-2(O)	18	52	3	8	9	0
OPC-66(O)	4	7	75	3	11	0
OPC-315(O)	6	4	78	4	8	0
OPC-1190(O)	2	4	81	0	13	0

Table A.1: Phases distribution in Al<sub>2</sub>O<sub>3</sub> characterized by <sup>27</sup>Al-NMR of various materials. These results are given from Laboratory ‘**L**aboratoire de **S**pectrochimie **I**nfrarouge et **R**aman (**L**ASIR)’, Lille University of Science and Technology, France, by Grégory Tricot.

## APPENDIX A. MATERIALS AND METHODS

Materials	Phases distribution in Al <sub>2</sub> O <sub>3</sub> , Molar (%)					
	CAH/TAH	AFm	AFt	Al(V)	C-A-S-H	Unknown
C3S-AFm8-b	2.3	6.3	91.4	0	0	0
C3S-AFm2-b	0.0	5.7	94.3	0	0	0
C3S-AFm8-a-Ref	5.5	76.4	18.1	0	0	0
OPC(3)	17.7	75.9	6.3	0	0	0
OPC-3	0.0	16.4	83.6	0	0	0
OPC-66	2.5	5.5	92.0	0	0	0
OPC-66(O)	0.0	4.5	95.5	0	0	0
OPC-140(O)	7.7	11.7	80.6	0	0	0
OPC-540(O)	1.9	7.9	90.3	0	0	0
OPC-1190(O)	3.5	10.7	85.9	0	0	0

Table A.2: Phases distribution in Al<sub>2</sub>O<sub>3</sub> characterized by <sup>27</sup>Al-NMR of various materials. These results are given by <sup>27</sup>Al-NMR characterizations, performed at [Department of Chemistry](#), Aarhus University, Denmark.

Material	CaO/SiO <sub>2</sub>		Al <sub>2</sub> O <sub>3</sub> /SiO <sub>2</sub>				$\rho_{C(A)SH}$ , g/cm <sup>3</sup>
	‘Combi’	SEM-EDS	‘Combi’	SEM-EDS	<sup>27</sup> Al-NMR	<sup>27</sup> Al-NMR*	
OPC(3)	1.5	1.9	0.03	0.03	0.03	0.0	2.3
OPC-3	1.2	1.2	0.01	0.01	0.01	0.0	2.3
OPC-66	1.5	1.9	0.03	0.02	0.02	0.0	2.7
OPC-66(O)	1.5	1.9	0.02	0.02	0.02	0.0	2.7
C3S-AFm8-a	1.5	N/A	0.0	N/A	N/A	0.0	1.9
C3S-AFm8-b	1.6	1.6	0.02	0.02	0.02	0.0	2.3

Table A.3: Ratios CaO/SiO<sub>2</sub>, Al<sub>2</sub>O<sub>3</sub>/SiO<sub>2</sub>, H<sub>2</sub>O/SiO<sub>2</sub> and density  $\rho_{C(A)SH}$  of the C-(A)-S-H gel for various samples based on various <sup>27</sup>Al-NMR measurements. ‘Combi’ indicates the ratios that must be considered for the C-(A)-S-H gel in order for the chemical composition calculated from the phase assemblages measured with the method ‘Combi’ to be close to the one measured with XRF. ‘SEM-EDS’ and ‘<sup>27</sup>Al-NMR’ indicate the ratios measured with SEM-EDS and <sup>27</sup>Al-NMR, respectively. The density of C-(A)-S-H  $\rho_{C(A)SH}$  is the one back-calculated from the phase assemblages given in Tab. 2.16 to retrieve the density of the solid phase given in Tab. 2.4. <sup>27</sup>Al-NMR and <sup>27</sup>Al-NMR\* stand for measurements given by Lille University of Science and Technology, France and Aarhus University, Denmark respectively.

### A.3. PHASE ASSEMBLAGE

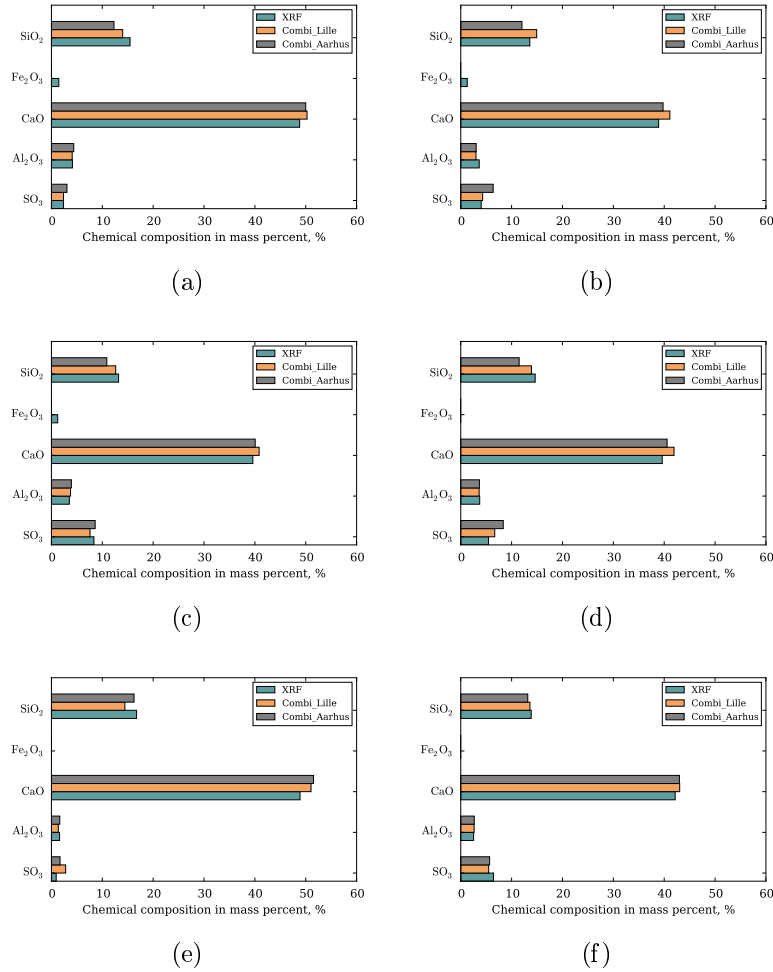


Figure A.2: Chemical compositions obtained in various materials based on various <sup>27</sup>Al-NMR measurements: (a) OPC(3), (b) OPC-3, (c) OPC-66, (d) OPC-66(O), (e) C3S-AFm8-a-Ref, (f) C3S-AFm8-b.

## APPENDIX A. MATERIALS AND METHODS

Materials	CH	C-(A)-S-H	Quartz	AFm	AFt	CaCO <sub>3</sub>	C <sub>3</sub> AH <sub>6</sub>	C\$
OPC-315-1190	7.8	55.5	0.0	1.9	25.1	5.6	2.6	2.1
OPC-140(O)	6.3	39.2	0.0	2.5	35.2	15.7	1.0	0.0
OPC-315(O)	10.6	41.9	0.0	0.8	35.3	10.6	0.8	0.0
OPC-540(O)	9.5	36.1	0.0	1.7	39.8	12.7	0.2	0.0
OPC-1190(O)	6.3	42.6	0.0	0.8	33.1	16.9	0.2	0.0
C3S-66	23.0	76.0	0.0	0.0	0.0	0.0	0.0	0.0
CH-AFm4	14.0	0.0	0.0	0.2	77	8.4	0.1	0.0
C3S-AFm4-b	27.7	55.6	0.0	0.3	13.1	0.0	1.1	0.0

Table A.4: Phase assemblage of other tested samples in this thesis, as obtained with the method ‘Combi’, in mass percentage.

Materials	CaO/SiO <sub>2</sub>	Al <sub>2</sub> O <sub>3</sub> /SiO <sub>2</sub>		$\rho_{C(A)SH}$ , g/cm <sup>3</sup>
	SEM-EDS	SEM-EDS	<sup>27</sup> Al-NMR	
OPC-3	1.2	0.01	0.01	2.3
OPC-3-66	1.6	0.01	0.01	2.8
OPC-66	1.9	0.01	0.02	2.7
OPC-1190	N/A	N/A	0.01	2.6
C3S-sand(e1)	N/A	N/A	N/A	N/A
CH-AFm4	N/A	N/A	N/A	N/A
C3S-AFm4-a-66	1.5	0.0	0.0	N/A
C3S-AFm4-a-66-1190	N/A	N/A	N/A	N/A
C3S-AFm8-a	1.9	0.0	0.0	N/A
C3S-AFm2-b(e2)	N/A	N/A	N/A	N/A
C3S-AFm4-b	N/A	N/A	N/A	N/A
C3S-AFm8-b	1.6	0.01	0.01	N/A

Table A.5: Ratios CaO/SiO<sub>2</sub>, Al<sub>2</sub>O<sub>3</sub>/SiO<sub>2</sub> of various material before testing were obtained by methods SEM-EDS and <sup>27</sup>Al-NMR. The density of C-(A)-S-H  $\rho_{C(A)SH}$  was estimated based on phase assembly displayed in Tab. 2.16 to retrieve the density of the solid phase displayed in Tab. 2.4.

# Appendix B

## Oedometric study of kinetics and role of mineralogy and microstructure

### B.1 Deformation evolution of referent samples: OPC-Ref(O), C3S-AFm4-a-Ref and C3S-AFm4-b-Ref

We performed referent tests in which the samples have been flushed uniquely by water. The Fig. B.1 displays the deformation evolution of referent samples OPC-Ref(O), C3S-AFm4-a-Ref(O) and C3S-AFm4-b-Ref(O). We did not observe any expansion after injections of water in these samples.

### B.2 SEM-EDS analysis on various samples

Beside to the results displayed in Ch. 3, we show also several results of SEM-EDS analysis on various samples C3S-AFm8-a, C3S-AFm8-b, C3S-AFm4-a, OPC.

By means of results displayed in Fig. B.2 and 3.6, there has been no ettringite or monosulfoaluminate within the C-S-H gel either before or after

## APPENDIX B. OEDOMETRIC STUDY OF KINETICS AND ROLE OF MINERALOGY AND MICROSTRUCTURE

---

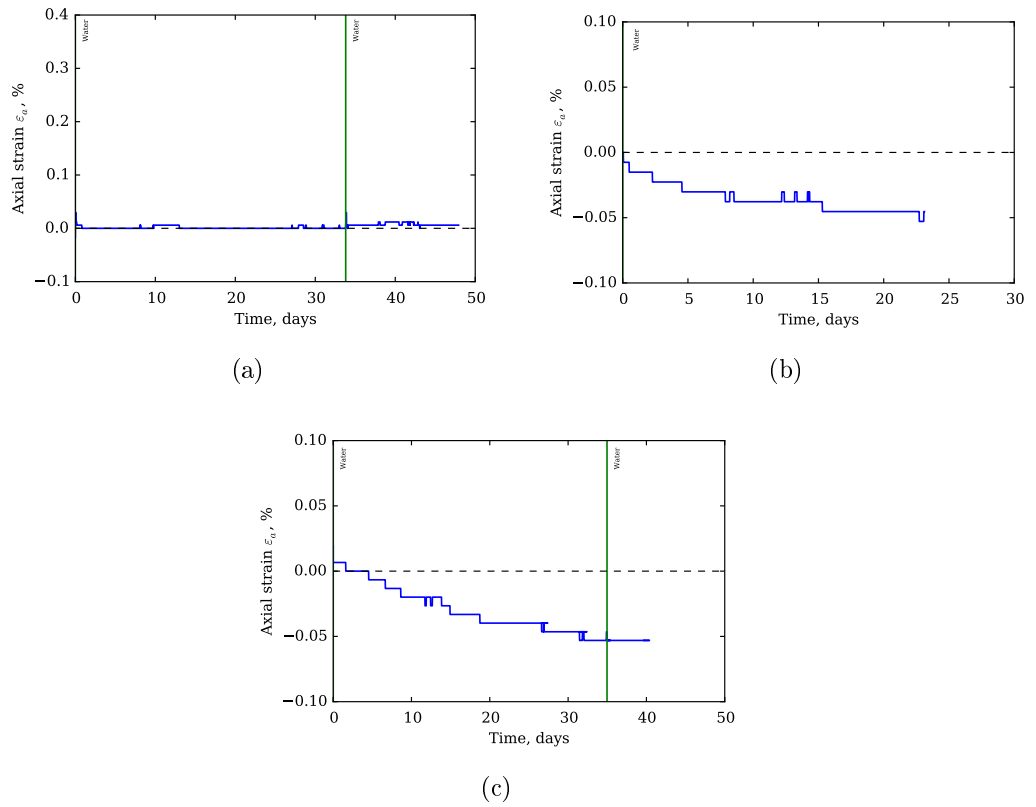


Figure B.1: Evolution of deformation of referent tests induced by injections of water: (a) OPC, (b) C3S-AFm4-a and (c) C3S-AFm4-b.

## B.2. SEM-EDS ANALYSIS ON VARIOUS SAMPLES

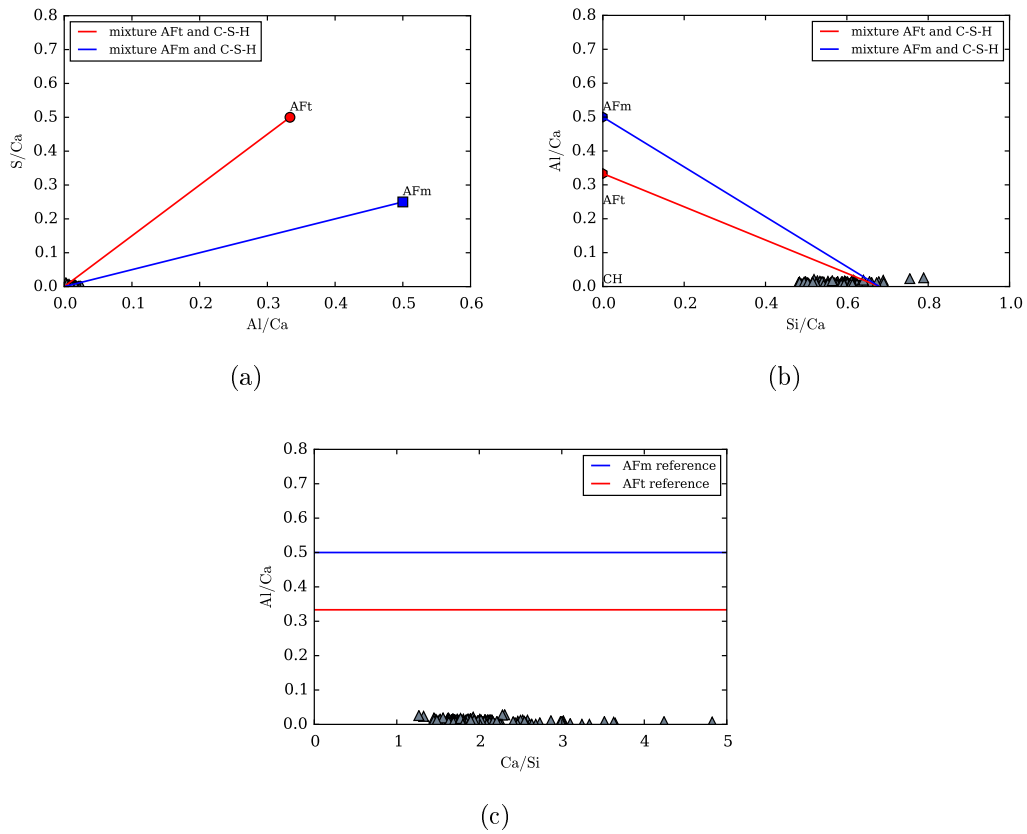


Figure B.2: SEM-EDS results on the sample 'C3S-AFm4-a-Ref': (a) Ratio of  $Al/Ca$  versus ratio of  $S/Ca$  in the mixture C-S-H and (b) Ratio of  $Si/Ca$  versus ratio of  $Al/Ca$  in the mixture C-S-H.

## APPENDIX B. OEDOMETRIC STUDY OF KINETICS AND ROLE OF MINERALOGY AND MICROSTRUCTURE

testing.

For sample OPC-Ref(O), the existence of mixture C-S-H with AFm has been widely recognized, as indicated by considerable points locating on tie line AFm in Fig. B.3. After testing, almost of that monosulfoaluminate (i.e., locating within C-S-H gel) has transformed into ettringite, as indicated by considerable points locating on tie line AFt in Fig. B.4. This observation has been also recognized in sample C3S-AFm8-b, as displayed in Fig. B.5.

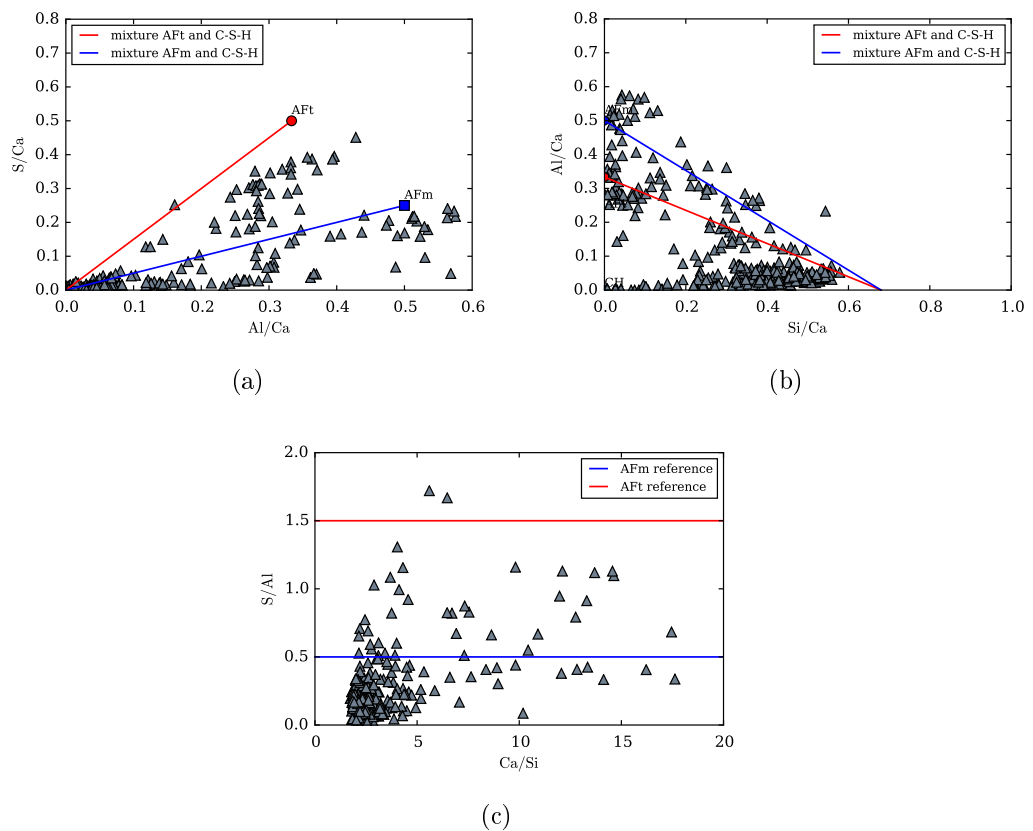


Figure B.3: SEM-EDS results on the sample 'OPC-Ref(O)': (a) Ratio of Al/Ca versus ratio of S/Ca, (b) Ratio of Si/Ca versus ratio of Al/Ca and (c) Ratio of Ca/Si versus ratio of S/Al.

## B.2. SEM-EDS ANALYSIS ON VARIOUS SAMPLES

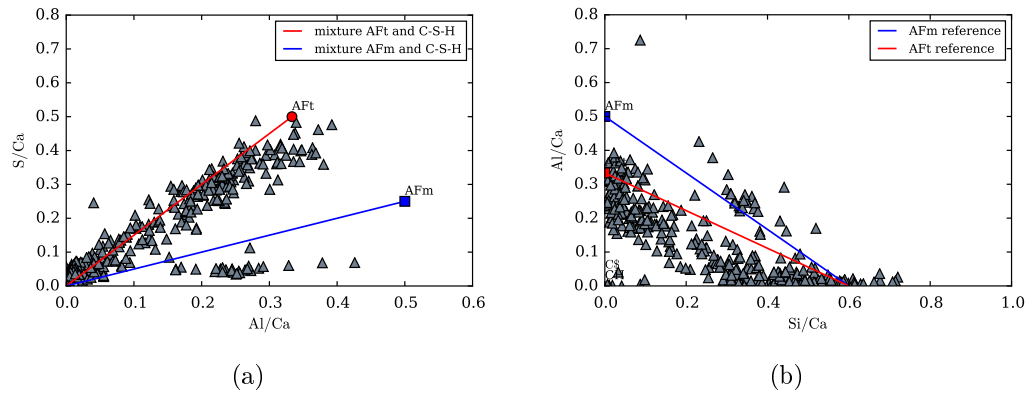


Figure B.4: SEM-EDS results on the sample 'OPC-66(O)' flushed by a solution at 66 mM: (a) Ratio of Al/Ca versus ratio of S/Ca, (b) Ratio of Si/Ca versus ratio of Al/Ca and.

APPENDIX B. OEDOMETRIC STUDY OF KINETICS AND ROLE OF MINERALOGY AND MICROSTRUCTURE

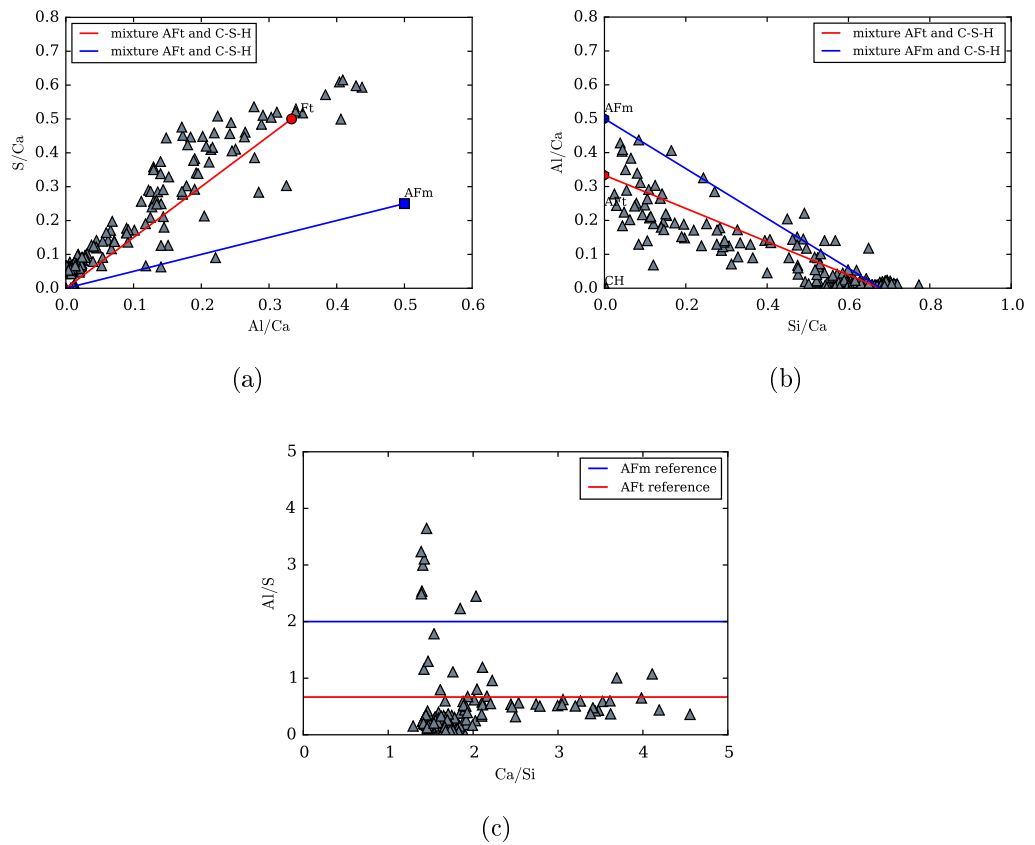


Figure B.5: SEM-EDS results on the sample 'C3S-AFm8-b' flushed by a solution at 66 mM: (a) Ratio of Al/Ca versus ratio of S/Ca, (b) Ratio of Si/Ca versus ratio of Al/Ca and (c). Ratio of Ca/Si versus ratio of Al/S.

# Appendix C

## Oedometric study of the role of gypsum crystallization in expansion

### C.1 Oedometric study of material OPC

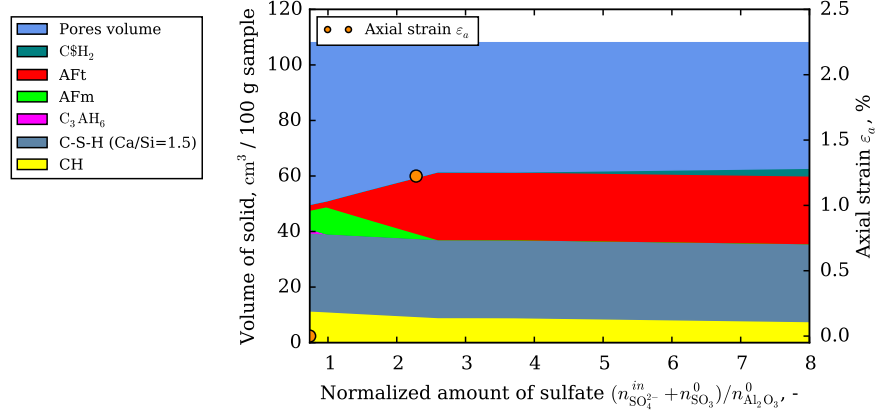
*It is recommended to see also the Chap. 5 to a better understand theses bellow results.*

In this chapter, we performed also oedometric testings with material OPC whose mineralogy and microstructure features are expected to be more complex than C3S-AFm4-a and C3S-AFm8-a. The oedometric testings were carried-out with various concentrations of sulfate such as 66, 140, 315, 540, 1190 mM. We recall that the label OPC-1190(O) stand for an oedometric testing with material OPC flushed by a solution of sulfate concentration of 1190 mM (see Tab. 2.18).

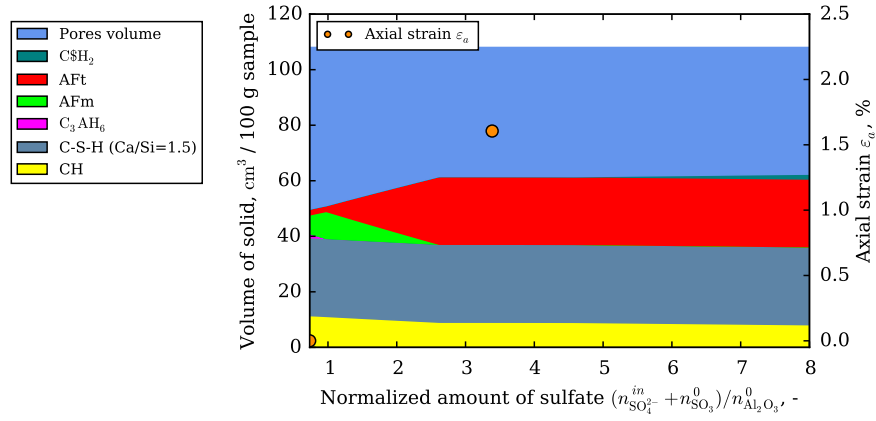
The deformation evolution of various samples are displayed in Fig. 4.20. We waited long enough before ending the test or performing the next injection in order for the expansion to have roughly stabilized. Those strains are expected as equilibrium strains.

The mineralogical evolution of the various samples over the injection process is displayed in Fig. 4.21 and C.1. For a typical result of sample OPC-66,

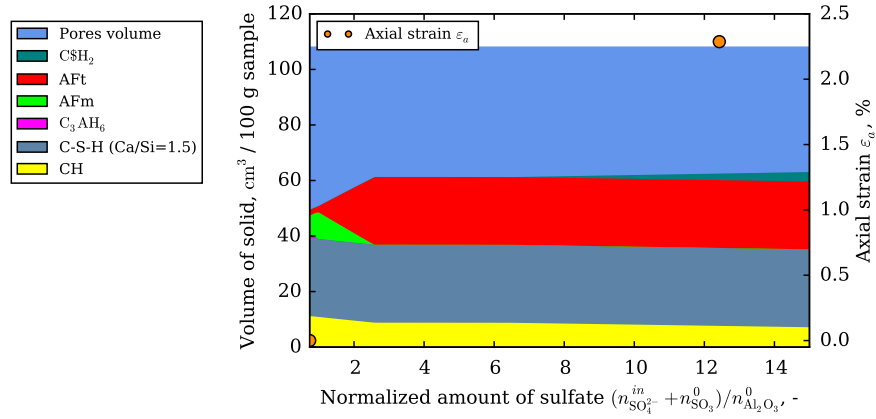
APPENDIX C. OEDOMETRIC STUDY OF THE ROLE OF GYPSUM  
CRYSTALLIZATION IN EXPANSION



(a)



(b)



(c)

Figure C.1: Phase assemblage evolution of various samples together with profile of sulfate concentration of input solution in related with normalized amount of sulfate  $(n_{SO_4}^{in} + n_{SO_3}^0) / n_{Al_2O_3}^0$  where:  $n_{SO_4}^{in}$  stands for amount of injected sulfate (mmol),  $n_{SO_3}^0$  and  $n_{Al_2O_3}^0$  stand for initial amount of sulfate and aluminate oxidation within sample respectively (mmol) which are give by XRF: (a) OPC-315(O), (b) OPC-540(O) and (c) OPC-1190(O).

the sulfate ingress reacted firstly with AFm to form ettringite. Once, almost of reactive monosulfoaluminate reacted with sulfate, the sulfate ingress continued reacting with CH to form gypsum within material. We introduced a corrective parameter  $\alpha$  ( $\alpha=0.8$ ) defined in Eq. (5.1) and (5.2) to retrieve accurately the mineralogical and chemical composition within material after testing. The mineralogical and chemical composition of various sample predicted by thermodynamic modeling are displayed in Fig. C.3 (a) and C.2 (a). The results obtained by thermodynamic modeling show a good agreement with experimental results (i.e., XRF and method Combi).

By an analogy, we performed also thermodynamic modeling for remaining samples as results displayed in Fig. 4.21 and C.1. It is noted that the corrective parameter  $\alpha$  is equal to 1.0 for whole samples except OPC-66(O). The results given by thermodynamic modeling show a good agreement with experimental results. However, a slight difference between both methods may be due to the fact of the lack of thermodynamic data of phases like C-(A)-S-H, as mentioned already in Chap. 2.

## C.2 Loading effect on expansion

The loading effect can be observed in oedometric tests OPC(0.52), OPC(0.88) and OPC(1.44), as displayed in Fig. C.5. It seems that in a given condition, a greater applied stress (i.e.,  $\sigma_a$ ) leads to a lower expansion.

APPENDIX C. OEDOMETRIC STUDY OF THE ROLE OF GYPSUM  
CRYSTALLIZATION IN EXPANSION

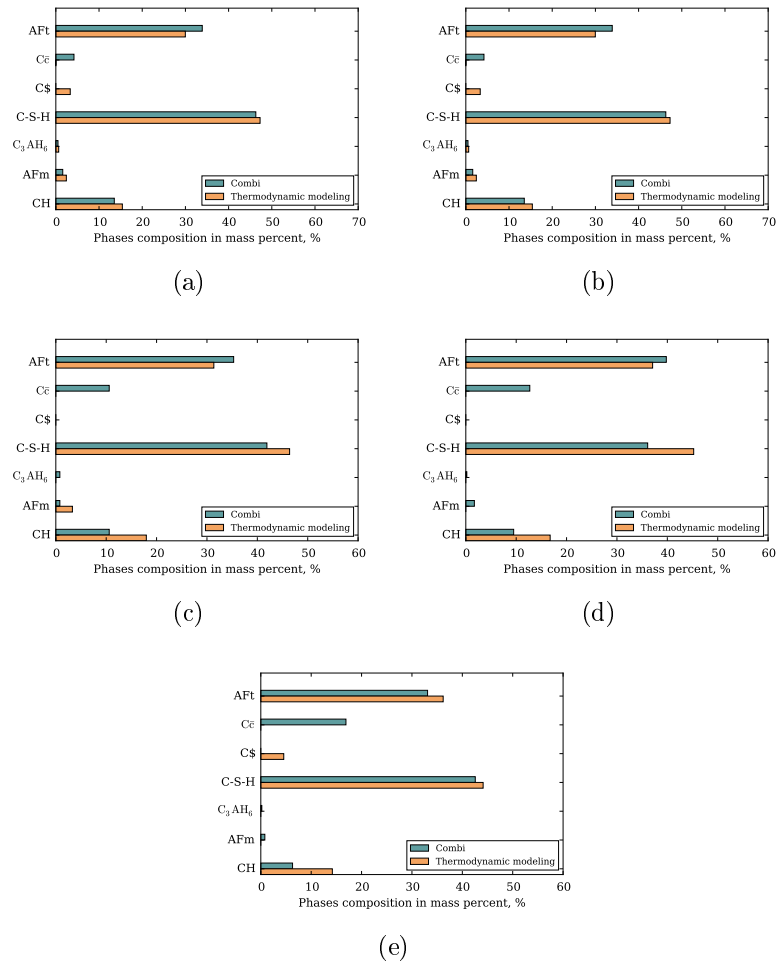


Figure C.2: The final phase assembly predicted by thermodynamic modeling are compared with the results given by method Combi: (a) OPC-66(O), (b) OPC-140(O), (c) OPC-315(O), (d) OPC-540(O) and (e) OPC-1190(O).

## C.2. LOADING EFFECT ON EXPANSION

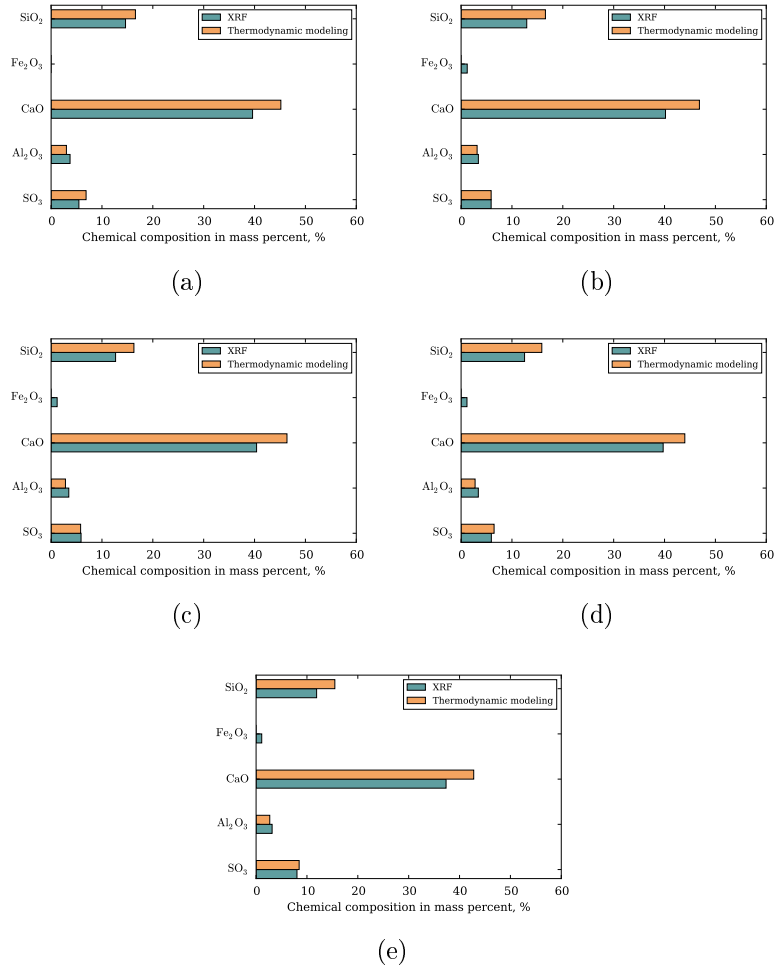


Figure C.3: The final chemical composition predicted by thermodynamic modeling are compared with the results given by method XRF in various samples: (a) OPC-66(O), (b) OPC-140(O), (c) OPC-315(O), (d) OPC-540(O) and (e) OPC-1190(O).

## APPENDIX C. OEDOMETRIC STUDY OF THE ROLE OF GYPSUM CRYSTALLIZATION IN EXPANSION

---

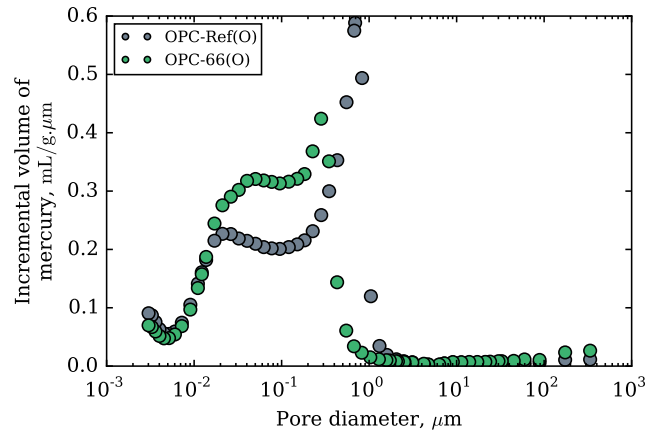


Figure C.4: In case of OPC-66(O): Pore structures of material before and after testing obtained by MIP.

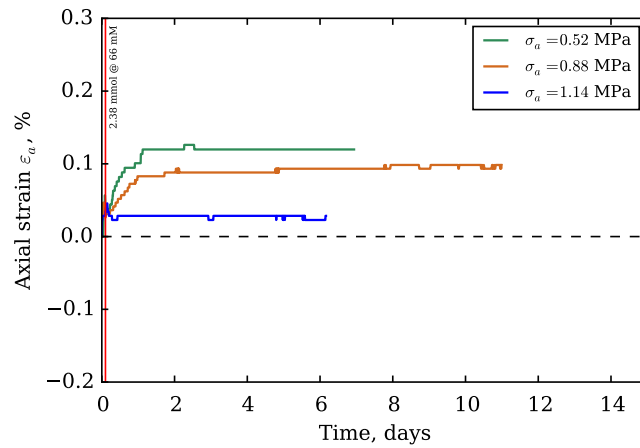


Figure C.5: Expansion evolution in various samples: OPC(0.52), OPC(0.88) and OPC(1.44).

# Appendix D

## Isochoric study of factors governing expansion stress

### D.1 Thermodynamic modelling in relation with amount of sulfate remaining in sample

We recall that, here, to remain consistent with what was done in the previous chapters, all thermodynamic calculations were performed by inputting into CHESS the injected amounts of sulfates. However, since in this chapter we measured the amounts of sulfates having remained in the sample, we could as well use those amounts as inputs for the thermodynamic modeling. Those results are displayed in Fig. D.1 to Fig. D.5.

In case of OPC-3, the evolution of aqueous fraction of  $[\text{SO}_4^{2-}]$  did not correlate to the evolution of sulfate concentration of output solution  $[\text{SO}_4^{2-}]^{out}$ . Because this frame work can not take into account the dissolution of CH while the amount of remaining sulfate remained constant as indicated in Fig. D.1 (a).

We address also the evolution of volume of solid phases as a function of the amount of remaining sulfate, as results displayed in Fig. D.4.

## APPENDIX D. ISOCHORIC STUDY OF FACTORS GOVERNING EXPANSION STRESS

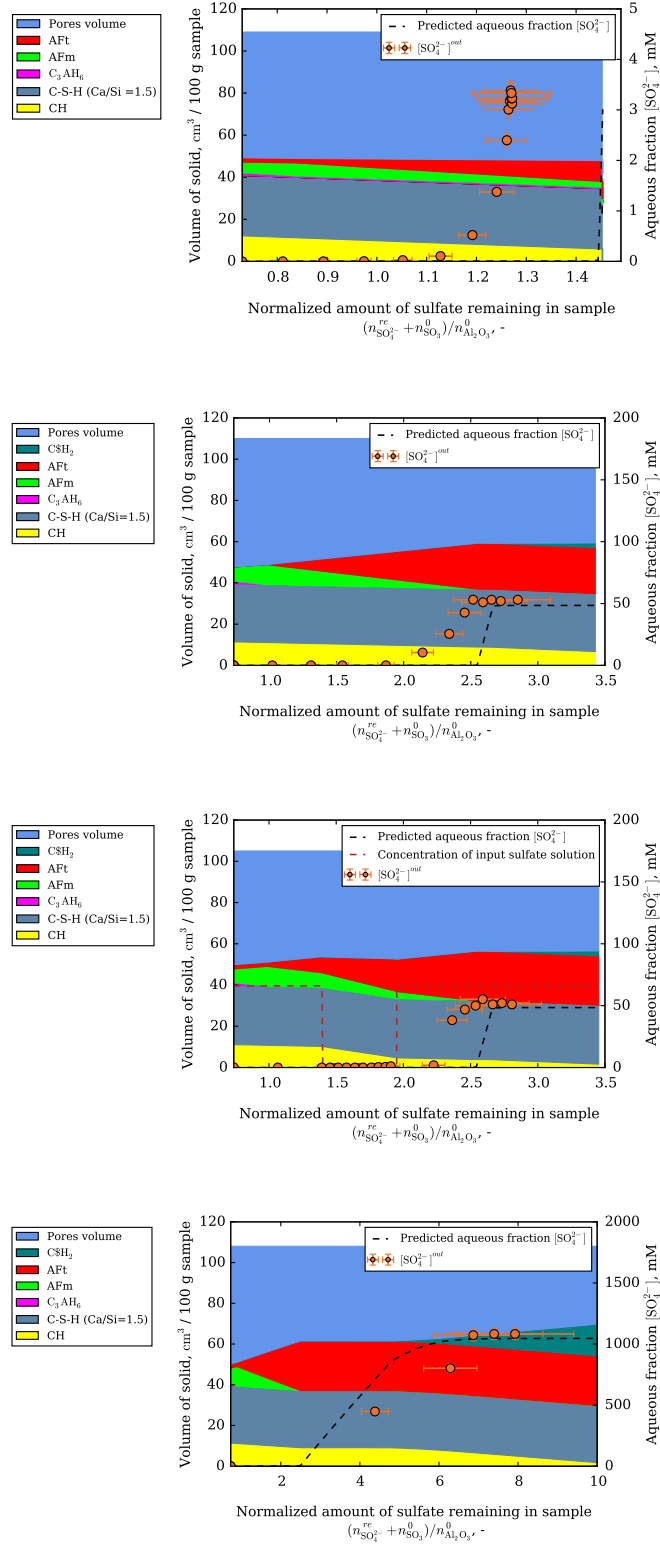


Figure D.1: Phases evolution with amount of sulfate remaining in sample: (a) OPC-3, (b) OPC-66, (c) OPC-3-66 and (d) OPC-1190.

## D.1. THERMODYNAMIC MODELLING IN RELATION WITH AMOUNT OF SULFATE REMAINING IN SAMPLE

---

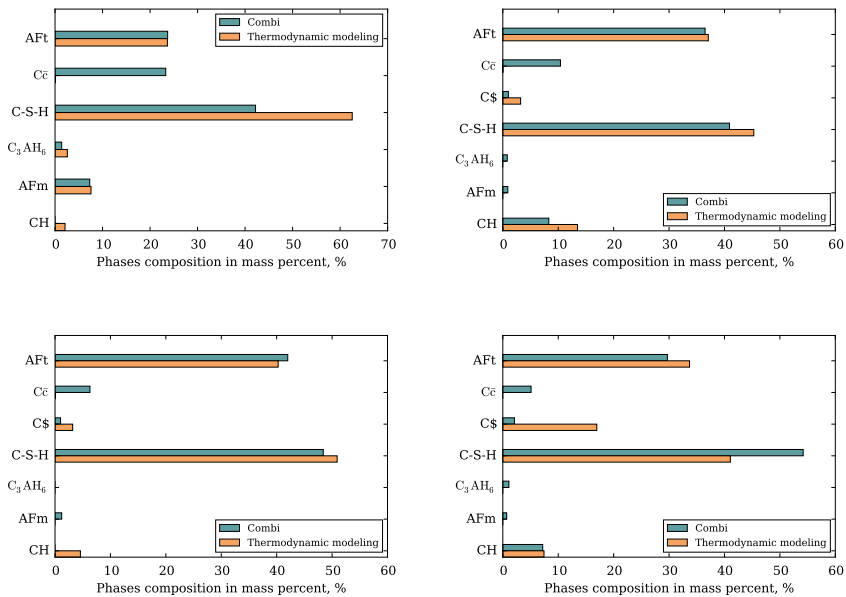


Figure D.2: Thermodynamic prediction based on amount of injected sulfate: chemical composition in compared with XRF on various samples after experiments: (a) OPC-3, (b) OPC-66, (c) OPC-3-66 and (d) OPC-1190.

## APPENDIX D. ISOCHORIC STUDY OF FACTORS GOVERNING EXPANSION STRESS

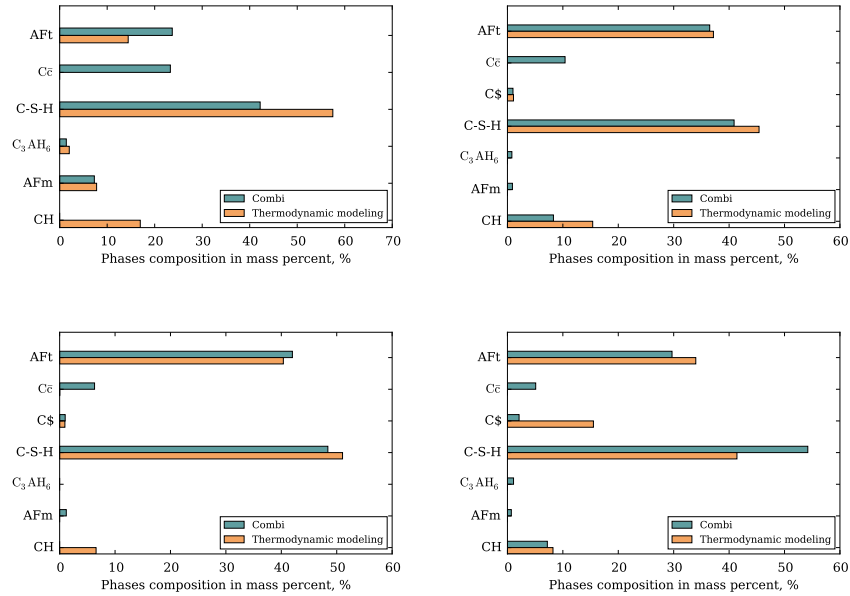


Figure D.3: Thermodynamic prediction based on amount of remaining sulfate: phases composition compared with experimental characterizations on various samples after experiments: (a) OPC-3, (b). OPC-66, (c). OPC-3-66 and (d). OPC-1190.

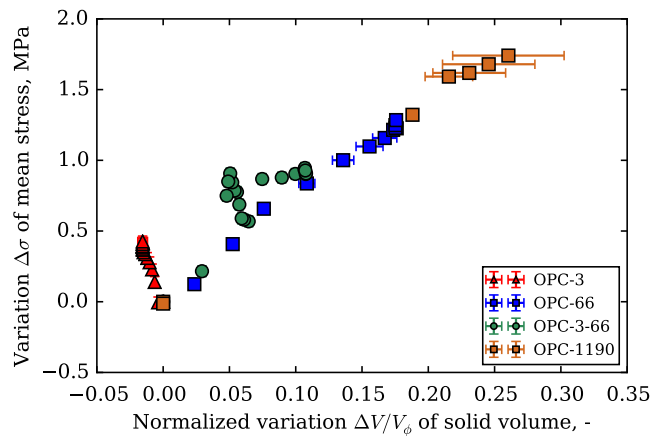


Figure D.4: Volume change of solid phases of various samples such as OPC-3, OPC-66, OPC-3-66 and OPC-1190, which is based on amount of sulfate remaining in sample.

D.1. THERMODYNAMIC MODELLING IN RELATION WITH  
AMOUNT OF SULFATE REMAINING IN SAMPLE

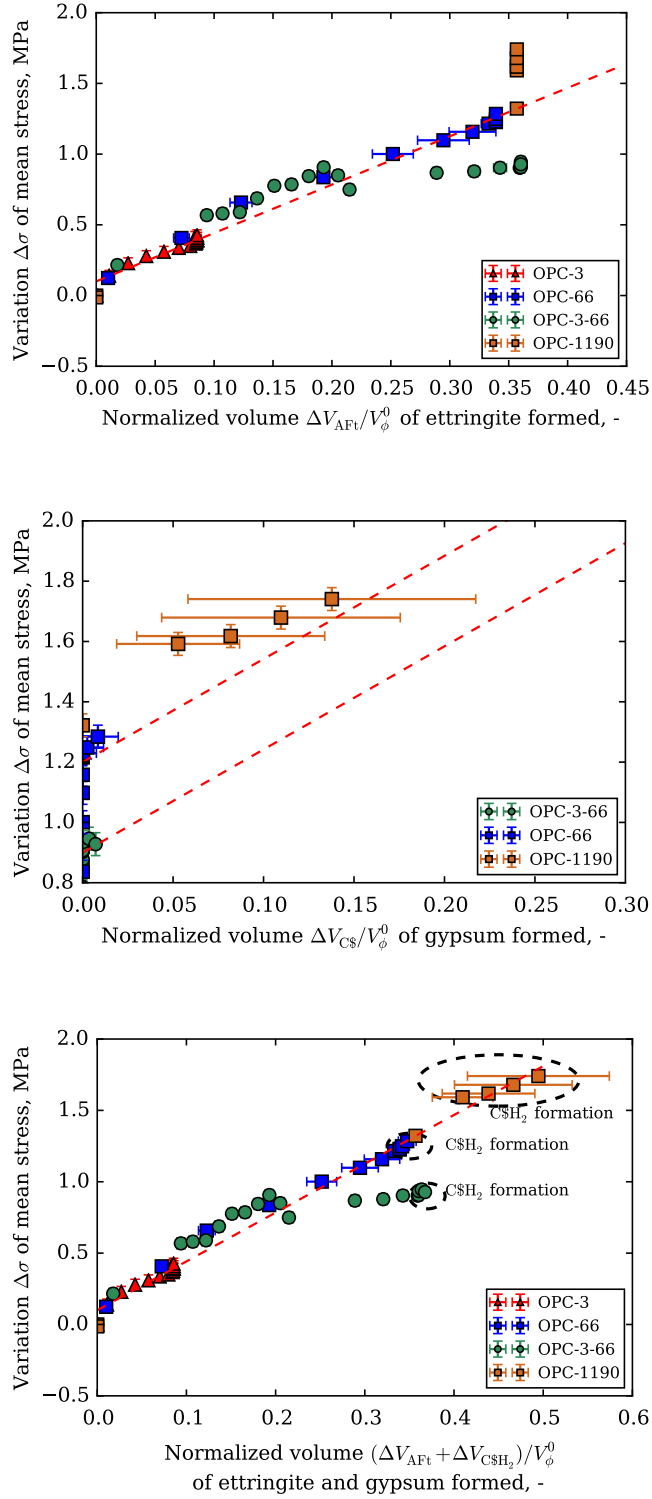


Figure D.5: a. Expansion stress in function of normalized amount of: (a) Ettringite; (b) Gypsum and (c) Ettringite and gypsum. On all figures, the slope of the dashed lines is 3.42 MPa.

## D.2 Delay of axial stress

Concerning axial stress evolution, there has some non-equilibrium points resulting from the last injections on each sample (see Fig. 5.3 and 5.4). Here, we did not aim at characterizing the axial stress because of those non-equilibrium points. According to results, there appears to be a threshold volume of crystal formed below which no axial stress is observed, as indicated in Fig. D.6. It confirms again the delay of axial stress phenomenon which has been recognized in ischoric testings (see more details in Chap. 5). It seems the trend of axial stress in the sample OPC-1190 may be coherent with deformation observed in Fig. 4.21.

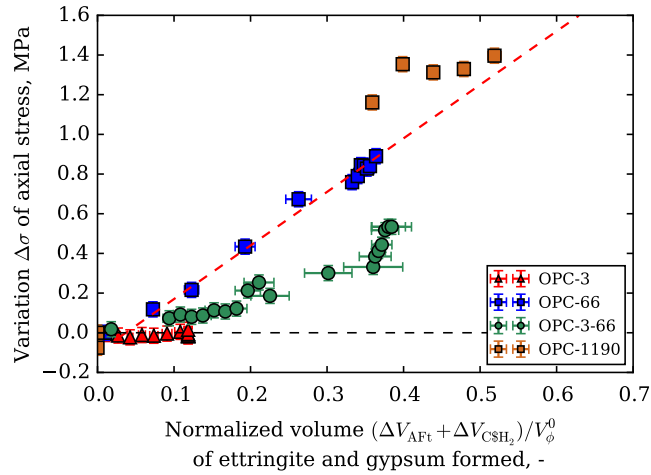


Figure D.6: Axial stress in function of volume of Ettringite and Gypsum formed which is normalized with initial volume of pores. The slope of the red dashed line is 2.7 MPa.

## D.3 Evolution of permeability

Fig. D.7 show that there is a correlation between permeability evolution and solid volume evolution as indicated in Fig. 5.21.

### D.3. EVOLUTION OF PERMEABILITY

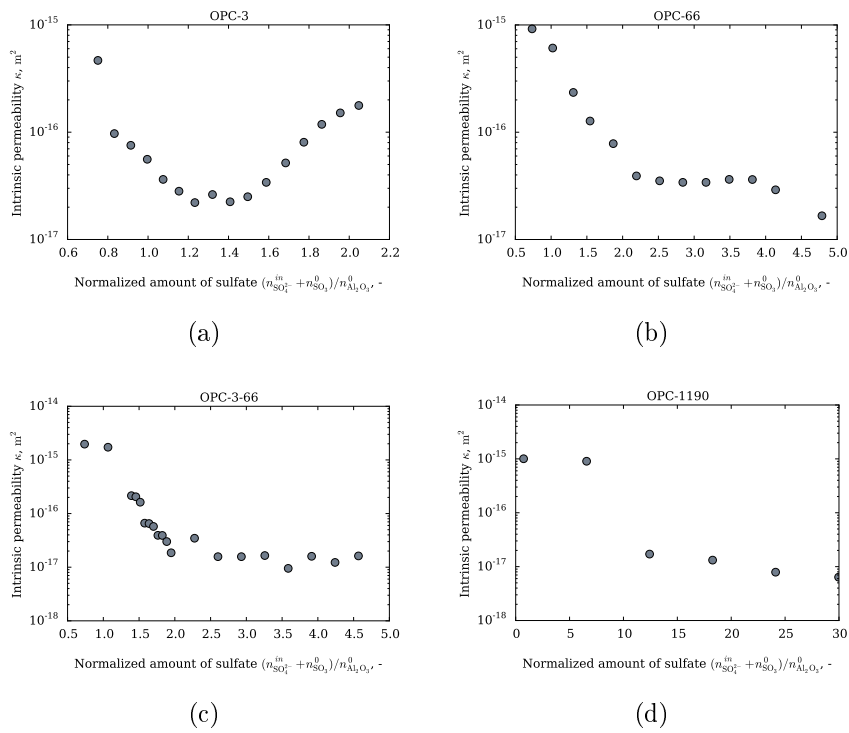


Figure D.7: Evolution of permeability in function of amount of injected sulfate: (a) OPC-3; (b) OPC-66; (c) OPC-3-66 and (d) OPC-1190.

## D.4 Loading effect on expansion stress?

We performed two experiments with same experimental conditions but the initial axial stress in both samples were different. Before testing, we applied an initial axial stress on sample OPC-I(0.52) equal to 0.52 MPa which was lower than the one in sample OPC-66.

We observed a greater expansion stress in the sample of lower initial stress (i.e., OPC-I(0.52)), as results displayed in Fig. D.8. Even though it appeared a significant gradient sulfate concentration between inlet and outlet at the last injection of solution, the homogeneity within material after experiment still is confirmed in such case, as results displayed in Fig. D.9. After experiment, a part of AFm was only consumed for the transformation into AFt. We observed no reaction front in such sample. An adequate study on this phenomenon is necessary to better understand how mineralogy evolves within sample after injection of solution. The loading effect on expansion stress is still an open subject for further studies.

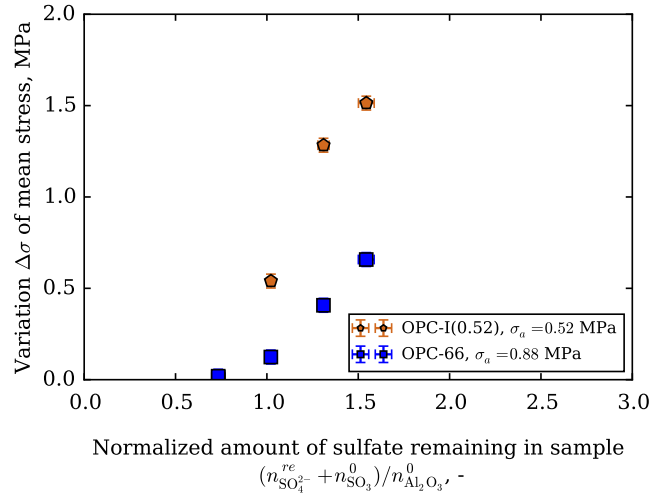


Figure D.8: Variation of means stress in function of amount of sulfate remaining in samples: OPC-I(0.52) and OPC-66.

#### D.4. LOADING EFFECT ON EXPANSION STRESS?

---

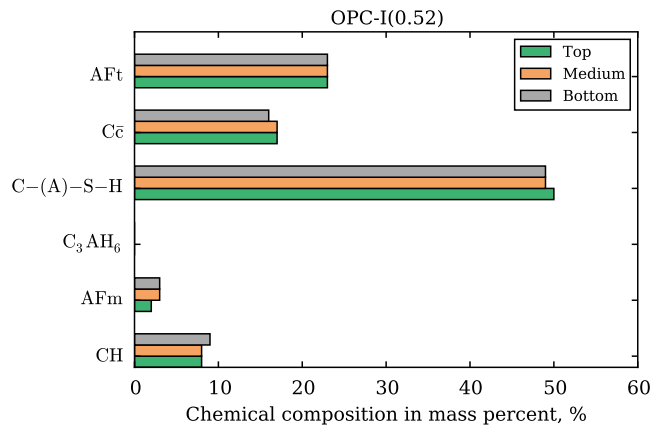


Figure D.9: Mineralogy distribution over the height of sample OPC-I(0.52).

APPENDIX D. ISOCHORIC STUDY OF FACTORS GOVERNING  
EXPANSION STRESS

---

# Bibliography

- Aõ, P.-c. (2000). Cements of yesterday and today Concrete of tomorrow. *Cement and Concrete Research*, 30:1349–1359. *Cited page 58*
- ANDRA (2005a). Evaluation of the feasibility of a geological repository in an argillaceous formation. Technical Report December, ANDRA. *Cited page 55*
- ANDRA (2005b). Les recherches de l’ANDRA sur le stockage géologique des déchets radioactifs à haute activité et à vie longue, résultats et perspectives. Technical report, ANDRA. *Cited pages 39, 55, and 56*
- ANDRA (2012). Inventaire national des matières et déchets radioactifs-ANDRA. Technical report, ANDRA. *Cited page 55*
- Association française de Normalisation (2004). Norme NF EN 206-1 Béton. Partie 1: Spécifications, performances, production and conformité. *Cited page 58*
- Auger, J. (2009). *Mise au point et développement d’un procédé d’aide à la déconstruction des ouvrages en béton armé*. PhD thesis, Université de Toulouse. *Cited page 59*
- Barbarulo, R. (2002). *Comportement des matériaux cimentaires: Actions des sulfates et de la température*. PhD thesis, ENS Cachan. *Cited pages 49 and 52*
- Bary, B. (2008). Simplified coupled chemo-mechanical modeling of cement pastes behavior subjected to combined leaching and external sulfate at-

## BIBLIOGRAPHY

---

- tack. *International Journal Numerical Analytical Methods Geomechanics*, 32(February):1791–1816. *Cited pages 45 and 65*
- Bary, B., Leterrier, N., Deville, E., and Le Bescop, P. (2014). Coupled chemo-transport-mechanical modelling and numerical simulation of external sulfate attack in mortar. *Cement and Concrete Composites*, 49:70–83. *Cited pages 44, 45, 65, 134, and 146*
- Basista, M. (2008). Micromechanical modelling of sulphate corrosion in concrete : influence of ettringite forming reaction. *Theoretical and Applied Mechanics*, 35(1):29–52. *Cited pages 45 and 65*
- Becker, G. F. and Day, A. L. (1916). Note on the linear force of growing crystals. *Journal of geology*, 4:313–333. *Cited page 60*
- Bellmann, F., Möser, B., and Stark, J. (2006). Influence of sulfate solution concentration on the formation of gypsum in sulfate resistance test specimen. *Cement and Concrete Research*, 36:358–363. *Cited page 49*
- Bizzozero, J. (2014). *Hydration and dimensional stability of calcium aluminate cement based systems*. PhD thesis, EPFL. *Cited pages 45 and 148*
- Bizzozero, J., Gosselin, C., and Scrivener, K. L. (2014). Expansion mechanisms in calcium aluminate and sulfoaluminate systems with calcium sulfate. *Cement and Concrete Research*, 56:190–202. *Cited pages 45 and 148*
- Bo, H. (2007). Assessment of material use in relation to climate in historical buildings. *Building and environment*, 42:970–978. *Cited page 57*
- Bonen, D. and Cohen, M. D. (1992a). Magnesium sulfate attack on portland cement paset- II. Chemical and mineralogical analyses. *Cement and Concrete Research*, 22:707–718. *Cited page 41*
- Bonen, D. and Cohen, M. D. (1992b). Magnesium Sulfate Attack on Portland Cement Paste-I. Microstructural Analysis. *Cement and Concrete Research*, 22(1):169–180. *Cited page 41*

- Bonen, D. and Sarkar, S. (1993). Replacement of Portlandite by gypsum in the interfacial zone and cracking related to crystallization pressure. In *Ceramics Transactions, Vol 37, Cement-based materials: present, future, and environmental aspects*, pages 49–60, Westerville, OH. American Ceramic Society. *Cited page 47*
- Bouzabata, H., Multon, S., Sellier, A., and Houari, H. (2012). Effects of restraint on expansion due to delayed ettringite formation. *Cement and Concrete Research*, 42(7):1024–1031. *Cited page 53*
- Bowitz, E. and Ibenholt, K. (2009). Economic impacts of cultural heritage e Research and perspectives. *Journal of Cultural Heritage*, 10(1):1–8. *Cited page 57*
- Bruhms, W. and Meckelenburg, W. (1913). Über die sogenannte "kristallisationskraft". *6. jahresbericht d. Niedersachischen geologischen vereins*, pages 92–115. *Cited page 60*
- Candlot, E. (1898). *Ciments et chaux hydrauliques: fabrication–propriétés–emploi*. Librairie polytechnique baudry et cie, Paris. *Cited page 39*
- Cardell, C., Delalieux, F., Roumpopoulos, K., Moropoulou, A., Auger, F., and Grieken, R. V. (2003). Salt-induced decay in calcareous stone monuments and buildings in a marine environment in SW France. *Construction and Building Materials*, 17:165–179. *Cited page 57*
- Caruso, F. and Flatt, R. J. (2014a). Further steps towards the solution of Correns ' dilemma. In Clercq, H. D., editor, *SWBSS 2014 Third International Conference on Salt Weathering of Buildings and Stone Sculptures*, number October, pages 199–209, Brussels. *Cited page 62*
- Caruso, F. and Flatt, R. J. (2014b). Measuring crystallization pressure: can Correns's experiments be repeated. In *International Congress on the Deterioration and Conservation of Stone*, pages 1–7, New York. *Cited page 61*
- CEMBUREAU (2014). World cement production by region - Evolution 2001-2014. Technical report, CEMBUREAU, Brussels. *Cited page 58*

## BIBLIOGRAPHY

---

- Chabreliè, A. (2010). *Mechanisms of Degradation of Concrete by External Sulfate Ions under Laboratory and Field Conditions*. PhD thesis, EPFL.  
*Cited pages 39, 42, 43, and 44*
- Chanvillard, G. and Barbarulo, R. (2011). Stress from confined crystallization occurring by internal phase change: Application to the case of delayed ettringite formation in hardened cement paste. *Mechanics and Physics of Porous Solids (MPPS) - A tribute to Prof. Olivier Coussy*, pages 71–93.  
*Cited page 40*
- Chen, J. J., Sorelli, L., Vandamme, M., Ulm, F. J., and Chanvillard, G. (2010). A coupled nanoindentation/SEM-EDS study on low water/cement ratio portland cement paste: Evidence for C-S-H/Ca(OH)<sub>2</sub> nanocomposites. *Journal of the American Ceramic Society*, 93:1484–1493.  
*Cited pages 107 and 115*
- Chengsheng Ouyang and Wen F. Chang, A. N. (1987). Sulfate Attack Resistance of Portland Cement Mixtures Containing Phosphogypsum. *Special Publication*, 100:2007–2026.  
*Cited page 41*
- Chwast, J., Todorović, J., Janssen, H., and Elsen, J. (2014). Gypsum efflorescence on clay brick masonry: field survey and literature study. *Construction and Building Materials*, 85:57–64.  
*Cited page 54*
- Colas, J. (2013). *Etude de la valorisation des déblais de chantiers de tunnels riches en sulfates en granulats à béton*. PhD thesis, Paris-Est.  
*Cited page 41*
- Convention France-UNESCO (2006). Cultural heritage & local development. Technical report, UNESCO.  
*Cited page 57*
- Correns, C. W. (1949). Growth and dissolution of crystal under linear pressure. *Discuss Faraday Soc*, pages 5–267. *Cited pages 54, 60, 61, and 63*
- Correns, C. W. and Steinborn, W. (1939). Experimente zur Messung und Erklärung der sogenannten Kristallisationskraft. *Z Krist (A)*, 101:117–133.  
*Cited pages 54, 60, and 63*

- Coussy, O. (2006). Deformation and stress from in-pore drying-induced crystallization of salt. *Journal of the Mechanics and Physics of Solids*, 54(8):1517–1547. *Cited pages 54, 55, 63, and 65*
- Coussy, O. (2011). *Mechanics and physics of porous solids*. John Wiley & Sons, Inc, New York. *Cited pages 54 and 60*
- Coussy, O. and Monteiro, P. J. M. (2007). Unsaturated poroelasticity for crystallization in pores. *Computers and Geotechnics*, 34(4):279–290. *Cited pages 53 and 54*
- Coussy, O. and Monteiro, P. J. M. (2008). Poroelastic model for concrete exposed to freezing temperatures. *Cement and Concrete Research*, 38:40–48. *Cited pages 53 and 54*
- Cramond, N. J. (1984). Examination of mortar bars containing varying percentages of coarsely crystalline gypsum as aggregate. *Cement and Concrete Research*, 14:225–230. *Cited page 41*
- Cramond, N. J. (1985). Quantitative X-ray diffraction analysis of ettringite, thaumasite and gypsum in concretes and mortars. *Cement and Concrete Research*, 15:431–441. *Cited page 41*
- Damidot, D. and Glasser, F. (1993). Thermodynamic investigation of the CaO-Al<sub>2</sub>O<sub>3</sub>-CaSO<sub>4</sub>-H<sub>2</sub>O system at 25°C and the influence of Na<sub>2</sub>O. *Cement and Concrete Research*, 23(8):221–238. *Cited page 49*
- Damidot, D., Lothenbach, B., Herfort, D., and Glasser, F. (2011). Thermodynamics and cement science. *Cement and Concrete Research*, 41(7):679–695. *Cited pages 49 and 97*
- Derluyn, H., Moonen, P., and Carmeliet, J. (2014). Deformation and damage due to drying-induced salt crystallization in porous limestone. *Journal of the Mechanics and Physics of Solids*, 63:242–255. *Cited page 65*
- Désarnaud, J. (2009). *Mécanisme de Croissance et de dissolution de cristaux de KCl sous Charge : Apport dans la connaissance des mécanismes*

## BIBLIOGRAPHY

---

- d'altération des pierres par les sels*. PhD thesis, Université Paul Cézane Aix-Marseille III. *Cited pages 61 and 67*
- Doehne, E. (2002). Salt Weathering : A Selective Review. *Geological Society Special Publication*, 205:51–64. *Cited pages 57 and 67*
- Doehne, E. and Clifford, A. P. (2010). *Stone Conservation : An Overview of Current*. Getty Conservation Institute, Los Angeles, CA. *Cited pages 54, 57, and 67*
- Drouet, E. (2011). *Impact de la température sur la carbonatation des matériaux cimentaires : prise en compte des transferts hydriques*. PhD thesis, ENS Cachan. *Cited page 105*
- EC (1996). Origin, mechanisms and effects of salts on degradation of monuments in marine and continental environments. In Zezza, F., editor, *Origin, mechanisms and effects of salts on degradation of monuments in marine and continental environments*, number 4, Bari, Italy. *Cited pages 57 and 67*
- Escadeillas, G. and Hornain, H. (2008). La durabilité des bétons vis-à-vis des environnements chimiquement agressifs. In *La durabilité des bétons*, pages 613–705. Presse de l'École des Ponts et Chaussées. *Cited pages 39, 40, 41, 43, 45, 59, and 63*
- Espinosa-Marzal, R. M., Franke, L., and Deckelmann, G. (2008). Model for the mechanical stress due to the salt crystallization in porous materials. *Construction and Building Materials*, 22(7):1350–1367. *Cited pages 54 and 55*
- Espinosa-Marzal, R. M., Hamilton, A., McNall, M., Whitaker, K., and Scherer, G. (2011). The chemomechanics of crystallization during rewetting of limestone impregnated with sodium sulfate. *Journal of Materials Research*, 26:1472–1481. *Cited page 55*

- Espinosa-Marzal, R. M. and Scherer, G. (2008). Crystallization of sodium sulfate salts in limestone. *Environmental Geology*, 56(3-4):605–621. *Cited page 55*
- EU (2009). *Preserving our heritage , Improving our environment, Vol II*, volume II. European Communitites. *Cited pages 57, 58, and 67*
- Feng, P., Garboczi, E. J., Miao, C., and Bullard, J. W. (2015). Microstructural origins of cement paste degradation by external sulfate attack. *Construction and Building Materials*, 96:391–403. *Cited pages 45 and 65*
- Flatt, R. J. (2002a). Hydration pressure: a bad case of crystallization pressure. In *SALTeXPERT Workshop*, Prague. *Cited page 66*
- Flatt, R. J. (2002b). Salt damage in porous materials: how high supersaturations are generated. *Journal of Crystal Growth*, 242(3-4):435–454. *Cited pages 45, 54, 62, 63, 68, 183, 184, and 232*
- Flatt, R. J., Caruso, F., Maria, A., Sanchez, A., and Scherer, G. W. (2014). Chemomechanics of salt damage in stone. *Nature Communications*, 5:1–5. *Cited pages 55 and 65*
- Flatt, R. J. and Scherer, G. W. (2008). Thermodynamics of crystallization stresses in DEF. *Cement and Concrete Research*, 38(3):325–336. *Cited pages 49, 146, 177, and 211*
- Flatt, R. J., Scherer, G. W., and Bullard, J. W. (2011). Cement and Concrete Research Why alite stops hydrating below 80 % relative humidity. *Cement and Concrete Research*, 41(9):987–992. *Cited page 230*
- Flatt, R. J., Steiger, M., and Scherer, G. W. (2006). A commented translation of the paper by C.W. Correns and W. Steinborn on crystallization pressure. *Environmental Geology*, 52(2):187–203. *Cited pages 60, 63, and 98*
- Garboczi, E. J. and Bentz, D. P. (1998). The microstructure of portland cement-based materials: computer simulation and percolation theory. In *Material research Society Symposium Proceedings*, pages 89–100, San Francisco. *Cited page 67*

## BIBLIOGRAPHY

---

- Gartner, E. M. (2009). Cement and Concrete Research Cohesion and expansion in polycrystalline solids formed by hydration reactions — The case of gypsum plasters. *Cement and Concrete Research*, 39(4):289–295.  
*Cited page 155*
- Germaine, J. T. (2009). *Measurements for Engineers*. John Wiley & Sons, Inc.  
*Cited pages 82 and 88*
- Germinario, L., Claudio, M., and Lara, M. (2014). Euganean trachyte in the monumental built environment: archaeometric discriminating criteria and weathering analysis. Technical report, Università degli Studi di Padova.  
*Cited page 57*
- Gollop, R. S. and Taylor, H. F. W. (1992). Microstructural and microanalytical studies of sulfate attack. *Cement and Concrete Research*, 22:1027–1038.  
*Cited pages 40, 41, 42, 43, 44, 45, 46, 48, 140, and 146*
- Gollop, R. S. and Taylor, H. F. W. (1995). Microstructural and microanalytical studies of sulfate attack III. Sulfate-resisting portland cement: Reactions with sodium and magnesium sulfate solutions. *Cement and Concrete Research*, 25(7):1581–1590.  
*Cited page 41*
- Gollop, R. S. and Taylor, H. F. W. (1996). Microstructural and microanalytical studies of sulfate attack. V. Comparison of different slag blends. *Cement and Concrete Research*, 26(7):1029–1044. *Cited pages 39 and 41*
- Gonzalez, M. A. and Irassar, E. F. (1997). Ettringite formation in low C3A portland cement exposed to sodium sulfate solution. *Cement and Concrete Research*, 27(7):1061–1072.  
*Cited page 48*
- Goto, S. and Roy, D. M. (1981). The effect of w/c ratio and curing temperature on the permeability of hardened cement paste. *Cement and Concrete Research*, 11(1):575–579.  
*Cited page 41*
- Goudie, A. and Viles, H. (1997). *Salt weathering hazards*. John Wiley and sons, New York.  
*Cited pages 54 and 66*

- Gupta, S. (2013). *Sodium chloride crystallization in drying porous media : influence of inhibitor*. PhD thesis, Eindhoven University of Technology.  
*Cited page 54*
- Haynes, H. (2002). Sulfate Attack on Concrete: Laboratory vs. Field Experience. In *Concrete International*, volume 24, pages 64–70.  
*Cited pages 39 and 59*
- Hjorth, L. (1983). Development and application of high-density cement-based materials. *Philosophical Transactions of the Royal Society of London*, 310:167–173.  
*Cited page 41*
- Hopital, E. (2014). *Aluminium and alkali uptake in calcium silicate hydrates ( C - S - H )*. PhD thesis, EPFL.  
*Cited pages 96 and 100*
- Huet, B. (2005). *Comportement à la corrosion des armatures dans un béton carbonaté . Influence de la chimie de la solution interstitielle et d 'une barrière de transport*. PhD thesis, INSA Lyon.  
*Cited page 100*
- Irassar, E. F., Bonavetti, V. L., and Gonza, M. (2003). Microstructural study of sulfate attack on ordinary and limestone Portland cements at ambient temperature. *Cement and Concrete Research*, 33:31–41.  
*Cited pages 43 and 49*
- Irassar, E. F. and Di Maio, A. (1996). Sulfate attack on concrete with mineral admixtures. *Cement and Concrete Research*, 26(1):113–123. *Cited page 44*
- Jennings, H. M. (2008). Refinements to colloid model of C-S-H in cement: CM-II. *Cement and Concrete Research*, 38:275–289.  
*Cited pages 107 and 203*
- Jödecke, M., Xia, J., Pérez-Salado Kamps, A., and Maurer, G. (2015). Influence of (phenol and sodium sulfate) on the solubility of carbon dioxide in water. *The Journal of Chemical Thermodynamics*, 86:123–129.  
*Cited page 100*
- Kopp, H. (1855). Uber die bildung von krystallen mit kernen,. *Ann. Chem. Pharm.*, 44:124.  
*Cited page 60*

## BIBLIOGRAPHY

---

- Kreijger, P. C. (1983). Environmental factors affecting building and its durability. In *Séminaire Durabilité des bétons et des pierres*, Paris. Cited page 40
- Kretz, T., Technical for Centre for Roads, B., and Transport (2011). Large road bridges management - Special features Implementation of risk analysis in ordinary bridge management. Cited page 58
- Kunther, W. (2012). *Investigation of sulfate attack by experimental and thermodynamic means*. PhD thesis, EPFL. Cited page 44
- Kunther, W., Lothenbach, B., and Scrivener, K. L. (2013). On the relevance of volume increase for the length changes of mortar bars in sulfate solutions. *Cement and Concrete Research*, 46:23–29. Cited pages 62, 67, 98, 134, and 177
- Kunther, W., Lothenbach, B., and Skibsted, J. (2015). Influence of the Ca/Si ratio of the C–S–H phase on the interaction with sulfate ions and its impact on the ettringite crystallization pressure. *Cement and Concrete Research*, 69:37–49. Cited pages 134, 146, and 155
- Lafuma, H. (1929). *Théorie de l'expansion des liants hydrauliques*. Revue des matériaux de construction et de travaux publics. Cited pages 39 and 45
- Lavalle, M. (1853). Recherches sur la formation de cristaux à la température ordinaire. *Compt. Rend. Acad. Sci.*, 34:493–495. Cited page 60
- Lawrence, C. D. (1995). Mortar expansions due to delayed ettringite formation. Effects of curing period and temperature. *Cement and Concrete Research*, 25(4):903–914. Cited page 52
- LCPC (2003). Recommandations pour la durabilité des bétons durcis soumis au gel. Technical report, Laboratoire Central des Ponts et Chaussées, Paris. Cited page 52
- Le Bescop, P. and Solet, C. (2006). External sulphate attack by ground water. Experimental study on CEM I cement pastes. *Revue Européenne de Génie Civil*, 10(November):1127–1145. Cited pages 39, 40, and 43

- Le Chatelier, H. (1887). *Recherches expérimentales sur la constitution des mortiers hydrauliques*. PhD thesis, Paris. *Cited page 39*
- Lecampion, B. (2010). Stress-induced crystal preferred orientation in the poromechanics of in-pore crystallization. *Journal of the Mechanics and Physics of Solids*, 58(10):1701–1715. *Cited page 50*
- Lee, J. V. D. (1998). *Thermodynamic and mathematical concepts of CHESSE, Technical Report Nr. LHM/RD/98/39*. Centre d’Informatique Géologique of the Ecole des Mines de Paris, Ecole des Mines de Paris, Fontainebleau, France. *Cited page 97*
- Lothenbach, B., Bary, B., Le Bescop, P., Schmidt, T., and Leterrier, N. (2010). Sulfate ingress in Portland cement. *Cement and Concrete Research*, 40(8):1211–1225. *Cited pages 40, 44, and 134*
- Lothenbach, B. and Winnefeld, F. (2006). Thermodynamic modelling of the hydration of Portland cement. *Cement and Concrete Research*, 36(2):209–226. *Cited pages 97 and 185*
- Maltais, Y., Samson, E., and Marchand, J. (2004). Predicting the durability of Portland cement systems in aggressive environments — laboratory validation. *Cement and Concrete Research*, 34:1579–1589. *Cited page 43*
- Mantellato, S., Palacios, M., and Flatt, R. J. (2015). Cement and Concrete Research Reliable specific surface area measurements on anhydrous cements. *Cement and Concrete Research*, 67:286–291. *Cited pages 168, 191, and 249*
- Marchand, J., Odler, I., , and Skalny, J. P. (2002a). Case histories. In *Sulfate attack on Concrete*. CRC Press. *Cited page 39*
- Marchand, J., Odler, I., , and Skalny, J. P. (2002b). Introduction. In *Sulfate attack on Concrete*. CRC Press. *Cited page 59*
- Marchand, J. and Odler, I. (2002). Assessment of cement and concrete performance under sulfate attack. In *Sulfate attack on Concrete*. CRC Press. *Cited page 155*

## BIBLIOGRAPHY

---

- Massiot, D., Fayon, F., Capron, M., King, I., Le Calvé, S., Alonso, B., Durand, J. O., Bujoli, B., Gan, Z., and Hoatson, G. (2002). Modelling one- and two-dimensional solid-state NMR spectra. *Magnetic Resonance in Chemistry*, 40:70–76. *Cited page 93*
- Mather, B. (1964). Effects of sea water on concrete. *Highway Research Record*, 113:23. *Cited pages 39 and 59*
- Mather, B. (1996). Discussion of “the process of sulfate attack on cement mortars. *Advanced cement based materials*, pages 109–110. *Cited page 46*
- Matschei, T. (2007). *Thermodynamics of Cement Hydration*. PhD thesis, University of Aberdeen. *Cited page 185*
- Matschei, T., Lothenbach, B., and Glasser, F. P. (2007). Thermodynamic properties of Portland cement hydrates in the system CaO–Al<sub>2</sub>O<sub>3</sub>–SiO<sub>2</sub>–CaSO<sub>4</sub>–CaCO<sub>3</sub>–H<sub>2</sub>O. *Cement and Concrete Research*, 37(10):1379–1410. *Cited page 97*
- Mehta, P. (1983). Mechanism of sulfate attack on portland cement concrete — Another look. *Cement and Concrete Research*, 13:401–406. *Cited pages 45 and 140*
- Mehta, P. (1992). *Sulfate attack on concrete—A critical review*. Amer Ceramic Society, Westerville, OH. *Cited page 47*
- Mehta, P., Pirtz, D., and Polivka, M. (1979). Properties of alite cements. *Cement and Concrete Research*, 9:439–450. *Cited page 47*
- Meijer, J. and Van Rosmalen, G. (1984). Solubilities and supersaturations of calcium sulfate and its hydrates in seawater. *Desalination*, 51:255–305. *Cited pages 40 and 59*
- Meulenyzer, S. and Chen, J. J. (2013). Spectral-spatial image processing strategies for classifying multispectral SEM-EDS X-Ray maps of cementitious materials. In *14th Euroseminar on Microscopy Applied to Building Materials*, number JUNE, Helsingor, Denmark. *Cited page 95*

- Meybeck, M. (2003). Chemical characteristics of rivers. *Fresh surface water*, I(iii). *Cited pages 40 and 59*
- Michaux, L. (1994). Géochimie et migration en milieu granitique, interaction avec les ouvrages de stockage. Rôle et évolution des matériaux argileux de barrières ou- vrages. Technical report, CEA. *Cited page 56*
- Moore, A. E. and Taylor, H. F. W. (1970). Crystal structure of ettringite. *Acta Crystal*, B26:Acta Crystal. *Cited page 45*
- Mortensen, H. (1933). Die "Salzspaltung" und ihre bedeutung für die regional-klimatische gliederung der wüsten. *Petermanns Geographische Mittheilungen*, 5-6:130–135. *Cited pages 60 and 66*
- Müllauer, W., Beddoe, R. E., and Heinz, D. (2013). Sulfate attack expansion mechanisms. *Cement and Concrete Research*, 52:208–215. *Cited pages 45, 48, 49, 50, 51, 140, and 155*
- Novak, G. a. and Colville, A. a. (1989). Efflorescent mineral assemblages associated with cracked and degraded residential concrete foundations in Southern California. *Cement and Concrete Research*, 19(c):1–6. *Cited page 39*
- OECD (2006). The Roles of Storage in the Management of Long-lived Radioactive Waste Practices and Potentialities in OECD Countries. Technical Report 6043, OECD, Paris. *Cited page 55*
- Ouhadi, V. R. and Yong, R. N. (2008). Ettringite formation and behaviour in clayey soils. *Applied Clay Science*, 42(1-2):258–265. *Cited page 59*
- Ouyang, C., Nanni, A., and Chang, W. F. (1988). Internal And External Sources of Sulfate Ions In Portland Cement Mortar: Two Types of Chemical Attack. *Cement and Concrete Research*, 18(c):699–709. *Cited pages 40 and 41*
- Padgett, J., Desroches, R., Nielson, B., Yashinsky, M., Kwon, O.-s., Burdette, N., and Tavera, E. (2008). Bridge Damage and Repair Costs

## BIBLIOGRAPHY

---

- from Hurricane Katrina. *Journal of Bridge Engineering*, (February):6–14.  
*Cited page 58*
- Parnell, S. and Oldfield, S. (2014). *The Routledge handbook on cities of the global south*. Routledge, New York, 1st editio edition. *Cited page 58*
- Parsegian, V. (2011). Hydration forces: Observations, explanations, expectations, questions. *Current Opinion in Colloid & Interface Science*.  
*Cited page 60*
- Ping, X. and Beaudoin, J. J. (1992a). Mechanism of sulfate expansion I. Thermodynamic Principle of Crystallization Pressure. *Cement and Concrete Research*, 22(1):631–640. *Cited pages 49 and 62*
- Ping, X. and Beaudoin, J. J. (1992b). Mechanism of sulfate expansion II. Validation of thermodynamic theory. *Cement and Concrete Research*, 22(i):845–854. *Cited pages 41, 49, and 62*
- Pinson, M. B., Masoero, E., Bonnaud, P. a., Manzano, H., Ji, Q., Yip, S., Thomas, J. J., Bazant, M. Z., Van Vliet, K. J., and Jennings, H. M. (2015). Hysteresis from Multiscale Porosity: Modeling Water Sorption and Shrinkage in Cement Paste. *Physical Review Applied*, 3:064009. *Cited page 107*
- Plowman, C. and Cabrera, J. G. (1996). The use of fly ash to improve the sulphate resistance of concrete. *Waste Management*, 16:145–149.  
*Cited page 41*
- Polivka, M. (1973). Factors influencing expansion of expansive cement concretes. *ACI SP-38*, pages 239–250. *Cited pages 60 and 67*
- Poulsen, S., Jakobsen, H. J., and Skibsted, J. (2009). Methodologies for measuring the degree of reaction in Portland Cement blends with supplementary cementitious materials by  $^{27}\text{Al}$  and  $^{29}\text{Si}$  MAS NMR spectroscopy. *Proc., 7th IBAUSIL – Internationale Baustoffagung*,, pages 177–188.  
*Cited page 93*

- Powers, T. C. (1945). A Working Hypothesis for Further Studies of Frost Resistance of Concrete. In *Journal Proceedings- American Concrete Institute*, volume 41, page 245. *Cited page 53*
- Powers, T. C. (1958). Structure and Physical Properties of Hardened Portland Cement Paste. *Journal of the American ceramic society*, 41:1. *Cited page 82*
- Ramon, A. and Alonso, E. (2012). Crystal growth under bridge foundations. In *International Workshop of Young Doctor in Geomechanics*, number 61, pages 61–66, Paris. *Cited page 59*
- Rasheeduzzafar, B. and Abduljawwad, S. N. (1994). Magnesium-sodium sulfate attack in plain and blended cements. *Journal of Materials in Civil Engineering*, 6(2):201–222. *Cited page 41*
- Reading, T. J. (1982). Physical Aspects of Sodium Sulfate Attack on Concrete. *Special Publication*, 77. *Cited page 39*
- Reed, C. (2002). Soggy soil sours Egyptian sandstone. *Geotimes*, 47(9):28–29. *Cited page 57*
- Rijniers, L. (2004). *Salt crystallization in porous materials : an NMR study*. PhD thesis, Eindhoven University of Technology. *Cited pages 54, 61, and 65*
- Rijniers, L. A., Huinink, H. P., Pel, L., and Kopinga, K. (2004). Salt crystallization as damage mechanism in masonry. In *International Brick and Block Masonry Conference*, pages 1–6, Amsterdam. *Cited page 65*
- Rijniers, L. A., Huinink, H. P., Pel, L., and Kopinga, K. (2005). Experimental Evidence of Crystallization Pressure inside Porous Media. *Physical Review Letters*, 075503(February):23–26. *Cited pages 63 and 65*
- Rodriguez-Navarro, C. (1999). Salt Weathering : Influence of Evaporation Rate , Supersaturation and Crystallization Pattern. *Earth Surface Processes and Landforms*, 24(March):191–209. *Cited pages 54 and 66*

## BIBLIOGRAPHY

---

- Rodriguez-Navarro, C. and Doehne, E. (1998). The role of sepiolite-palygorskite in the decay of ancient egyptian limestone sculptures. *Clays and Clay Minerals*, 46(4):414–422. *Cited page 57*
- Rodriguez-Navarro, C., Doehne, E., and Sebastian, E. (2000). How does sodium sulfate crystallize? Implications for the decay and testing of building materials. *Cement and Concrete Research*, 30(10):1527–1534. *Cited page 54*
- Rossen, J. E. (2014). Stability of C-A-S-H in pastes of alite and cement blended with supplementary cementitious materials. *Laboratory of construction material*, 6294. *Cited page 96*
- Roy, S. and Fouillac, a. M. (2004). Uncertainties related to sampling and their impact on the chemical analysis of groundwater. *TrAC - Trends in Analytical Chemistry*, 23(3):185–193. *Cited page 56*
- Rozière, E., Loukili, a., El Hachem, R., and Grondin, F. (2009). Durability of concrete exposed to leaching and external sulphate attacks. *Cement and Concrete Research*, 39(12):1188–1198. *Cited page 42*
- Rzonca, B. G. F., Pride, R. M., and Colin, D. (1990). Concrete deterioration, east losangeles county area : case study. *Journal of Performance of Constructed Facilities*, 4(1):24–29. *Cited page 39*
- Saidov, T. A. (2012). *Sodium sulfate heptahydrate in weathering phenomena of porous materials*. PhD thesis, Eindhoven University of Technology. *Cited page 54*
- Saidov, T. a., Pel, L., and Kopinga, K. (2015). Crystallization Pressure of Sodium Sulfate Heptahydrate. *Crystal Growth & Design*, 15:2087–2093. *Cited page 64*
- Salome, E. and Sigurdsson, A. (2014). Chemical composition of precipitation and river water in southern Iceland : effects of Eyjafjallajökull volcanic eruptions and geothermal power plants . *Procedia Earth and Planetary Science*, 10:358–364. *Cited page 59*

- Scherer, G. W. (1993). Freezing gels. *Journal of Non-Crystalline Solids*, 155:1–25. *Cited page 53*
- Scherer, G. W. (1999). Crystallization in pores. *Cement and Concrete Research*, 29:1347–1358. *Cited pages 45, 53, 54, 57, 59, 62, 63, 68, 146, and 232*
- Scherer, G. W. (2004). Stress from crystallization of salt. *Cement and Concrete Research*, 34:1613–1624. *Cited pages 54, 59, 63, 146, 183, and 184*
- Schmidt, T. (2007). *Sulfate attack and the Role of Internal carbonate on the formation of thaumasite*. PhD thesis, EPFL. *Cited pages 41 and 49*
- Schmidt, T., Lothenbach, B., Romer, M., Neuenschwander, J., and Scrivener, K. (2009). Physical and microstructural aspects of sulfate attack on ordinary and limestone blended Portland cements. *Cement and Concrete Research*, 39(12):1111–1121. *Cited pages 39, 42, 44, 45, 49, 134, and 140*
- Schmidt, T., Lothenbach, B., Romer, M., Scrivener, K., Rentsch, D., and Figi, R. (2008). A thermodynamic and experimental study of the conditions of thaumasite formation. *Cement and Concrete Research*, 38:337–349. *Cited page 41*
- Scrivener, K. (2004). Backscattered electron imaging of cementitious microstructures: Understanding and quantification. *Cement and Concrete Composites*, 26:935–945. *Cited page 231*
- Scrivener, K. (2012). Expansive degradation mechanisms in concrete: linking chemical reactions with mechanical consequences. In *W(H)YDOC 2012*, Paris. Ecole des Ponts ParisTech. *Cited pages 43, 46, and 155*
- Scrivener, K. and Campas, A. (2003). Calcium aluminate cements. *Advanced concrete technology: Constituent materials*, 2:1–2. *Cited page 41*
- Sekerka, R. F. and Cahn, J. W. (2004). Solid–liquid equilibrium for non-hydrostatic stress. *Acta Materialia*, 52(6):1663–1668. *Cited page 230*

## BIBLIOGRAPHY

---

- Siedel, H. and Leisen, H. (2008). Salt load and deterioration of sandstone at temple of Angkor Wat, Cambodia. In Lukaszewicz, J. and Niemcewicz, P., editors, *International Congress on Deterioration and Conservation of Stone*, volume I, pages 267–274. *Cited page 57*
- Skibsted, J. (1997). Hydration kinetics for the alite, belite, and calcium aluminate phase in Portland Cements from 27 Al and 29 Si MAS NMR spectroscopy. In *10th\_ICCC*. *Cited page 93*
- Skibsted, J., Henderson, E., and Jakobsen, H. (1993). Characterization of calcium aluminate phases in cements by aluminum-27 MAS NMR spectroscopy. *Inorganic chemistry*, 32:1013–1027. *Cited page 93*
- Steiger, M. (2005a). Crystal growth in porous materials—I: The crystallization pressure of large crystals. *Journal of Crystal Growth*, 282(3-4):455–469. *Cited pages 54, 63, and 64*
- Steiger, M. (2005b). Crystal growth in porous materials—II: Influence of crystal size on the crystallization pressure. *Journal of Crystal Growth*, 282(3-4):470–481. *Cited pages 23, 63, 64, and 148*
- Taber, S. (1916). The growth of crystals under external pressure. *American Journal of Science*, 41:532–556. *Cited pages 23, 60, and 61*
- Taber, S. (1917). Pressure phenomena accompanying the growth of crystals. *Geology*, 3(4):297–302. *Cited page 60*
- Taylor, H. F. W. (1996). Ettringite in cement paste and concrete. In *Int. Rilem Conf., Concrete: from material to structure*, pages 55–76, Arles. *Cited page 40*
- Taylor, H. F. W. (1998). *Cement chemistry*. Thomas Telford, London. *Cited pages 40, 41, 48, 52, 59, 67, 93, and 144*
- Taylor, H. F. W., Famy, C., and Scrivener, K. (2001). Delayed ettringite formation. *Cement and Concrete Research*, 31(5):683–693. *Cited pages 52 and 67*

- Texas Department of Transportation (2005). Guidelines for Treatment of Sulfate-Rich Soils and Bases in Pavement Structures. Technical Report September, Texas Department of Transportation. *Cited page 59*
- The Getty Conservation Institute (2000). Values and Heritage Conservation. Technical report, The Getty Conservation Institute, Los Angeles, CA. *Cited page 57*
- Thorvaldson, T. (1954). Chemical aspects of the durability of cement products. In *Proceedings of the 3rd International Symposium on the Chemistry of Cement, Cement and Concrete Association*, page 436, London. *Cited page 47*
- Tian, B. and Cohen, M. D. (2000). Does gypsum formation during sulfate attack on concrete lead to expansion? *Cement and Concrete Research*, 30:117–123. *Cited pages 48 and 155*
- Tulliani, J. M., Montanaro, L., Negro, A., and Collepardi, M. (2002). Sulfate attack of concrete building foundations induced by sewage waters. *Cement and Concrete Research*, 32:843–849. *Cited page 39*
- Ulm, F. J., Constantinides, G., and Heukamp, F. H. (2004). Is concrete a poromechanics materials?-A multiscale investigation of poroelastic properties. *Materials and Structures*, 37(February):43–58. *Cited page 40*
- Wakim, J. (2006). *Influence des solutions aqueuses sur le comportement des roches argileuses*. PhD thesis, Ecole nationale supérieure des mines de Paris. *Cited page 56*
- Wang, J. G. (1994). Sulfate attack on hardened cement paste. *Cement and Concrete Research*, 24(4):735–742. *Cited page 47*
- Wellman, H. and Wilson, A. (1965). Salt weathering, a neglected geological erosive agent in coastal and arid environments. *Nature*, 205:1097–1098. *Cited page 63*
- Wellman, H. and Wilson, A. (1968). *Salt weathering or fretting*. The Encyclopedia of Geomorphology, Stroudsburg, Pennsylvania. *Cited page 63*

## BIBLIOGRAPHY

---

- Yang, S., Zhongzi, X., and Mingshu, T. (1996). The Process of Sulfate Attack on Cement Mortars. *Advanced cement based materials*, 7355(96).  
*Cited page 47*
- Ye, G., Hu, J., Breugel, K., and Stroeven, P. (2002). Characterization of the development of microstructure and porosity of cement-based materials by numerical simulation and ESEM image analysis. *Materials and Structures*, 35(December):603–613.  
*Cited page 67*
- Yu, C., Sun, W., and Scrivener, K. (2013). Mechanism of expansion of mortars immersed in sodium sulfate solutions. *Cement and Concrete Research*, 43:105–111.  
*Cited pages 39, 42, 43, 44, 45, 46, 49, 68, 134, 140, 146, and 155*
- Yu, C., Sun, W., and Scrivener, K. (2015). Degradation mechanism of slag blended mortars immersed in sodium sulfate solution. *Cement and Concrete Research*, 72:37–47.  
*Cited pages 45 and 134*
- Zeng, Q., Fen-Chong, T., Dangla, P., and Li, K. (2011). A study of freezing behavior of cementitious materials by poromechanical approach. *International Journal of Solids and Structures*, 48(22-23):3267–3273.  
*Cited pages 53 and 54*
- Zeza, F. and Mad, F. (1995). Marine aerosol and stone decay. *the Science of the Total Environment*, 167:123–143.  
*Cited pages 54 and 57*